

NASA Conference Publication 3231

Joint Acoustic Propagation Experiment (JAPE-91) Workshop

Compiled by
William L. Willshire
and David Chestnutt
Langley Research Center
Hampton, Virginia

Proceedings of a workshop jointly sponsored by
the National Aeronautics and Space Administration,
Washington, D.C., and the University of Mississippi,
Oxford, Mississippi, and held in
Hampton, Virginia
April 28, 1993

NASA
National Aeronautics and
Space Administration
Office of Management
Scientific and Technical
Information Program

1993



Preface

In theory the sound a vehicle emits can be used to detect, track and identify the vehicle. In fact, in the case of underwater acoustics the navies of the world have used passive sonar techniques as a primary means of gathering target information. In principle, the sound airborne vehicles emit can also be used for these purposes and, in fact, artillery ranging has been used in one form or another for many years.

Acoustic propagation in air differs from that in water in a few major ways. The sound propagation speed in air is much slower than in water while the vehicle speeds are much greater in air than in water. Therefore, vehicle Mach numbers are much greater in air than in water. Additionally, the time constants under which propagation conditions can radically change are generally much shorter in air than in water. The potentially rapid changes in propagation conditions in air make acoustic system performance estimation difficult, particularly within any practical confidence bounds.

As in underwater applications, in air the major thrust of research is in developing validated propagation models. The Joint Acoustic Propagation Experiment (JAPE), performed under the auspices of the NATO AC/243, Panel 3, Research Study Group 11 (RSG 11) on Automatic Pattern Recognition in Battlefield Surveillance with Mechanical Waves, was conducted to obtain a comprehensive set of acoustic propagation data to validate outdoor, long range propagation models. Of primary importance in the performance of this experiment was the extensive characterization of the atmosphere, including turbulence measurements during the tests. The quality and quantity of the meteorological data collected make this experiment unique.

The JAPE-91 workshop was held in Hampton, Virginia, USA on April 28, 1993. The purpose of the meeting was to exchange information and results from the experiment. The hosts would like to express their appreciation to the participants for attending and for sharing their knowledge and expertise.

Henry E. Bass
Professor of Physics
The University of Mississippi
Oxford, Mississippi

David Chestnutt
Head, Applied Acoustics Branch
NASA Langley Research Center
Hampton, Virginia

William L. Willshire, Jr.
Research Engineer
Applied Acoustics Branch
NASA Langley Research Center
Hampton, Virginia

CONTENTS

Preface	iii
Joint Acoustic Propagation Experiment (JAPE)	1-7
Benny L. Carnes, Robert O. Olsen, and Bruce W. Kennedy	
Some Results Gained From JAPE—An Overview	19-2
Gunnar R. Becker	
Intercomparison of Remote and Balloon-Borne Sensors Operated at JAPE-91	31-3
Richard J. Okrasinski, Greg J. Cook, and Robert O. Olsen	
Effects of Atmospheric Variations on Acoustic System Performance	41-4
Robert Nation, Stephen Lang, Robert Olsen, and Prasan Chintawongvanich	
Comparison of Measured and Predicted Pure Tone Propagation Levels from JAPE-1: An Evaluation of the Performance of ASOPRAT	55-5
Carl K. Frederickson, Henry E. Bass, Richard Raspet, and John Messer	
Ground Characterization for JAPE	65-6
Keith Attenborough and Shahram Taherzadeh	
JAPE 91: Influence of Terrain Masking on the Acoustic Propagation of Helicopter Noise	79-7
P. Naz	
Comparisons of Calculated and Measured Helicopter Noise Near Instrument Hill	87-8
Henry E. Bass and Chulsoo You	
Preliminary Analysis of Amplitude and Phase Fluctuations in the JAPE Multiple Tone Data to Distances of 500 Meters	93-9
James Rogers, Radomir Sokolov, Daniel Hicks, and Lloyd Cartwright	
Dimensional Analysis of Acoustically Propagated Signals	107-10
Scott D. Hansen and Dennis W. Thomson	
Comparison Between 1-Minute and 15-Minute Averages of Turbulence Parameters	119-11
John M. Noble	
Beamforming in an Acoustic Shadow	129-130
David Havelock, Michael Stinson, and Gilles Daigle	
Analysis of Passive Acoustic Ranging of Helicopters from the Joint Acoustic Propagation Experiment	131-13
Benny L. Carnes and John C. Morgan	
Acoustic Target Detection and Classification Using Neural Networks	171-174
James A. Robertson and Mark Conlon	
Preliminary Analysis of the JAPE Ground Vehicle Test Data With an Artificial Neural Network Classifier	181-185
Nathan F. Larsen and Ben L. Carnes	

**JAPE-91 Workshop
Participant List**

NAME	Organization & Address	Telephone
Erik A. Andersen	Danish Defence Research Establishment	(45)39272233
Keith Attenborough	The Open University, Milton Keynes, UK	(908) 652766
Henry E. Bass	Univ. of Mississippi, University, MS 38677	(601)232-5840
Gunnar R. Becker	Atlas Elektronik, POB 448545, D 28 Bremen 44	+49-421-457-3275
Ben L. Carnes	USAE WES, Vicksburg, MS	(601) 634-2231
David Chestnutt	NASA Langley Research Center, MS 460, Hampton, VA 23681	(804) 864-5263
Prasan Chintawongvarich	Physical Science Lab, Las Cruces, NM 88003	(505) 522-9142
Mark Conlon	IIT Research Institute, Las Cruces, NM	(505) 521-3014
David A. Dadley	Defence Research Agency U.K.	0959 532222
Idar Dyrdal	Norwegian Defence Research Establishment	(47) 63807513
Bernard F. Engebos	US Army Research Lab, AMSRL-BE-M, White Sands Missle Range, NM 88003	(505) 678-1489
Carl Frederickson	Univ. of Mississippi, University, MS 38677	(601) 232-5768
Georges R. Garinther	US Army Research Lab, HRED, APG. MD 21005-5425	(410) 278-5984
Scott Hansen	Penn State University, University Park, PA	(814) 865-2859
David I. Havelock	NRC, Canada	(613) 993-7661
Joel T. Kalb	US Army Research Lab, HRED AMSR L-HR-SD, Aberdeen Proving Grounds, MD 21005-5425	(410) 278-5983
Geoff Kerry	University of Salford, UK	061 745 5582
Richard Lacoss	MIT Lincoln Lab 02173	(617) 981-7212
Claude Lahaze	Defence Research Establishment, Valcartier	(418) 844-4684
Tom Landers	Northrop Corporation	(213) 600-5727
Stephen W. Lang	Lockheed-Sanders, Nashua, NH	(603) 885-9067
Nathan Larsen	US Army Waterways Exp. Station	(601) 634-3504
Philip Le Masurier	Sikorsky Aircraft, Stratford, CT 06601	(203) 383-3499
Jerry R. Lundien	USACE/CERD-M	(202) 272-1847
Cyril Maillet	DGA/DAT/SEFT (French MOD)	(33)-1-4095-3480
Arnold Mueller	NASA Langley Research Center, MS 460, Hampton, VA 23681	(804) 864-5277
Robert Nation	Lockheed Sanders, Nashua, NH	(603) 885-9815
Pierre Naz	French German Research Institute of St. Louis	(33) 89695098

**JAPE-91 Workshop
Participant List
(continued)**

NAME	Organization & Address	Telephone
John M. Noble	US Army Research Lab, AMSRL-BE-M, White Sands Missile Range, NM 88002	(505) 678-3751
Richard Okrasinski	Physical Science Lab, Box 30002 Las Cruces, NM 88003	(505) 522-9496
William A. Peterson	US Army Research Lab, AMSRL-BE-A, White Sands Missle Range, NM 88002	(505) 678-1465
Jim Robertson	IIT Research Institute, Dayton, OH	(513) 252-9969
Jim Rogers	Michigan Tech, KRC	(906) 487-2750
Peter J. Soilleux	DRA (Malvern), St. Andrews Rd., Malvern, Worcs UK (WR143PS)	0684 894841
Huub van Hoof	Physics & Electronics Lab, FEL-TND, The Hague, Netherlands	3170 326 4221
Klemens Vattrodt	Fraunhofen-Gesellschaft, Karlsruhe, GE	49-721-6091-252`
Michael J. White	US Army Constr. Eng. Res. Lab	(217) 352-6511
William L. Willshire	NASA Langley Research Center, MS 460, Hampton, VA 23681	(804) 864-5270

JAPE-91 WORKSHOP
PRELIMINARY AGENDA

8:30	Ben Carnes and Robert Olsen	"Overview of Joint Acoustic Propagation Experiment"
8:50	Gunnar R. Becker	"Some Results Gained from JAPE - An Overview"
9:10	Richard Okrasinski, Greg Cook and Robert Olsen	"Intercomparison of Remote and Balloon Borne Sensors Operated During Jape 91"
9:30	Steve Lang, Rob Nation, Prasan Chintawongvanich and Robert Olsen	"Analysis of Jape Acoustic and Meteorological Data"
9:50	Break	
10:15	Carl Frederickson, Henry E. Bass and Richard Raspet	"Comparison of Measured and Predicted Pure Tone Propagation Levels from JAPE-91: An Evaluation of the Performance of ASOPRAT"
10:45	Keith Attenborough and Shahram Teherzadeh	"Ground Characterization for the JAPE Site"
11:00	Pierre Naz	"JAPE 91: Influence of Terrain Masking on the Acoustic Propagation of Helicopter Noise"
11:20	Chulsoo You and Henry Bass	"Comparisons of Calculated and Measured Helicopter Noise near Instrument Hill"
11:45	Lunch	
1:15	James Rogers, Radomir Sokolov, Daniel Hicks and Lloyd Cartwright	"Analysis of Signal Amplitude and Phase Fluctuations in the Jape Short Range Propagation Data"
1:45	Scott D. Hansen	"Micrometeorologically Forced Intermittency in Atmospherically Propagated Signals"
2:00	John Noble	"Comparison Between 1-Minute and 15-Minute Averages of Turbulence Parameters"
2:20	Dave Havelock	"Beamforming in an Acoustic Shadow"
2:50	Benny L. Carnes and John C. Morgan	"Analysis of Passive Acoustic Ranging of Helicopters from the Joint Acoustic Propagation Experiment"
3:20	Break	
3:40	James A. Robertson	"Acoustic Target Detection and Classification Using Neural Networks"
4:00	Nathan F. Larsen	Preliminary Analysis of the JAPE Ground Vehicle Test Data with an Artificial Neural Network Classifier
4:20	Benny L. Carnes	Summary and Closing Remarks

JOINT ACOUSTIC PROPAGATION EXPERIMENT (JAPE)

Benny L. Carnes
 Structures Laboratory
 USAE Waterways Experiment Station
 Vicksburg, Mississippi

201613
 P. 17

Robert O. Olsen
 U.S. Army Research Laboratory
 Battlefield Environment Directorate
 White Sands Missile Range, New Mexico

Bruce W. Kennedy
 Physical Science Laboratory
 New Mexico State University
 Las Cruces, New Mexico

ABSTRACT

The Joint Acoustic Propagation Experiment, performed under the auspices of NATO and the Acoustics Working Group, was conducted at White Sands Missile Range, New Mexico, USA, during the period 11-28 July 1991. JAPE consisted of 220 trials using various acoustic sources including speakers, propane cannon, various types of military vehicles, helicopters, a 155mm howitzer, and static high explosives. Of primary importance to the performance of these tests was the intensive characterization of the atmosphere before and during the trials. Because of the wide range of interests on the part of the participants, JAPE was organized in such a manner to provide a broad cross section of test configurations. These included short and long range propagation from fixed and moving vehicles, terrain masking, and vehicle detection. A number of independent trials were also performed by individual participating agencies using the assets available during JAPE. These tests, while not documented in this report, provided substantial and important data to those groups. Perhaps the most significant feature of JAPE is the establishment of a permanent data base which can be used by not only the participants but by others interested in acoustics.

A follow-on test was performed by NASA Langley Research Center during the period 19-29 August 1991 at the same location. These trials consisted of 59 overflights of supersonic aircraft in order to establish the relationship between atmospheric turbulence and the received sonic boom energy at the surface.

1.0 EXECUTIVE SUMMARY**1.1 The NATO Research Study Group 11 (RSG 11) on Automatic Pattern Recognition in Battlefield Surveillance with Mechanical Waves**

The RSG 11 on Automatic Pattern Recognition in Battlefield Surveillance with Mechanical Waves as an element of NATO AC/243, Panel 3, was established for the purpose of conducting cooperative research on the exploitation of mechanical waves (i.e. waves propagating by transfer of energy from particle to particle) for detecting, locating and identifying friendly and enemy men and machines on the battlefield or other areas of related military activity. Mechanical waves provide the opportunity for development of sensor systems capable of meeting this critical concern.

1.2 Tasking of Working Group Terms of Reference

JAPE was proposed to meet one of the objectives as stated in RSG-11 Terms of Reference, Objective II 3(a) exchange data and references, develop field experiment designs, organize cooperative field programs, and develop theoretical models that will enable

- (i) Improved understanding and utilization of acoustic-to-seismic coupling of seismic sensing devices and systems,
- (ii) Creation of new algorithms and systems for exploitation of the acoustic and seismic phenomenon in battlefield scenarios,
- (iii) Production of site objective acoustic and seismic processing algorithms capable of dealing with a wide range of terrain and meteorological conditions including cold, temperate and tropical environments.

Working within the guidelines of RSG-11 objectives, the member nations successfully organized and conducted the Acoustic Measurement Initiatives (AMI) field tests. AMI I was held at Schweinfurt, Germany, July 1987, and AMI II at Druex, France, September 1988. The test experiments have been analyzed and the results reported at RSG-11 meeting and detailed reports published and distributed by NATO. Shortfalls in AMI I and AMI II field tests were the limited amount of meteorological coverage available for evaluating various acoustic propagation codes and better defined acoustic seismic coupling measurements. These shortfalls prompted the organization of a new field test named Joint Acoustic Propagation Experiment, or JAPE, to be conducted at White Sands Missile Range, New Mexico, USA. Because of the excellent capability of the test range to provide an isolated location, and the capability of the U.S. Army Atmospheric Sciences Laboratory (now the Army Research Laboratory) to provide extensive meteorological measurements, the previous deficiencies could be corrected.

1.3 The JAPE test objectives were:

- a. To evaluate the performance of existing sound propagation models under different atmospheric conditions,
- b. To expand the database for which atmospheric boundary conditions are either poorly modeled or not modeled at all,
- c. Acquire limited target signature data accompanied by carefully documented meteorological and terrain conditions.

1.4 Participants in JAPE are as follows:

- a. U.S. Army Engineer Waterways Experiment Station
- b. U.S. Army Laboratory Command, S³TO (now Army Research Laboratory)
- c. U.S. Army Atmospheric Sciences Laboratory (now Army Research Laboratory)
- d. University of Mississippi
- e. MIT Lincoln Laboratory
- f. Physical Science Laboratory, New Mexico State University
- g. Krupp-Atlas-Elektronik GmbH, Germany
- h. Los Alamos National Laboratory
- i. U.S. Army Harry Diamond Laboratory, SLCTO (now Army Research Laboratory)
- j. French-German Institute of Research

- k. NASA Langley Research Center
- l. IIT Research Institute
- m. Pennsylvania State University
- n. National Research Council, Canada
- o. Defence Research Establishment Valcartier, Canada
- p. University of Texas at El Paso
- q. Danish Research Establishment
- r. Lockheed Corporation
- s. Wyle Laboratories
- t. The Bionetics Corporation

1.5. Summary of results

Perhaps the most significant accomplishment of the JAPE tests is the establishment of a comprehensive and accessible data base with a variety of acoustic sources and atmospheric conditions. What some participants referred to as the "common experiment", which was the propagation portion of the test, will serve as a solid foundation on which to develop, analyze, and modify acoustic models. Of course the other parts of JAPE, which included military vehicle signatures, terrain masking, individual participant's side tests, and the sonic boom trials, provide data which is important to those individual agencies. The feature of JAPE which sets it aside from previous field tests is the comprehensive set of meteorological data collected during the trials. This set of data will permit the acoustic scientist to carefully study the influence of the atmosphere on observed acoustic information.

2.0 BACKGROUND

It is critical to the development of military acoustic sensors to achieve a systematic capability for evaluation of concepts and constraints on application. This systematic capability relies on the use of acoustic propagation models and the application of measured data where validated models are not available. Presently, there are a number of prediction techniques for projecting acoustic amplitudes as a function of source-to-sensor range for atmospheric models having relatively strong constraints on homogeneity or coordinate symmetries, such as layered homogeneous velocity propagation profiles. Models predicting the effects of terrain obstructions on sound propagation are also under development, and work has been conducted to predict the propagation effects of a turbulent atmosphere. However, these techniques are not well developed and supporting data for documenting the degree of variation in amplitude and phase of the received signatures are very limited.

A number of acoustic propagation tests have been conducted previously. The degree of meteorological and ground surface characterization within the boundary layer (i.e. from the ground surface to 1 km) has generally been inadequate for careful comparison of model performances, particularly when confronted with the specific signal characteristics and propagation distances associated with military targets.

Recent concepts for acoustic detection, location, and ranging are limited by the amplitude characteristics of the propagation wavefronts, but may be more limited in their achievable performance by temporal variations in the shapes of successive wave fronts or distortions from spherical or cylindrical spatial distributions. Detection distances tend to be greater than predicted in upward refracting atmospheres because of non-homogeneous atmospheric conditions. Super resolution processing is likely to be limited in its ability to achieve theoretical precision because actual data do not follow the statistical distribution assumptions. Contributors to less-than-

theoretical performances include biases of measured distributions of phase or amplitude away from Gaussian distributions, apparent frequency variation due to temporal alteration of propagation paths, and reduction of spatial or temporal coherence. Frequency-sensitive variations in phase-dependent propagation may also constrain concepts for separating signatures from the same source from other signatures in a multiple environment.

3.0 JAPE PROJECT SUMMARY

The Joint Acoustic Propagation Experiment (JAPE) was conducted at White Sands Missile Range (WSMR), New Mexico, during the period 11 -28 July 1991 and 19-29 August 1991. The host was the U.S. Army Atmospheric Sciences Laboratory (ASL). The experimental objectives were:

- a. To evaluate the performance of existing sound propagation models under different atmospheric conditions
- b. To expand the database for which atmospheric and boundary conditions are either poorly modeled or not modeled at all
- c. To acquire limited target signature data accompanied by carefully documented meteorological and terrain conditions
- d. To perform seismic, magnetic, acoustic, and optical measurements according to the specific objectives of the various participants
- e. To study the effects of the atmosphere on sonic boom propagation

To meet the objectives of the test the experiment was separated into four categories:

Long/short range propagation trials. These were conducted to collect data, to evaluate existing propagation models, and to predict transmission losses in different atmospheric conditions. Critical model input parameters and sound pressure levels from both fixed and moving sources were measured. The short range measurements focused on turbulence characterization.

Terrain masking tests. During these tests the effects of non-horizontal boundaries on sound propagation were measured with the source both in front of and behind an isolated hill.

Military vehicle signatures. Signatures included ground vehicles and helicopters. They were acquired with emphasis on careful atmospheric characterization. Receiver arrays were configured for source detection using beam forming algorithms.

Sonic Boom Propagation Test. The Sonic Boom Propagation Test, a field experiment designed and funded by the Applied Acoustic Branch, NASA Langley Research Center, Hampton, VA, was conducted at White Sands Missile Range (WSMR), NM, during the period 19-29 August 1991. The objective of the test was to study the influence of turbulence, scattering, and refraction due to wind and temperature gradients on the propagation of sonic booms, particularly the statistical variability of the received signals at ground level. The tests consisted of flying the test aircraft, including T-38, F-15, F-111, and SR-71, over a ground-based microphone array at altitudes of 30,000 feet above ground level (AGL). In the case of the SR-71, flight altitudes were over 70,000 feet AGL.

4.0 TEST SITE

4.1 General features.

The experiment was conducted in the extreme southeastern corner of White Sands Missile Range, NM, at a location known as the Dusty Infrared Test (DIRT) Site. The northern portion of the Fort Bliss military reservation known as maneuver area B7 near the Orogrande Range Camp was also used. Figure 1 shows the relative location of the test areas and the orographic features in the vicinity. The Jarilla Mountains are approximately three kilometers east of the DIRT Site rising approximately 300 meters above the surrounding plain. A small hill that was designated Instrument Hill, approximately three kilometers south of the DIRT Site near the Orogrande Range Camp, was used for the terrain masking experiment. The DIRT Site, where most of the trials were conducted, provided a gently sloping terrain consisting of sandy soil covered with typical semi-arid vegetation such as mesquite and greasewood. Although the surrounding mesquite-covered sandhills were 1.5 to 2.5 meters high, the DIRT Site in years past had been leveled along a path approximately 200 meters wide by 2000 meters long. Smaller vegetation grew only to approximately one meter in height in this area.

4.2 Site characterization

a. Terrain: The DIRT site is in a desert alluvial valley known as the Tularosa Basin. It is bounded at 3-5 km distance on the east by the Jarilla Mountains and 50 km to the west by the Organ and San Andres Mountains. Surface topography is relatively flat with a general slope from east to west. The surface elevation at the site varies by less than 2 m with some minor variations of 5 m.

b. Surface soil: The soil at the DIRT site was determined to be a SM (silty sand) by the Unified Soil Classification System. It also occasionally had traces of gravel. The soil porosity was between 40 and 48 percent. Soil strength was an average of 4 to 9 percent near the surface and 12 to 25 percent below 25 cm.

c. Flow resistivity: These measurements were made at five locations between the two towers near the sensor line. The average flow resistivity of the site ranged between 960 and 1220 rayl/cm.

d. Site vegetation: Plants identified at the DIRT site are typical of those common to deserts in the western United States. They included *Larrea tridentata* (creosote bush), *Ambrosia dumosa* (white bur sage), *Salvia dorrii* (desert sage), *Atriplex confertifolia* (shadescale), *Ceratoides lanata* (winter fat), *Cercidium microphyllum* (foothill yellow palo verde), *Fouquieria splendens* (ocotillo), *Olneya tesota* (desert ironwood), and *Sarcobatus vermiculatus* (greasewood).

e. Seismic refraction: A seismic refraction survey was conducted to characterize subsurface layering and seismic propagation conditions relevant to detection, analysis, and modeling of ground targets. The survey revealed a first layer that had a thickness of approximately 0.5 m, a p-wave (compression) velocity ranging from 177-204 m/s, and an s-wave (shear) velocity of approximately 110 m/s. The second layer thickness varied from 0.9-1.2 m from north to south, the p-wave velocity from 381-418 m/s, and the s-wave velocity was 233 m/s. The third layer thickness was approximately 2.1 m, the p-wave velocity varied from 549-594 m/s, and the s-wave velocity was 312 m/s. Because of the length of the geophone line the depth of the fourth layer and the s-wave velocity were not discernable, but the p-wave velocity varied from 680-738 m/s.

5.0 TRIALS

The following types of trials were performed: short range propagation, long range

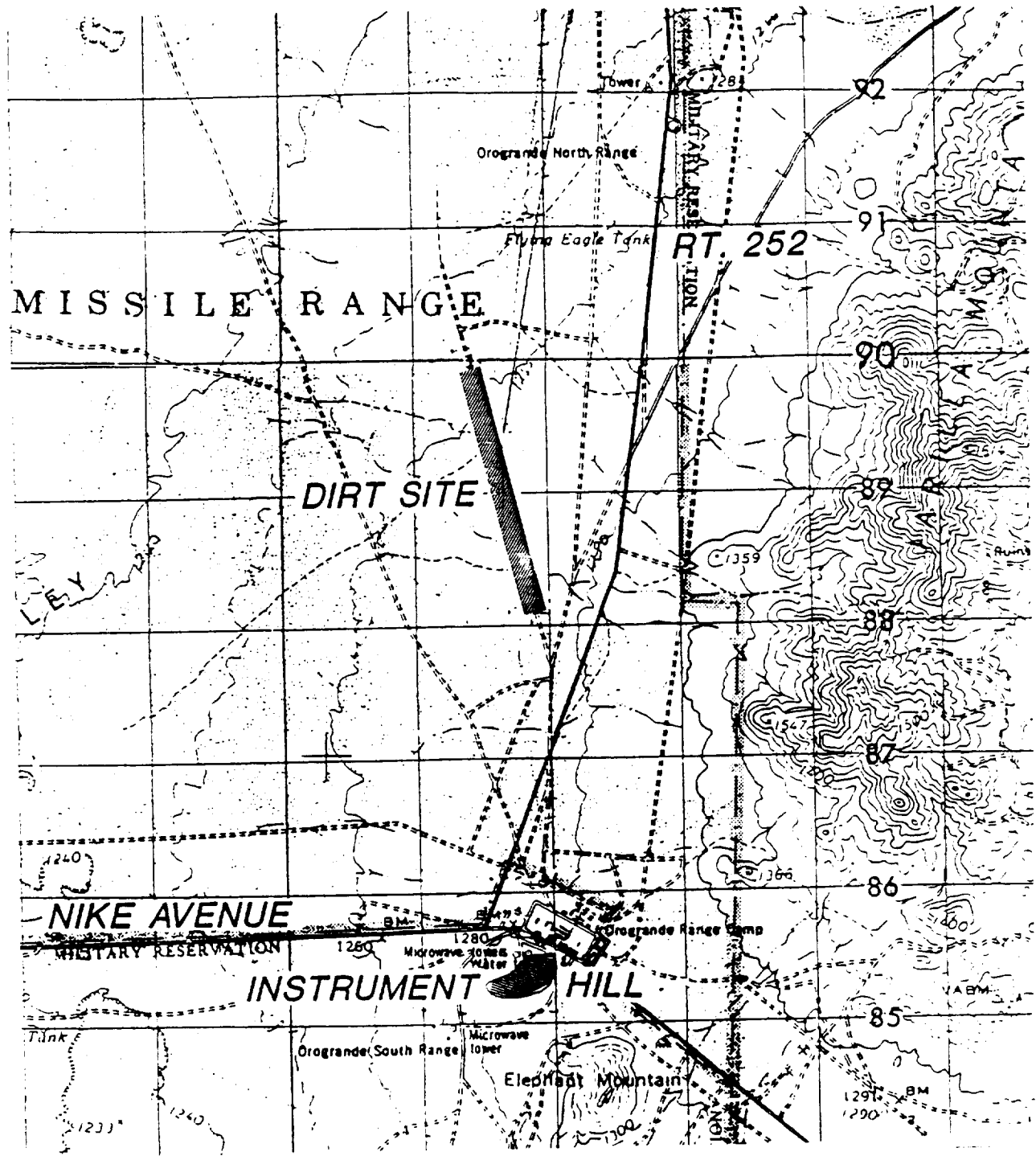


Figure 1. This map shows the location and orientation of the DIRT Site in the extreme southeast corner of White Sands Missile Range, New Mexico. The Jarilla Mountains are east of the site and rise 300 meters above the surrounding terrain. The Instrument Hill was used for the terrain masking experiment. Nike Avenue to the south and WSMR route 252 to the east were the main roads near the site. Traffic caused occasional interference with the tests.

propagation (moving), long range propagation (fixed), terrain masking, vehicle detection, individual participant trials (undocumented), and a category called Other trials. Table 1 lists the JAPE trial types by day, and each is described below.

Table 1. Summary chart of trials by date, type of trial, and time interval.

DATE	TRIAL TYPE	START TIME MDT	END TIME MDT
11 July	Short range propagation	2130	2309:20
13 July	Long range propagation (moving)	1748:05	2326
14 July	Short range propagation	1817:20	2350
16 July	Long range propagation (moving)	0401:15	0512:38
16 July	Penn State turbulence test	1122	1221
17 July	Long range propagation (fixed)	0504	1222
18 July	Short range propagation	0452	1218:30
20 July	Vehicle detection	2332	2400
21 July	Vehicle detection	0000	0659:30
22 July	Vehicle detection	0910	1549:30
23 July	Vehicle detection	0913	1131:45
25 July	Other (Blackhawk)	0920:15	1710:06
27 July	Terrain masking	1602:30	1959
28 July	Terrain masking	0901	1209:30

5.1 Propagation tests.

The propagation tests were designed to provide a common experiment on which the relationship between atmospheric turbulence and acoustic-to-seismic coupling could be determined. The core instrumentation for these trials included speakers located at the top and base of the north and south towers (W1 and W2), propane cannons at the same locations, and an array of microphones and seismic sensors deployed between the two towers. See figure 2. Paragraph 6.2 describes the acoustic sensor configuration for the propagation trials.

a. Short Range Propagation

These trials were conducted from the 30 meter meteorological towers located at the south and center areas of the DIRT Site. The towers, designated W1 and W2, were 1000 meters apart. Speakers and propane cannons were placed near the top and at the base of each tower. The typical trial sequence was as follows:

- Top speaker at the north tower
- Top speaker south tower
- Top propane cannon north tower
- Top propane cannon south tower
- Base speaker north tower
- Base speaker south tower
- Base cannon north tower
- Base cannon south tower

The speaker sequence, which took approximately 16 minutes to complete, transmitted frequencies at 25, 50, 100, 200, 300, 400, 500, 650, 850, 1000, 2000, and 3000 Hertz in sequence, followed by a mixture of 80, 200, and 500 Hertz tones. Each propane cannon was fired eleven times. The first firing was typically lower in intensity than the subsequent shots, and was usually not coincident with the trial start time. The Pennsylvania State University also ran a special short range test for a turbulence experiment.

DIRT SITE

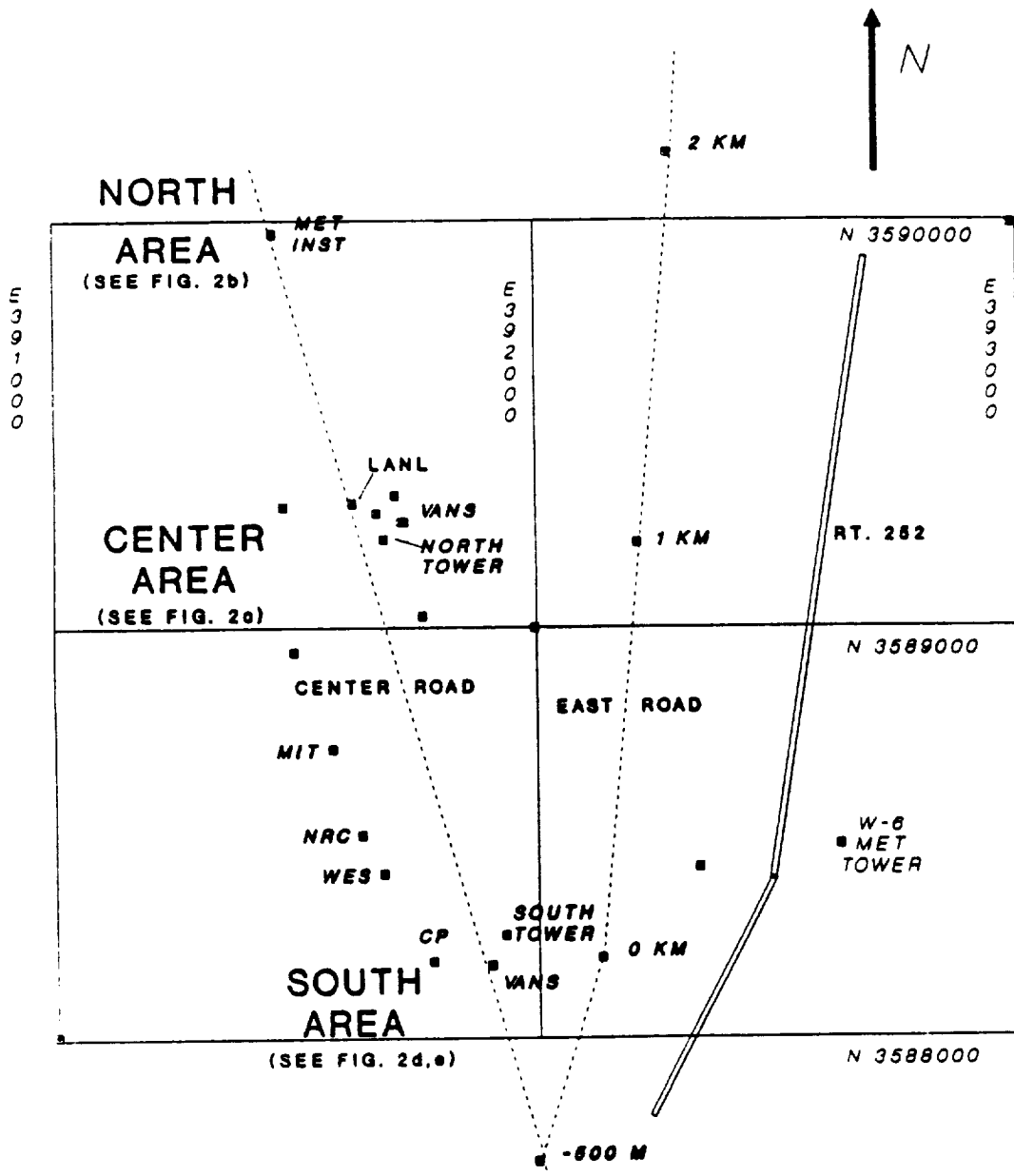


Figure 2. This drawing shows the orientation of the DIRT Site and the major instrumentation areas. The center and east roads were used for vehicle and long range fixed propagation tests, while the short range experiments were conducted from the north and south towers.

b. Long Range Propagation (Moving)

These trials consisted of a UH-1 helicopter flying a pattern from 20 kilometers north of the DIRT Site to 10 kilometers south. Flight altitudes were from 100 to 180 meters above ground level (AGL). Altitudes were increased after dark for safety reasons. Position data were collected by on-board Global Positioning System equipment and ground-based radar track.

c. Long Range Propagation (Fixed)

Several types of acoustic sources were used for these trials and included speakers, propane cannon, 155mm howitzer, and high explosive charges. All trials were conducted on the EAST road, which ran parallel to range road 252 and just east of the DIRT Site in a northerly direction. Range markers were placed at one kilometer intervals beginning near the south end of the DIRT Site, thus the one kilometer location was just east of W2, the north meteorological tower. The speakers and a propane cannon were mounted on a stake bed truck and moved from position to position on the east road. Speakers and the propane cannon were 1.7 meters above ground level and the speakers were separated by 1.15 meters. These sources were pointed in a southerly direction. The M198 155mm howitzer was positioned near the 8 kilometer range mark. It fired inert rounds at one minute intervals at an azimuth of 343 degrees (the muzzle pointed away from the DIRT Site) and a quadrant elevation of 15 degrees. The propellant was the M119A2Z7 red bag charge which weighed 22.5 pounds (10.2 kg). High explosive charges of C-4 were detonated during daylight hours only. Charge sizes of 1.25 and 5 pounds were used and were placed one meter above ground level. Several misfires were encountered thus causing uncertainty in the actual detonation times for trial 051304. Detonations were scheduled to be at 30 second intervals.

5.2 Terrain Masking

Two types of sources were used during the terrain masking: a UH-1 helicopter and C-4 high explosives. All trials were performed in and around Instrument Hill just south of the Orogrande Range Camp and northwest of Elephant Mountain in Fort Bliss maneuver area B7. See figures 3a and 3b. Most of the instrumentation used to measure the acoustic energy and the meteorological instrumentation were deployed from the top of the hill toward the north. The locations for the C-4 detonations were surveyed and designated TM HE-1, approximately 200 meters south of the southern base of the hill; TM HE-2, 100 meters south of the base; TM HE-3, 50 meters from the base; and TM HE-4, located at the southern base of the hill. These locations were also used as overflight positions for the helicopter patterns. When the helicopter was instructed to fly at nap-of-earth (NOE) over the 200 meter ground location, it went over TM HE-1. NOE for this exercise was selected by the pilot for safety considerations at 12 meters above ground level. However, on the east-west patterns the pilot had to climb to avoid high voltage power lines which ran between the hill and Elephant Mountain. The flight profiles are listed in trial summary remarks.

5.3 Vehicle Detection

Several types of military vehicles were used for the vehicle detection tests including an M1 tank, M60 tank, M114 armored personnel carrier, M35 cargo truck, and M561 Gamma Goat. The truck and Goat were used in individual participant trials which are not documented in this report. Trials were initiated on the CENTER road which ran through the middle of the DIRT Site. They started at a location approximately one kilometer south of the command post (CP) and ended approximately two kilometers north of the CP. Calibrations were performed with the tracked vehicles at six separate locations along the road and in two directions, north and south. At these stopping points the vehicles ran at idle and a high RPM for one minute each. At the Canadian

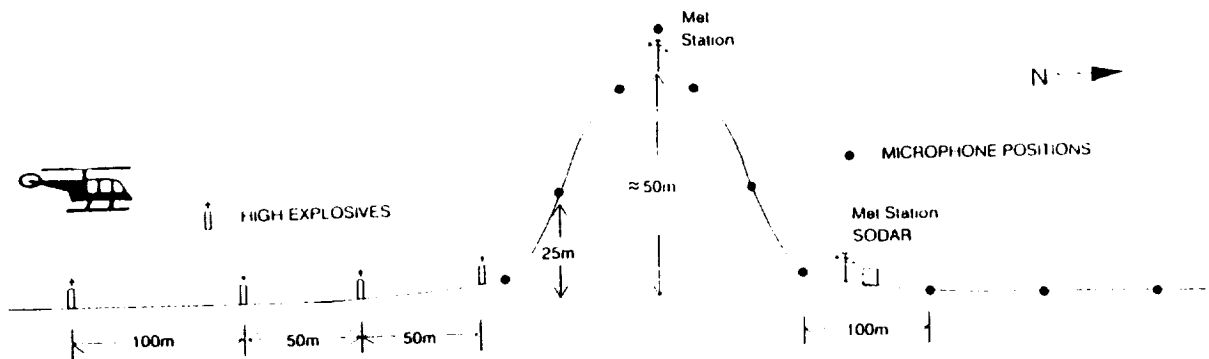


Figure 3a. Terrain Masking experiment layout showing sensor positions and high explosive locations.

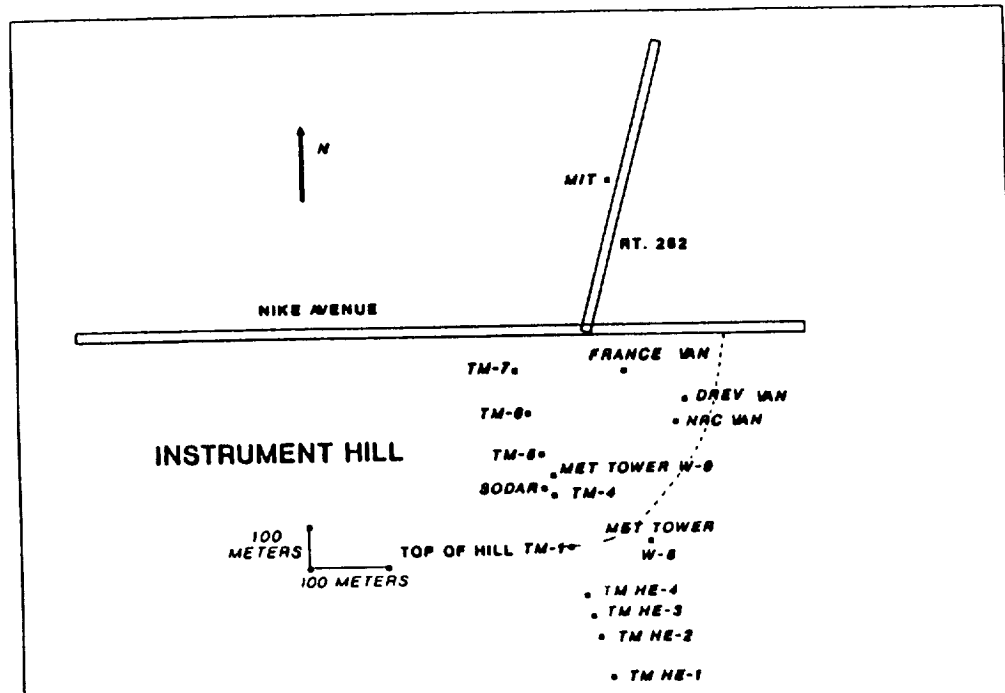


Figure 3b. Terrain Masking experiment at Instrument Hill showing the vans, reference instrument lines TM-1 through TM-7, and the locations of the high explosive detonation points, TM HE-1 through TM HE-4.

calibration point the M60 and APC were alternately stopped and started for several minutes. The APC did not have a tachometer, so accurate RPM was not measured. The vehicles were also operated on the CENTER road, both north and south at speeds of 20 miles per hour and at alternating speeds of between 15 and 20 miles per hour.

Only the M1 and M60 tanks were tested on the EAST road at ranges from one kilometer south of the CP to six kilometers north. Both vehicles traveled at speeds of 20 miles per hour although there were several deep gullies which caused the tanks to reduce speed temporarily. On one trial the M1 was asked to shut down and restart at the six kilometer range.

5.4 Individual Participant Trials

Participants including Los Alamos National Laboratory and Defence Research Establishment Valcartier, Canada, performed individual tests with the military vehicles. These tests were independent of other trials and are not documented in this report.

5.5 Other Trials

A Blackhawk helicopter from Fort Rucker, Alabama was used to fly numerous patterns to satisfy the various requirements of participants in this experiment. The patterns are not documented in this report.

5.6 Sonic boom trials

A total of 59 trials were conducted during the test period including flights of two SR-71, six F-111, twenty-one F-15, and thirty T-38 aircraft. One overflight was considered as one trial. Figure 4 shows the approximate flight path at 30000 feet altitude for all aircraft except the SR-71 which flew a north-to-south and east-to-west pattern at 65000 feet. Table 2 shows the type and number of trials as a function of time period.

TABLE 2. Supersonic trials grouped by type of aircraft and time of day. Times are Mountain Daylight Time and are approximate.

AIRCRAFT	0600-1000	1000-1400	1400-1600
SR-71			2
F-111		2	4
F-15	7	8	6
T-38	12	11	7

6.0 INSTRUMENTATION

6.1 Meteorological

The acoustic meteorological test bed consisted of two 32 meter walkup towers that were instrumented at five levels (2-, 4-, 8-, 16-, and 32 m) with various meteorological sensors. The towers were placed at one kilometer separation on an azimuth of about 345 degrees. The north tower measured temperature, winds, humidity, pressure, and solar radiation. The south tower contained sonic anemometers and hot wire anemometers. Additional measurements were made using a 924 MHz wind profiler, a radio acoustic sounding system (RASS), upper air radiosonde,

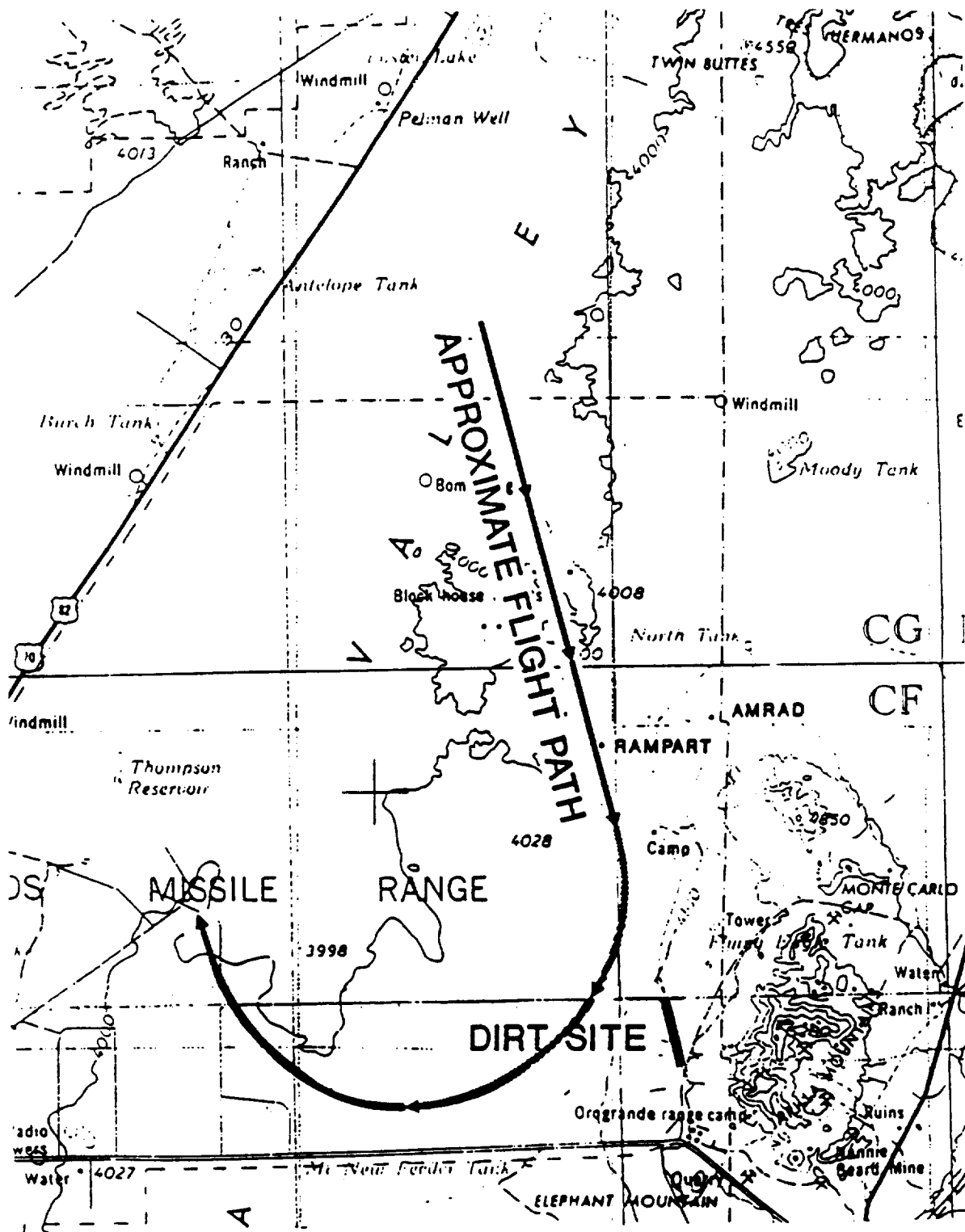


Figure 4. Map showing the approximate flight path of the aircraft flown during the Sonic Boom trials.

tethersonde, SODAR wind profiler, and numerous surface weather stations in and around the test area. The following list contains the meteorological equipment deployed during JAPE:

1. Upper air, surface to 5000m (north area release)
2. Hot film, south tower, four levels (south area)
3. Sonic anemometer, south tower W1 (south area), five levels; north tower W2 (center area), three levels
4. Thermistor, south tower W1 (south area), five levels
5. PAMS tower W4, three levels (north area)
6. TACS tower, 10m, two levels, five locations around DIRT Site (W5 approx. 1km west of center area; W6 approx. 1km east of center area; W7 approx. 8km north of center area; W8 at top of Instrument Hill; W9 at base of Instrument Hill)
7. TACS tower W3, 30m, five levels (center area)
8. Microwave temperature profiler (center area), 14 data levels between 30m and 10668m
9. RASS virtual temperature, 12 levels up to approximately 133m (north area)
10. Wind profiler (north area), data to 5000m
11. AO SODAR (north area) and PA2 SODAR (base of Instrument Hill), winds up to 750m
12. Tethersonde, surface to <600m (north and south areas)

6.2 Acoustic instrumentation for propagation trials

The acoustic sensor configuration for the propagation trials consisted of two source microphones, two vertical arrays, one longitudinal array, one transverse array, and one direction finding array as shown in figure 5. A vertical array of microphones was placed on each of the two 32 meter towers. Microphones were placed at 0, 1, 2, 4, 8, 16, and 32 meters on each of the two towers. The eleven microphones that made up the longitudinal array were placed on the ground 100 meters apart along a line between the two towers. The transverse array was placed perpendicular to the longitudinal array midway between the two towers. Microphones in the transverse array were placed both on the ground and 1 meter above the ground at 1, 3, 7, and 15 meters east of the center microphone pair and 31 meters west of the center pair. The direction finding array consisted of eight elements: one in the center surrounded by seven evenly spaced on a circle with a 1.85 meter radius. This array was located about 50 meters west of the midway point between the two towers. Source microphones were positioned approximately 2 meters in front of the source. The seismic sensor array consisted of two horizontal geophones placed at the intersection of the longitudinal and transverse acoustic arrays and three vertical geophones spaced 0.75 meters apart placed along the longitudinal axis.

6.3 Acoustic instrumentation for sonic boom trials

The primary acoustic array employed in the sonic boom propagation experiment was a 16 element, ground based, linear array as shown in figure 6. It consisted of Boom Event Analyzer/Recorder (BEAR) microphone systems specifically designed to measure sonic booms. The BEAR systems were deployed in a linear array with at least a 200 foot distance between them. The BEAR systems each consisted of a microphone, digitizer, microprocessor, and storage medium, and were used with ground plates and wind screens. Additional microphones were installed by the Army Research Laboratory and Physical Science Laboratory.

7.0 TECHNICAL REPORTS

The following is a partial list of technical reports written as a result of the JAPE tests.

1. Henry E. Bass, Patrice Boulanger, Robert Olsen, and Prasan Chintawongvanich, **Sonic Boom Propagation Test Low Level Turbulence Report**, University of Mississippi, Army Research Laboratory, and Physical Science Laboratory.

2. H.E. Bass, R. Raspet, S. Hausman, D. Schein, G. Daigle, **Analysis of Non-line-of-sight Data Collected at JAPE - 91**, University of Mississippi, Northrop Corp, NRC Canada.
3. Henry E. Bass and Carl Frederickson, **JAPE-1 Data Analysis**, University of Mississippi.
4. Gunnar R. Becker, **Efforts of Atlas Elektronik GmbH at the Joint Acoustic Propagation Experiment**, Atlas Elektronik GmbH, Germany.
5. Gunnar R. Becker, **The Masking of Sound by a Hillside**, Atlas Elektronik GmbH, Germany.
6. Gunnar R. Becker, **Terrain Masking Experiment: High Explosive Tests**, Atlas Elektronik GmbH, Germany.
7. Jacques Bedard, **DREV Field Measurements during JAPE**, Defence Research Establishment, Quebec, Canada, presented to the 24th meeting of NATO AC/243, Panel 3, RSG.11, Los Angeles, CA, November 1991.
8. Richard K. Brienz, **Joint Acoustic Propagation Experiment**, MIT Lincoln Laboratory.
9. Thelma Chenault, Rene' Klein, Ascencion Acosta, Jr., **Digital Signal Processing Techniques used to Reduce Acoustics Data from the JAPE Test**, Atmospheric Sciences Laboratory, White Sands Missile Range, NM.
10. Thelma Chenault, Rene' Klein, John Fox, Don Foiani, **JAPE Positioning Data**, Atmospheric Sciences Laboratory, White Sands Missile Range, NM.
11. Prasan Chintawongvanich and Robert Olsen, **Measurements of Temperature and Velocity Structure Parameters from Sonic Anemometers**, Physical Science Laboratory, New Mexico State University, and U.S. Army Atmospheric Sciences Laboratory.
12. Ron Frankel, **Data Collection and Signal Processing Techniques**, Army Research Laboratory, Adelphi, MD, 21 November 1991.
13. David Havelock, **NRC/CA Participant's Report Joint Acoustic Propagation Experiment**, National Research Council, Canada.
14. D.I. Havelock, M.R. Stinson, G.A. Daigle, **Observations of Signal Coherence in Space Time and Frequency**, RSG-11 Meeting, 26-29 Oct 1992, Quebec City, National Research Council, Ottawa, Canada.
15. Fred Homuth, Jerome Chen, and Ed VanEckhout, **Fiber Optics - A New Method for Measuring Stress Changes**, Los Alamos National Laboratory, Los Alamos, NM.
16. Marjorie Klugerman and Henry E. Bass, **Measurements Needed for Impedance Calculations**, Acoustics Laboratory, University of Mississippi.
17. P. Naz and G. Parmentier, **Joint Acoustic Propagation Experiment**, ISL, France.
18. P. Naz, **JAPE 91: First Result of the Terrain Masking Experiment**, ISL/APS, France.

19. P. Naz, G. Parmentier, **Joint Acoustic Propagation Experiment, Phase 1 Results of Long Range/Short Range Propagation Experiment**, ISL, France.
20. R. J. Okrasinski, **Intercomparison of Remote and Balloon-Borne Sensors**, Physical Science Laboratory, New Mexico State University.
21. William L. Willshire Jr., **The Effect of Turbulence on the Propagation of Sonic Booms**, NASA Langley Research Center.

8.0 DATA BASE

All data and reports produced from the JAPE tests are catalogued and archived in a central repository. For more information contact the following individual:

IIT Research Institute
ATTN. Jim Robertson
4140 Linden Ave., Suite 201
Dayton, Ohio 45432
USA
Phone: 513-252-9969 ~
FAX:513-252-6831

LONG/SHORT RANGE PROPAGATION

SENSOR CONFIGURATION

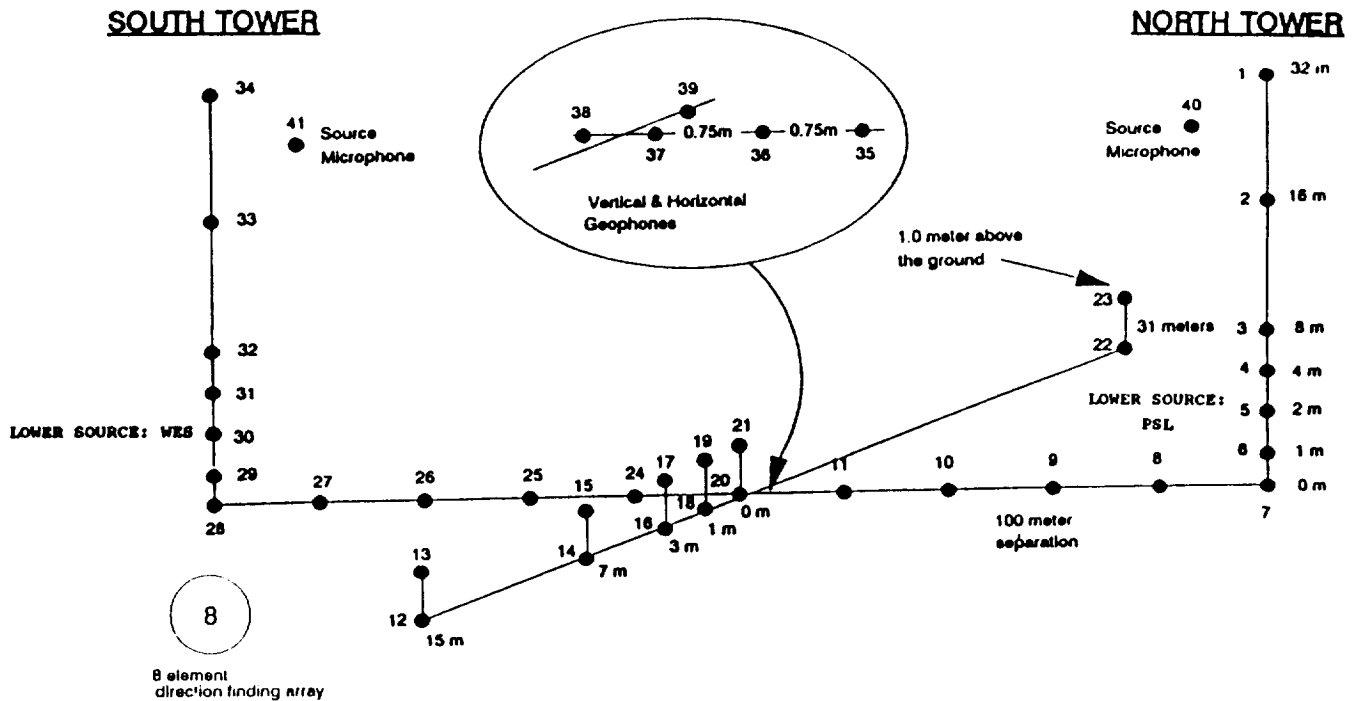


Figure 5. Acoustic sensor layout showing sensor positions and identification numbers.

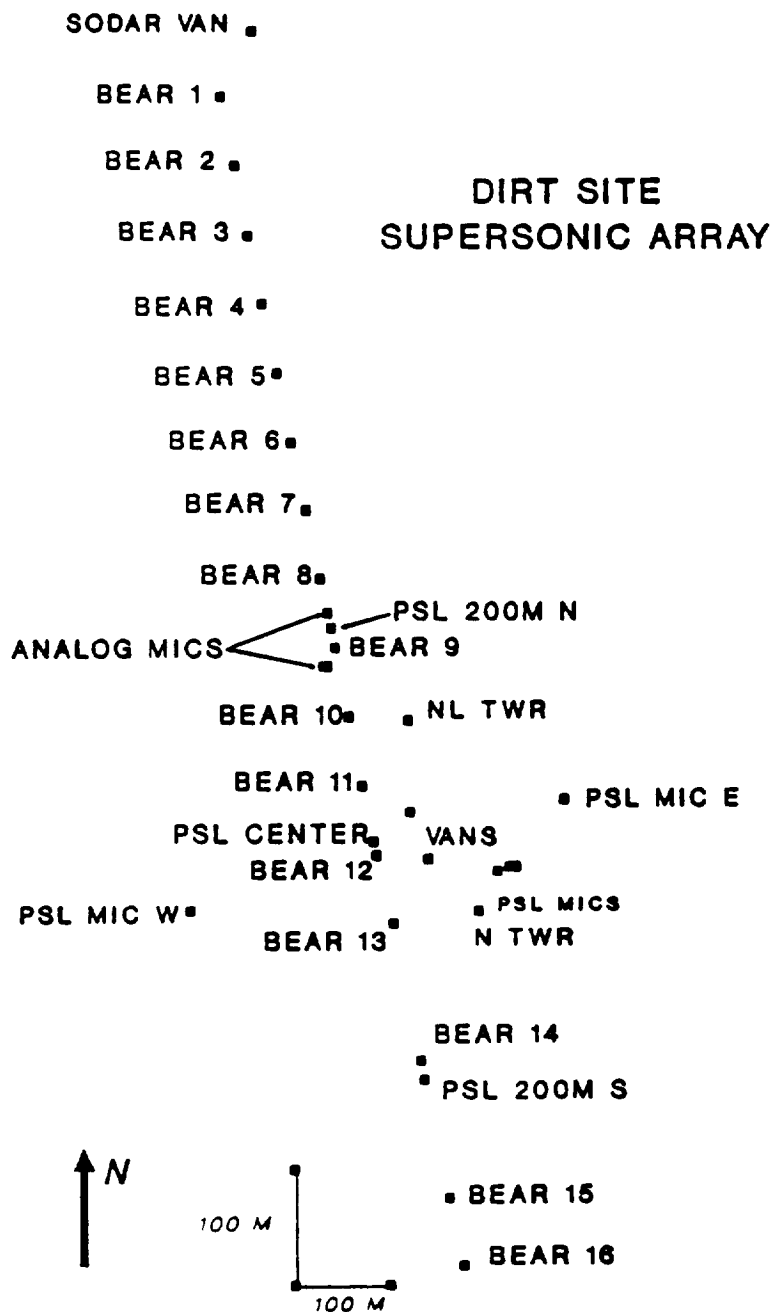


Figure 6. Locations of the microphone arrays deployed by NASA Langley and the Atmospheric Sciences/Physical Science Laboratories.



SOME RESULTS GAINED FROM JAPE - AN OVERVIEW*

Gunnar R. Becker
 ATLAS ELEKTRONIK GmbH
 Bremen, FRG

D2-71
 10/16/74
 P. 12

SUMMARY

During JAPE a variety of sound propagation experiments have been conducted, including long range measurements and investigations of the masking of sound by natural barriers. An overview of the measurements is given below. A comparison between measured SPL's and theoretical estimates is presented.

INTRODUCTION

The influence of meteorological conditions on outdoor sound propagation is of major interest, because the detectability of acoustic sources depends on the characteristics of the transmission channel. Since ATLAS ELEKTRONIK has limited access to met instrumentation, the JAPE offered a unique chance to conduct meteorological and acoustical measurements at one time.

Sensor Layout

ATLAS ELEKTRONIK operated a linear acoustic array during the experiments. During the first series of the measurements this array was located beyond the northern met-tower, heading in a south-to-north-direction. The sensor spacing was 100 m and eight microphones (type: Sennheiser MKH-110) were in use.

The mike close to the met-tower was collocated to the northernmost mike of the MIT sensor layout. Thus it was possible to link our results to those of the other teams having sensors displaced along the baseline of the sensor layout.

During the vehicle test additional geophones (type: Geospace GSC-300-3D, Sensor SM 6) and mikes were located close to the track.

The Terrain Masking trials finished the JAPE. For this purpose the sensors were deployed across the Elephant Hill, which was located south of the Dirt Site. Figure 1 is showing the sensor geometry as used during the trials.

* This work was funded by the German MOD, Rü T III 4.

SELECTED RESULTS

Ambient Noise

Measurements of the ambient noise took place at least once a day. Figure 2 presents a spectral analysis of such a measurement. The variation of the spectral content of the background noise is shown over a period of two minutes. The frequency band displayed is ranging from DC to 200 Hz.

In order to enhance spectral lines the broadband contribution has been removed. The effect of this procedure can be seen from the comparison of both upper graphs. They are showing an averaged spectrum before (top) and after the normalization (below) has been applied.

In the spectrogram a set of stable spectral lines can be seen. They are generated by the mechanical noise of transformers, air conditioners, etc. In addition there are sources with varying frequency content. Mostly these kinds of signals could be identified as noise coming from passing vehicles.

Short Range Measurements

During the short range tests measurements including pure sinusoidal tones emitted by a loudspeaker and pulses from a propane cannon were conducted. Figure 3 shows the averaged lapse of the SPL vs range at three different frequencies, i.e. 80 Hz, 200 Hz and 500 Hz. These three frequencies were emitted simultaneously. The loudspeaker was mounted on top of the southern met tower (approx. 30 m AGL, 1000 m apart) and the integration time was 15 seconds.

At 80 Hz no major changes in the SPL can be seen within the presented range interval. Both other frequencies show a slight decrease at first, but beyond 1600 m even the energy at 500 Hz increases again. The met conditions showed a light upward refraction during these trials. The total velocity gradient close to the ground ($z \leq 100$ m) was about 0.28/sec. From this the shadow zone can be estimated to begin about 920 m off the source.

A spectral analysis of this measurement is presented in Figure 4. The frequency band shows ranges from 400 Hz to 600 Hz. The 500 Hz tone is the dominating spectral line in this band. The other narrowband contributions are due to nonlinearities of the loudspeaker.

The graph to the left is showing the total energy (left line) and the broadband energy (right line) in the given frequency band. The difference corresponds to the narrowband contributions. Since the 500 Hz line is by far the strongest line, it can be concluded that the variations in the difference is caused by fluctuations of this line. Indeed these variations are very strong though there have been only light winds (≈ 3 m/s). The relative SPL varies between 24 dB and 48 dB and the strongest change occurred about 40 seconds after the measurement started: the relative SPL dropped about 20 dB within six seconds.

Long Range Measurements

A number of helicopter flights have been conducted starting about 20 km north of the test site, approaching with constant speed and altitude. Since there were good propagation conditions the helicopter could be detected over a large distance. This can be seen in Figure 5, which is showing the first minute after starting the run. The blade passing frequencies can be detected after about 15 seconds. Figure 6 shows the analysis while the helicopter was close to the CPA.

This trial has been chosen to compare the measured SPL as a function of range with the theory. In a first step the sound pressure power density at two discrete frequencies, i.e. 50 Hz and 200 Hz, and in the frequency band between 25 Hz to 225 Hz has been evaluated. The result is shown in Figure 7. All three levels behave in a similar way. In Figure 8 the measured level at 50 Hz is compared with three theoretical estimates. The dotted lines represent geometrical spreading plus absorption only. The full line shows the estimated level according to the CERL-FFP-model. All theoretical results have been fitted with the measurement at a distance of 10 km. It can be seen from Figure 8 that the result obtained with the CERL-FFP-algorithm fits best with the measurement. Especially at closer ranges there is a good correlation, whereas the model seems to predict higher levels at larger ranges than really have been measured.

Terrain Masking

The aim of these measurements was the investigation of the masking of sound by a natural barrier. For this purpose ATLAS deployed its microphones across a hillside as shown in Figure 1.

Both helicopters and high explosives were used during these trials. In the following only results obtained from helicopter measurements will be presented. The insertion loss of the barrier has been derived by calculating the spectral difference between the microphone in the shadow and the one on top of the hill. This one was used as a free field reference (labelled CH-3 in Figure 1). Figure 9 is showing the result of such a measurement. The helicopter was hovering 200 m south of the hill at an altitude of 65 ft above ground level (AGL). Since the height of the hill was approximately 100 ft, the helicopter was masked at all microphone positions beyond the hill (CH-7 to CH-12).

Two microphone outputs have been analyzed, i.e. CH-9 at the northern toe of the hill and CH-12 at the end of the sensor layout. The analysis has been restricted to the harmonics of the blade passing frequencies. Beyond 175 Hz the S/N was too poor to obtain reliable results. Both channels show a very similar lapse of the relative SPL. The calculated lapse follows a simple relation: insertion loss IL [db] $\sim 0.1 * f$ [Hz]. At helicopter altitude of 330 ft AGL there are line-of-sight (LOS) conditions between the helicopter and the microphone at location CH-12. The microphone at the toe of the hill, however, is still masked by the hill. The result of the analysis is shown in Figure 10. The lapse of the IL for the microphone located at CH-9 is very similar to the previous results. The signal received at CH-12 seems to be almost unaffected by the barrier, as would be expected under LOS conditions.

SUMMARY

In this paper a short overview of the results obtained from the JAPE is given. The most important results gained up to now are:

Even under almost good met conditions strong changes of the SPL can occur. At 500 Hz variations of 20 dB and more have been measured over a transmission distance of 1000 m.

The level of the sound emitted by an approaching helicopter has been analyzed at ranges starting at 20 km. These results were compared with theoretical estimates and it was found that the CERL-FFP fits reasonably well with the measurements.

From the Terrain Masking experiment it turned out that within the investigated frequency range the insertion loss in decibels is almost linear related to frequency, i.e. $IL [dB] \sim -0.1 \cdot f [Hz]$.

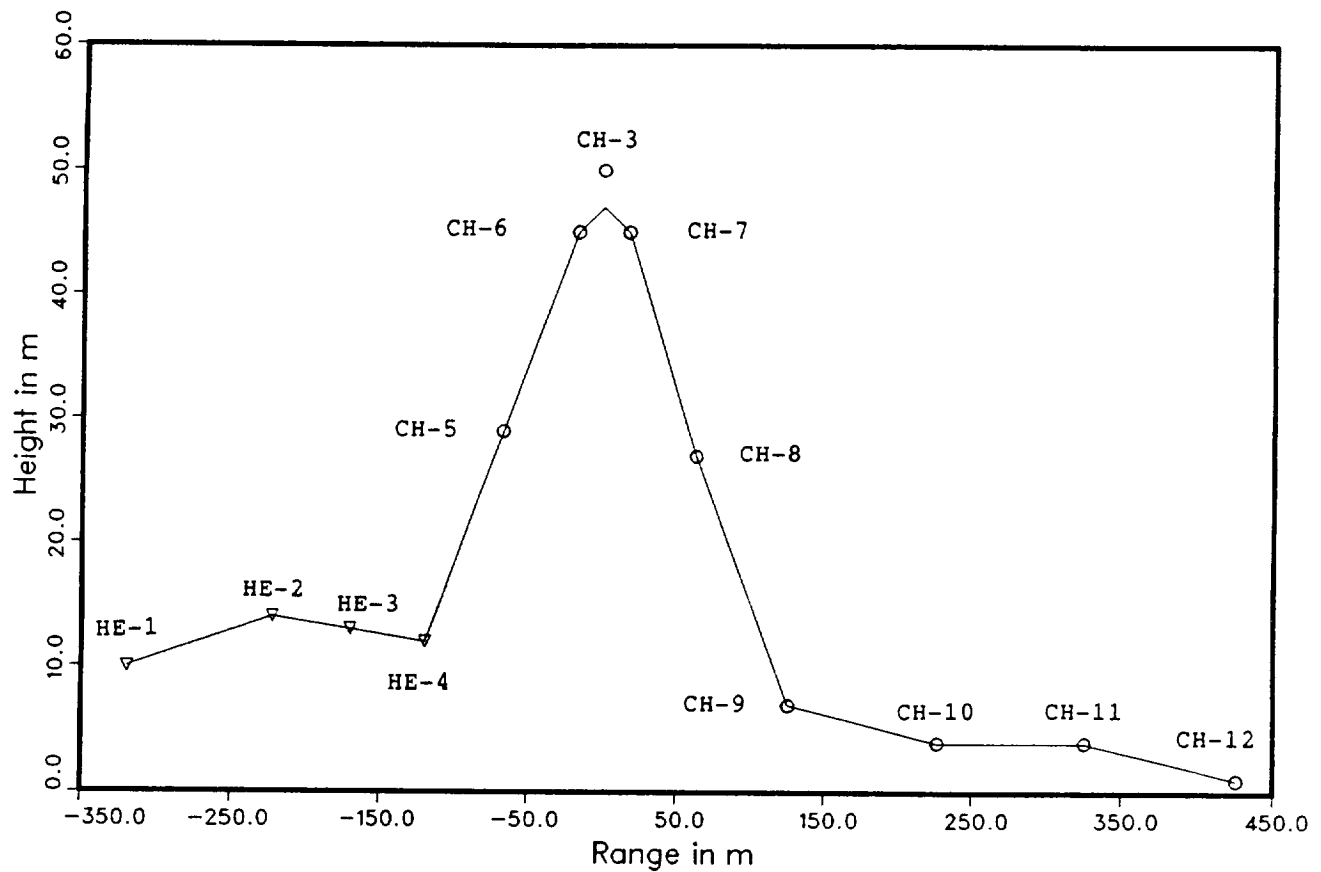


Figure 1: Topography and sensor layout during the Terrain Masking trials. Circles indicate the positions of the microphones; triangles indicate the positions of the high explosives.

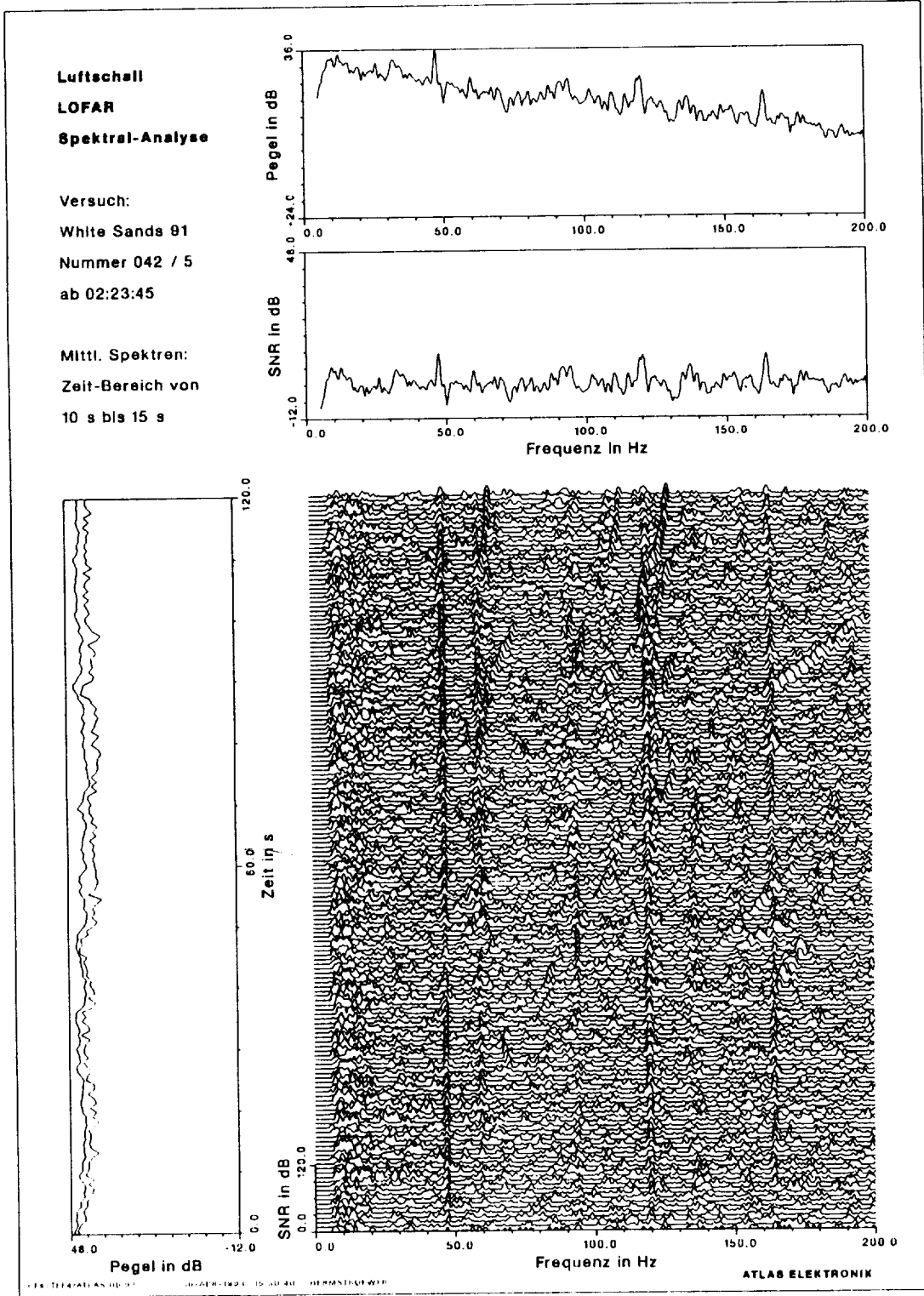


Figure 2: Ambient noise measurement. Top: averaged reference spectrum before and after (below) the broadband contributions are removed. Right: spectrogram of the ambient noise. Left: energy in the shown frequency band (left) and broadband contribution in the same band (right).

JAPE: FIXED SOURCE TRIALS

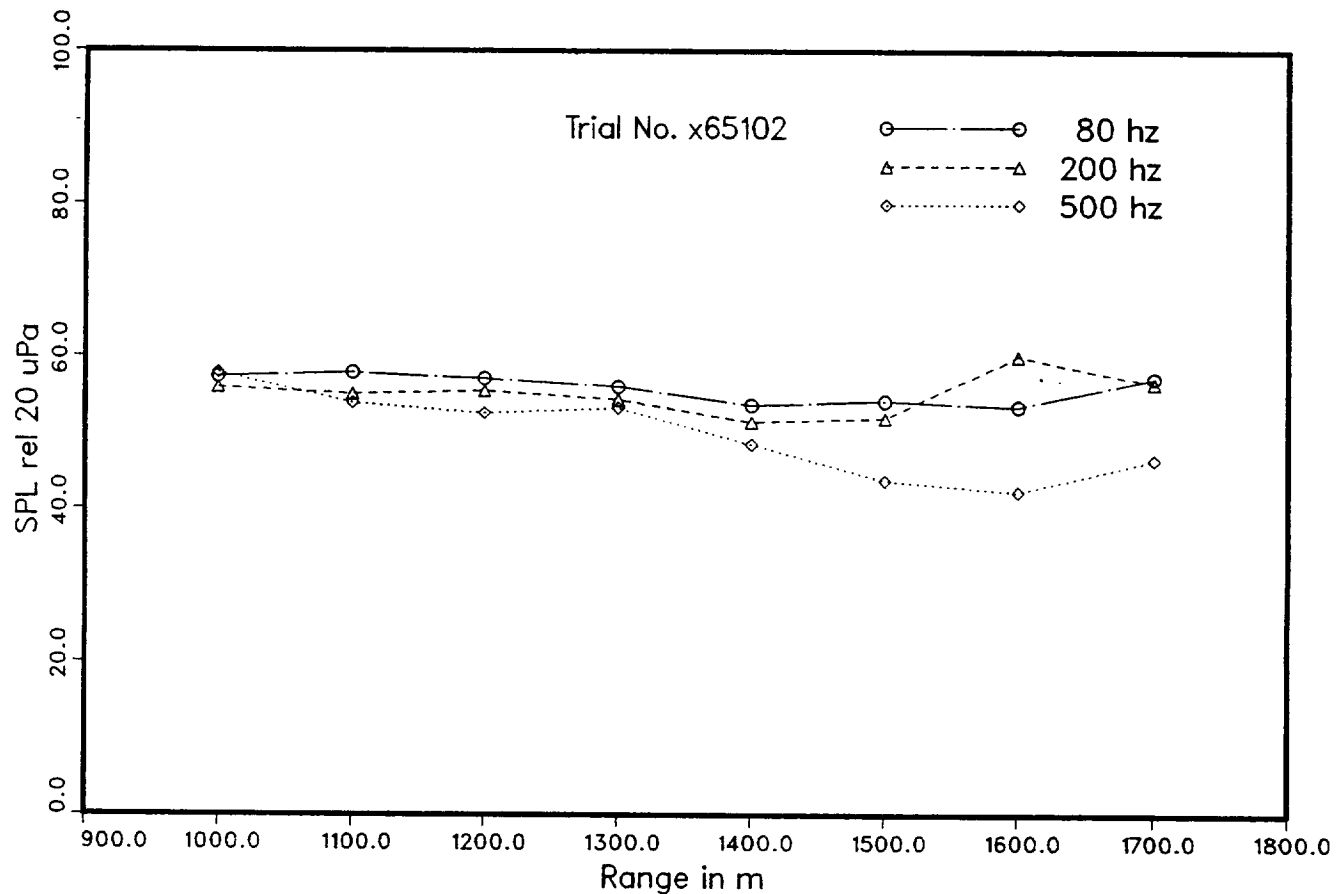


Figure 3: Averaged SPL as a function of range at three different frequencies. The loudspeaker was mounted on top of the southern met tower.

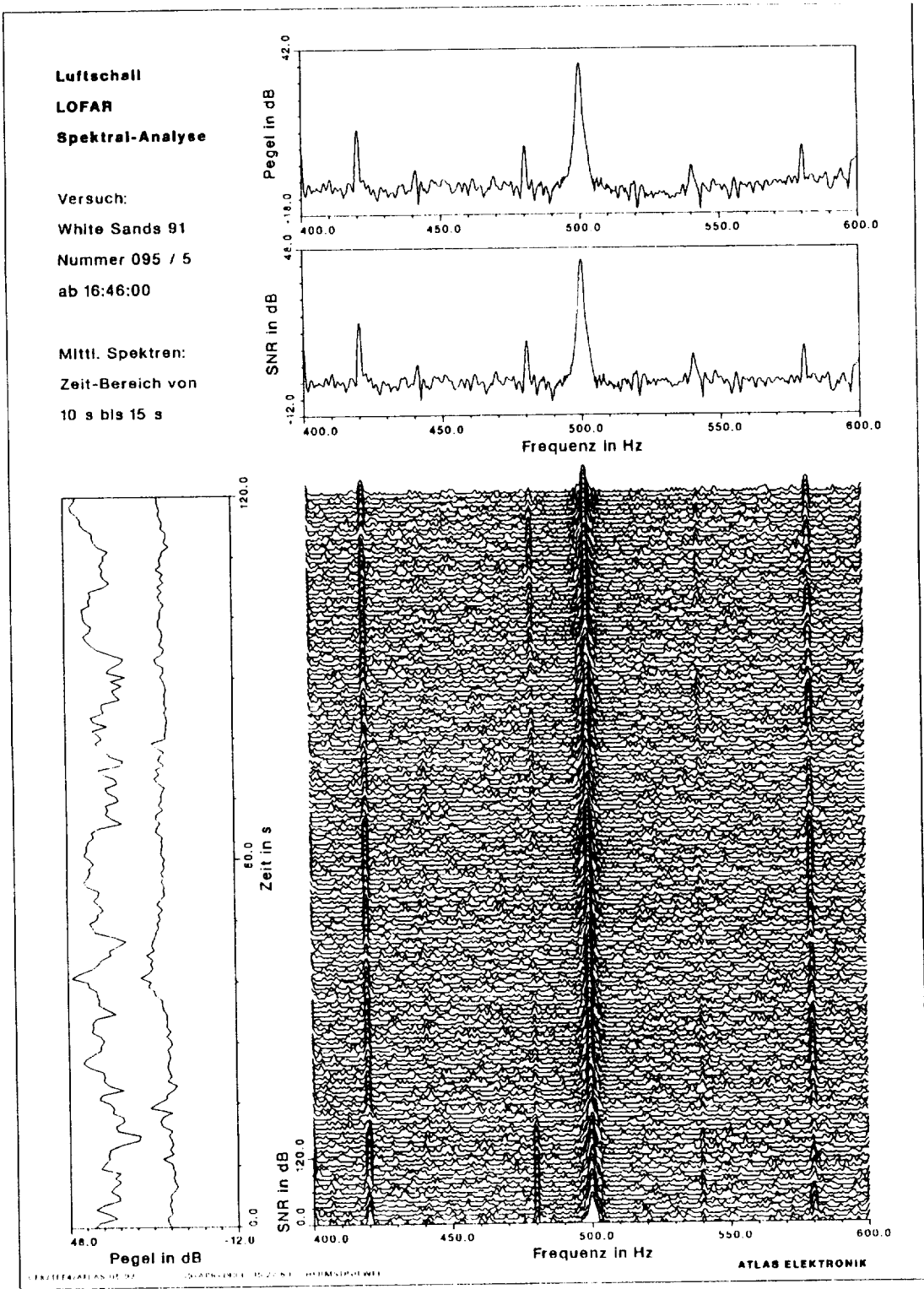


Figure 4: Spectrogram of a pure tone (500 Hz). The SPL shows strong variations due to changing propagation conditions.

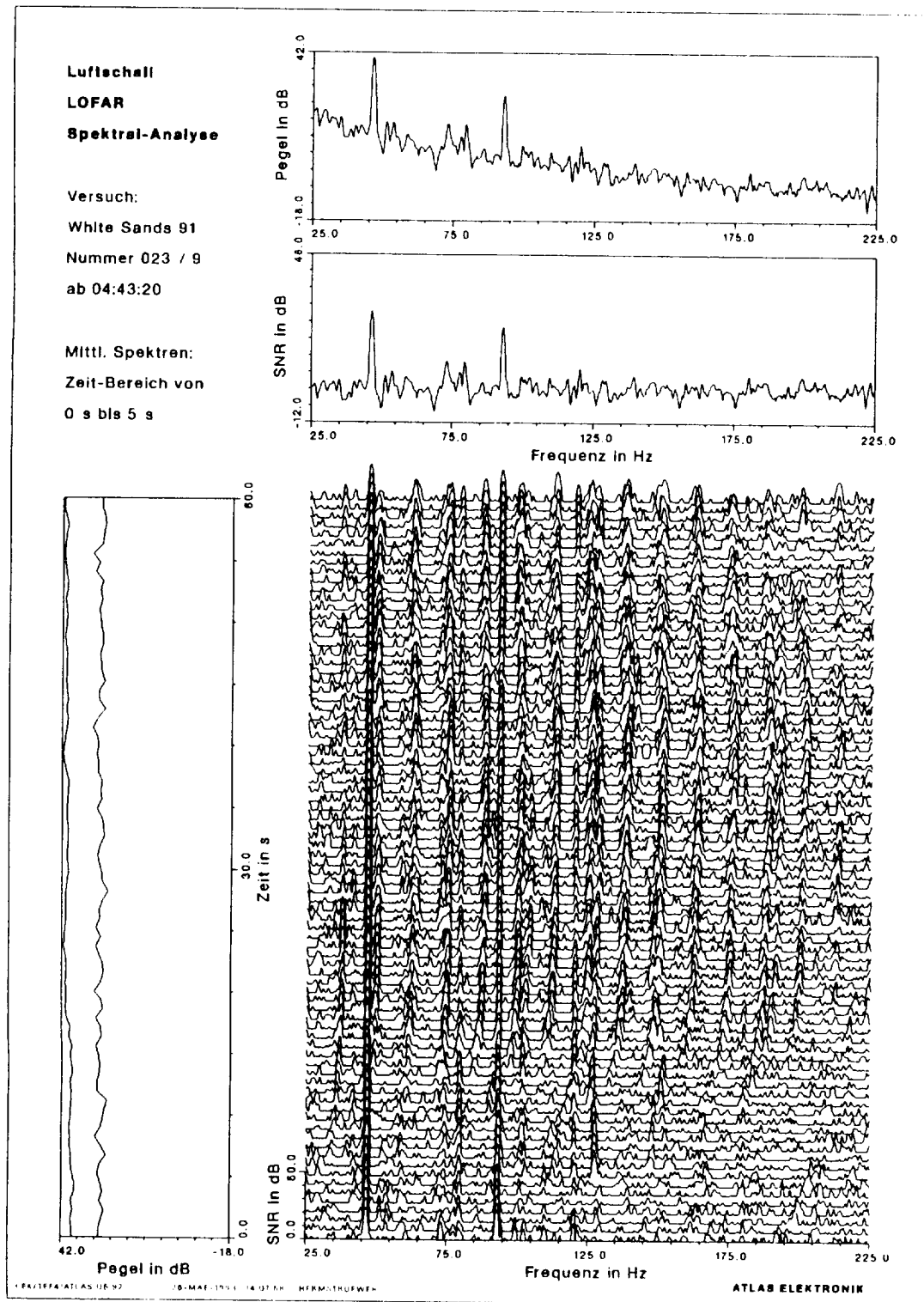


Figure 5: Spectrogram of an approaching helicopter. Beginning of the run.

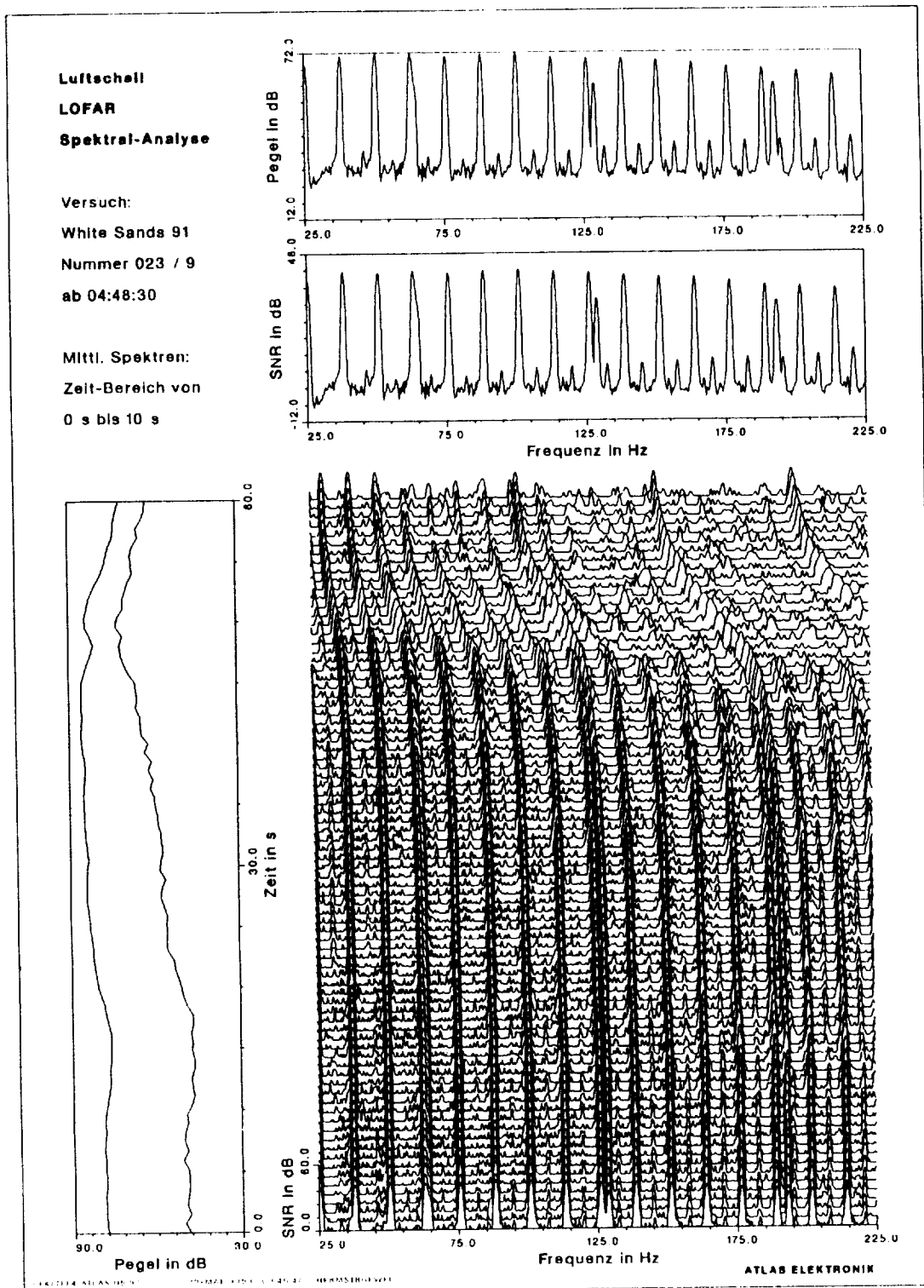


Figure 6: Spectrogram of an approaching helicopter close to the CPA.

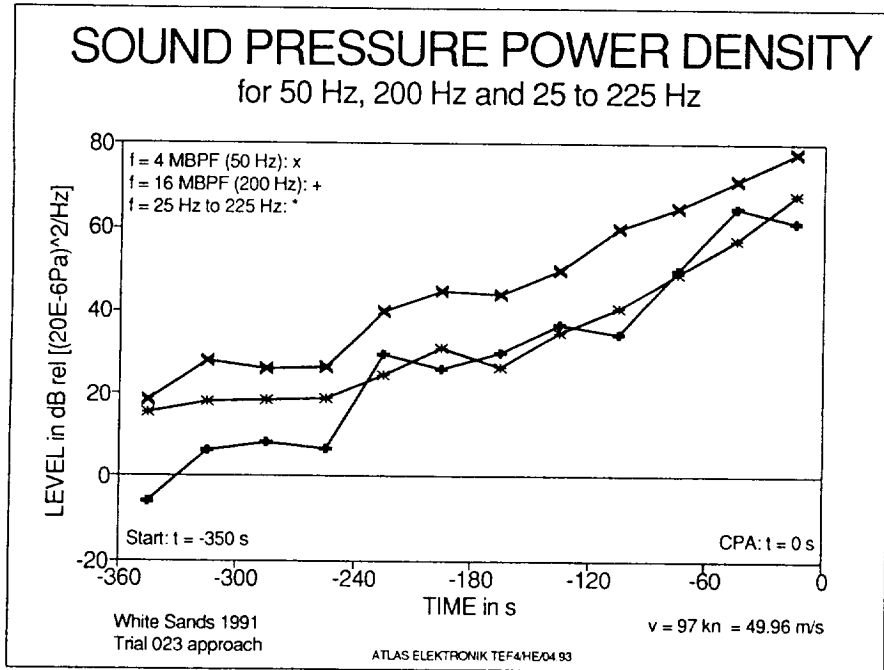


Figure 7: Measured sound pressure power density as a function of time. Same trial as in Figs. 5 and 6.

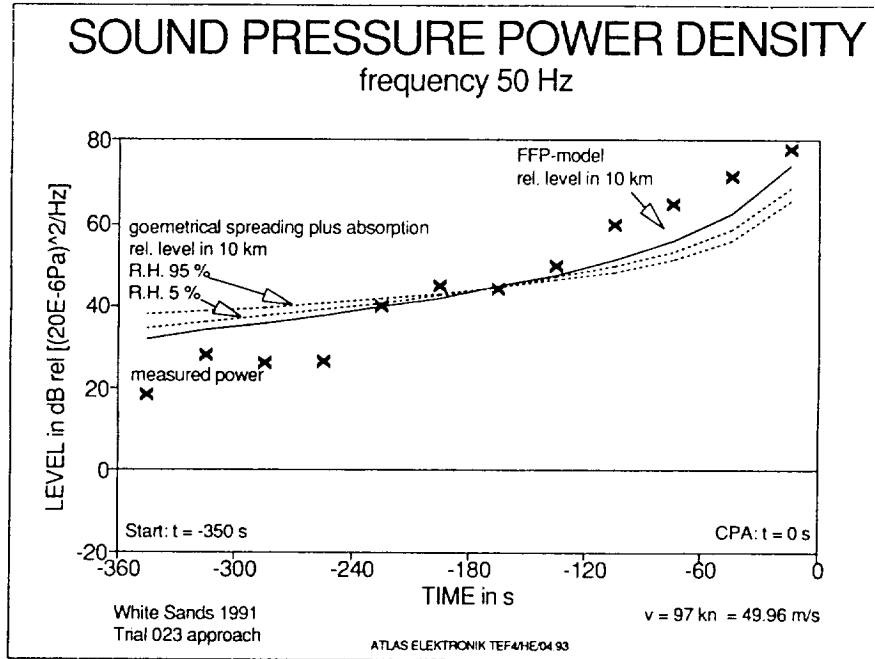


Figure 8: Comparison of the measured lapse of the SPL with theoretical models.

JAPE 1991 Terrain Masking

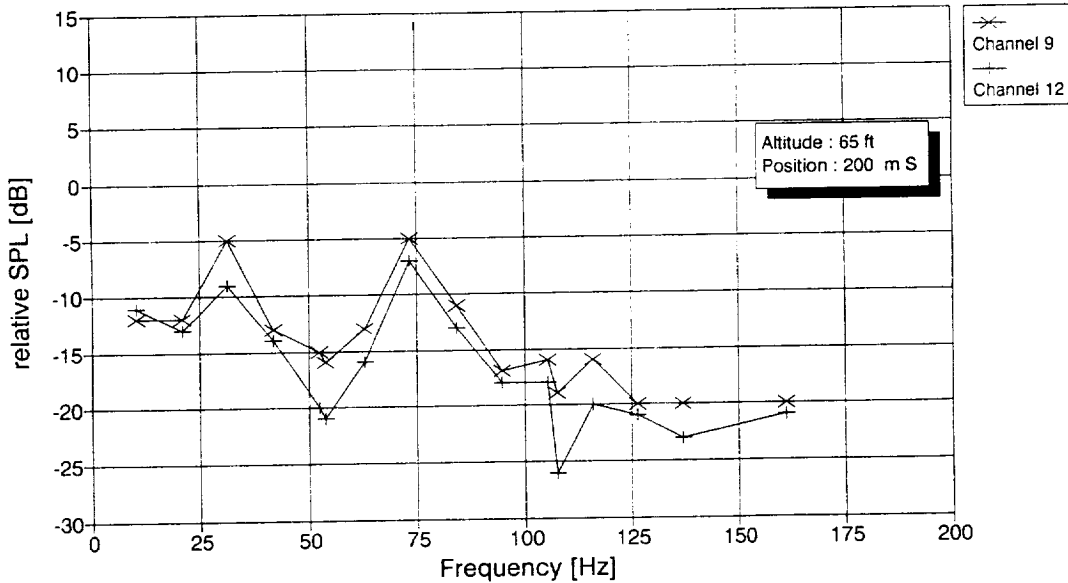


Figure 9: Frequency dependence of the insertion loss of a natural barrier for two microphone positions (see Fig. 1 for comparison). The helicopter is totally masked.

JAPE 1991 Terrain Masking

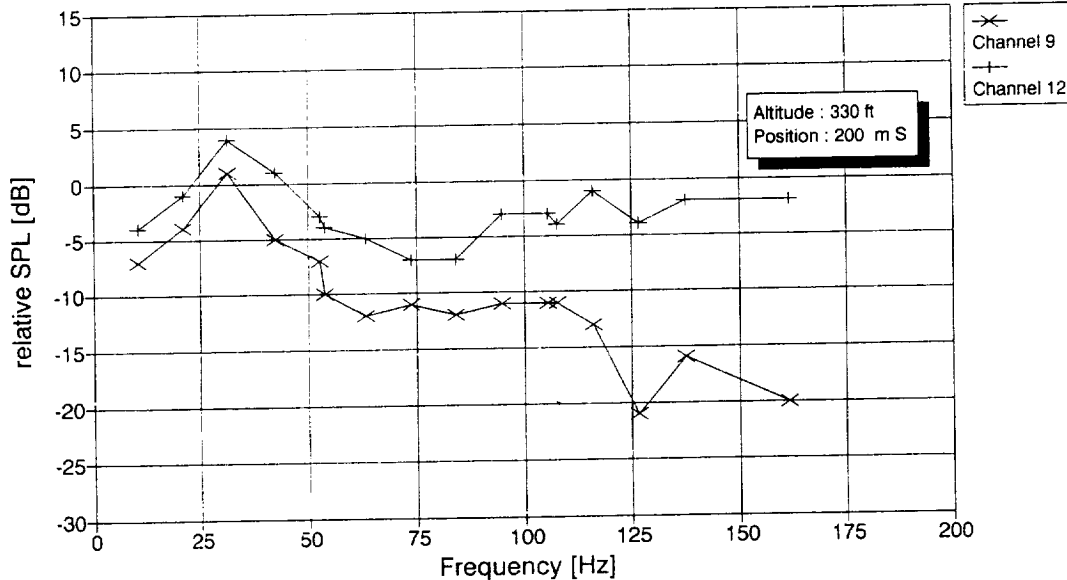


Figure 10: Frequency dependence of the insertion loss of a natural barrier for two microphone positions (see Fig. 1 for comparison). There are line-of-sight conditions between the helicopter and microphone CH-12.

INTERCOMPARISON OF REMOTE AND BALLOON-BORNE
SENSORS OPERATED AT JAPE-91

S3 - 71
24-245
P-9

Richard J. Okrasinski and Greg J. Cook
Physical Science Laboratory
New Mexico State University
Las Cruces, NM

Robert O. Olsen
U.S. Army Research Laboratory
Battlefield Environment Directorate
White Sands Missile Range, NM

SUMMARY

In recent years, there has been an increased availability of different types of remote sensors for measuring atmospheric parameters. With the introduction of remote sensors into field operation, questions arise as to their accuracy and precision. An attempt was made to address this issue by analyzing and intercomparing sets of wind and temperature data obtained during the Joint Acoustic Propagation Experiment (JAPE-91) conducted at White Sands Missile Range, New Mexico, in July and August, 1991. The remote sensing systems that were deployed included a 924 MHz wind profiler, two Doppler acoustic sodars, and a Radio Acoustic Sounding System (RASS). In situ measurements of wind, temperature, and humidity were also obtained from radiosondes. Individual system characteristics and the results of intercomparing the derived wind and temperature data from each of the systems are presented.

INTRODUCTION

The Joint Acoustic Propagation Experiment (JAPE-91) was conducted at White Sands Missile Range in south central New Mexico during July 11 - 28 and August 19 - 29, 1991. Two Doppler sodars, a 924 MHz wind profiler, and a Radio Acoustic Sounding System (RASS) were deployed by the U.S. Army Research Laboratory to collect boundary-layer wind and temperature data in support of the experiment. Upper-air wind, temperature, and humidity data were also collected by periodically released rawinsondes.

This information was later analyzed to evaluate the capabilities of the four remote sensors. Wind data from the UHF profiler and temperature data collected by the RASS were statistically compared with concurrent rawinsonde measurements. Similarly, simultaneous measurements from the two sodars were compared with each other and with concurrent wind profiler data. The percent

of time that data were successfully measured at each sampling height was also calculated to determine the functional vertical range of each sensor.

INSTRUMENT DESCRIPTION

Both sodars, manufactured by REMTECH, Inc., transmit one vertical and two tilted acoustic beams. Changes in the acoustic refractive index caused by temperature fluctuations scatter some of the transmitted energy back to the antennas. Doppler shifts in these backscattered signals are used to derive the wind velocities along the three beam paths from which horizontal wind speeds and directions are then computed. The sodars are used to measure winds between 50 and 750 m above the surface.

The older A0 model uses a trailer-mounted array of three acoustic antennas, two of which are tilted 18° from the vertical, and the newer PA2 uses a single phased array antenna with three electronically steered beams, two of which are directed 30° from the vertical and 90° from each other. Frequency coded transmissions are propagated at frequencies centered at 1600 Hz with an acoustic power of 60 W by the A0 and at 2100 Hz with an acoustic power of 140 W by the PA2.

The wind profiler transmits three 924 MHz beams, one vertical and two tilted 15° from vertical, from three antennas. Doppler shifts in the backscattered signals are used to derive the wind velocities along the beam paths. One-hour-averaged horizontal wind data are computed from the radial velocities using a random sample consensus technique. The maximum measurement height is a function of the intensity of the backscattering and the vertical resolution of the wind data, but is usually between 2 and 4 km. Peak pulse power is 500 W.

The vertical radar antenna is also used to track 2000 Hz acoustic beams transmitted by the conjunctive RASS. Doppler shifts in the backscattered energy determine the speed of the acoustic signal, which is proportional to the virtual temperature of the medium. Maximum measurement height is about 1 km. Both the wind profiler and the RASS were developed by the NOAA Wave Propagation Laboratory.

Different radiosonde systems were deployed for the July and August phases of JAPE. In July, a system manufactured by Atmospheric Instrument Research, Inc. (AIR) was used, which consists of a 1680 MHz sonde tracked by an automatic radio theodolite using a phase array antenna. Height, temperature, humidity, and balloon-to-ground azimuth and elevation angles were recorded for every 4 - 5 seconds of flight. In August, an Omega Navaid system, using equipment manufactured by Vaisala Oy, was substituted to collect data at greater heights. Vaisala RS-80 radiosondes tracked by a Vaisala Digicora ground station provided measurements for every 10 seconds of flight.

DATA COLLECTION

JAPE-91 was conducted in the extreme southeast corner of White Sands Missile Range in south central New Mexico. This is an arid region situated in a broad basin between two mountain ranges. The nearest significant feature is the 300-m high Jarilla Mountains approximately 4 km to the east. The test area slopes from an elevation of 1275 to 1254 m above sea level from south to north.

The A0 sodar, the wind profiler and RASS, and the radiosonde station were located at the same site. The PA2 sodar was situated approximately 4.5 km south, next to a 40-m hill. Other than the hill, there were no significant terrain features in the vicinity of the two locations.

Fifteen-minute-averaged wind data were collected by the PA2 sodar during July 21 - 29 every 50 m from 50 to 750 m. Concurrent A0 winds were measured every 50 m from 50 to 750 m from 2045 on July 20 to 1515 on July 27 MDT, and from 50 to 600 m the rest of the time. Both sodars were operated more than 90% of the time between midnight July 21 and 0930 on July 29 MDT. Only the A0 was operated in August.

Two sets of one-hour-averaged UHF wind profiler data were collected. Winds with a vertical resolution of 101 m were measured at 25 levels between 167 and 2601 m, and 203-m resolution winds were measured at 24 levels between 246 and 4911 m. The profiler was turned off during several testing periods to avoid interfering with other instrumentation. A total of 84 hours of data were collected in July.

Five-minute-averaged virtual temperatures were collected hourly by the RASS between 127 and 1283 m above the ground at 12 equally spaced heights. Forty-five hours of data were collected in July and 144 hours were collected in August.

Thirty-three AIR radiosondes were flown during July and tracked to 5 km above the surface. Seven Vaisala sondes, tracked to 15 - 20 km, were released during August.

DATA COMPARISONS

UHF Wind Profiler

In most cases, the wind profiler does not successfully collect data at all of its programmed altitudes. The strength of the returned signal is a function of the intensity of the turbulent scattering in the region being probed and is often too weak to be interpreted. Lower resolution winds are measured with greater success, because longer pulse lengths and more energy are transmitted. The profiler height range, therefore, is dependent on both the state of the atmosphere and the resolution of the measurement. The percent of time that one-hour wind profiler measurements were successfully collected in July was computed for each interrogation height and plotted in

Figure 1. Considerably more low-resolution data were obtained. At 2 km, for example, 101-m and 203-m resolution winds were collected about 55% and 90% of the time, respectively.

To investigate the accuracy of these measurements, low-resolution (203-m) wind profiler data collected in July were statistically compared with data from 20 rawinsonde soundings that were launched within 30 minutes of one of the profiler interrogation times. The rawinsonde winds were calculated for 200-m layers and interpolated to the profiler heights, so that both data sets had approximately the same vertical scale. There is still a rather large temporal difference, however, because the profiler winds were averaged over one hour and the rawinsonde winds were computed for approximately 40 seconds of flight. In addition, the balloon drifts away from the site as it rises. Nevertheless, the agreement between the rawinsondes and profiler was fairly good, as shown in Figure 2, where the rms wind speed and vector wind differences are plotted versus height. The latter were calculated by taking the square root of the sum of the mean square differences in the east-west and north-south component winds and are, therefore, a function of the differences in both wind speed and direction. Most of the rms vector differences were close to 2.5 m s^{-1} . This is not much larger than the $1.5 - 2.0 \text{ m s}^{-1}$ vector differences that were found between the same radiosonde system and a reference high-precision radar during a radiosonde intercomparison experiment (ref. 1). These statistics also compare favorably with the results of another study (ref. 2) in which the standard deviation of the differences in the east-west and north-south wind velocities measured by a wind profiler and rawinsondes were found to be about 2.5 m s^{-1} .

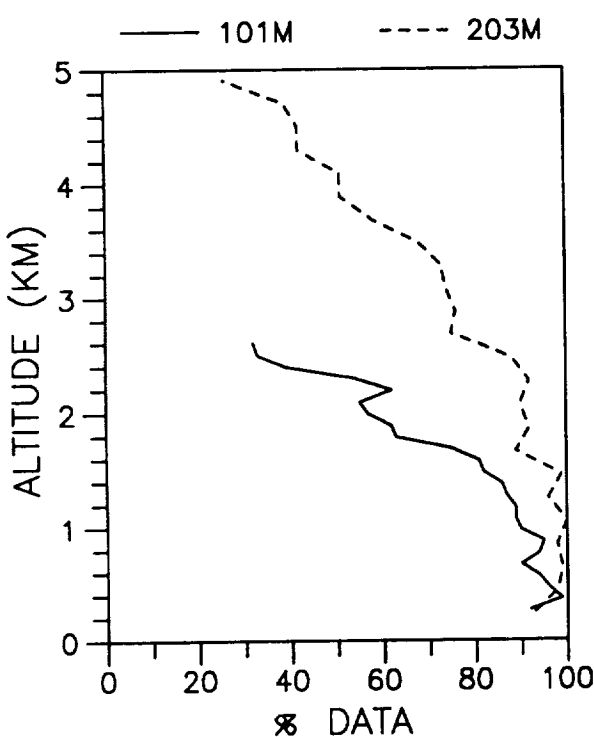


Figure 1. Percent of time wind data were successfully collected by the UHF wind profiler at 101-m (solid line) and 203-m (dashed line) resolutions.

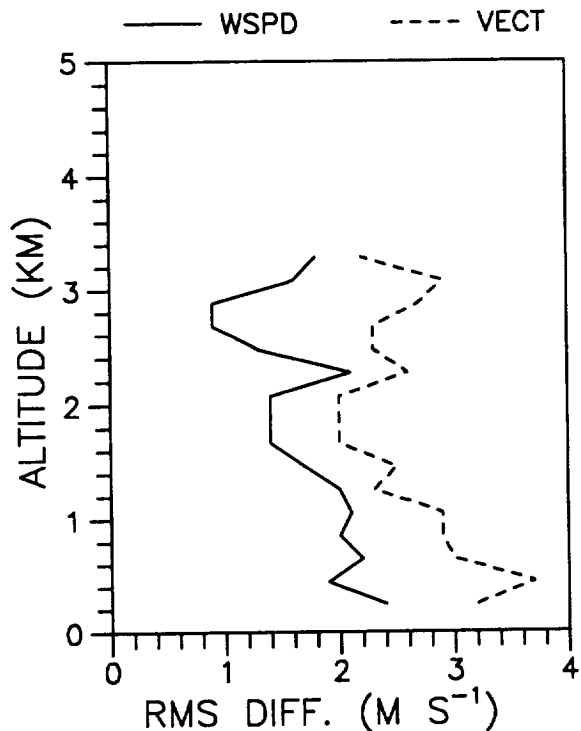


Figure 2. Rms wind speed differences (solid line) and vector wind differences (dashed line) of concurrent UHF wind profiler and rawinsonde data.

Sodars

Because the strength of the backscattered sodar signal is largely a function of the intensity and scale of the temperature fluctuations in the region being probed, the sodar height ranges vary greatly with atmospheric conditions. Using 15-minute-averaged wind data collected by the A0 and PA2 sodars between July 21 - 29, the success rate of data collection was computed as a function of altitude and is shown in Figure 3. The PA2, as expected, had a greater range. At 600 m, for example, the A0 and PA2 sodars obtained a measurement approximately 40% and 85% of the time, respectively.

Using this same data set, the comparability of the two sensors was studied by calculating statistics of the differences between their simultaneous measurements. The number of concurrent data points ranged from 616 at 100 m to 300 at 600 m. The rms wind speed and vector wind differences, plotted in Figure 4, were close to 2 and 3 m s^{-1} , respectively, at all altitudes. Means and standard deviations of the differences in wind speed and direction, shown in Figure 5, were also calculated for comparison with the results of an earlier analysis of 20-minute-averaged wind data collected by two collocated A0 sodars (ref. 3). The mean differences found in that study are comparable in magnitude to the JAPE statistics, but their wind speed and direction standard deviations of 1.1-1.4 m s^{-1} and 22 - 32°, respectively, are somewhat smaller. The poorer JAPE statistics may be partially due to the 4.5 km separation of the two sodars.

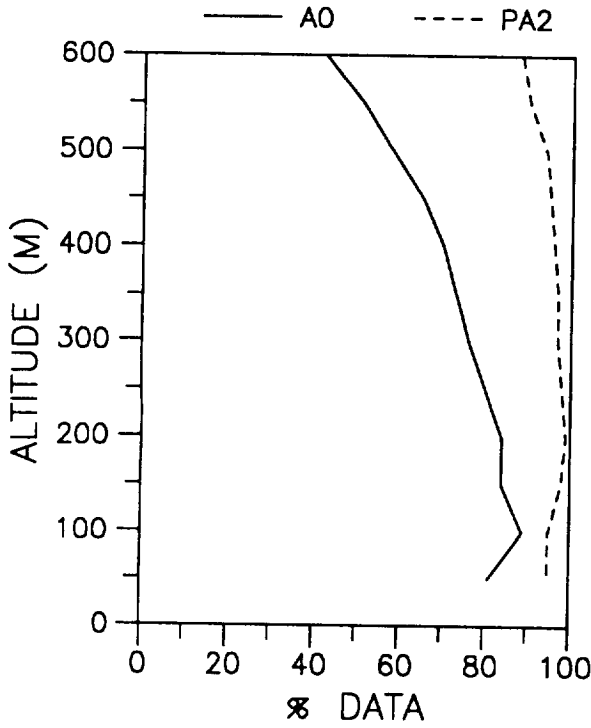


Figure 3. Percent of time horizontal wind data were successfully collected by the A0 (solid line) and PA2 (dashed line) sodar.

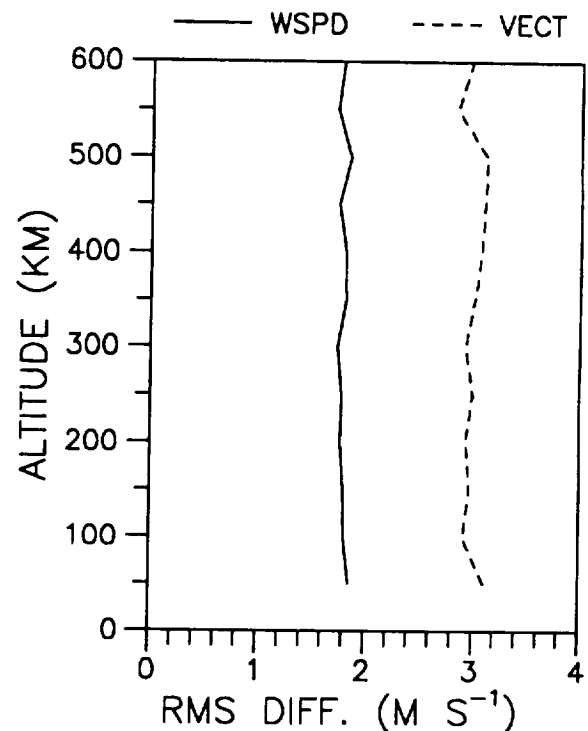


Figure 4. Rms wind speed differences (solid line) and vector wind differences (dashed line) of concurrent A0 and PA2 sodar wind data.

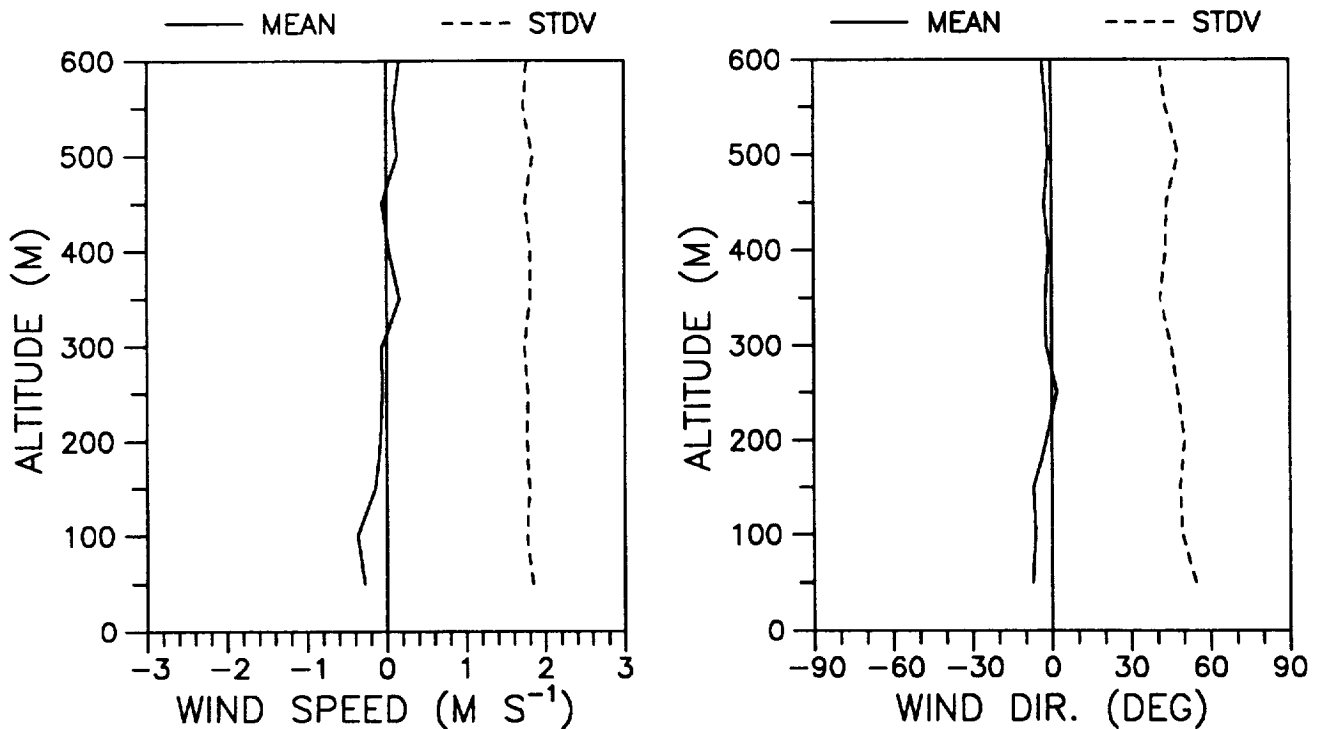


Figure 5. Means (solid lines) and standard deviations (dashed lines) of the differences in concurrent A0 and PA2 sodar wind speeds and directions.

A similar comparison of concurrent sodar and wind profiler measurements was also conducted. The sodar data were first averaged over one-hour periods and vertically interpolated to the profiler heights. Statistics of the differences between simultaneous one-hour sodar and profiler data were then calculated using only those periods when data were available from all three sensors. The rms wind speed and vector wind differences are shown in Table I. The A0 sodar, which was at the same site as the wind profiler, was found to be in better agreement with the profiler than the more distant PA2.

Radio Acoustic Sounding System (RASS)

The height range of the RASS, which consists of a sodar and a radar, also varies with atmospheric conditions. The data collection success rate, calculated with measurements from both the July and August phases of JAPE, is shown in Figure 6. Almost no data were obtained above 652 m. Measurements up to this level were statistically compared with virtual temperatures computed from 22 radiosonde soundings, which were released within 30 minutes of one of the RASS interrogation times. Means, standard deviations, and root-mean-squares of the differences are printed in Table II. The rms differences of .7 - .9 °C are comparable with those found in an earlier study (ref. 4).

Table I. Sodar-UHF Profiler Rms Differences

ALT (m)	WIND SPEED		VECTOR WIND		NPTS
	A0-UHF	PA2-UHF (m s ⁻¹)	A0-UHF	PA2-UHF (m s ⁻¹)	
268	1.5	2.0	1.9	2.5	25
369	1.5	2.0	1.9	2.5	15
471	1.4	1.9	1.7	2.5	13

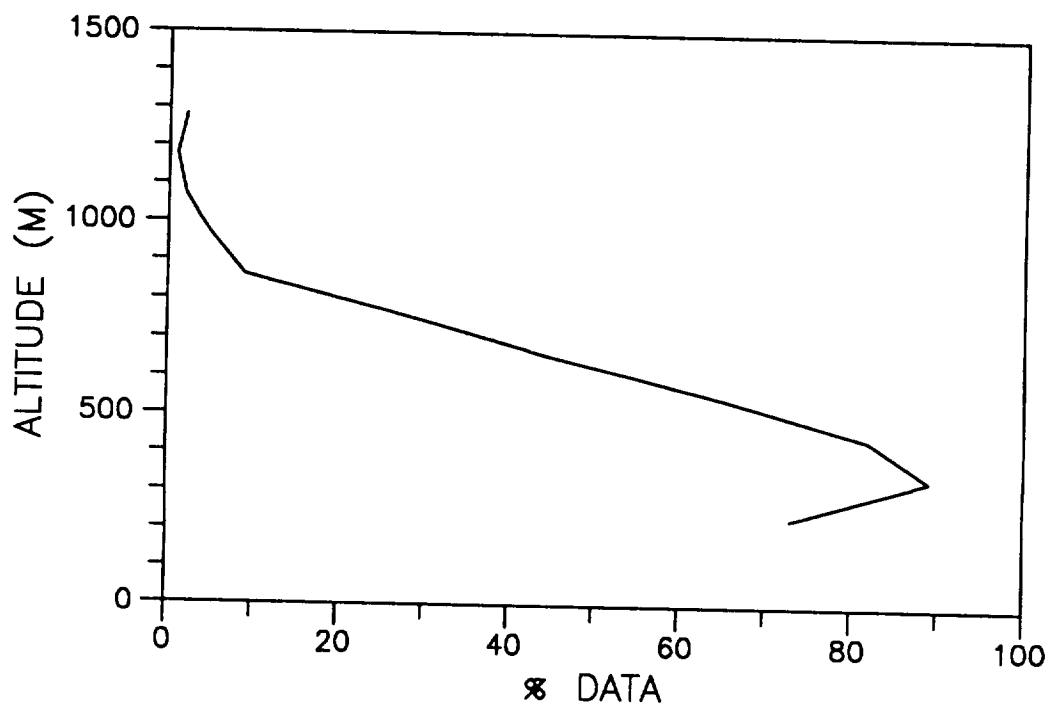


Figure 6. Percent of time temperature data were successfully collected by the RASS.

Table II. RASS-Radiosonde Differences in Virtual Temperature

ALT (m)	MEAN	SDEV (°C)	RMS	NPTS
233	.0	.7	.7	20
338	.3	.7	.8	22
442	.6	.7	.9	21
548	.5	.6	.8	17
652	.4	.7	.8	12

CONCLUSIONS

Statistical agreement between the radiosonde data and the wind profiler and RASS measurements collected at JAPE was comparable with the results of other similar studies. The rms temperature and vector wind differences between concurrent measurements were approximately .8 °C and 2.5 m s⁻¹, respectively. Standard deviations of the differences in the sodar wind speeds and directions, however, were somewhat greater than those that were found between two collocated sodars in a previous study. This may be partially due to the 4.5 km separation of the two sensors. The sodar rms vector wind differences were about 3 m s⁻¹.

Data were successfully collected at least 50% of the time at all heights below 600 m by the A0 sodar, below 652 m by the RASS, and below 2.3 and 4.3 km by the UHF wind profiler at 101-m and 203-m vertical resolutions, respectively. More than 85% of the PA2 data were collected at all altitudes up to 600 m.

REFERENCES

1. Olsen, R. O.; Okrasinski, R. J.; and Schmidlin, F. J.: Intercomparison of Upper Air Data Derived from Various Radiosonde Systems. In *Preprints: 7th Symp. on Meteor. Observations and Instrumentation*, Amer. Meteor. Soc., Jan. 1991, pp. 232-236.
2. Weber, B. L.; and Wuertz, D. B.: Comparison of Rawinsonde and Wind Profiler Radar Measurements. *J. Atmos. Oceanic Technol.*, vol. 7, no. 1, Feb. 1990, pp. 157-174.
3. Chintawongvanich, P.; Olsen, R. O.; and Biltoft, C. A.: Intercomparison of Wind Measurements from Two Acoustic Doppler Sodars, a Laser Doppler Lidar, and In Situ Sensors. *J. Atmos. Oceanic Technol.*, vol. 6, no. 5, Oct. 1989, pp. 785-797.

4. May, P. T.; Moran, K. P.; and Strauch, R. G.: The Accuracy of RASS Temperature Measurements. *J Appl. Meteor.*, vol. 28, no. 12, Dec. 1989, pp. 1329-1335.

DISCLAIMERS

The citation of trade names and names of manufacturers in this paper is not to be construed as official Government endorsement or approval of commercial products or services referenced herein.



N94-24211

EFFECTS OF ATMOSPHERIC VARIATIONS
ON
ACOUSTIC SYSTEM PERFORMANCE

54-71
201076

P. 13

Robert Nation
Stephen Lang
Lockheed Sanders, Inc
Nashua, New Hampshire

Robert Olsen
U.S. Army Atmospheric Sciences Laboratory, WSMR
WSMR, New Mexico

Prasan Chintawongvanich
Physical Sciences Laboratory, NMSU
Las Cruces, New Mexico

SUMMARY

Acoustic propagation over medium to long ranges in the atmosphere is subject to many complex, interacting effects. Of particular interest at this point is modeling low frequency (less than 500 Hz) propagation for the purpose of predicting ranges and bearing accuracies at which acoustic sources can be detected. A simple means of estimating how much of the received signal power propagated directly from the source to the receiver, and how much was received by turbulent scattering was developed. The correlations between the propagation mechanism and detection thresholds, beamformer bearing estimation accuracies, and beamformer processing gain of passive acoustic signal detection systems were explored.

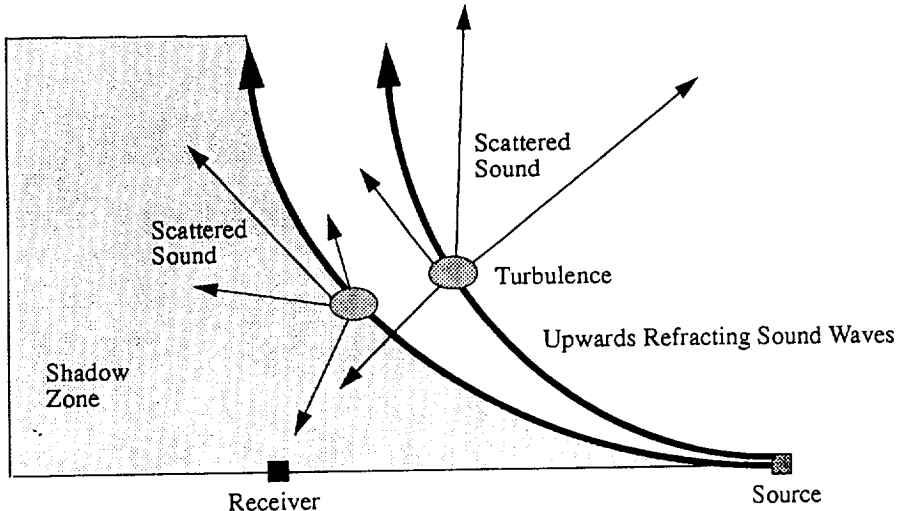


Figure 1: Upwards refraction and scattering effects on a sensor in an acoustic shadow zone.

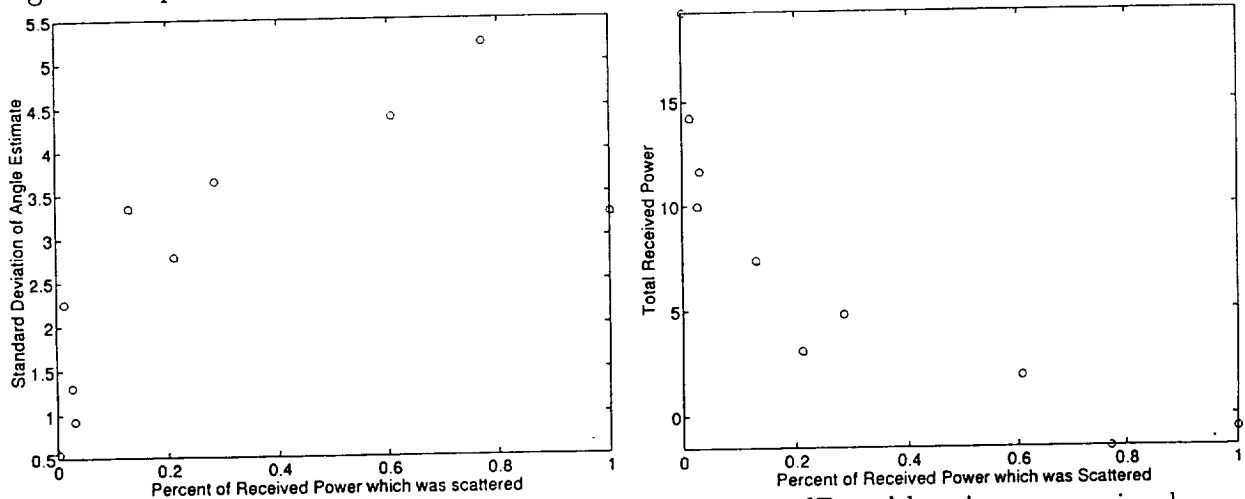


Figure 2: Received signals were attenuated by as much as 20 dB and bearing accuracies decreased by as much as 5 times when the sensor was in a shadow zone.

INTRODUCTION

Refraction and scattering together are the limiting factors in acoustic detection systems under adverse (upwards refracting) conditions, since most of the received sound is scattered (see Figure 1). Analysis of the 300 Hz tones from the short range ground to ground propagation tests at JAPE showed the sound scattered into a shadow zone was 10 to 20 dB lower in amplitude than sound which propagated directly. Bearing accuracies were reduced by as much as a factor of 5, signal detection thresholds were raised by as much as 7 dB to achieve the same probability of detection and probability of false alarm, and loss of sensor to sensor signal coherence caused as much as 2.5 dB of loss of beamforming gain when the sensor moved into a shadow zone. Figure 2 shows the effect of a shadow zone on the received signal power and bearing estimation accuracy.

IS RECEIVED POWER COHERENT OR SCATTERED?

When scattering is significant, the received signal can be modeled in the frequency domain as $S = a + b$, where a is a constant and represents the coherent, unscattered portion of the received signal, and b is the scattered component, which has had its phase randomized. b is complex normally distributed, with zero mean and variance σ_b^2 . Under these conditions, the measured signal will have a Ricean distributed amplitude, or a non-central-Chi-squared distributed power.

McBride, et al [1] concluded that acoustic signals received by a sensor in a shadow zone are suitably modeled as having a Ricean distributed amplitude, where the standard deviation of the received amplitude divided by the mean is 0.52 if the signal is received entirely by scattering (in which case it is Rayleigh distributed), and the ratio decreases with an increasing directly propagating component. Alternately, we can model this as having a received power which has a non-central Chi-squared distribution, and the non-centrality factor $\lambda = 2a^2/\sigma_b^2$ increases with increasing direct propagation. λ is the amount by which the mean of the received power is increased beyond that of a central chi-squared distributed (completely scattered) signal.

The expected value of the measured power is

$$E(P) = \frac{\sigma_b^2}{2} [2 + \lambda] \quad (1)$$

and the variance of the measured power is

$$\sigma_P^2 = \frac{\sigma_b^4}{2} [2 + \lambda] \left[1 + \frac{\lambda}{2 + \lambda} \right] \quad (2)$$

We expect to observe a central Chi-squared (2 degrees of freedom) distribution for a totally scattered signal. If we chose to use the variance divided by the mean squared of the received signal as the metric of scattered-ness, then, for a completely scattered signal, the metric, r , will be 1:

$$r = \frac{\sigma_P^2}{E^2(P)} = \frac{4 + 4\lambda}{(2 + \lambda)^2} \quad (3)$$

Note that, as the direct component of the received signal increases, the non-centrality factor, λ , increases, and r approaches 0. As the scattered component increases, λ approaches 0 and r approaches 1.

We can now solve for the scattered and direct components of the received signals:

$$\hat{P}_S = \sigma_b^2 = \frac{rE(P)}{1 + \sqrt{1 - r}} \quad (4)$$

$$\hat{P}_S = E(P) - \sigma_b^2 \quad (5)$$

where \hat{P}_S is the scattered component of the power, \hat{P}_C is the directly propagating component, and $E(P)$ is the average received power. The percent of the received power which is scattered is $100r/(1 + \sqrt{1 - r})$.

Verification with JAPE data

A suitable subset of the MIT Lincoln Laboratory's JAPE data set was identified for verification purposes. The selected tests were the ones which contained samples of ground to ground propagation of a 300 Hz sinusoid over a 500 meter distance. 300 Hz was selected because it is in the middle of the frequency range of interest, and is high enough in frequency to have a good SNR, but not so high that anti-aliasing filter concerns need to be addressed. A total of 10 such tests were identified, consisting of 5 pairs of tests in which North to South and South to North propagation was tested in rapid succession. More information about the JAPE tests can be found in [2].

Based on Equations 4 and 5 the direct and refracted component of the received power was estimated for each test. The results are shown in Table 1. By using the percent scattered power from the table, an upward/downward refraction condition decision was made, and compared to the decision made based on ray-trace plots. In 6 out of 10 cases, the decision was the same as obtained by examining ray-trace plots. The ray-trace plots were generated based on meteorological measurements. In the remaining 4 cases, the decision made based on Equations 4 and 5 better suited the received power levels than the decision made based on the ray trace plots. When looking at the revised refraction condition estimates, we note that, for all downward refracting cases, the received power was 3 dB or more. For upwards refracting conditions, the received power was 2 dB or less. This clean separation of received power levels into different classes was not obtained with decisions made based on the ray-trace plots, and gives us confidence in our separation criteria. Figure 3 plots the portion of the signal which is received by direct propagation and by scattering vs. percent scattered power, and is consistent with theory. Note that the received scattered power levels are fairly constant, regardless of refraction conditions, but that the coherent portion of the received signal decreases dramatically as upwards refraction begins to dominate. The scattered component of the received power is negligible under downwards refracting conditions.

Some possible explanations for the poor correlation between the raytrace plots and the measured acoustic data include:

- The raytraces are up to an hour different in time than the tests.
- The raytraces are apparently intended for looking at propagation over a 10-20 km range, not a 500 meter range.

- With only the raytraces, we are forced to make an upwards/downwards refracting decision, instead of percent upwards and percent downwards.
- Vertical sampling of the meteorological data near the ground may not have been adequate to accurately model conditions [3].

Table 1: Percent of Received Power which was Refracted

Test	Percent Scattered Power	Scattered Power (dB)	Coherent Power (dB)	Total Power (dB)	Refraction Condition (Note 3)	Refraction Condition (Note 4)
T005102	61	-0.3	-2.2	1.90	Up	Down
T006102	28	-0.6	3.4	4.8	Down	Down
T025102	3	-3.4	11.5	11.7	Down	Up
T026102	13	-1.5	6.8	7.4	Down	Down
T033102	21	-3.7	2.1	3.1	Down	Up
T034102	3	-5.8	9.9	10.0	Down	Down
T060102	100	-0.4	-4.9	-0.7	Up	Up
T061102	1	-4.4	14.2	14.3	Down	Down
T068102	77	-2.6	-7.9	-1.5	Up	Up
T069102	0	-7.7	19.3	19.3	Down	Up

Notes:

- For test T060102, the percent scattered power was calculated at 114%, which was attributed to statistical variation, and rounded down to 100%.
- Powers are measured in dB in a 0.25 Hz band relative to an arbitrary reference.
- The refraction conditions in column 6 are derived by examining the percent scattered power. 0-50 is Down, 50-100 is Up.
- Refraction conditions in column 7 are based on raytrace plots.
- Results are for 300 Hz tones only.
- Percent Scattered Power is $r/(1 + \sqrt{1 - r})$.

IMPACT OF REFRACTION CONDITION ON DETECTION THRESHOLD

If a high probability of detection ($P_d = 0.90$) is required coherent signals can be detected at 7 dB less signal-to-noise ratio (SNR) than incoherent, or scattered signals. Figure 4 shows the probability of detection vs SNR curves for both types of signals. The non-fluctuating case is a coherent signal, modeled as a sinusoid, and the fluctuating case is a Swerling I model [4]. The false alarm rate for the points in Figure 4 is a constant $P_f = 10^{-4}$.

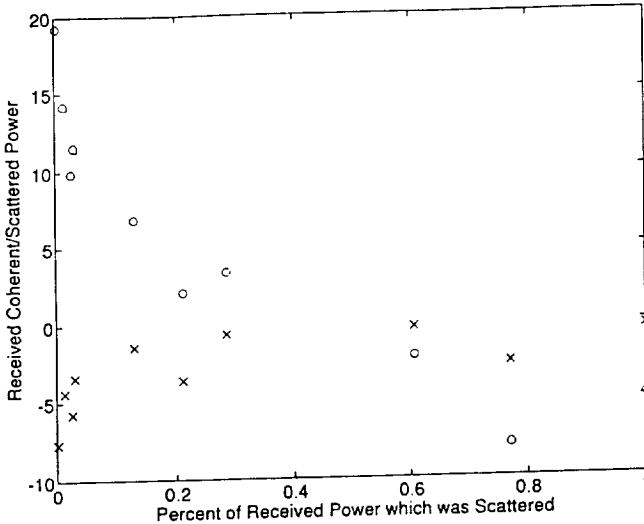


Figure 3: Scatter plot of coherent and scattered components of received power vs. percent scattered power. Coherent component is plotted with circles, and scattered component is plotted with X's. As expected, the directly propagating component increases as the percent scattered power approaches zero, and vanishes as it approaches 1. The scattered power levels are fairly constant, regardless of refraction conditions.

For low probabilities of detection, fluctuating signals are more detectable than non-fluctuating signals, since the fluctuating signal occasionally has a high SNR and is detected. Since the crossover point is about $P_d = 0.27$, this is not particularly useful.

IMPACT OF REFRACTION CONDITION ON BEARING ESTIMATION ACCURACY

Acoustic detection systems can be used as target tracking or cuing systems if they can provide a sufficiently reliable bearing estimate to the target. Bearing estimates are affected by received SNR, signal coherence, and propagation path effects. A sensor in a shadow zone, receiving primarily scattered power, experiences a loss of received SNR compared to a directly propagated signal, a loss of coherence associated with scattering, and an indirect propagation path. The combined effect for the JAPE data was a degradation in bearing accuracy of up to a factor of 5 when compared to a directly propagated signal. The loss of bearing accuracy may also result in a reduction in the system's ability to determine that two signals originated from different sources, based on their angle of arrival.

For a correlating beamformer,

$$\hat{\theta} = \max_{\theta} \left(\sum_i S_i e^{-j(\vec{k}(\theta) \cdot \vec{r}_i)} \right) \quad (6)$$

where $\vec{k}(\theta)$ is the wave vector, and \vec{r}_i is the location of the sensor relative to a reference point.

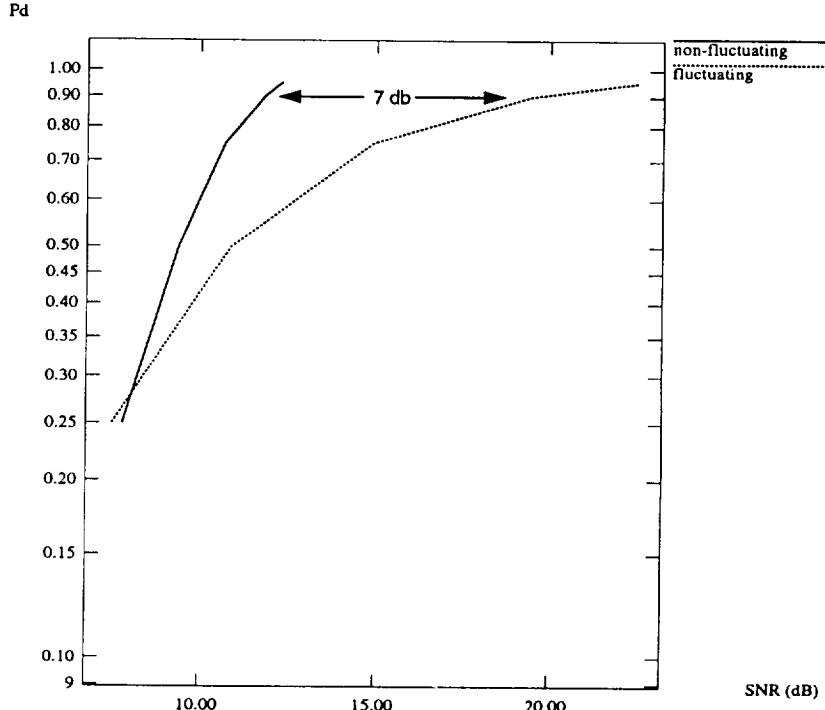


Figure 4: Coherent signals can be detected at 7 dB less SNR than incoherent signals, for $P_d = 0.9$ and $P_f = 10^{-4}$

All sensors are assumed to have the same gain. If the received power level is the same for all sensors (a valid assumption for small aperture arrays), and the array is circular, then the bearing accuracy is

$$\sigma_{\hat{\theta}}^2 = \frac{c^2 D_s}{(N-1)(2\pi\rho f)^2} \quad (7)$$

where c is the acoustic propagation speed, D_s is the average phase structure function for all sensors, N is the number of sensors, ρ is the radius of the sensor array, and f is the signal frequency.

Daigle studied straight line propagation [5] (which we expect to be roughly descriptive of downwards refracting conditions), and determined that

$$D_s(R, \rho) = \langle [\phi_1 - \phi_2]^2 \rangle \approx \sqrt{\pi} \langle \mu^2 \rangle k^2 RL \quad (8)$$

where $\langle \mu^2 \rangle$ is the fluctuation in the acoustic index of refraction, which is written as $n = 1 + \mu$, k is the signal wave-number, R is the propagation path length, and L is correlation length. C_n^2 , the acoustic index of refraction squared, is related to $\langle \mu^2 \rangle$ by $C_n^2 |r^{2/3}| = \langle \mu^2 \rangle$, where r is the sensor separation. C_n^2 can be computed [6] from measurements taken at JAPE via

$$C_n^2 = \frac{C_v^2}{c_o^2} + \frac{C_T^2}{4T_o^2} \quad (9)$$

where C_v is the speed of sound structure function, c_o is the average speed of sound, C_T is the temperature structure function, and T_o is the average temperature [7].

From the above equations, we can see that the bearing estimation error of an acoustic direction-finding system is proportional to the phase structure function of the received signal, and inversely proportional to its frequency. The phase structure function is proportional to the fluctuation in the acoustic index of refraction.

McBride, *et al.* [1, 8] show that, in an upwards refracting environment, propagation can be appropriately modeled by having upwards propagating signals scattered off of a finite number of turbules which lie in their paths. The loss of the coherent portion of the received signal under upwards refracting conditions is expected to cause bearing estimation accuracy to decrease when compared to downwards refracting conditions.

These equations neglect an important factor relating to bearing estimation: if we examine a short segment of data, during which time the refraction conditions did not change, then, at the same time that turbulence is increasing the phase structure function, and degrading bearing estimation accuracy, it is increasing the amount of energy which is scattered, and the amount of received energy, which improves bearing accuracy. The relationship between received SNR and bearing error is

$$\sigma_\theta^2 = \frac{c^2}{(N - 1)(2\pi f \rho)^2 SNR} \quad (10)$$

where SNR is the received signal-to-noise power ratio. The relative importance of phase perturbation and signal-to-noise ratio varies depending on signal strength.

Verification against JAPE data

Using the data presented in Table 2 we can compare the average bearing accuracy during periods of upwards refraction (4.3°) to the average bearing accuracy during periods of downwards refraction (2.2°). The expected degradation associated with upwards refraction is observed.

Figure 5 shows the relationship between C_n^2 , the total received power, and the phase structure function, for a short period of time during upwards refracting conditions. Note all but one increase in the phase structure function occurred at the exact same time as a dip in the received power levels, but the relationship between C_n^2 and the received power and phase structure function is not so obvious. From this we conclude that, for this data segment, over short periods of time the bearing estimation accuracy is dominated by changes in the received power levels, not by changes in C_n^2 . Note that the C_n^2 data was delayed 250 seconds to allow for the turbulence field to move

Table 2: Comparison of bearing estimation accuracy to other key parameters.

Test	C_n^2	Refraction	Received Acoustic Power (dB)	Received SNR (dB)	Phase Structure Function (radians 2)	σ_θ (degrees)
T005102	2.45e-6	Up	1.9	41	2.3e-1	4.4
T006102	2.45e-6	Down	4.8	42	1.6e-1	4.1
T025102	6.61e-7	Down	11.7	51	7.8e-3	0.9
T026102	1.13e-6	Down	7.4	47	1.1e-1	3.3
T033102	8.20e-7	Down	3.1	40	7.0e-2	2.8
T034102	4.43e-7	Down	10.0	50	1.5e-2	1.3
T060102	1.24e-6	Up	-0.7	37	9.7e-2	3.3
T061102	1.30e-6	Down	14.3	51	5.3e-2	2.3
T068102	2.17e-6	Up	-1.5	35	4.0e-1	5.2
T069102	2.88e-6	Down	19.3	55	1.2e-2	0.6

Notes:

1. C_n^2 measurements are 15 minute averages at 2 meter altitude.
2. Refraction is determined by computing the percent scattered power Eqs 3 through 5.
3. Powers are 30 second averages, in dB relative to an arbitrary pressure, for a 300 Hz tone.

from the meteorological measurement tower to the center of the propagation path. This delay, which assumes that the turbulence field is frozen, may contribute to the poor correlation.

For the tests examined earlier, the received SNR was between 35 and 55 dB, which induces angular errors of between 0.37 and 0.04 degrees, which was not significant compared to the measured errors. For the data in figure 5, the received signal's average SNR was only 18 dB, which causes an average bearing error of $\sigma_\theta = 2.6^\circ$. If we examine the received power vs. time curve from Figure 5, we note that the power has drop-outs of 20 dB or more, making the received SNR during these times a mere -2dB, resulting in an expected σ_θ of 26° , and a phase structure function of about 1.6 radians 2 , which is exactly what was observed. The received power on this trial was lower than on the other trials that were explored, because a set of tones was played, instead of a single tone. Since the other trials were single tones, the received SNR was higher, and the dropouts in received power levels were less significant. Unfortunately, the other tests did not last long enough to look for a short term correlation between phase structure function and C_n^2 .

The results obtained from Figure 5 are significant to acoustic detector design, since average received SNRs of 18 dB are well into the detectable range for such systems. The conclusion is that the direct effect of atmospheric turbulence on the bearing accuracy of such systems can be neglected, but the indirect effect, which causes drop-outs in received power levels, and results in a decrease in angular accuracy, can not be neglected. Acoustic detectors should be designed to make bearing

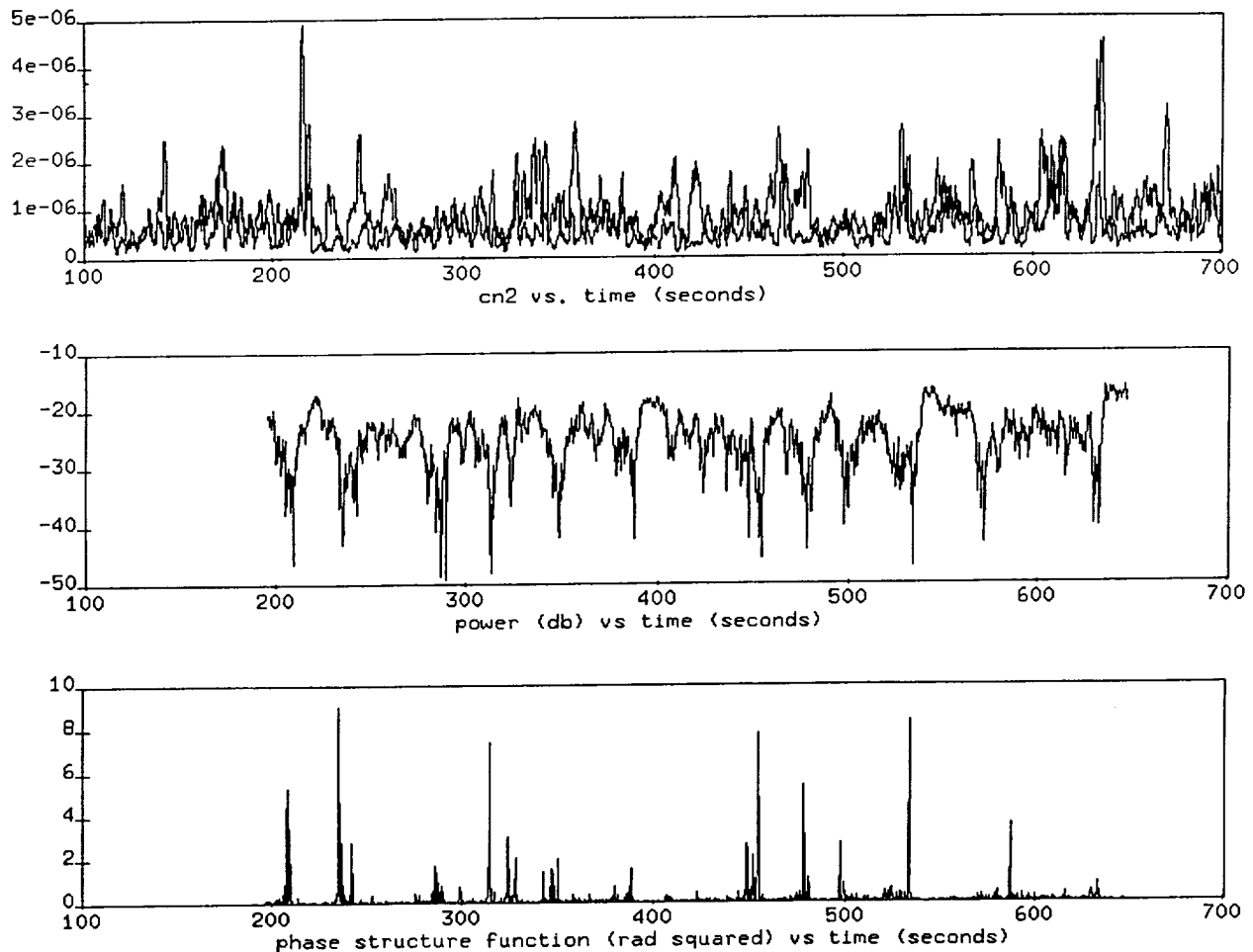


Figure 5: C_n^2 data, measured at 8 and 16 meters altitude, is delayed 250 seconds and plotted on the same scale as received power and phase structure function. Note that all but one increase in the phase structure function is matched in time to a dip in the received power. Also note that the two strongest peaks in C_n^2 match two strong increases in received power.

estimates during the peaks in the received power levels, and should avoid using the data received during the drop-outs.

Further tests to look for short-term correlation between C_n^2 and angular accuracy are needed. The tests which are missing from the JAPE data consist of playing a single, loud tone over a 500 meter propagation distance, for a long period of time (10 minutes or more). Meteorological data should be collected at a point as close to the midpoint of the propagation path as possible, and for a time covering about 10 minutes before and after the acoustic test.

IMPACT OF REFRACTION CONDITION ON BEAMFORMER PROCESSING GAIN

Beamforming gain is one of the most significant contributors to processing gain. Gain is achieved by attenuating sound from all directions but one. This attenuation is also exploited for direction finding. For perfectly correlated signals, beamforming gain is approximately

$$G = 10 \log N \quad (11)$$

where N is the number of sensors. This level of gain is achieved because target signals add coherently, so that the output power is N^2 times the input power, while noise and interference signals add incoherently, so that output power is N times the input power.

Coherence is used to measure how well signals are correlated. Coherence is defined as

$$\Gamma_{ij} = \frac{\langle S_i S_j \rangle}{\langle S_i \rangle \langle S_j \rangle} \quad (12)$$

It can be shown that

$$\Gamma(r, \rho) = e^{-D(r, \rho)/2} = e^{-(D_X + D_S)/2} \quad (13)$$

where $D(r, \rho)$ is the signal's structure function after propagating a distance r to two sensors which are ρ apart, D_X is the amplitude structure function, and D_S is the phase structure function.

For a correlating beamformer, the loss of beamformer gain due to loss of coherence is

$$L = -10 \log \left[\frac{\sum_{ij} \Gamma_{ij}}{N^2} \right] \quad (14)$$

where N is the number of sensors, and Γ_{ij} is the coherence between sensors i and j . If we assume that all $\Gamma_{ij} = \Gamma$ if $i \neq j$ and $\Gamma_{ii} = 1$, then this reduces to

$$L = -10 \log \left[\frac{1 + (N - 1)\Gamma_{ave}}{N} \right] \quad (15)$$

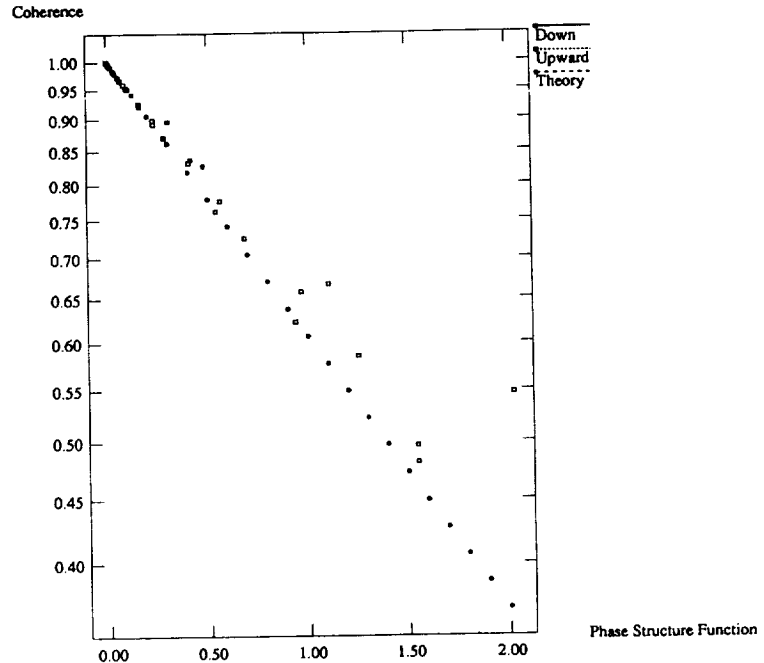


Figure 6: An expected relationship between signal coherence and phase structure function was observed.

Verification with JAPE data

Equation 13 describes the expected relationship between the phase structure function and the coherence between the signal received on two sensors. The relationship is borne out by the data, if D_X is neglected as Daigle suggests (D_X has been shown to be smaller than D_S in practice). Figure 6 shows the relationship for upwards and downwards refracting cases, and for Equation 13.

The effect of coherence on beamformer gain has been stated in Equation 15. From Figure 6, we can see that, for downwards refracting cases, the minimum measured coherence was 0.8, which results in a loss of 0.84 dB of gain in an eight element, 1 meter radius correlating beamformer. While small, this loss is measurable. For upwards refracting cases, the smallest measured coherence was 0.5, resulting in a loss of beamformer gain of 2.5 dB, which is significant.

SUGGESTIONS FOR FUTURE WORK

Additional data collection tests would allow a more thorough investigation of some interesting phenomena:

- long duration (10 minutes or more), short range, single tone tests could be used to look for the expected short-term correlation between micro-met and acoustic data. Although we looked for this correlation, the data set was not sufficient to make a definite decision about whether or not this correlation existed.
- time-of-arrival fluctuation tests for medium and long range propagation of impulsive noises would aid in designing and evaluating acoustic ranging systems.
- tests to verify scattering model predictions, ie. bearing estimation error and frequency correlation bandwidth, under upwards refracting conditions. Existing data can be used to measure bearing estimation error, but there were not many tests performed under upwards refracting conditions.

References

- [1] Walton E. McBride, Henry E. Bass, Richard Rasspet, and Kenneth E. Gilbert. Scattering of sound by atmospheric turbulence: A numerical simulation above a complex impedance boundary. *The Journal of the Acoustical Society of America*, 90(6):3314–3325, 1991.
- [2] Bruce W. Kennedy, Robert Olsen, John R. Fox, Richard Savage, George Mitchler, and Richard Okrasinski. Joint acoustic propagation experiment project summary. Technical report, The Bionetics Corporation and the US Army Atmospheric Sciences Laboratory and the Physical Sciences Laboratory of the New Mexico State University, September 1991.
- [3] J. S. Robertson. Numerical simulation of intensity fluctuations caused by wind gusts. *The Journal of the Acoustical Society of America*, 87(3):1353–1355, March 1990.
- [4] Lamont V. Blake. *Radar Range-Performance Analysis*. Artech House, Inc., 1986.
- [5] G. A. Daigle, J. E. Piercy, and T. F. W. Embleton. Propagation of sound in the presence of gradients and turbulence near the ground. *The Journal of the Acoustical Society of America*, 79(3), 1986.
- [6] Edmund H. Brown and S. F. Clifford. On the attenuation of sound by turbulence. *The Journal of the Acoustical Society of America*, 64(4), October 1976.
- [7] P. Chintawongvanich and Robert Olsen. Experimental study of temperature structure parameter in the surface layer. *Seventh Symposium on Meteorological Observations and Instrumentation and Special Sessions on Lower Atmospheric Studies*, January 1991.
- [8] Walton E. McBride, Henry E. Bass, Richard Rasspet, and Kenneth E. Gilbert. Scattering of sound by atmospheric turbulence: Predictions in a refractive shadow zone. *The Journal of the Acoustical Society of America*, 91(3):1336–1340, 1992.

**COMPARISON OF MEASURED AND PREDICTED PURE TONE
PROPAGATION LEVELS FROM JAPE-1: AN EVALUATION OF THE
PERFORMANCE OF ASOPRAT.**

Carl K. Frederickson, Henry E. Bass, Richard Raspet and John Messer

Physical Acoustics Research Group

University of Mississippi

University, Mississippi 38677

55-71

2/10/71

PL 10

ABSTRACT

Joint Acoustic Propagation Experiment Phase One (JAPE-1) short range propagation data has been used to evaluate the performance of the Advanced Sound Propagation in the Atmosphere (ASOPRAT) prediction code. The pure tone short range data has been Fourier analyzed giving the propagated pressure levels as a function of frequency. Meteorological profiles measured at the experimental site were used as input for the acoustic prediction routine ASOPRAT. Predicted and measured propagation levels are compared in decibels (dB) relative to one of the measurement positions for receivers on the line passing between the two thirty meter towers. Agreement between predicted and measured levels is very good. Source strength data has not been available so the comparisons show good agreement as to the shape of the propagation loss curve not necessarily the propagation levels.

INTRODUCTION

During JAPE-1, short range acoustic propagation data was gathered in which the source was a speaker emitting a pure tone. The data was gathered by MIT Lincoln Laboratory microphones located between the two source towers and in some cases by the French-German Research Institute of Saint Louis (ISL) microphones located about the South tower. The set up for the microphone data to be discussed is shown in Fig. 1. ISL data exists for only one of the data sets used in this paper. Fourier analysis of the measured time series is used to find the acoustic propagation levels for a particular frequency.

Along with the acoustic data, meteorological data was also taken. Using the data, sound-speed profiles can be calculated and used to predict the acoustic propagation levels. This met-data was used in ASOPRAT to predict the propagation levels. The levels predicted by ASOPRAT were then compared to the measured levels.

Analysis of four data sets will be included in this paper. Figure 2 shows the effective sound speeds ($c_{ef} = c + w$, c is the sound speed and w is the component of the wind along the direction of propagation) for the four data sets. For data sets 001102 and

057102 the source height is 30m. For data sets 025102 and 061102 the source height is 2m. For each of the source heights there is one effective sound speed profile in Fig. 2 that is upward refracting and one that is downward refracting. In choosing the data to be discussed, the source height and effective sound speed profile were considered, not which tower the source was located in. The propagation will be determined by the wind direction and the sound speed profile. One disadvantage of using these four sets is that the measured data does not cover the same range. For the two data sets with the source on the South tower, 057102 and 061102, there are no measurements closer than 500m, while for data set 025102 there is no data past 500m from the source.

DATA ANALYSIS

Figure (3a) shows one example of the pressure time series measured in the short range experiments. Figure 3b shows the Fourier analyzed signal for this time series. The MIT data was low pass filtered at 670Hz so there are no measured signals above 650Hz.

The data files containing the time series are very large. The analysis was done on a workstation equipped with both 'C' and Fortran compilers. A sample size of 2048 points was used as this represents about 1 second of data. An unwindowed FFT was performed on the data and the power spectrum calculated. To arrive at the dB levels shown in Fig. 3b the power spectrum of a 1/3 octave band was summed to get p^2 . The dB level is given by

$$\text{dB} = 10.0 \log_{10} (p^2). \quad (1)$$

Equation (1) represents the dB level at a particular frequency at one time. Figure 3b was produced by displaying the dB levels of a single frequency for consecutive one second samples.

The length of time each frequency signal was broadcast is readily apparent in Fig. 3b. It is also evident that the propagation level over that time changes. In order to arrive at a level that can be compared to theory an average propagation level was found. Each of the broadcast signals in Fig. 3b was summed and divided by the broadcast length providing an average level over the broadcast. This is the level that will be used in the comparison to theoretical predictions.

ASOPRAT

ASOPRAT is an outdoor acoustic propagation routine that has been developed by the Physical Acoustics Research Group of the Department of Physics and Astronomy at the University of Mississippi (PARGUM). A meteorological profile is read by the code which is used to construct a sound speed profile and a wind speed profile along the direction of propagation. The wind and sound speed profiles are used in raytracing calculations or in Fast Field Program (FFP) calculations to predict the level of an acoustic signal.

ASOPRAT employs either a raytrace or an FFP calculation when needed. Raytracing is used first as it is much faster, especially when multiple frequencies are being run. The ground is treated as an impedance surface. The Attenborough four parameter impedance model is used to calculate the impedance. The raytrace function will attempt to locate rays leaving the source that meet at the receiver. It only uses the four most intense rays to calculate the propagation level, two direct rays and two one bounce rays, if they exist. No multiple bounce rays are considered. The Fast Field Program is used if raytracing cannot find any rays that reach the receiver (shadow zone) or when a focus occurs at the receiver.

When raytracing fails a Fast Field Program (FFP) is used to complete the prediction. The FFP calculation must be done separately for each frequency. The calculations take longer than the raytrace calculation. As the calculation involves spatial FFT's, finding the propagated level at a set of specific points is impractical. For the purposes of the paper, however, the FFP can be run once using the maximum range and the output of the calculation for each position out to the maximum range saved. This calculation uses the effective sound speed and the impedance ground to get the prediction.

COMPARISON

Predicted acoustic propagation levels are shown along with the measured levels from the JAPE-1 measurement in Figs. 4-7. The measured acoustic level will depend on the source level of the signal. At this time we have no information on the source levels for any data we have analyzed. In the figures, the level at one of the receivers has been used as a reference level for all other points. In Fig. 4 the ISL microphone at 800m from the North Tower was used as all of the measured data shown has a value there. In Fig. 5 the microphone at 100m from the North Tower is used as the raytrace calculation and is not valid for any of the microphones further away. Both Figs. 6 and 7 use the microphone at 500m as this is the closest microphone to the source on the South Tower.

Except for a few points, the predictions of ASOPRAT's raytrace and FFP calculations are very close to the measured values. For the sources located at 2m above the ground the raytrace calculation fails at a very short range. In these cases the FFP will be the main means of prediction. With the source at a height of 30m raytrace worked well out to 900m for the upward refracting 057102 and for all of the data for the downward refracting 001102 data set.

The comparisons shown in Figs. 4-7 show very good agreement between the measured and predicted propagation levels. There is very good agreement between the shapes of the predicted propagation curves and the measured data for Figs. 5-7. In Fig. 4 there is quite a discrepancy between the shape of the theory and the data. This is the only set of data with an appreciable cross-wind present. At this time ASOPRAT does not take into account cross-winds.

In comparing the actual measured and predicted propagation levels a common reference point was needed. As was discussed earlier the reference point was arbitrarily chosen to be one of the microphones. With this in mind the measured and predicted levels again compare very well except for data set 001102. Note however that by using a microphone that is a distance away from the source as a reference some of the effects of turbulence may be canceled. For example if the reference point is a shadow zone the underprediction of the sound level will not be seen due to normalization to the higher than expected shadow level.

CONCLUSION

Comparison of the JAPE-1 pure tone acoustic data to predictions from ASOPRAT shows very good agreement. The shape of the calculated propagation loss curves agreed very well with the data. As there is no source level data the comparisons use one of the data points as a reference for the dB representation. This did allow for the easier comparison of the shape of the propagation loss curve. However, the very good agreement between the measured and predicted levels may be invalid. The worst agreement is seen in the data set with the largest cross-wind.

For future work, the source levels will be needed to determine the proper reference levels. It would be preferred to have the data collected by the WES group. This would provide data spaced at 100m over a full kilometer regardless of the location of the source. It might be useful to try and estimate the met-profile at the time each data set was acquired. This may be done with a code provided by Dr. A. K. Blackadar at Pennsylvania State University. This could provide met-profiles which better describe the propagating medium.

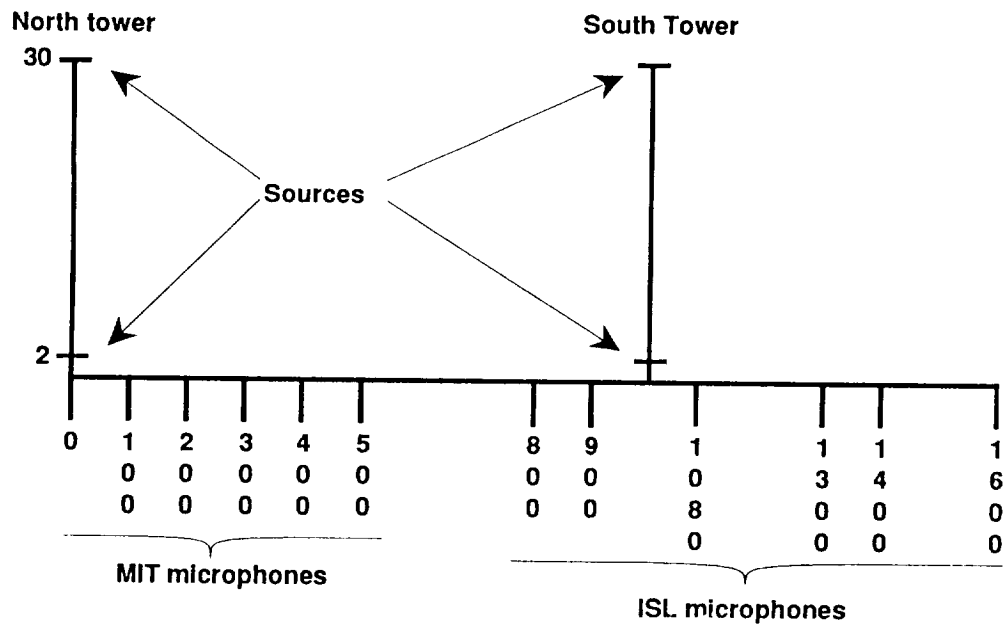


Figure 1. This figure shows the locations of the sources and microphones for the pure tone measurements.

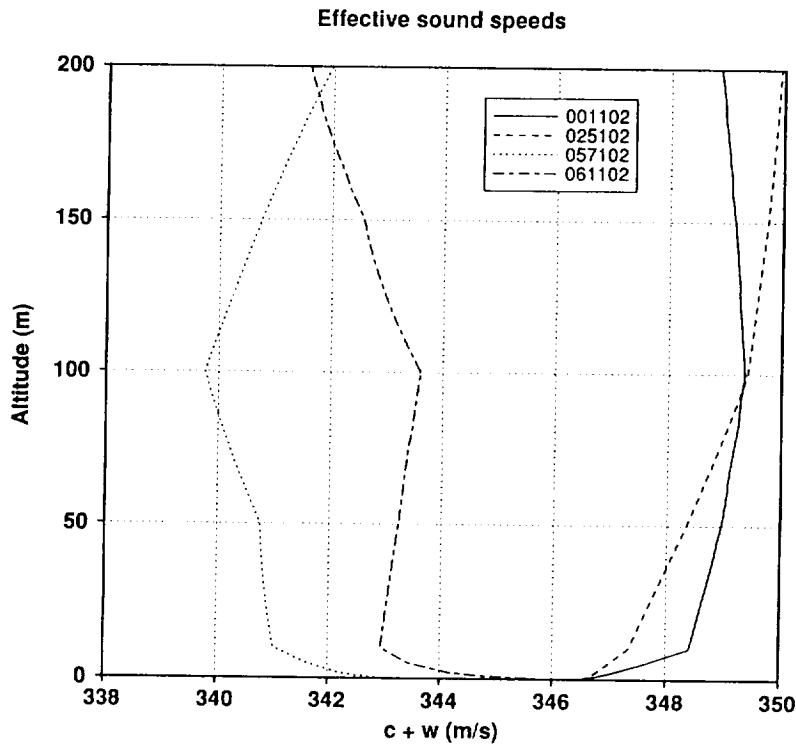


Figure 2. The effective sound speeds for the four data sets analyzed. The effective sound speed is the sum of the sound speed and the velocity component of the wind in the direction of propagation.

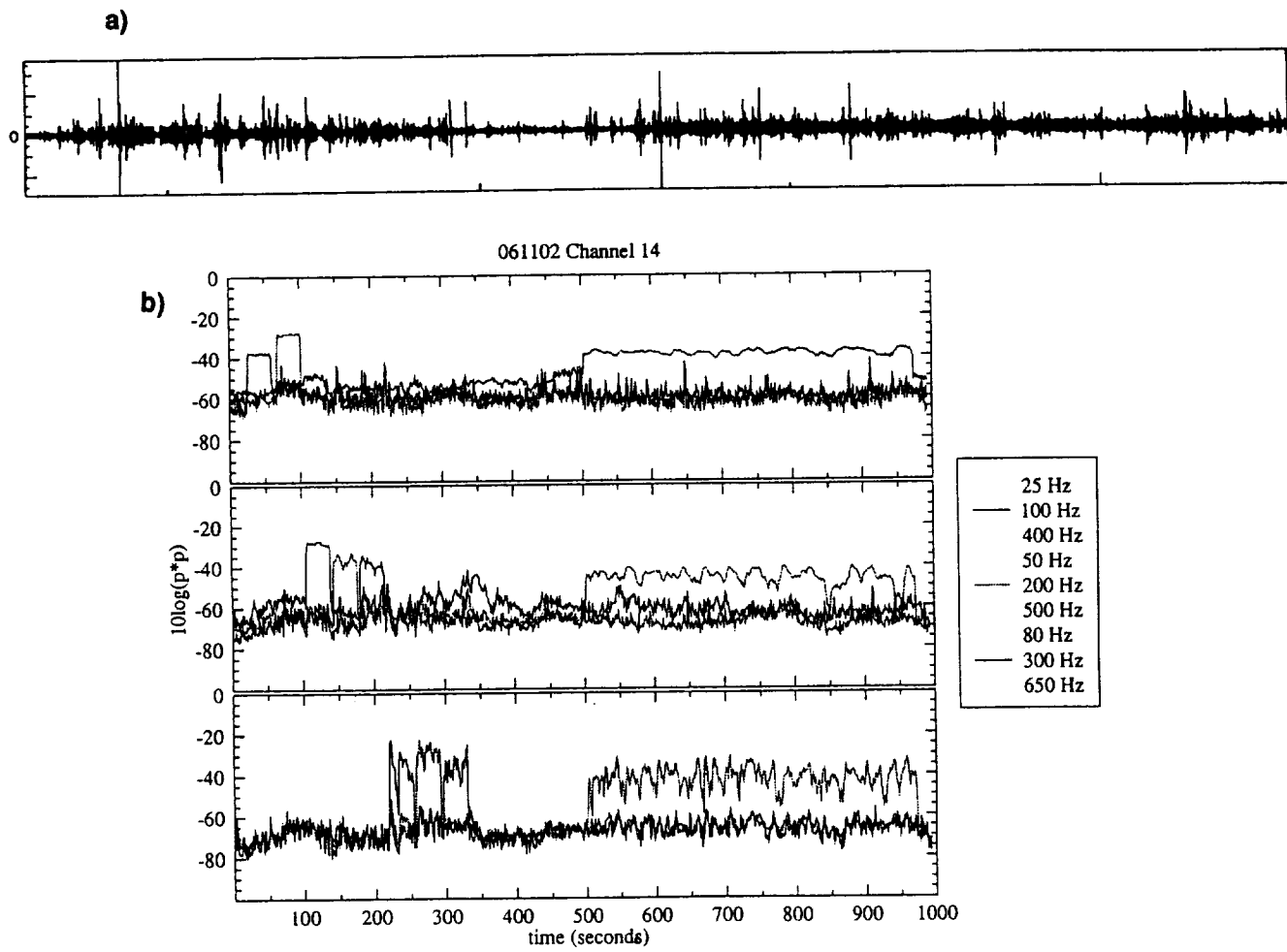


Figure 3. a) The raw time trace from channel 14 of the MIT recording for data set 061102. b) The Fourier analyzed data set for the time trace in (a).

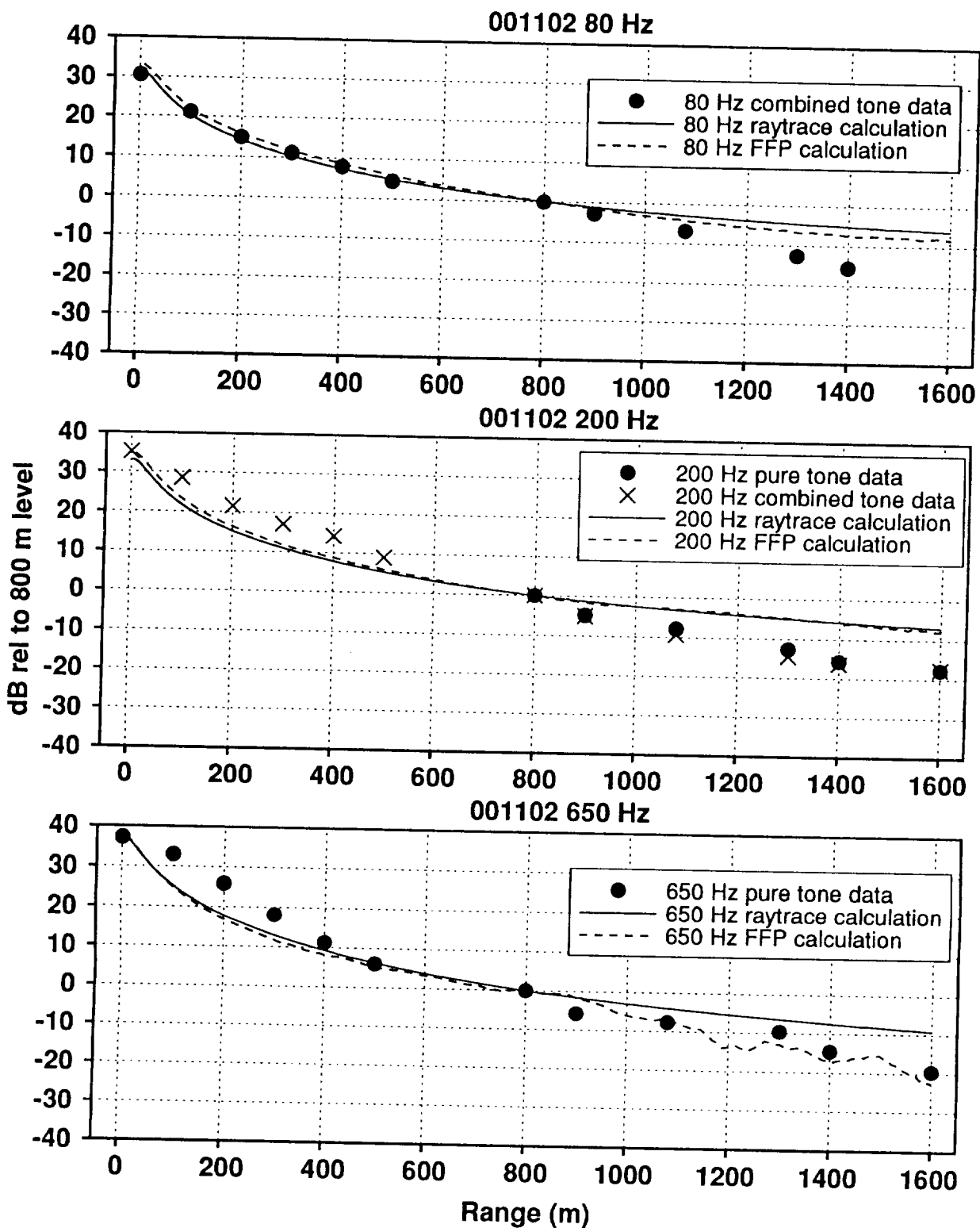


Figure 4. Comparison of ASOPRAT predictions and measured propagation levels for data set 001102.

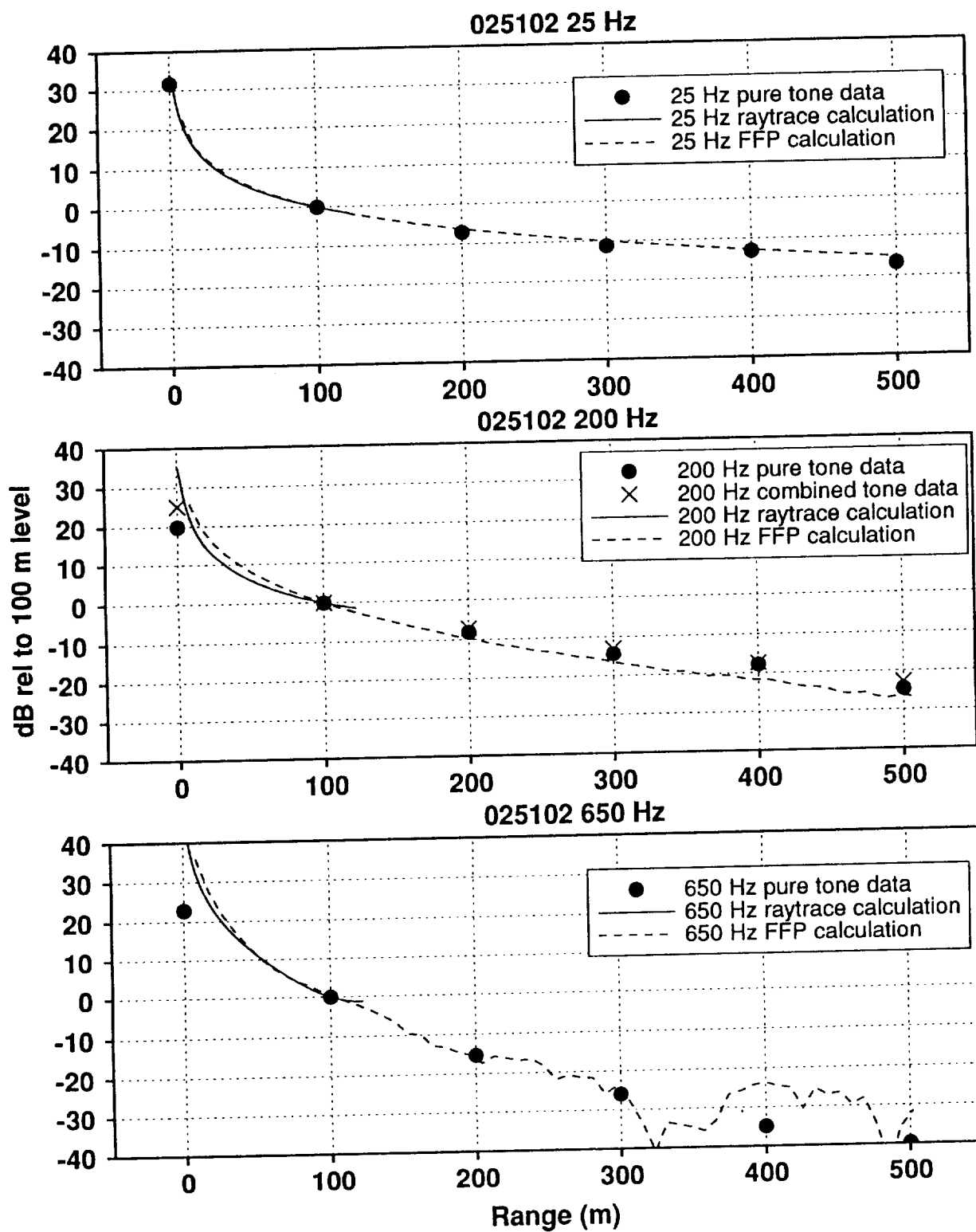


Figure 5. Comparison of ASOPRAT predictions and measured propagation levels for data set 025102.

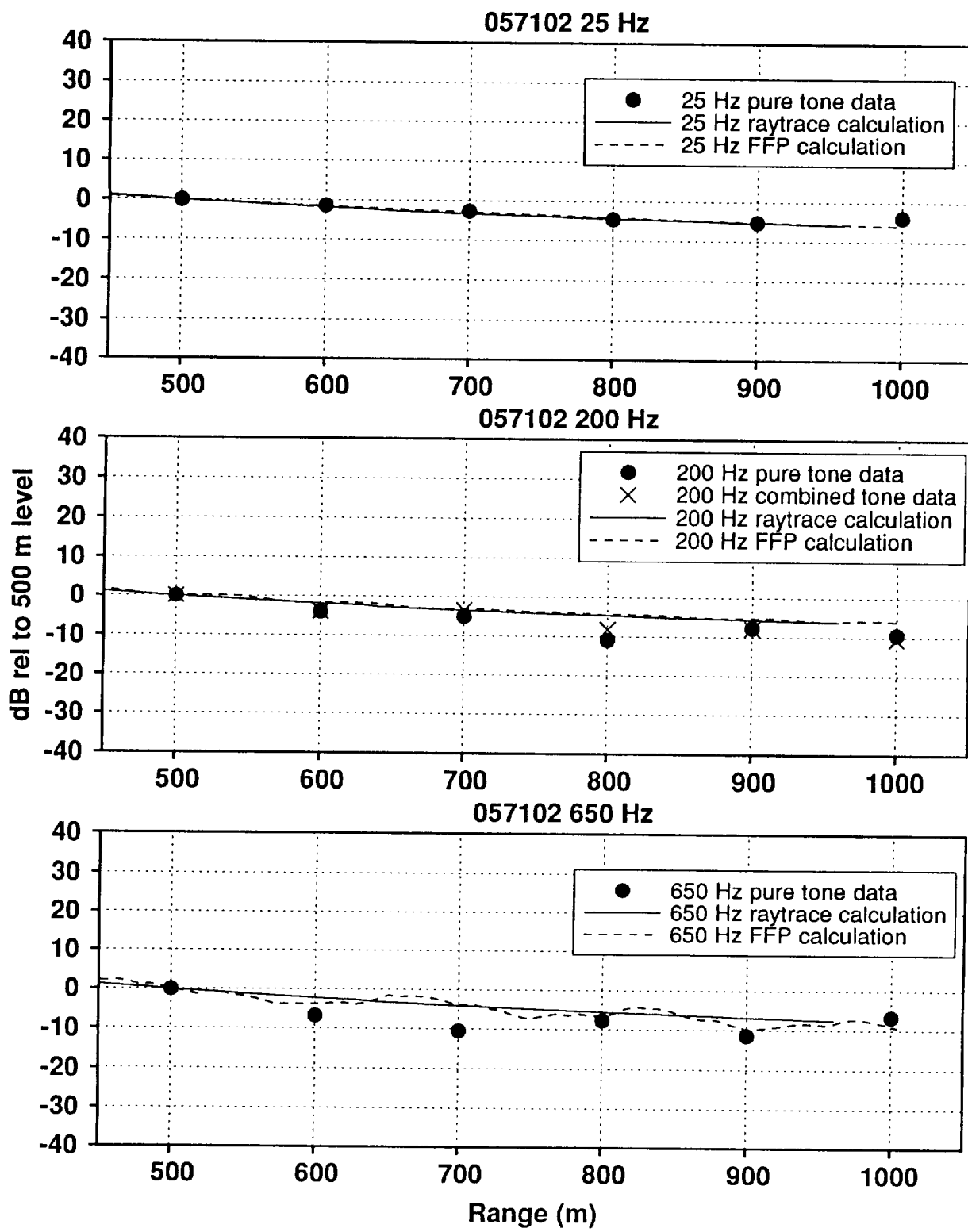


Figure 6. Comparison of ASOPRAT predictions and measured propagation levels for data set 057102.

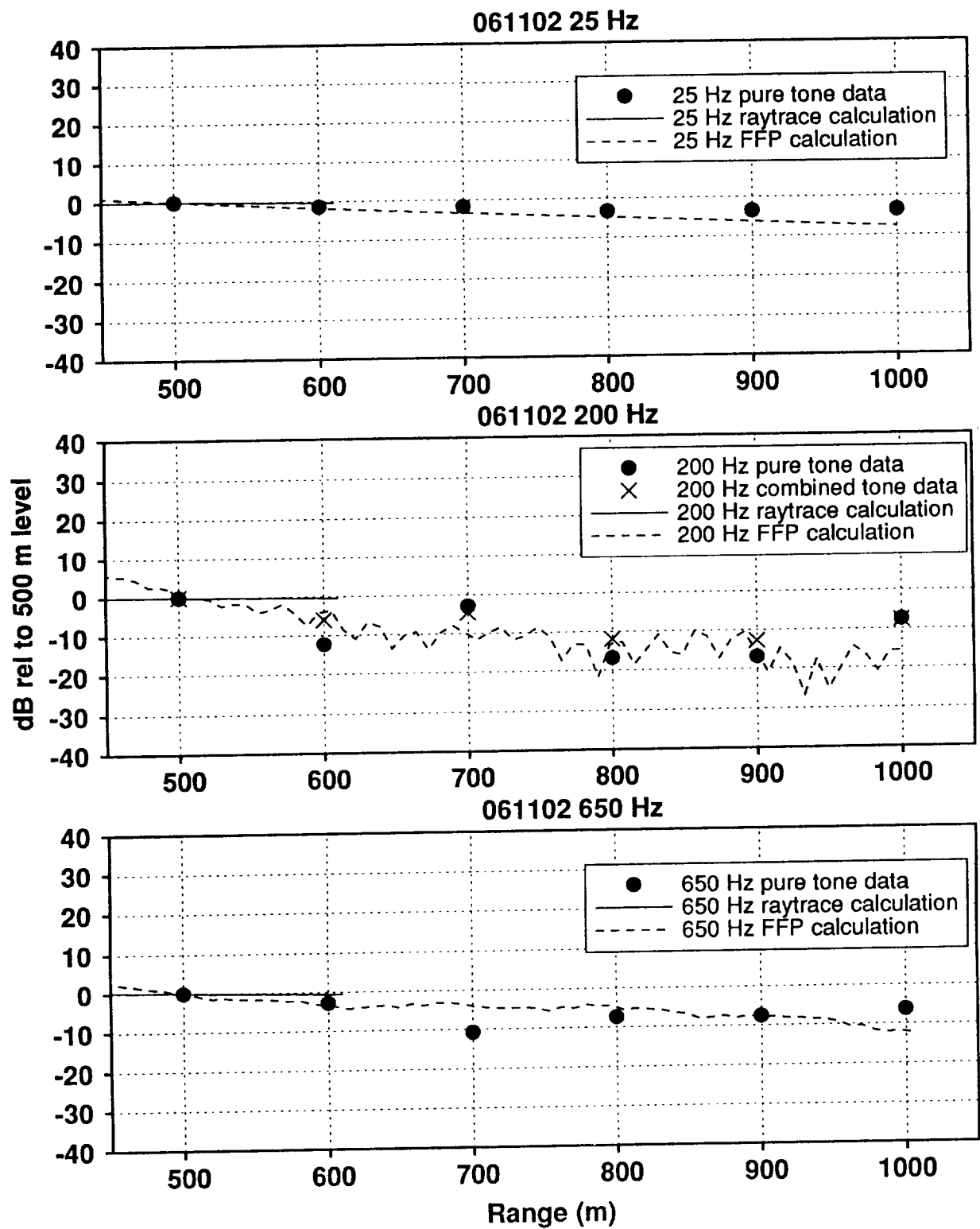


Figure 7. Comparison of ASOPRAT predictions and measured propagation levels for data set 061102.

GROUND CHARACTERIZATION FOR JAPE*

Keith Attenborough
 Engineering Mechanics Discipline
 Faculty of Technology
 Milton Keynes MK7 6AA
 England

56-71

11-18

JL 14

Shahram Taherzadeh
 Engineering Mechanics Discipline
 Faculty of Technology
 Milton Keynes MK7 6AA
 England

SUMMARY

Above-ground propagation modelling at the JAPE site requires a reasonably accurate model for the acoustical properties of the ground. Various models for the JAPE site are offered based on theoretical fits to short range data and to longer range data obtained with random noise and pure tones respectively from a loudspeaker under approximately quiescent isothermal conditions.

INTRODUCTION AND THEORY

A common feature of propagation models that takes into account various meteorological influences on sound propagating near to the ground is that they must also take account of the acoustical properties of the ground. Where direct impedance measurements are not available, advantage must be taken of indirect methods. Short range propagation measurements have been advocated often as one basis for indirect ground-characterization (refs. 1 and 2).

A short range measurement of the level difference spectrum between vertically-separated microphones at 0.1 and 1 m height and 1.75 m from a source at height 0.45 m, has been made at three positions (8, 24 and 27) on the JAPE site (ref. 3). Probe (buried) microphone measurements have been made also at short range. However these latter data were not available at the OU at the time of preparing this paper. Measurements that were made available to the OU included data from loudspeaker sources broadcasting pure tones at position 5 (2 m height on North tower), geophone receivers (channels 20 and 21 directly below microphones) and microphone receivers at 0 m and 1 m above ground at a range of 100 m, 200 m, 300 m, 400 m and 500 m from the source during meteorological conditions that indicated good mixing and the absence of any significant sound speed gradients. In this report we concentrate on the received level difference spectrum between microphones corresponding to channels 14 and 15 at a range of 500 m from the source.

The averaged level difference data at both short range (1.75 m) and longer range (500 m) have been analysed by (a) computing level difference spectra with assumed impedance values, (b) comparing computed spectra with measured ones and (c) proceeding until the best agreement was

* Work sponsored in part by the U.S. Army through its European Research Office.

achieved. This process requires use of an impedance model to provide some constraint on the frequency dependence of the impedance. Several such models have been considered in the literature (ref. 4). Three of these models are considered here:

(1) Delany and Bazley semi-infinite

$$Z_{DB} = 1 + 9.08 (1000 f/\sigma_e)^{-0.75} + i11.9 (1000 f/\sigma_e)^{-0.73} \quad (1)$$

where f is frequency (Hz) and σ_e is effective flow resistivity in mks rayls/m.

(2) Delany and Bazley hard-backed-layer of thickness d m

$$Z(d) = Z_{DB} \coth (-ik_{DB}d) \quad (2)$$

where

$$k_{DB} = \frac{2\pi f}{c} [1 + 10.8 (1000f/\sigma)^{-0.7} + i10.3 (1000f/\sigma)^{-0.59}] \quad (3)$$

(3) Two parameter non-hard backed layer (ref. 4)

$$Z = (\pi\gamma\rho)^{-1/2} (\sigma_e/f)^{1/2} (1 + i) + i c/(2\gamma\omega\Omega d) \quad (4)$$

where γ is the ratio of specific heats in air,

ρ is equilibrium air-density

$\sigma_e = 4s_p^2 \sigma/\Omega$

σ = flow resistivity

Ω = porosity

d = upper layer thickness

$\omega = 2\pi f$

s_p represents a pore shape factor ratio which must be frequency dependent as defined. However to be physically consistent in the low frequency limit, $4s_p^2 = 1$ (refs. 4 and 5). It should be noted that low frequency approximations have been used in the derivation of the above model.

For the purposes of the present computations, various values have been substituted for the constants resulting in

$$Z = 0.436 (1 + i) (\sigma_e/f)^{1/2} + 20 \alpha/f \quad (5)$$

where $\alpha = \frac{1}{\Omega d}$.

The level difference spectrum is computed from

$$LD = 20 \log | P_f/P_b | \quad (6)$$

where

$$P_t \text{ or } P_b = \frac{e^{ikr_1}}{r_1} + Q \frac{e^{ikr_2}}{r_2} \quad (7)$$

$$Q = R_p + (1 - R_p) F(w) \quad (8)$$

$$R_p = \frac{\cos \theta - \beta}{\cos \theta + \beta}, \quad \beta = \frac{1}{Z} \quad (9)$$

$$F(w) = 1 + i\pi w e^{-w^2} \operatorname{erfc}(-iw) \quad (10)$$

$$w = (ikr_2/2)^{1/2} (\cos \theta + \beta) \quad (11)$$

r_1 and r_2 are direct and specularly reflected path lengths to the receiver of interest and θ is the angle of incidence for specular reflection.

Finally it should be noted that both level difference spectra used in this paper represent averages. The short range data represent averages in space and time. The data at 500 m represent averages in time. Three FFTs 0.75 s apart were taken from the time series and the data used represent the averages. The error bars in Figure 1 indicate the deviations between the three readings.

RESULTS

Figure 2 shows that although good fits to the data at short range may be obtained with $\sigma_e = 1\ 000\ 000$ mks rayls/m in equation (1) or $\sigma_e = 300\ 000$ mks rayls/m and $\alpha = 1000/m$ in equation (5), these values result in poor fits to the 500 m data. Figure 3 shows that $\sigma_e = 900\ 000$ mks rayls/m and $d = 0.005$ m in equation (2), and $\sigma_e = 300\ 000$ mks rayls/m, $\alpha = 300/m$ in equation (5) give tolerable agreement with both long and short range data. As was remarked in reference (3), we find that a five parameter non-hard backed layer model with the measured value of flow resistivity (1 100 000 mks rayls/m) gives reasonable agreement with the short range data but relatively poor agreement with the data at 500 m.

It should be noted that, as was remarked in ref. 3, the first dip in the measured level difference spectrum at short range is deeper than can be predicted with any impedance model tried so far.

DISCUSSION

In principle JAPE should have presented the opportunity for testing the use of short range level difference spectrum for ground characterization. Indeed combinations of parameters for two different two-parameter impedance models have been found that enable tolerable agreement with both short range and 500 m data. However closer inspection reveals several shortcomings in the data available at short range. Figure 4 shows that the chosen geometry results in predicted level difference spectra that are insensitive to wide variations of the parameters in the impedance model. Figure 5 shows that lowering the

height of the upper receiver, to make it the same as that of the source, would have increased the sensitivity of the level difference spectrum predictions significantly. The calculations outlined in Appendix A show that after various simplifying assumptions it is possible to deduce an optimum geometry for short range ground characterization with a range of 1.75 m. The source and upper microphone heights should be between 0.19 m and 0.35 m.

Nevertheless it remains necessary to explain the fact that the first measured short range level difference spectrum dip is deeper than can be explained by impedance models alone. A possible explanation is the existence of a steep temperature gradient near to the ground during the measurement. Another possibility is directionality of the loudspeaker source.

CONCLUSIONS

Although short range level difference spectrum measurements have been used successfully for ground characterization over several soil types (ref. 2), there are problems with those obtained at the JAPE site. A major problem stems from the use of a short range measurement geometry which produces spectra that are relatively insensitive to the ground impedance in this case. In other locations, trial and error simulations of the sort shown in Figures 4 and 5 have been used to identify an appropriate geometry. Further work is reported here that enables a suitable choice of geometry without resort to such simulations or a need for prior knowledge of the likely range of flow resistivity of the ground of interest.

REFERENCES

1. Embleton, T.F.W., Piercy, J.E. and Daigle, G.A.: Effective flow resistivity of ground surfaces determined by acoustical measurements. *J.Acoust.Soc.Am.* 74 1983, pp.1239-1244.
2. Hess, H.M., Attenborough, K. and Heap, N.W.: Ground characterization by short range propagation measurements. *J.Acoust.Soc.Am.* 87 1990, pp.1975-1986.
3. Klugerman, M. and Bass, H.E.: Measurements needed for impedance calculations. Acoustics Laboratory, Univ. of MS, unpublished report 1992.
4. Attenborough, K.: Ground parameter information for propagation modelling. *J.Acoust.Soc.Am.* 92(1) July 1992, pp.418-427.
5. Champoux, Y. and Stinson, M.R.: On acoustical models for sound propagation in rigid frame porous materials and the influence of shape factors. *J.Acoust.Soc.Am.* 92(2) 1992, pp.1120-1131.

APPENDIX A Determination of optimum geometry for short range ground characterization

According to the Weyl van der Pol formula the excess attenuation due to ground effect may be approximated by

$$EA = 20 \log |1 + Q(r_1/r_2) \exp(ik(r_1 - r_2))| \quad (\text{A.1})$$

For source and receiver at equal heights, h , and separation, d , and Q replaced by R_p (the plane wave reflection coefficient) the quantity in the modulus sign becomes

$$1 + |R_p| \sin(\theta) \exp[i(2kh(\sec(\theta) - \tan(\theta)))] \quad (\text{A.2}).$$

This is minimum when

$$2kh\sec(\theta)(1 - \sin(\theta)) + \phi = \pi \quad (\text{A.3})$$

Using the low frequency/ high flow resistivity approximation of the four parameter impedance model

$$Z = 0.436(1+i)\sqrt{(\sigma/f)} \quad (\text{A.4})$$

it is possible to deduce that

$$|R_p| = \frac{\sqrt{\cos^2(\theta) + 4B^4(f/\sigma)^2}}{\cos^2(\theta) + 2B\sqrt{f/\sigma} \cos(\theta) + 2B^2(f/\sigma)} \quad (\text{A.5})$$

and that

$$\phi = \tan^{-1} \left[2B\sqrt{f/\sigma} \cos(\theta) / (\cos^2(\theta) - 2B^2(f/\sigma)) \right] \quad (\text{A.6}).$$

Substitution of (A.6) in (A.3) then leads to an equation for the frequency of the first ground effect dip in terms of the flow resistivity and the geometry. An example of the results of numerical solution of the resulting equation is shown in Figure 6.

Under the condition that (A.3) holds and defining

$$G = 1 - |R_p| \sin(\theta) \quad (\text{A.7})$$

it is necessary to find the value of θ for which $dG/d\sigma$ is maximum.

Figures 7 and 8 show examples of plots of $dG/d\sigma$ against θ for two values of σ .

If $d = 1.75$ m this shows that the upper receiver and source heights should be chosen to give $0.19 \text{ m} < h < 0.35 \text{ m}$ for greatest sensitivity to flow resistivity in the range $100,000 < \sigma < 1,000,000 \text{ Nsm}^{-4}$. Figure 9 confirms that the level difference spectrum is indeed very sensitive to variation in the ground parameters for $h = 0.27 \text{ m}$ and $d = 1.75 \text{ m}$.

White Sands Data fitted by 2_param model

Level Difference at 500.0 m, mics at 0.01 & 1.0 m

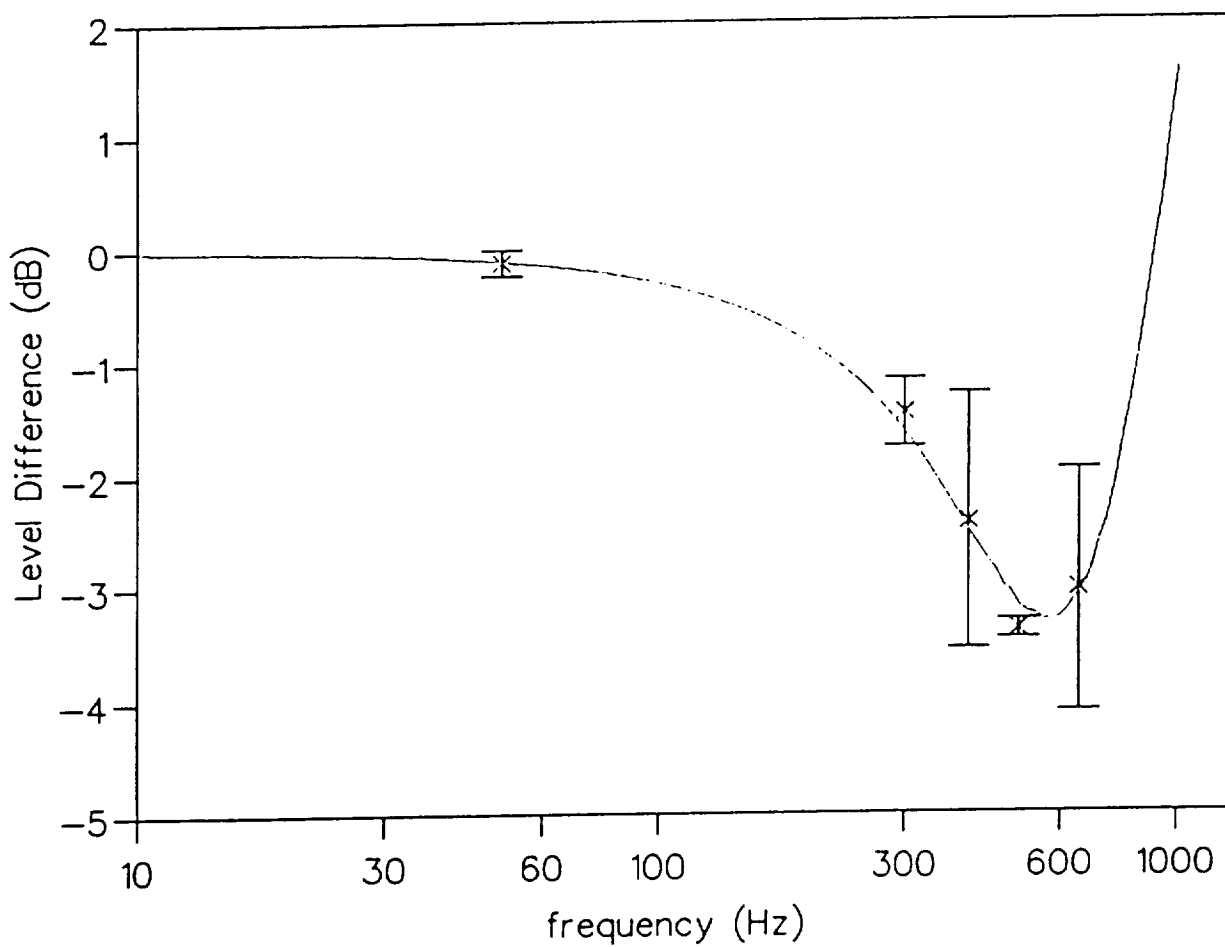
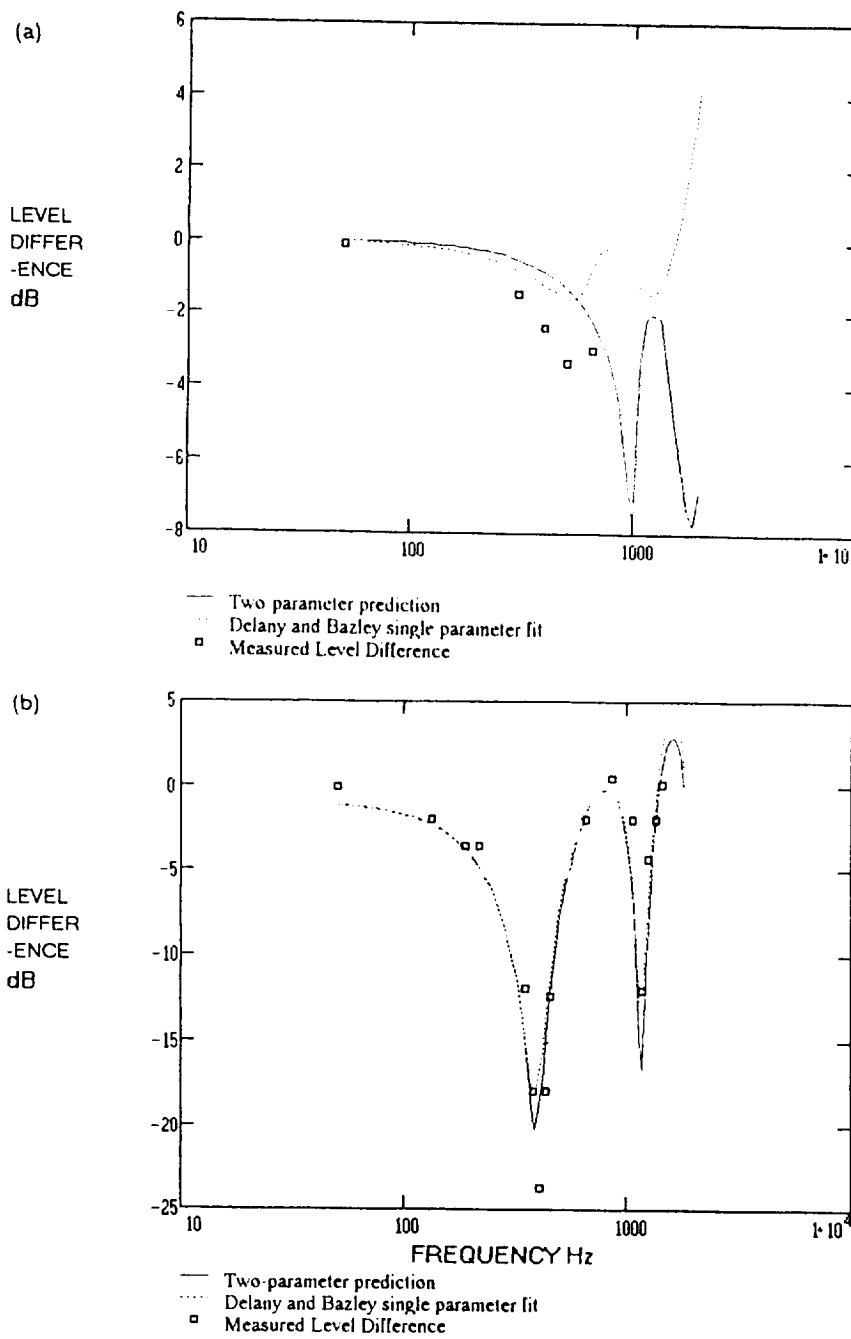
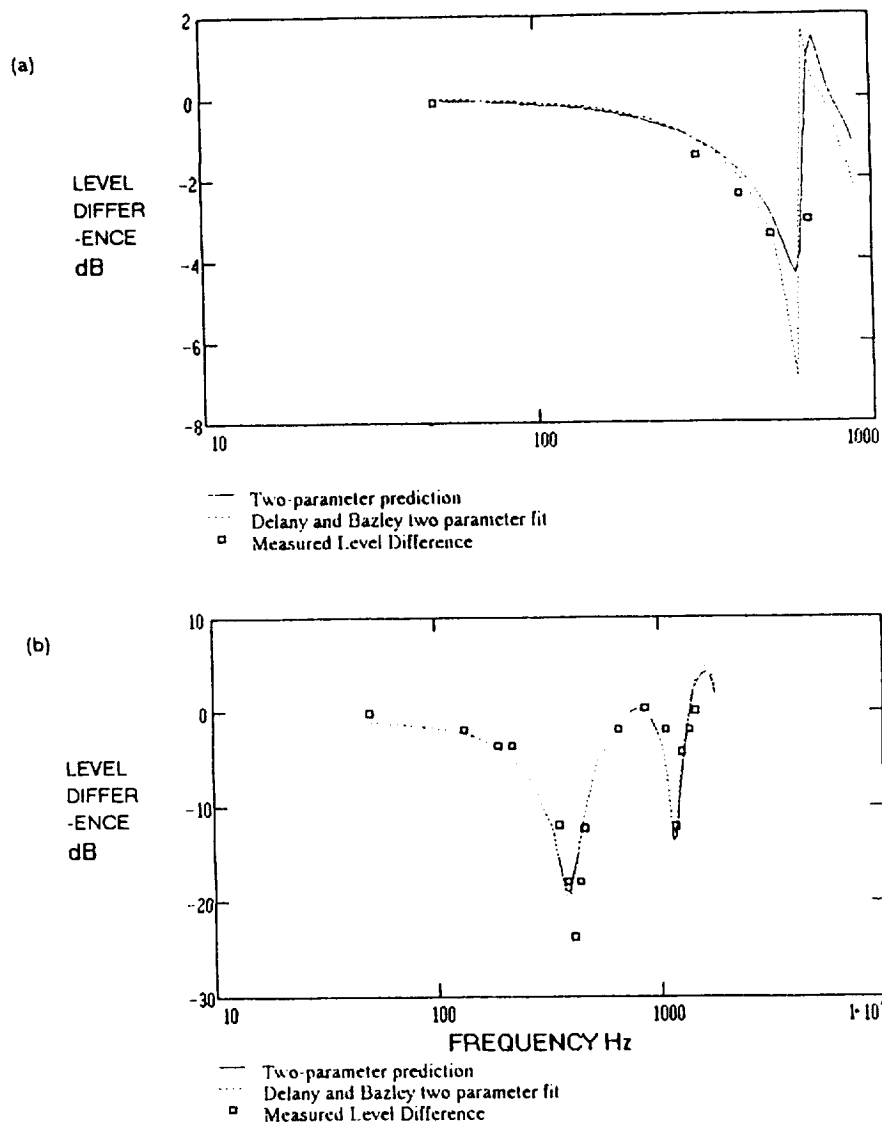


Figure 1. Pure tone data from the level difference at vertically-separated microphones at 1.0 and 0 m height with loudspeaker source at a height of 2 m and a range of 500 m. Error bars indicated range of data over several FFTs. A 2 parameter impedance model fit is shown using $\sigma_e = 300\ 000 \text{ mks rayls m}^{-1}$ and $\alpha_e = 10 \text{ m}^{-1}$.



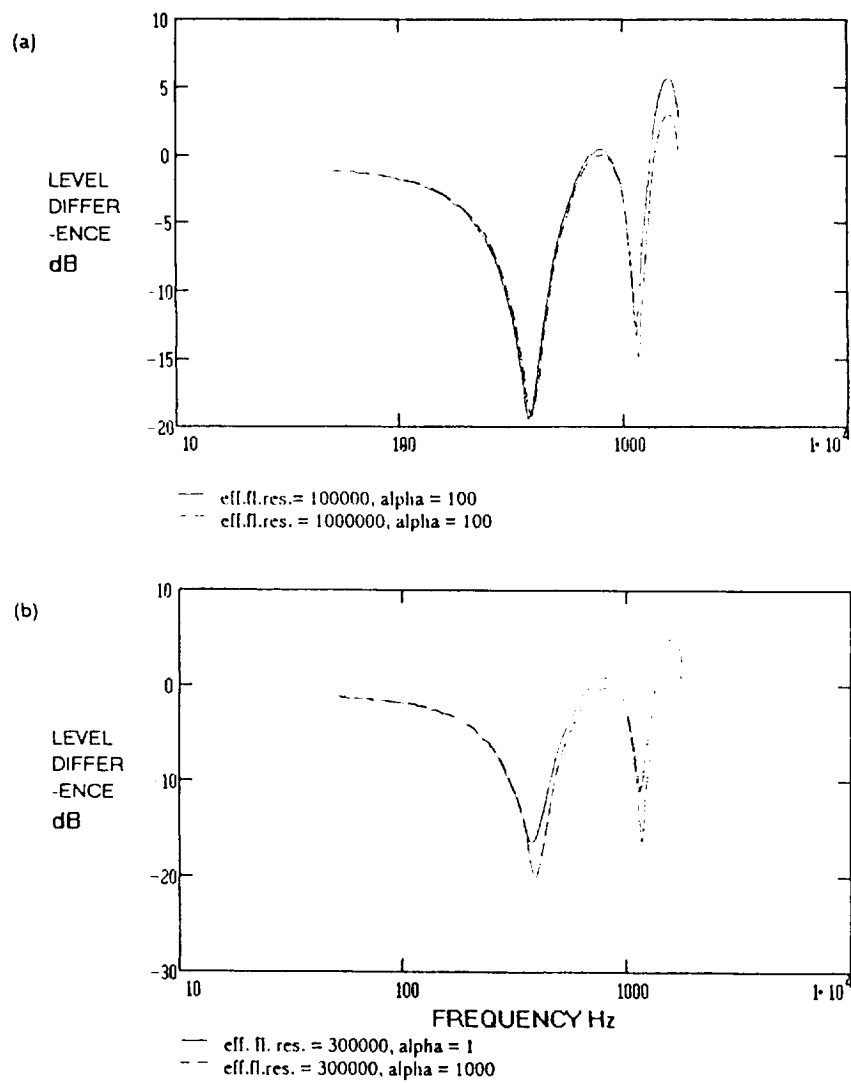
Level Difference geometries : (a) source height = 2.0 m, receiver heights = 1 m and 0.01 m, horizontal separation = 500 m. (b) source height = 0.45 m, receiver heights = 1 m and 0.1 m, horizontal separation = 1.75 m. Predictions using two-parameter fit with eff.fl.res. = 300 000 mks rayls/m and eff.alpha 1000 /m and Delany/Bazley with eff.fl.res. 1000000 mks rayls/m

Figure 2. Predicted and measured (u) level difference spectra (a) at long range; source height = 2 m, receiver heights 1 m and 0.01 m, horizontal separation 500 m and (b) at short range; source height = 0.45 m, receiver heights 1.0 and 0.1 m, horizontal separation 1.75 m. Predictions use two-parameter impedance model ($\sigma_e = 300 000 \text{ mks rayls m}^{-1}$, $\alpha_c = 1000 \text{ m}^{-1}$, continuous lines) and single parameter Delany and Bazley fit ($\sigma_c = 1 000 000 \text{ mks rayls m}^{-1}$, dotted lines).



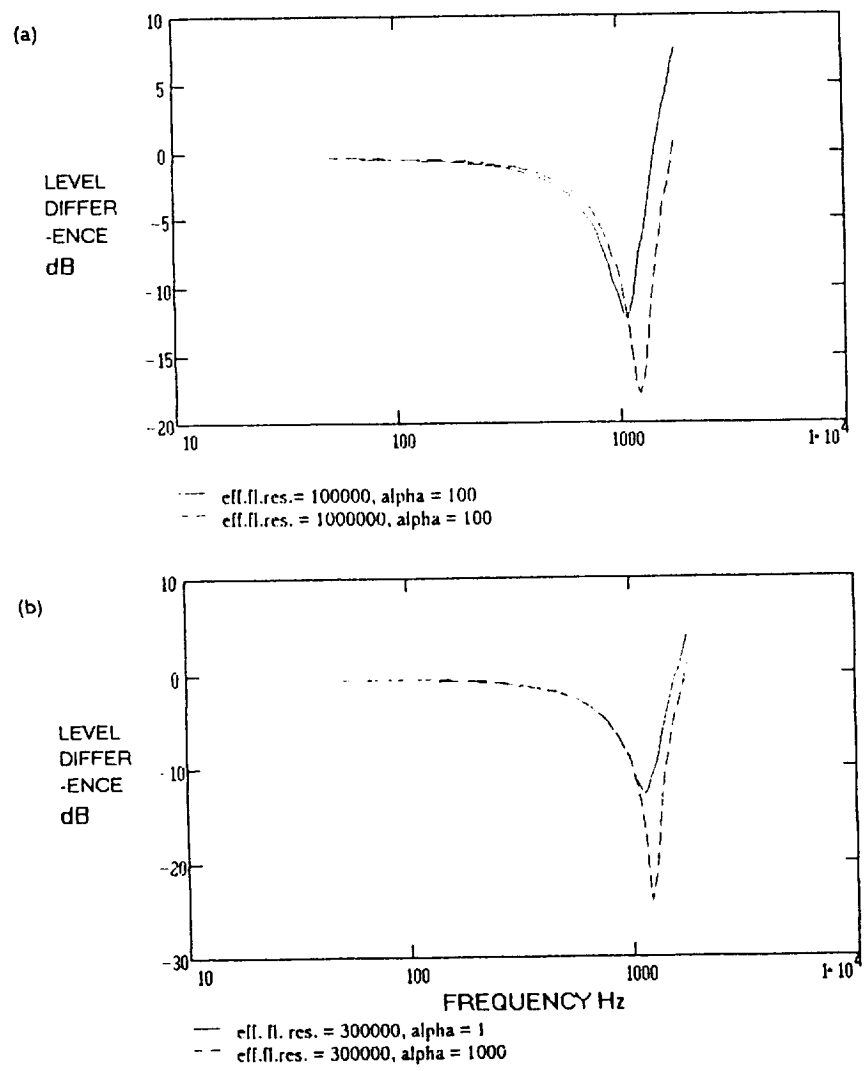
Level Difference geometries : (a) source height = 2.0 m, receiver heights = 1 m and 0.01 m, horizontal separation = 500 m. (b) source height = 0.45 m, receiver heights = 1 m and 0.1 m, horizontal separation = 1.75 m. Predictions using two-parameter fit with eff.fl.res. = 300 000 mks rayls/m and eff.alpha 300 /m and Delany/Bazley thin hard-backed layer fit with eff.fl.res. 900000 mks rayls/m and thickness 0.005 m

Figure 3. Predicted and measured level difference spectra at (a) long, and (b) short range. Continuous lines represent two-parameter fits with $\sigma_e = 300\ 000$ mks rayls m^{-1} and $\alpha_e = 300\ m^{-1}$. Dotted lines indicate 2-parameter Delany and Bazley fits with $\sigma_e = 900\ 000$ mks rayls m^{-1} and $d = 0.005\ m$.



Level Difference geometry : source height = 0.45 m, receiver heights = 1 m and 0.1 m, horizontal separation = 1.75 m. Predictions using two-parameter impedance model.
 (a) Porosity variation parameter kept constant and effective flow resistivity increased by a factor of 10 (b) Effective flow resistivity kept constant, porosity variation parameter increased by a factor of 1000.

Figure 4. Predicted dependence of short range (original geometry) level difference spectra on impedance model parameters (a) α_e constant, σ_e varies by a factor of 10, (b) σ_e constant, α_e varies by a factor of 1000.



Level Difference geometry : source height = 0.45 m, receiver heights = 0.45 m and 0.1 m. horizontal separation = 1.75 m. Predictions using two-parameter impedance model.

(a) Porosity variation parameter kept constant and effective flow resistivity increased by a factor of 10

(b) Effective flow resistivity kept constant, porosity variation parameter increased by a factor of 1000.

Figure 5. Predicted dependence of short range level difference spectra for modified geometry (source height 0.45 m, receiver heights 0.45 m and 0.1 m, range 1.75 m) on impedance model parameters (a) α_e constant, σ_e varies by a factor of 10, (b) σ_e constant, α_e varies by a factor of 1000.

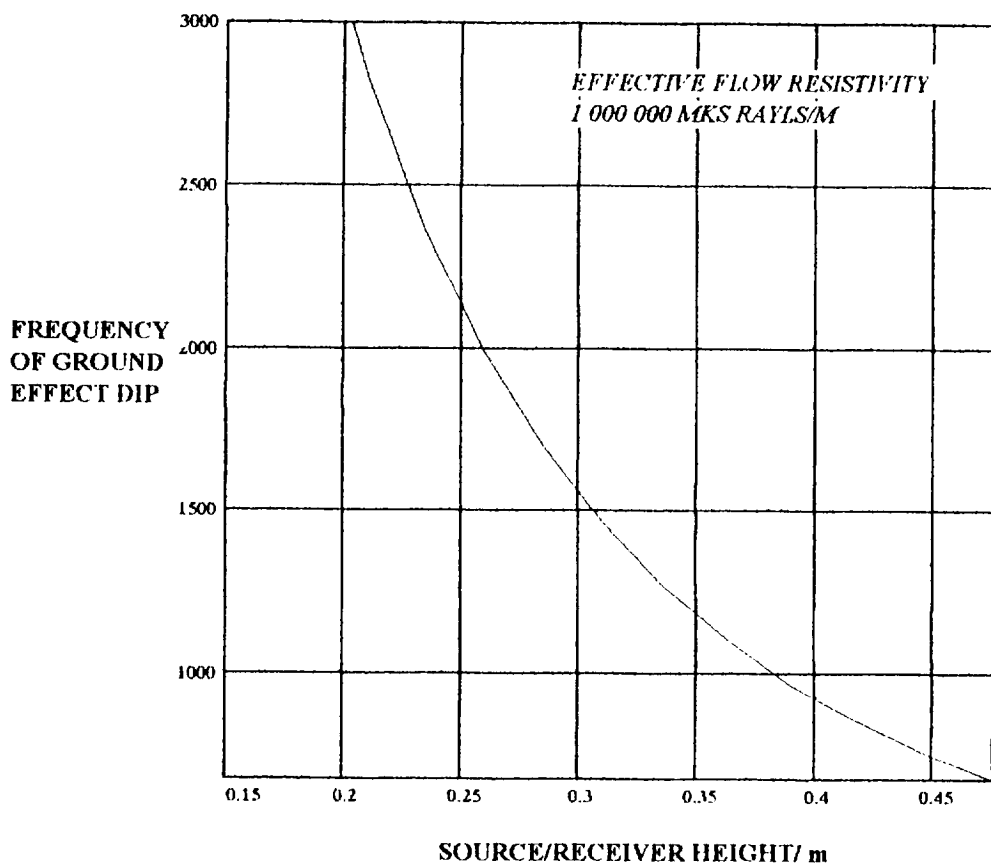
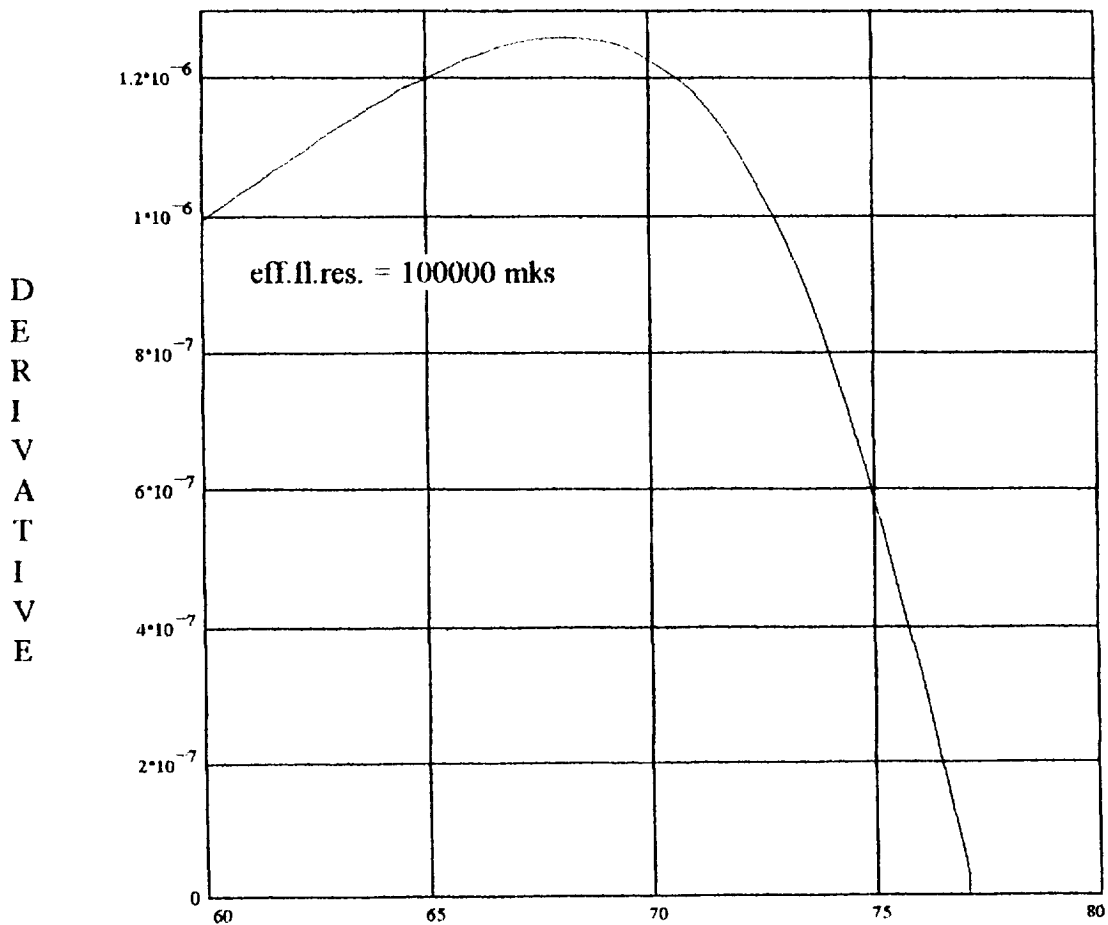


Figure 6. Predicted variation of frequency of (first) ground effect dip in excess attenuation with a height of direct (horizontal) path between point source and received over a surface characterized by a single parameter model with effective flow resistivity of 1000 000 NSm⁻⁴ and when source and receiver are separated by 1.75 m.



Plot of derivative of excess attenuation with respect to flow resistivity against specular angle for equal source and receiver heights.

Figure 7. Variation of derivative of excess attenuation (at frequency of first ground dip) with respect to flow resistivity as specular reflection angle varies for equal source and receiver heights over a ground with effective flow resistivity $100\ 000 \text{ NSm}^{-4}$. Maximum at 68° implies $H = 0.35 \text{ m}$ for separation of 1.75 m .

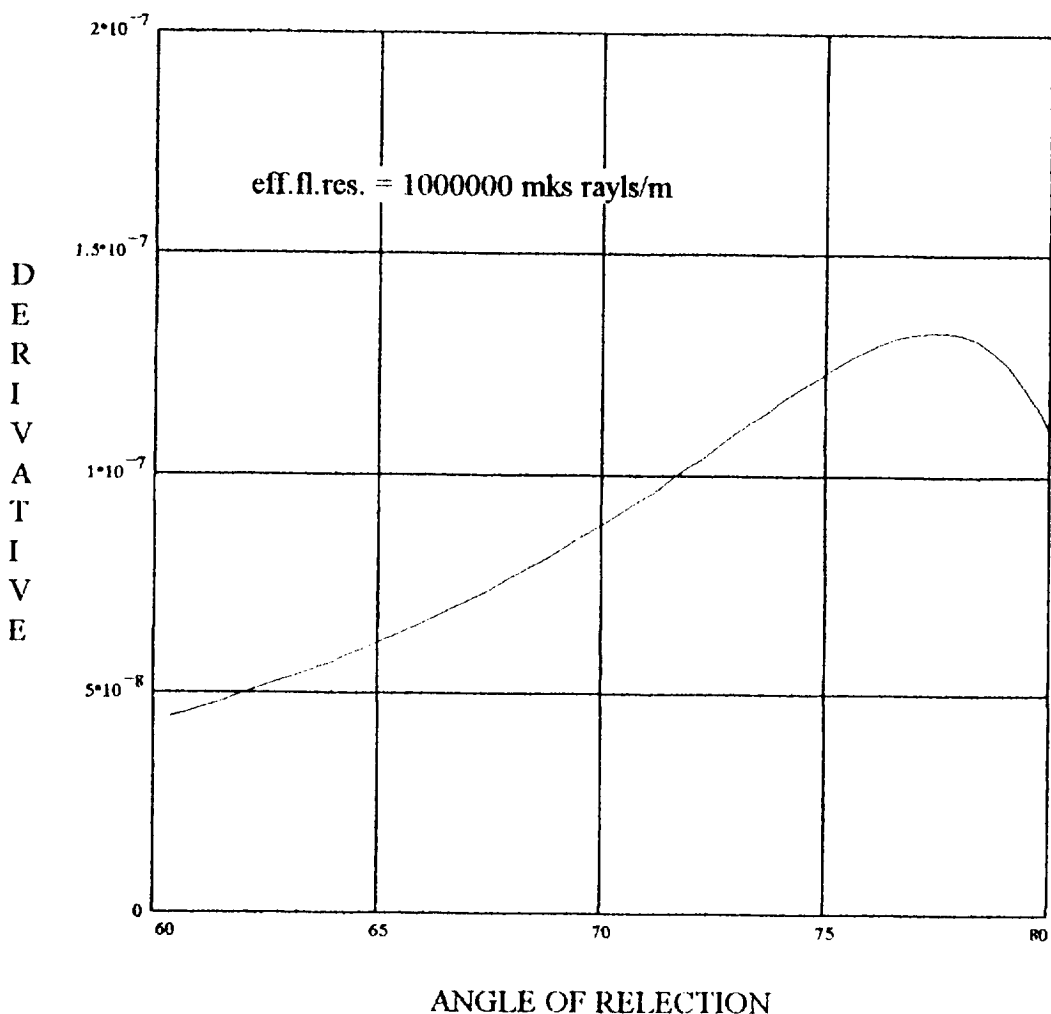
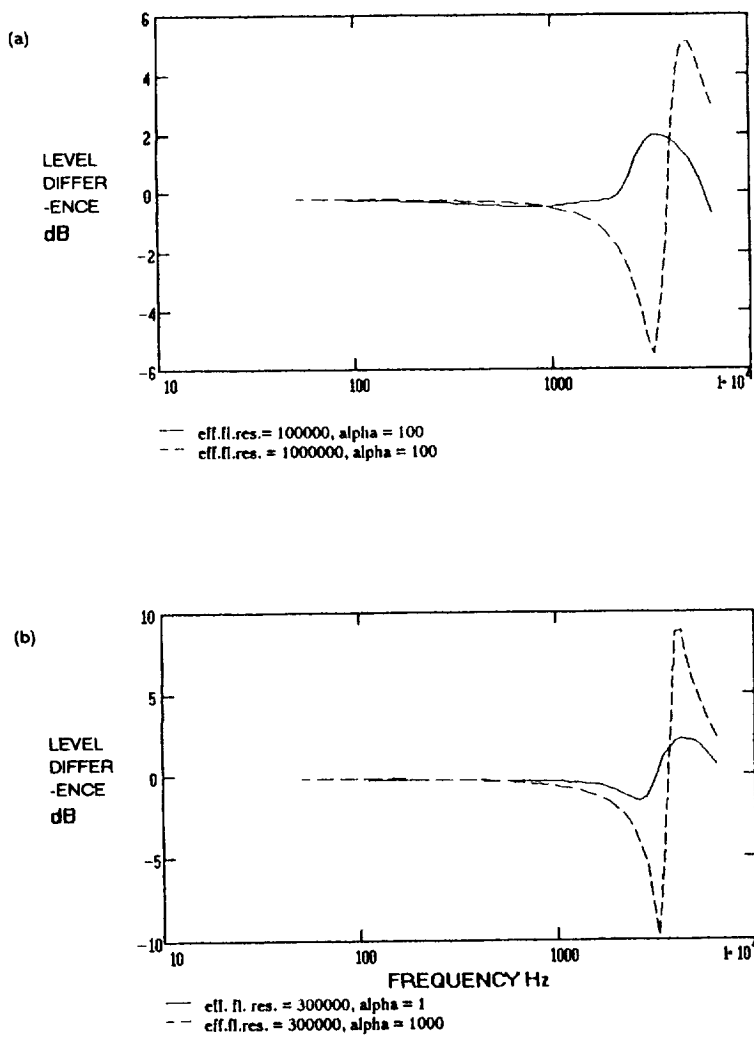


Figure 8. As for Figure 7 but effective flow resistivity is 1000 000 NSm⁻⁴. Maximum at 78 ° implies H = 0.19 m for separation of 1.75 m.



Level Difference geometry : source height = 0.27 m, receiver heights = 0.27 m and 0.1 m, horizontal separation = 1.75 m. Predictions using two-parameter impedance model.

(a) Porosity variation parameter kept constant and effective flow resistivity increased by a factor of 10

(b) Effective flow resistivity kept constant, porosity variation parameter increased by a factor of 1000.

Figure 9. Sensitivity of level difference spectrum to ground parameters for source and upper receiver height = 0.27 m, separation = 1.75 m, lower receiver height = 0.1 m.

N 94 - 24214

JAPE 91 : INFLUENCE OF TERRAIN MASKING ON THE ACOUSTIC PROPAGATION OF HELICOPTER NOISE¹

P. Naz

French-German Research Institute of Saint-Louis (ISL)
68 301 Saint-louis, France

57-71

201077

P-7

ABSTRACT

The acoustic propagation in the case of a noise source masked by a small element of terrain has been investigated experimentally. These data have been measured during the "terrain masking" experiment of the NATO JAPE 91 experimental campaign. The main objective of that experiment was to study the acoustic detection of a helicopter masked by a small hill. Microphones have been placed at different locations on the shadow zone of the hill to study the effect of the terrain obstruction on sound propagation. The results presented come from data measured by *Atlas Elektronik* and by *ISL*, and have been processed together. The terrain obstruction causes an excess attenuation of the SPL (Sound Pressure Level) for all the frequencies, but this attenuation is more effective for the high frequencies than for the low frequencies. Results typical of diffraction phenomena have been observed; the SPL is minimal at the foot of the hill and is relatively constant beyond it.

INTRODUCTION

Results of acoustic data measured during the NATO JAPE (Joint Acoustic Propagation Experiment) campaign are presented in this paper. Approximately 15 teams have taken part in this field trial hosted by the US Army White Sands Missile Range during the summer of 1991 (ref. 1).

The main objective of our experimental set-up is to study the physical phenomena which occur when an acoustic wave propagates around a small hill (figure 1). It is especially interesting to study the characteristics of the diffracted waves received by the microphones. This experiment also has some operational interest to evaluate the capability of the acoustic detection of helicopters for non line-of-sight configurations.

¹ This work has been done under a contract of "Direction des Recherches Etudes et Techniques", Paris (France).

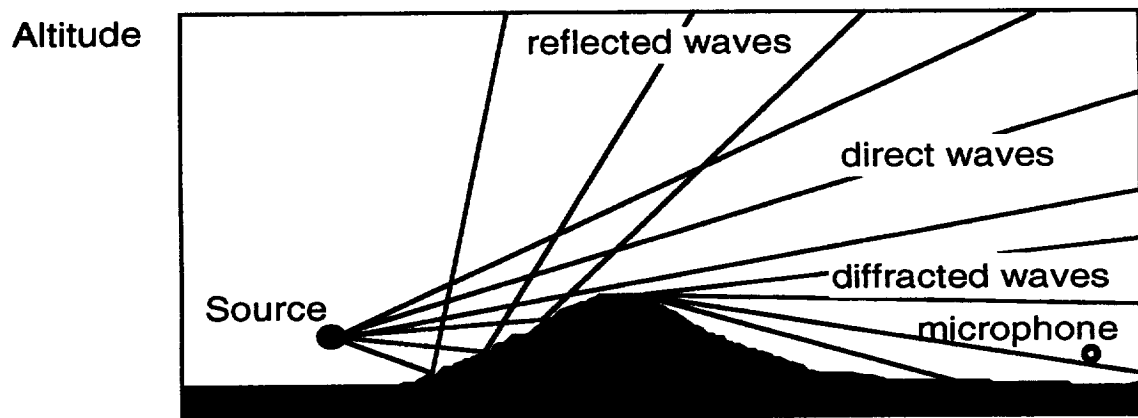


Figure 1. Trajectories of the acoustic waves

TEST SET-UP

For this experiment, the installation of the microphones and the recording of the acoustic data have been carried out by the German team of AE (Atlas Elektronik) and by the Franco-German team of ISL. The microphones are located along the profile of the hill on the north-south axis (AE) and on a perpendicular axis following the foot of the hill (ISL) (figure 2).

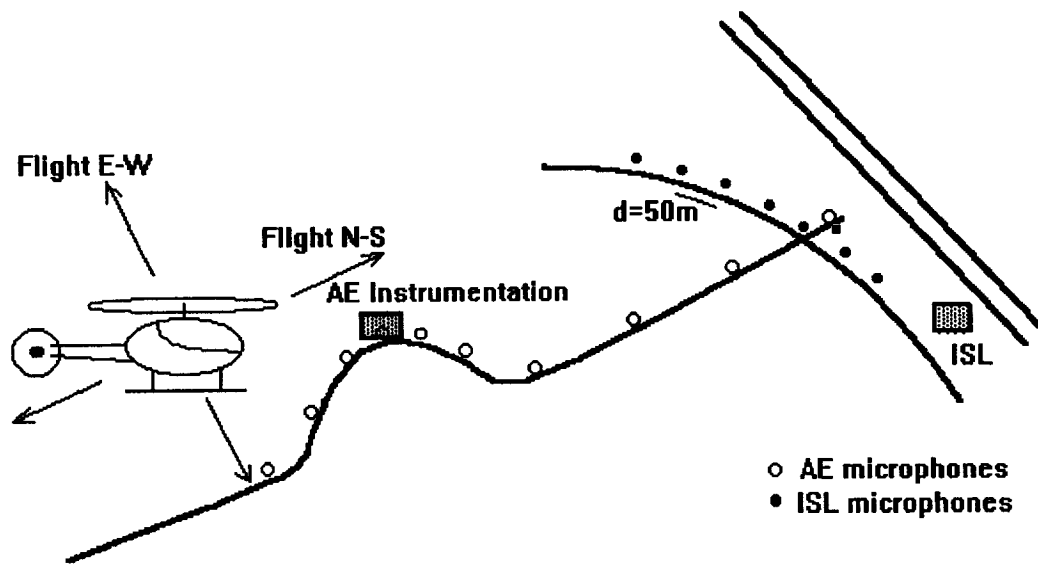


Figure 2. Experimental configuration

HOVERING POINTS

In a first series of trials, the helicopter made hovering points at different heights on the south side of the hill, the main part of the experimental set-up being situated on the opposite side. As an illustration of the effect of terrain masking, two acoustic spectra are plotted: one when the helicopter is masked and one when it is visible. On the first plot (figure 3), the helicopter makes hovering points on a vertical line. On the second plot (figure 4), the helicopter makes hovering points at the same altitudes as previously, but follows the profile of the hill (figure 4). In all these cases, the helicopter is well heard and the spectra have roughly the same shape. When the helicopter is masked, the value of the sound pressure level is lower. For the first harmonics of the main rotor frequency, the mask induces an attenuation of the SPL of approximately 10 dB. The higher harmonics do not emerge very well from the broad band noise. When the helicopter is close to the top of the hill, the acoustic level is greater than when the helicopter is at the same altitude but at the vertical of the base of the hill.

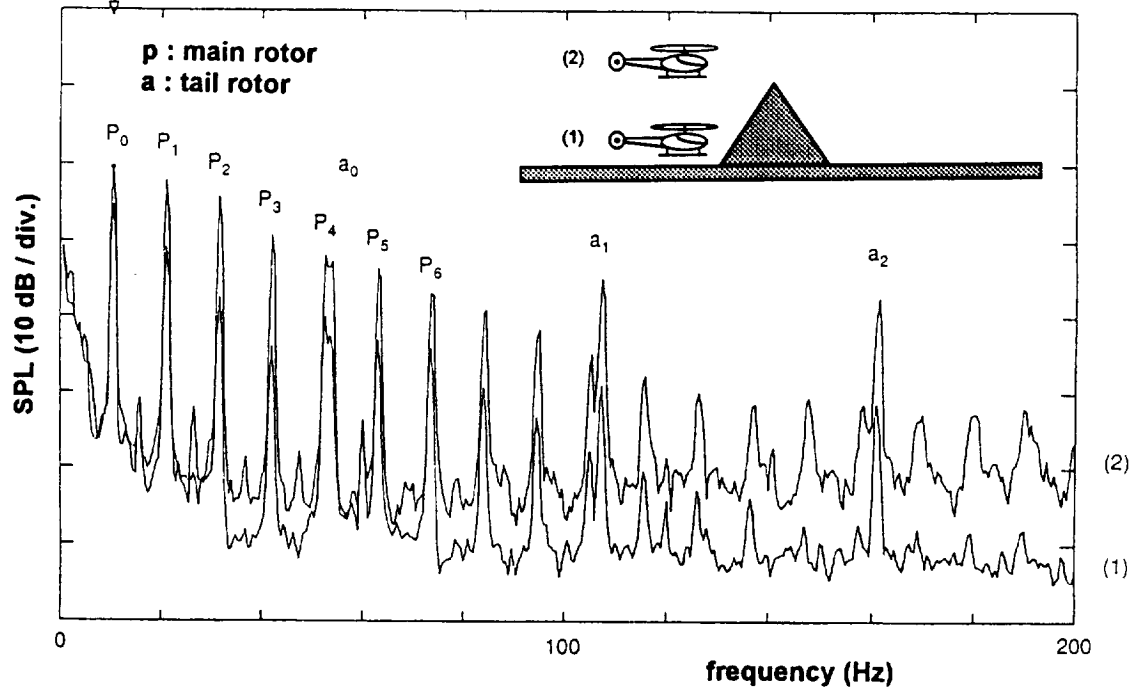


Figure 3. Acoustic spectrum

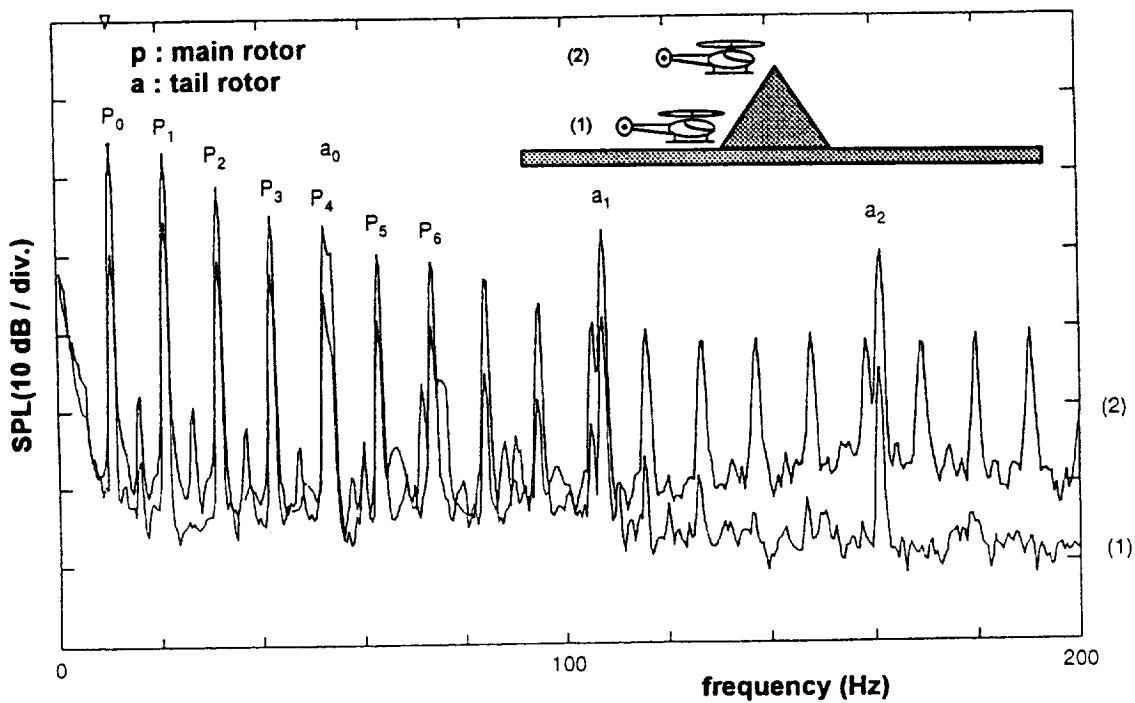


Figure 4. Acoustic spectrum

The evolution of the SPL shows a smooth and continuous variation for the main rotor frequency (f_1). For a higher frequency (f_2), approximately 400 Hz, a great variation is shown during the masked→unmasked transition (figure 5).

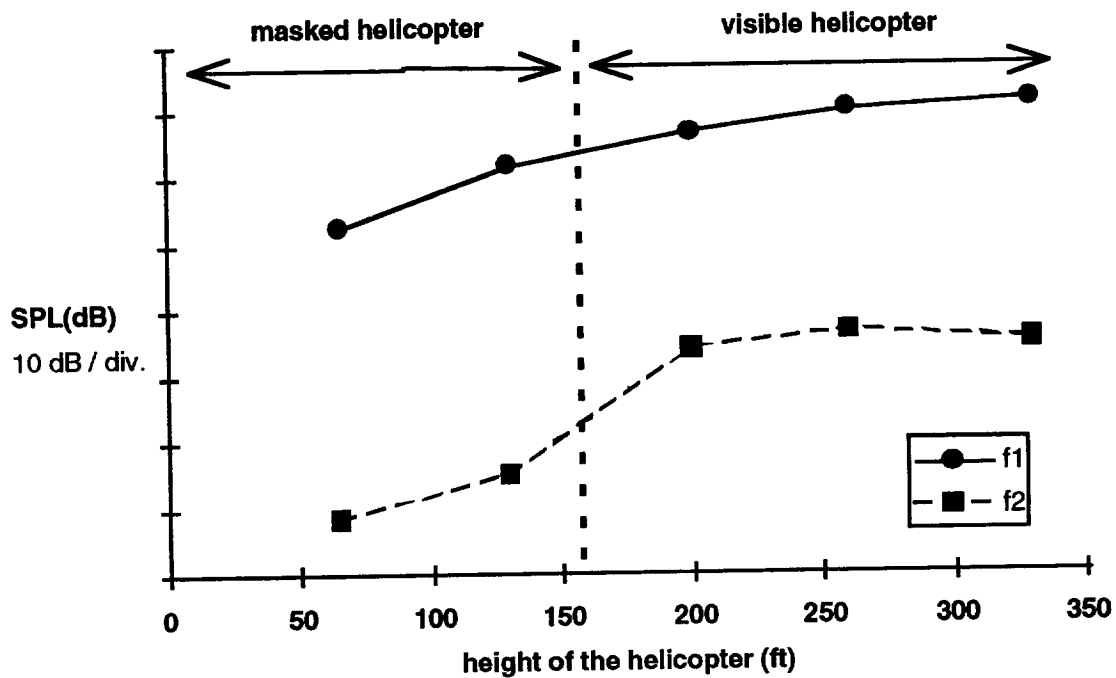


Figure 5. Influence of the altitude of the flight

The evolution of the SPL along the profile of the hill shows a fast decrease on the shadow side of the hill, and is relatively constant beyond it (figure 6). The maximum of the attenuation (minimum value of the curve) is reached at the foot of the hill. These two characteristics are typical of diffraction phenomena and are well known for the application of noise reduction by screens. The difference of the SPL values for the first point of the curve is explained by the helicopter-microphone distance which is quite different for the two heights of flight. For a better understanding, the profile of the hill is schematically plotted in the lower part of the graph.

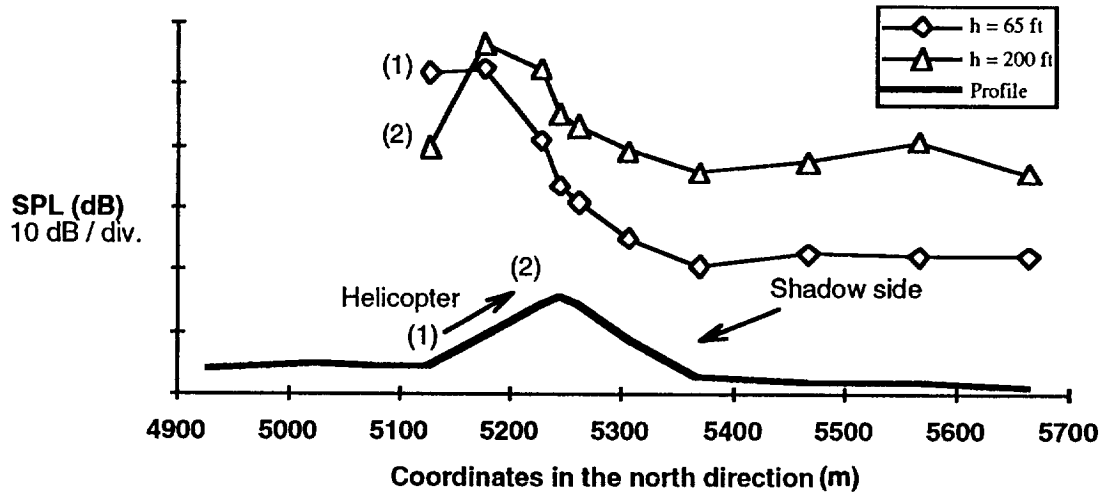


Figure 6. Influence of the altitude of the flight on the shadow zone ($f=10.5$ Hz)

The variations of the SPL along the profile for different discrete frequencies have all the same shape (Figure 7). If we take as references the SPL values measured at the top of the hill, the smallest frequency is less attenuated. As shown previously (figure 6), the SPL is relatively constant beyond the foot of the hill; we find again this characteristic for all the frequencies.

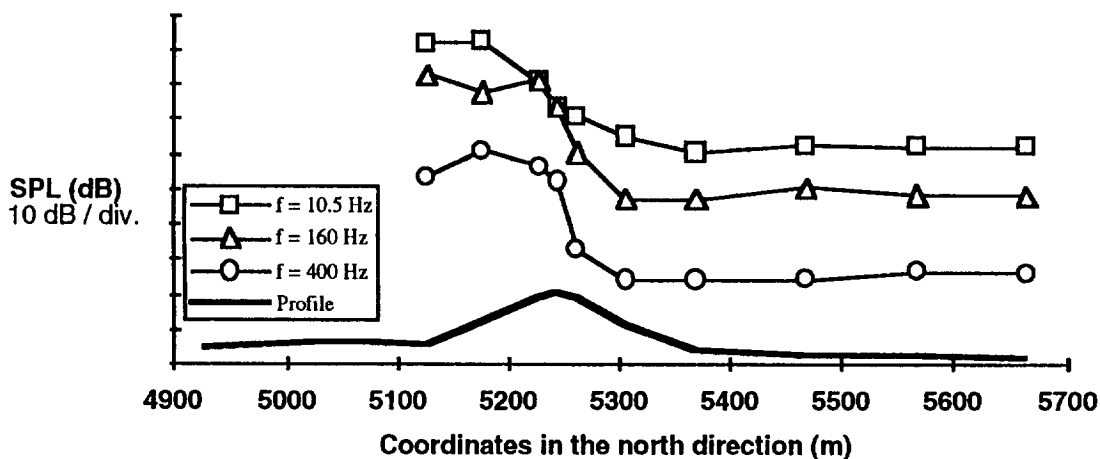


Figure 7. Characteristics of the shadow zone: influence of the frequency ($h=65$ ft)

TRANSLATION FLIGHTS

The development of the spectrum over time yields more information on translation flights. The acoustic level represented in pseudo-colours, as a function of frequency and time, allows the construction of an image with characteristics specific to the helicopter (line structure, Doppler shift), and specific to the effect of terrain masking.

Two different helicopter paths have been investigated. During the east-west flight, the helicopter path is partially behind the hill. The excess attenuation corresponds graphically to the gap visible in the line structure beginning at the 4th harmonic (figure 8). The maximum of this gap corresponds to the closest point of approach of the helicopter; it also corresponds to the inflection point of the Doppler shift pattern.

During the NOE (Nap of the Earth) flights in the north-south direction, the effect of the mask is not easily visible, because of the opposite effects which occur during this experiment (figure 9). The attenuation induced by the mask is partially compensated by the increase of the level of the noise source when the helicopter has to climb to avoid the hill.

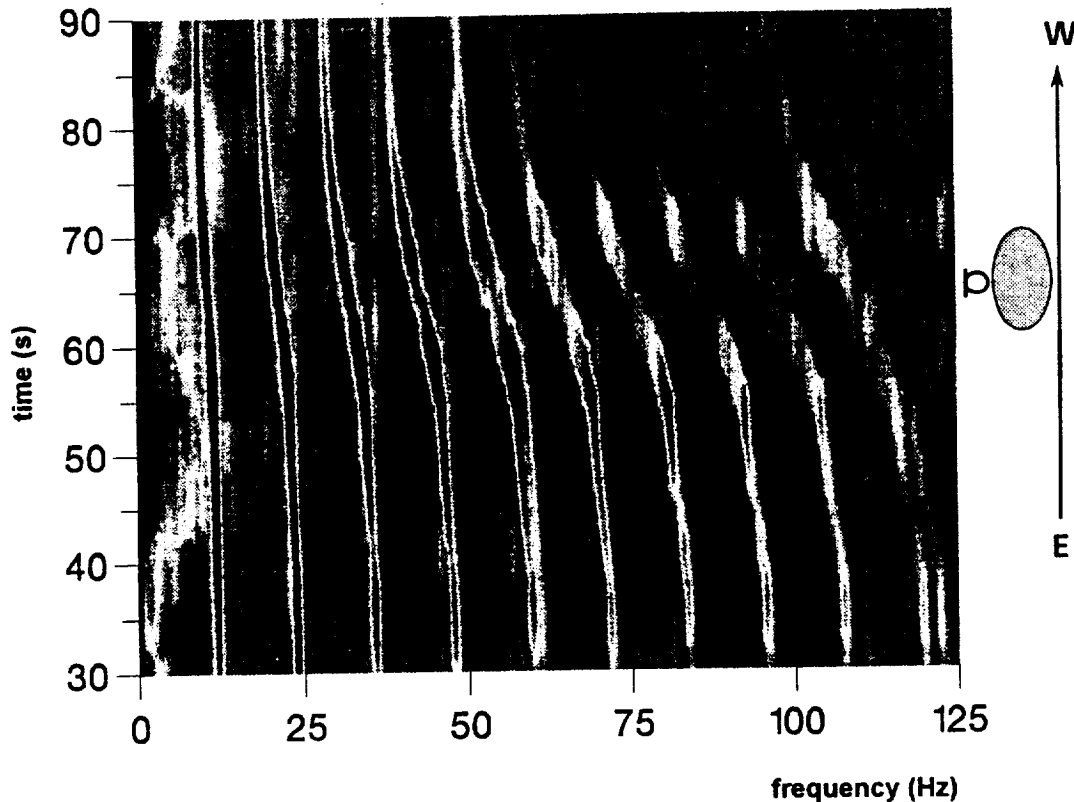


Figure 8. Evolution of the acoustic spectrum (east-west flight)

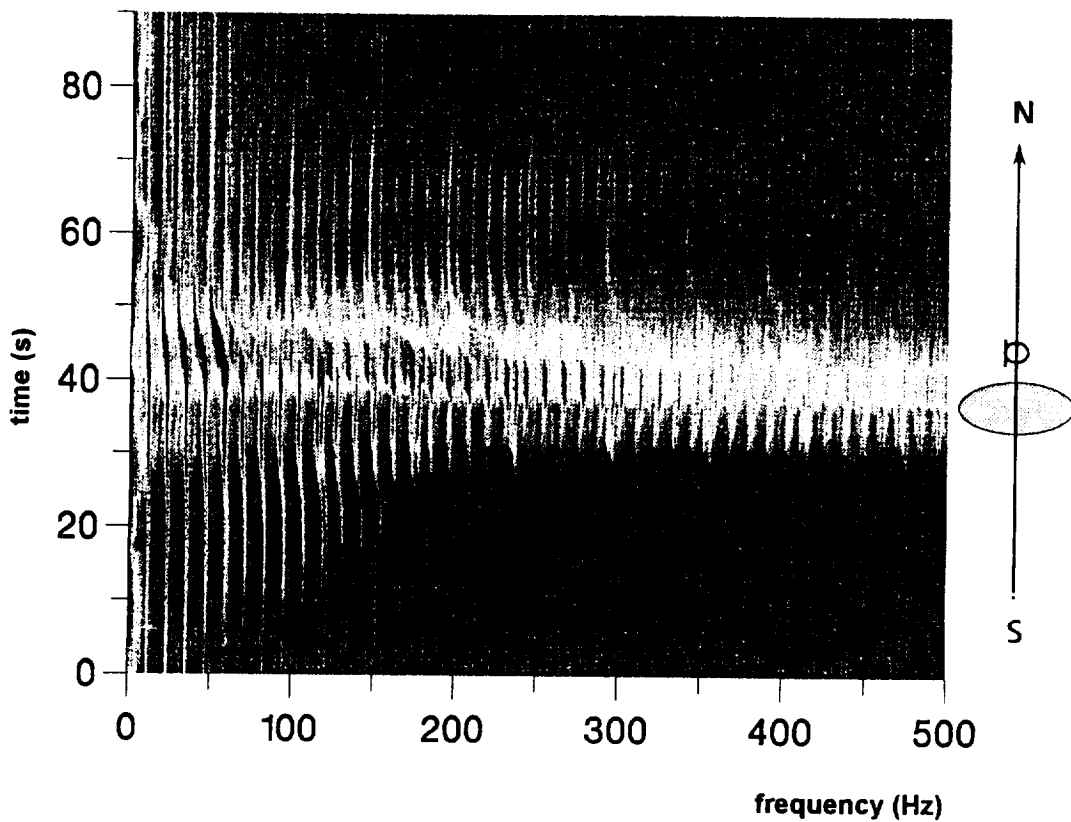


Figure 9. Evolution of the acoustic spectrum (east-west flight)

CONCLUSION

The influence of a small element of terrain on the acoustic propagation of the helicopter noise has been investigated experimentally. The characteristics of the shadow zone have been quantified. The attenuation due to the hill is relatively low for the main rotor frequency and its first harmonics. Consequently the helicopter is well heard, even on the shadow side of a small hill.

REFERENCE

1. B.W. Kennedy, R. Olsen, et al.
Joint Acoustic Propagation Experiment Project Summary
ASL, September 91



COMPARISONS OF CALCULATED AND MEASURED HELICOPTER NOISE NEAR INSTRUMENT HILL

53-71

Henry E. Bass and Chulsoo You
National Center for Physical Acoustics
The University of Mississippi
University, MS 38677

721480
16

SUMMARY

The polar parabolic equation (POPE) method solves for the diffraction of sound by a curved surface including a realistic sound speed profile. POPE is outlined briefly to describe diffraction which propagates the field over a hill. Experimental data are compared with POPE predictions using the measured sound speed profile and ground impedance. Two trial cases are considered for the comparisons: the helicopter located at the base of the hill and far away from the base of the hill, respectively. The physical mechanisms for sound propagation over a hill are examined with and of POPE calculations and experimental data. The shedding of rays from the hillside gives an interference effect with a wave along the flat surface beyond the base of a hill.

INTRODUCTION

The parabolic equation method¹ (PE) is a useful tool for outdoor sound propagation over flat, open, locally reacting ground surface with a realistic sound speed profile. The polar parabolic equation method is an extension of the PE method to solve non-line of sight sound propagation outdoors. POPE² introduces new coordinate systems into the PE to explain diffraction over a curved surface such as a hill. The coordinate system in POPE consists of the distance along the ground surface and the height perpendicular to the ground at any point. To introduce this coordinate system, the hill is segmented as shown in Fig. 1. The standard PE marches the field in range along the flat surface. POPE marches the field along the flat and curved surfaces.

COMPARISONS TO DATA

In order to verify POPE, the Terrain Masking experimental data are compared with POPE using a realistic sound speed profile. The Terrain Masking experiment was performed in the vicinity of Instrument Hill at White Sands Missile Range, New Mexico, during the period 27-28 July 1991. To use POPE, a hill shape is required which fits Instrument Hill as closely as possible. Figure 2 shows that the POPE hill and Instrument Hill fit very closely. Two trial cases are selected for the comparisons: Trial 172405 and trial 204405. The reference microphone was mounted 3 m above the top of the hill.

Trial 172405

The helicopter was hovering 10 m high above the ground surface, 200 m away from the south base of Instrument Hill. Figure 3 shows the comparison at 10 Hz and Fig. 4 shows the comparison at 21 Hz. They show reasonable agreement with each other.

Trial 204405

The helicopter was hovering 17 m above the south base of Instrument Hill. Figure 5 shows the comparison of the POPE prediction and data at 10 Hz. Figure 6 shows the comparison at 53 Hz.

The comparisons with experimental data indicate that POPE is a good tool for predicting non-line of sight sound propagation outdoors where the source is located at the base of a hill or far away from a hill.

DISCUSSIONS AND CONCLUSIONS

Generally, the data and POPE show that the sound level along the masked side of the hill decreases linearly and the sound level along the flat surface beyond the base of the hill stays approximately constant or decreases slowly. At some frequencies along the flat surface, the sound level fluctuates with distance. In the following, consider two different sections of the hill: the hillside and the flat surface beyond the base of the hill.

A creeping wave was introduced in the residue series solution³ for propagation over a curved surface. The creeping wave propagates over a curved surface within the shadow region corresponding to the hidden side over the top of a convex curved surface. The ground impedance mode was introduced for a wave propagating along the ground in the normal mode solution⁴ in a downward refracting atmosphere which corresponds to the concave surface along the hillside. Therefore, the creeping wave propagates and couples into a ground impedance mode along the hidden side of a hill.

The shedding of rays from the creeping wave can reach the ground surface beyond the base of the hill, but the ground impedance mode propagates parallel to the flat surface. Therefore, the total field along this surface is determined by the superposition of rays which have been shed from the creeping wave and a wave along the ground beyond the base of the hill. If the shedding rays and the wave along the flat surface are in phase, the field level is increased at around 100 m beyond the north base of the hill as shown in Figs. 3 through 6. The POPE calculation in Fig. 7 shows a deep interference minimum resulting from the shedding rays and the wave along the surface at around 570 m.

We conclude that POPE predicts the helicopter noise propagation over a hill. Further, the POPE calculations and experimental data explain the physical mechanisms for sound propagation over a hill.

REFERENCES

1. Gilbert, K.E.; and White, M.J.: Application of the Parabolic Equation to Sound Propagation in a Refracting Atmosphere. *J. Acoust. Soc. Am.*, vol. 85, 1989, pp. 630-637.
2. You, C.: Non-Line of Sight Sound Propagation Outdoors. Ph.D. dissertation. University of Mississippi, May 1993.
3. Pierce, A.D.: *Acoustics: An Introduction to Its Physical Principles and Applications*. American Institute of Physics, 1989.
4. Raspet, R.; Baird, G.E.; and Wu, W.: Normal Mode Solution for Low-Frequency Sound Propagation in a Downward Refracting Atmosphere above a Complex Impedance Plane. *J. Acoust. Soc. Am.*, vol. 91, 1992, pp. 1341-1352.

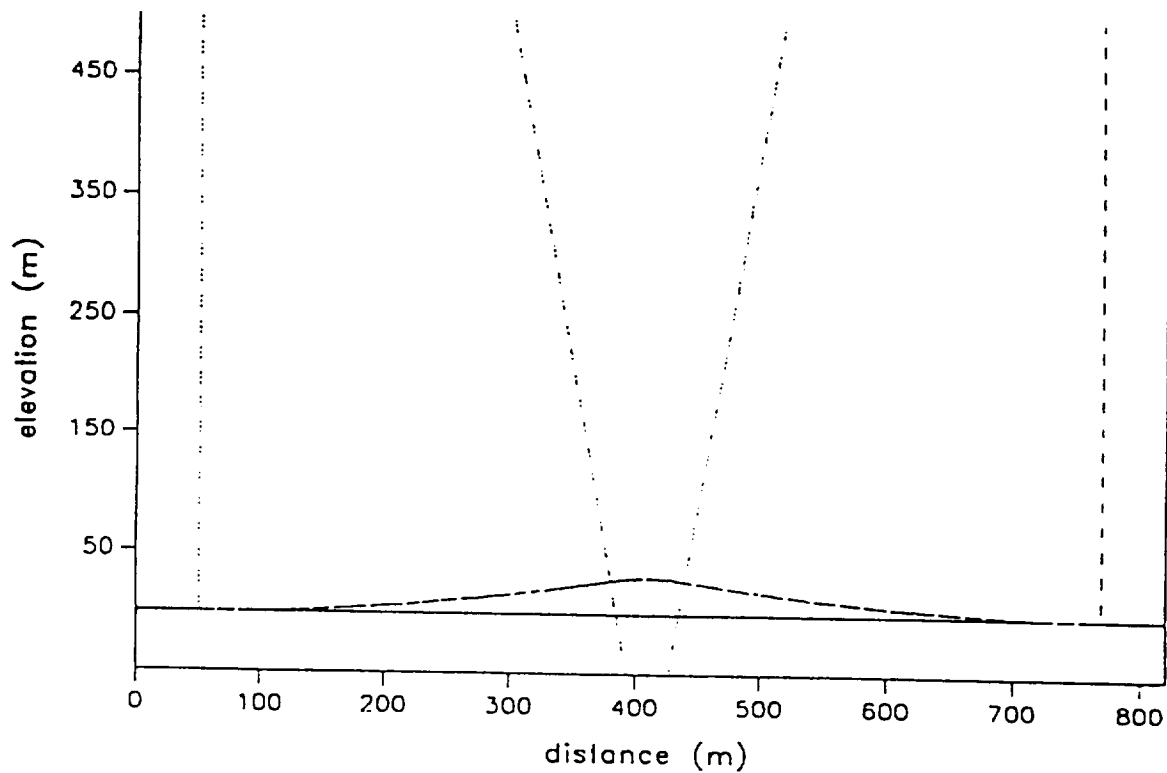


Figure 1. Segmenting a 30 meter hill for comparison with conformal mapping.

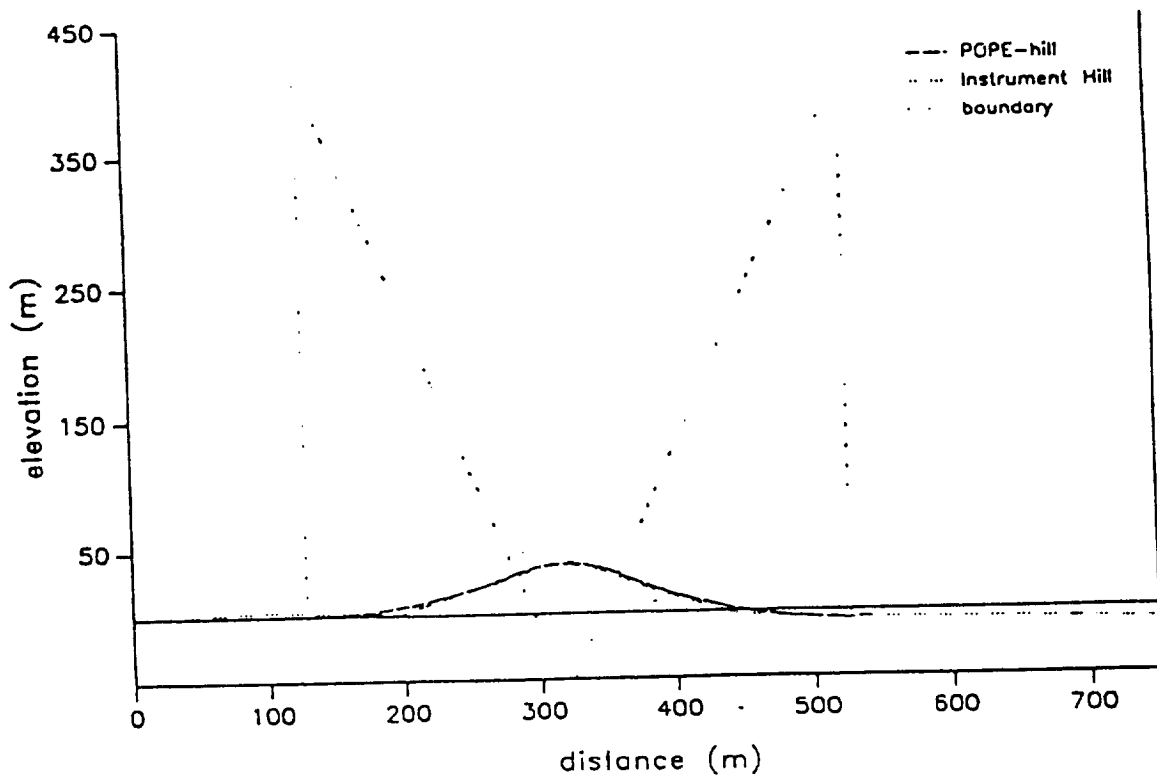


Figure 2. Elevation versus range for POPE-hill and Instrument Hill.

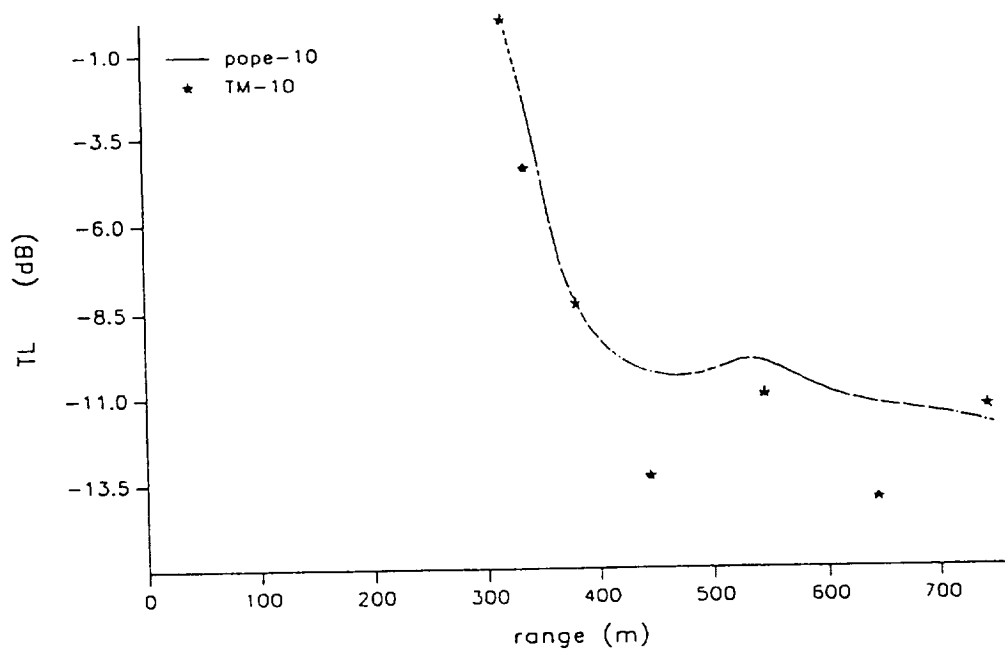


Figure 3. Comparison of Terrain Masking experimental data with POPE calculation at 10 Hz when helicopter hovers 10 m above the ground surface 200 m from the south base of Instrument Hill.

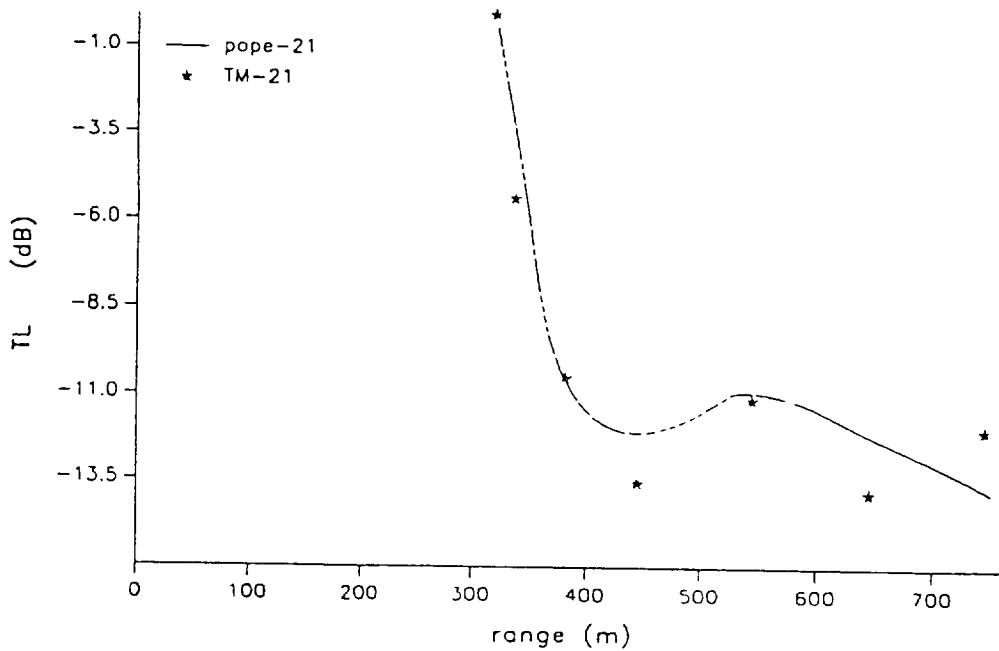


Figure 4. Comparison of Terrain Masking experimental data with POPE calculation at 21 Hz when helicopter hovers 10 m above the ground surface 200 m from the south base of Instrument Hill.

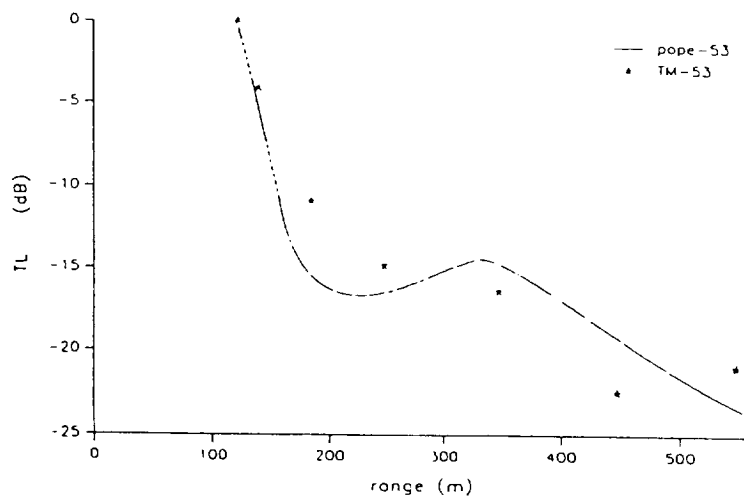


Figure 5. Comparison of Terrain Masking experimental data with POPE calculation at 10 Hz when helicopter hovers 17 m above the south base of Instrument Hill.

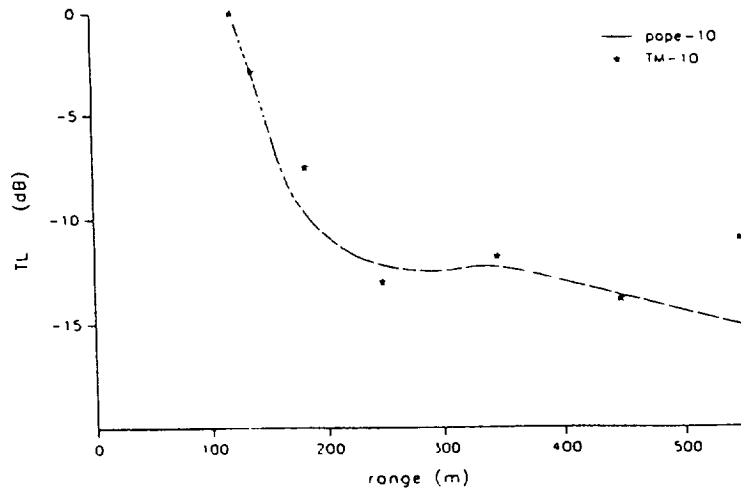


Figure 6. Comparison of Terrain Masking experimental data with POPE calculation at 53 Hz when helicopter hovers 17 m above the south base of Instrument Hill.

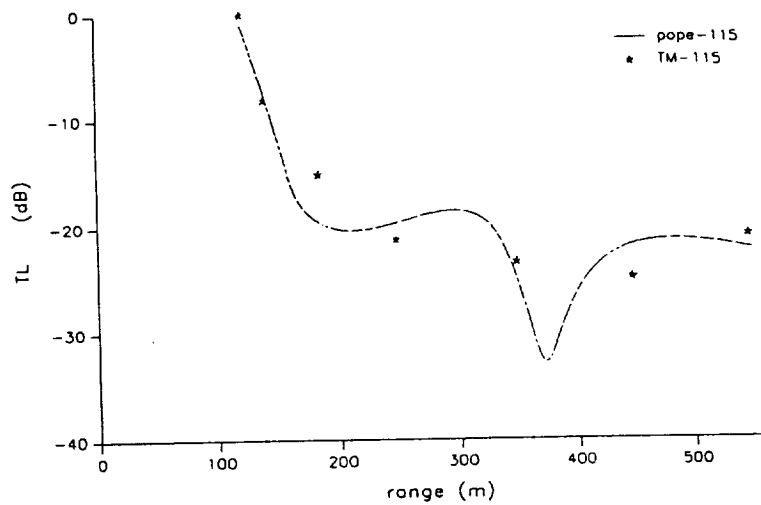


Figure 7. Comparison of Terrain Masking experimental data with POPE calculation at 115.7 Hz.

N94-2216

PRELIMINARY ANALYSIS OF AMPLITUDE AND PHASE FLUCTUATIONS IN THE JAPE
MULTIPLE TONE DATA TO DISTANCES OF 500 METERS

James Rogers, Radomir Sokolov
Michigan Technological University
1400 Townsend Drive
Houghton, Michigan 49931

59-71
100-1
P. 14

Daniel Hicks, Lloyd Cartwright
AMSTA-JCS
U.S. Army TARDEC
Warren, Michigan 48397-5000

INTRODUCTION AND PURPOSE

The JAPE short range data provide a good opportunity for studying phase and amplitude fluctuations of acoustic signals in the atmosphere over distances of several hundred meters. Several factors contribute to the usefulness of these data: extensive meteorological measurements were made, controlled sources were used, the data were recorded with a high dynamic range digital system that preserved phase information and a significant number of measurement points were obtained allowing both longitudinal and transverse studies. Further, Michigan Tech, in cooperation with the U.S. Army TARDEC, has developed phase tracking algorithms for studying vehicle acoustic signals. These techniques provide an excellent tool for analyzing the amplitude and phase fluctuations of the JAPE data.

The results of studies such as those reported here have application at several levels: the mechanisms of signal amplitude and phase fluctuations in propagating acoustic signals are not well understood nor are the mathematical models highly developed, acoustic arrays depend strongly on signal coherence and signal amplitude stability in order to perform to their design specifications and active noise control implementation in regions considerably removed from the primary and secondary sources depends upon signal amplitude and phase stability.

Work reported here is preliminary in nature but it does indicate the utility of the phase tracking and amplitude detection algorithms. The results obtained indicate that the phase fluctuations of the JAPE continuous multiple tone data (simultaneous transmission of 80, 200 and 500 Hz) are in general agreement with existing theories but the amplitude fluctuations are seen to be less well behaved and show less consistency.

THE MEASUREMENT SITE AND DATA ANALYZED

Figure 1 is a sketch depicting the short range propagation experiment site. The separation distance of the north and south towers is 1000 meters and the microphone array is located midway between them. The data analyzed here were from trial 033102 at time 22:50 (MDT). The speaker was located at the base of the north tower. Microphone spacing along the line was 100 meters while a variety of spacings were used for the array as shown in the figure. The numbering scheme used in the figure does not correspond with the channel numbers assigned during the experiment. Since some of the channels were not useful, the microphone at the base of the North tower was overdriven; while other microphones did not provide signals, the microphones were renumbered as indicated in the figure. Thus neither microphone 5 nor 6

has a corresponding microphone in the typical arrangement for a pair of microphones, one on the ground and one located one meter above that. This numbering arrangement seen in the figure facilitates later plots.

Two seconds of raw data are shown in Figure 2 where the bottom trace is the acoustic signal recorded at 400 m from the north tower base and the traces above that are from 300, 200, and 100 m respectively. The vertical scale of the traces is uncalibrated but it is the same for all traces. Wind noise is the principal feature of the traces but there is clearly a signal present. The three simultaneous tones at 80, 200 and 500 Hz present one hundred sixty cycles over the 2 second time span of the figure and are evidenced by the decreasing width of the signal trace from the top of the figure to the bottom. The trace corresponding to the 300 m distance shows little effects of wind when compared to the other three traces. No reason is known for this feature. The winds at the dirt site west tower were approximately 2 m/s and 3 m/s at 2 and 10 m elevations respectively. The direction was approximately 220 degrees.

The FFT amplitude spectra from the data in Figure 2 are shown in Figure 3, where the vertical scale is not calibrated. Background noise and wind noise are clearly evident in this figure as are the three simultaneous tones. In order to improve resolution of the tonal peaks the time series data record length transformed was 2.5 seconds. A principal advantage to analyzing the simultaneous tone data instead of data with single tones is that comparisons of the phase and amplitude fluctuations for a sequence of separate tones depend on the stability of the meteorological conditions. However, analysis of simultaneous tones does not require this. A trade off in this choice however is that the power in each single transmitted tone can be determined by the total system power available while for multiple tones the power in each tone is necessarily only a portion of the total system power available. Thus the signal to noise for each tone is worse for the multiple tone measurement.

PHASE AND AMPLITUDE EXTRACTION

Each of the three tones was analyzed separately but with a common algorithm. First the data were passed through an eight pole band pass filter with a 2.5 Hz bandwidth centered on the tone of interest. The filter had a linear phase characteristic throughout the passband. After a real signal to analytic signal conversion using an FIR Hilbert transformation, the signal amplitude was extracted. The next step in the analysis was phase tracking the received tone. Figure 4 is a conceptual diagram of the amplitude and phase extraction process.

Since the phase detector in the phase locked loop is sensitive to signal amplitude, the amplitude information previously obtained was used to restore the signal to a constant amplitude prior to phase tracking. The natural frequency of the phase lock loop was 0.75 Hz. In order to remove the signal component at twice the VCO frequency which is present after the phase detector an adaptive notch filter operating at twice the VCO instantaneous frequency was used. This filter is considerably above the bandwidth of the signal of interest and it is expected to have no effect on the phase information from the loop. It was possible to monitor the phase error of the tracking loop and to observe that phase lock was easily maintained with only insignificant phase errors. The final step in the phase analysis was removal of the difference frequency between the free running VCO and the frequency of the tone used in the experiment. It was observed that the values 80, 200 and 500 Hz were nominal and that the actual measurement frequencies were different from these values by a fraction of a Hz.

SPATIAL CHARACTERISTICS OF AMPLITUDE AND PHASE DATA

The theoretical development of the meteorological effects on propagating acoustic signals has roots in the work of Karavainikov, Chernov and Tatarskii (refs 1,2,3). Daigle, Piercy and Embleton (ref 4) reviewed the theory pertinent to line of sight propagation through atmospheric turbulence. McBride, Bass, Raspet and Gilbert approached the problem of sound scattering in atmospheric turbulence by developing a computer simulation of the effects of small scale turbulence (ref 5). The theory (ref 4) assumes homogeneous and isotropic turbulence. Large atmospheric eddies are formed by instabilities in the

boundary layer near the ground and additional instability produces progressively smaller eddies until they are dissipated by viscosity. After assuming a Gaussian turbulence distribution they develop expressions for the log-amplitude and phase fluctuations for pure tones propagated through a turbulent atmosphere near the ground. Only a brief overview of their presentation is given here to define the quantities which we present in later figures.

The log-amplitude, $M_{i,n}$, for the i-th microphone at the n-th time sample is

$$M_{i,n} = \ln \left(\frac{A_{i,n}}{A_{i,0}} \right) \quad (1)$$

where $A_{i,n}$ represents amplitude.

The average amplitude, $A_{i,0}$, over N samples at a fixed distance, is

$$A_{i,0} = \frac{1}{N} * \sum_{n=1}^{n=N} A_{i,n} \quad (2)$$

and mean square log-amplitude is given in Equation 3

$$\overline{M_{i,n}^2} = \frac{1}{N} * \sum_{n=1}^{n=N} M_{i,n}^2 \quad (3)$$

The phase structure function calculation is shown in Equation 4 of reference 4. The second term takes into account the mean phase difference of the measured data which may not be zero.

$$\overline{\Phi^2} = \frac{1}{N} \sum_{n=1}^{n=N} (\Phi_{i,n} - \Phi_{j,n})^2 - \left(\frac{1}{N} \sum_{n=1}^{n=N} (\Phi_{i,n} - \Phi_{j,n}) \right)^2 \quad (4)$$

$\Phi_{i,n}$ is the phase of the i-th microphone at the n-th sample.

Figure 5 shows sixteen seconds of the amplitude fluctuations for each of the three frequencies at distances of 100, 200, 300 and 400 m. Figure 6 presents the corresponding phase fluctuations for these frequencies and distances. The vertical scale on the amplitude plots is uncalibrated but it is the same for all plots. The vertical scale on the phase plots is the same for all plots and it is in radians. With some effort it is possible to clearly discern a pattern in the phase data: for all of the plots at a given frequency the least phase fluctuations occur at 100 m and the fluctuations increase with increasing distance. Another intriguing feature of the phase data for 80 and 200 Hz is the rather cyclic and regular nature of the fluctuations. For example the five second interval between 1 and 6 seconds on the 200 Hz plot for a distance of 400 m has regular fluctuations at a frequency of approximately 1.4 Hz. No explanation is presented for this character.

Figure 7 shows the logarithm of the average signal amplitude at three frequencies vs distance from the speaker. Also shown in the figure is a straight line with a slope of minus one which would be expected for signals with principal attenuation due to geometrical spreading. There is sufficient agreement between the trend of the data and the straight line that simple spreading is presumed to be the principal

attenuation mechanism at 500 Hz. However, there is some inconsistency in the data for 80 and 200 Hz where the signal loss appears to be less than that predicted by geometrical spreading.

Figure 8 shows mean square log-amplitude as a function of longitudinal distance from the source. The averaging time was 16 seconds. The plot generally shows increasing log-amplitude fluctuations with distance. Examination of the variations of signal amplitude with time shown earlier in Figure 5 suggests that 4 seconds is too short a time for calculating the average behavior and that 16 seconds may be more appropriate.

Figure 9 shows the dependence of mean square phase fluctuations as a function of longitudinal distance. There is a clear increase in phase fluctuations with longitudinal distance as is predicted by equation (2) (ref 4) which shows a linear dependence upon longitudinal distance. Also, increasing fluctuations with frequency are expected from the theory (refs 2,3).

All of the phase difference fluctuations between the microphones are portrayed in figure 10. The vertical axis is mean square phase fluctuations and it is scaled in radians. The two horizontal indexes correspond to microphone numbers which were indicated in Figure 1. Considerable information can be discerned from the figure. The intersection of microphone 12 with microphone 11 shows a small value for phase difference; microphone 12 is located directly above microphone 11 at an elevation of 1 m. The intersection of microphone 12 with microphone 10 shows a larger value for phase difference; both microphones are elevated 1 m and their horizontal separation is 1 m. Since the 8-9 and the 9-8 phase differences are the same, the redundant data are not shown in Figure 10. A general interpretation of the figure is that the phase fluctuations between microphones tend to increase with microphone separation distance. This trend is not seen in the first four microphones since their separation is 100 m which is considerably beyond the phase coherence predicted by the theory.

Figure 11 shows the phase coherence of the microphones in the transverse array located at 500 m. It is a plot of the mean square phase fluctuations between microphones in the array as a function of the logarithm of their separation distance. Also shown in the figure is a line with a slope of 5/3 which is predicted by theory (see equation 5). There is general agreement between the data and the theory for the shorter distances.

$$\overline{\Phi^2} = \text{const} * \left(\frac{f}{2 * \pi * c} \right)^2 * L * b^{\frac{5}{3}} * C \quad (5)$$

L	source -microphone distance
b	separation between two microphones
f	frequency
c	speed of sound
C	turbulence characteristic

Numerical analysis of the data in Figure 11 shows the 5/3 law is approximately valid for separation distances up to 3 m. However, the 5/3 law is less well adhered to for a signal frequency of 200 Hz (see Figure 12). Further increasing the signal frequency to 500 Hz shows even less adherence to the 5/3 law relationship. This observation shows that the outer scale of turbulence can be calculated when the range of validity of separation distance is estimated. We have not analyzed the meteorological data to determine the apparent fluctuations in the atmospheric index of refraction but these too would be expected to produce an outer scale on the order of a few meters. Consequently, at larger distances the phase fluctuations are not expected to follow a 5/3 relation.

DISCUSSION AND CONCLUSIONS

Given the rather large amount of unwanted noise present with each of the tones it is desirable to restrict the analysis bandwidth to ensure the greatest signal to noise for the analysis. However, a compromise is required in order to ensure that significant signal amplitude and phase fluctuations are allowed to pass through the system. The 2.5 Hz filter was a choice made for these preliminary results. Initial investigations indicated that this bandwidth is not too restrictive and that significant information is available from the analysis algorithm described above. Additional studies will be required to determine if there is a better choice for the analysis bandwidth. However, there is no hard threshold where the results change from useless to useful and a certain amount of judgment is therefore required in selection of the "proper" analysis bandwidth.

Another issue that is not addressed in the existing theory that requires additional study is determining the amount of data that should be used to calculate the RMS amplitude and phase fluctuations. It was seen earlier that the results from a 16 second average and from a 4 second average were quite different. This should be expected if one considers the variations in the amplitude vs time and phase vs time curves shown in Figures 5 and 6 respectively. The decision on the "proper" averaging time must be made using judgment based upon the time variability of these curves as there is no theory to provide adequate guidance on this issue.

The data analysis presented here is preliminary. It is necessary to examine additional data in order to better characterize the temporal and spatial variations of the acoustic data. The meteorological data too should be further examined so statistical parameters can be determined. Finally, an assessment of fluctuating amplitude and phase effects on microphone array performance and on the behavior of the active noise control (ACN) systems should be made.

REFERENCES

1. Karavainikov, V. N.: "Fluctuations of amplitude and phase in a spherical wave," Aakust. Zh. 3, 175-186, 1957.
2. Chernov, L. A.: Wave Propagation in a Random Medium, McGraw-Hill, New York, 1960.
3. Tatarskii, I.: The Effects of the Turbulent Atmosphere on Wave Propagation, Ketter, Jerusalem, 1971.
4. Daigle, G. A., Piercy, J. E. and Embleton, T. F. W.: Line-of-sight Propagation Through Atmospheric Turbulence Near the Ground, Journal of the Acoustical Society of America, Vol. 74, No. 5, Nov. 1983, pp 1505-1513.
5. McBride, W., Bass, H. E., Raspert, R., Gilbert, K. : Scattering of Sound by Atmospheric Turbulence: A Numerical Simulation Above a Complex Impedance Boundary, Journal of the Acoustical Society of America, vol. 90, No. 6, Dec. 1991, pp 3314-3325.

Short Range Propagation Experiments

White Sands Missile Range, July 1991

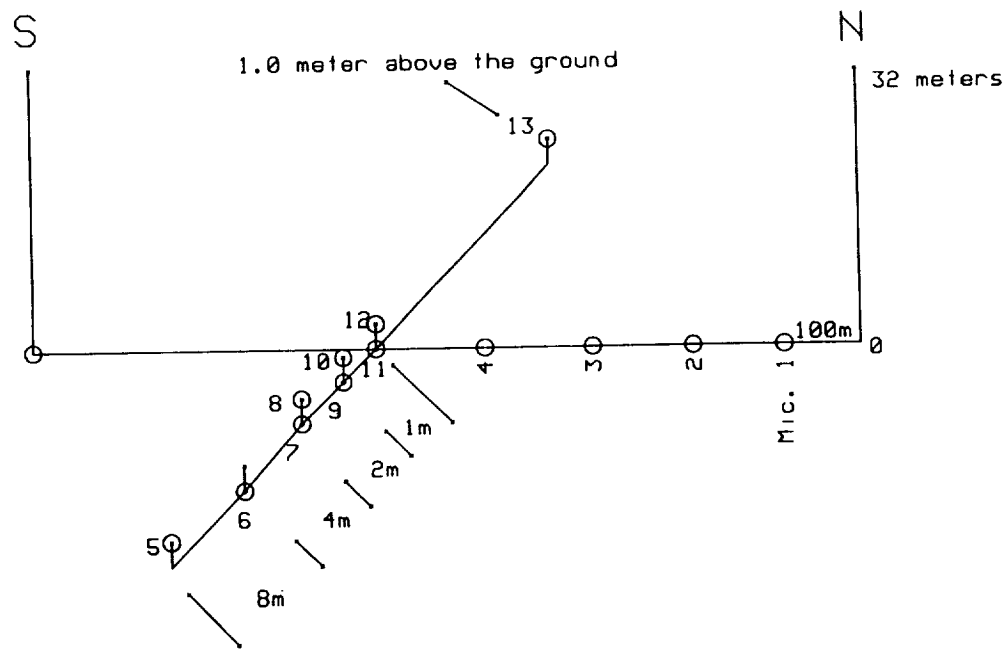


Figure 1 Short range propagation site

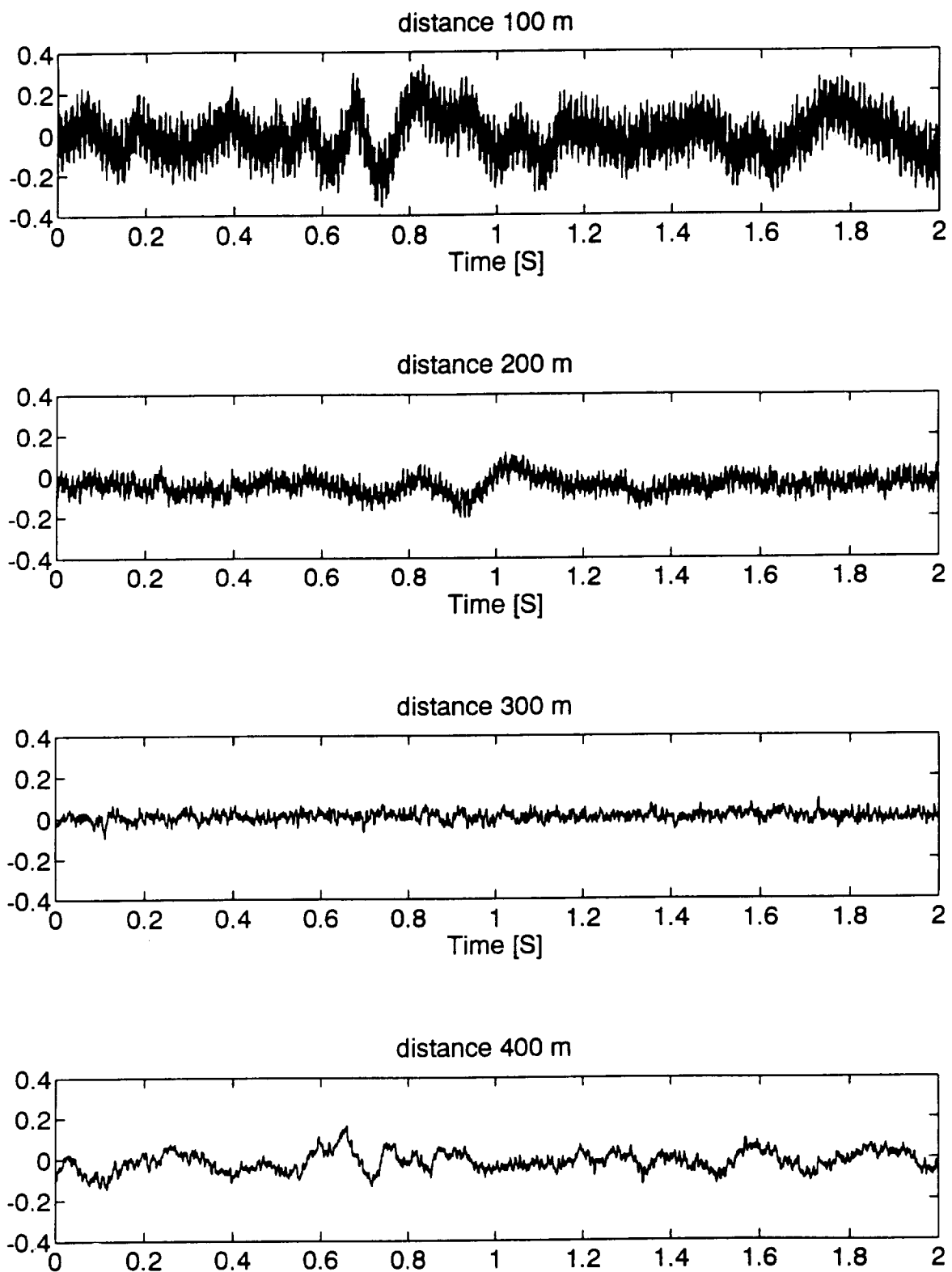


Figure 2 Recorded acoustic signals (100 - 400 m), trial No:03310 2.

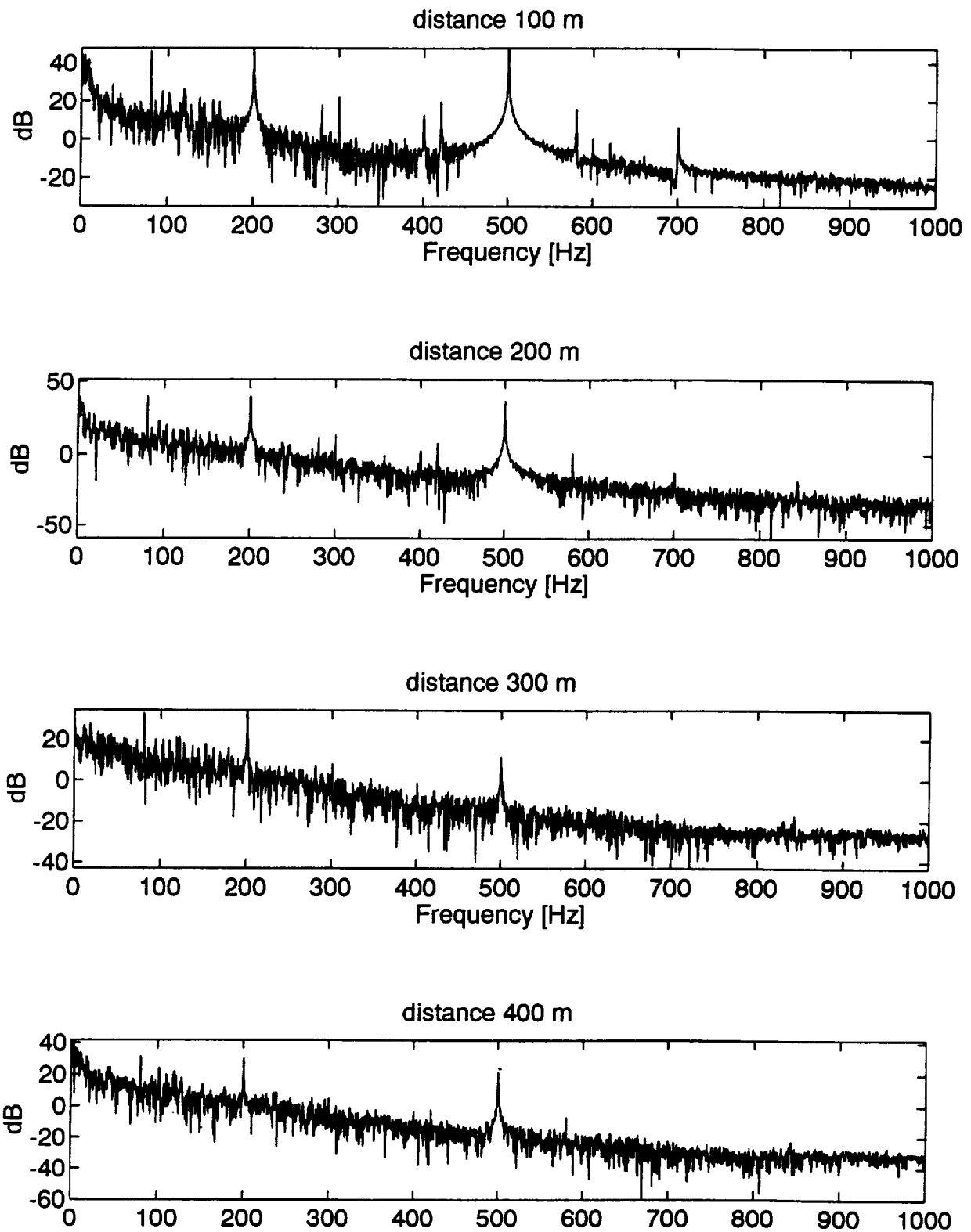


Figure 3 FFT spectra from the data in Figure 2.

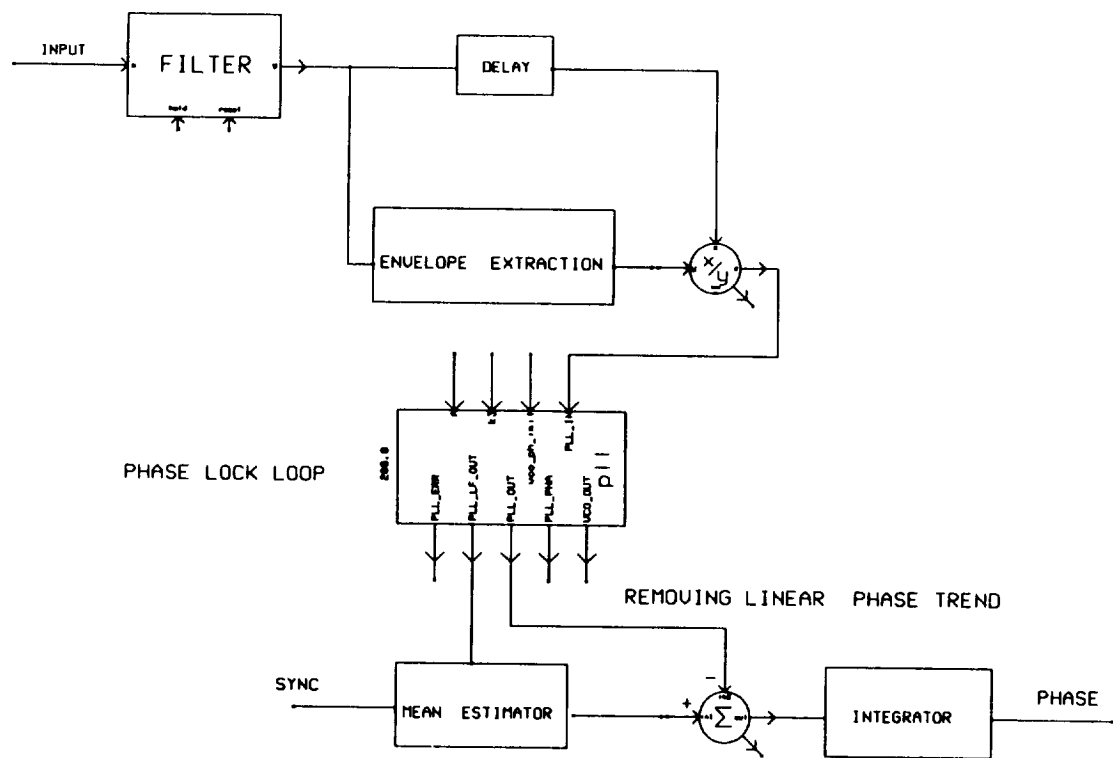
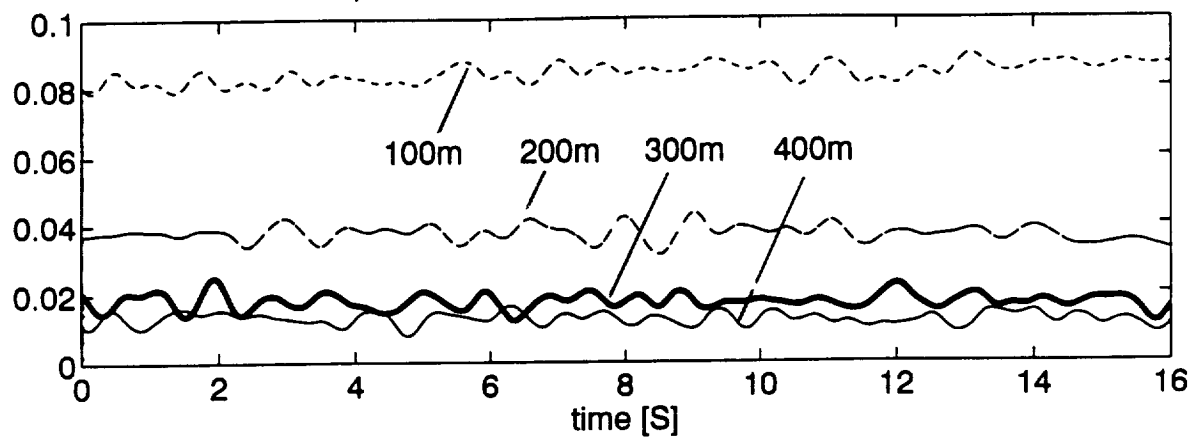
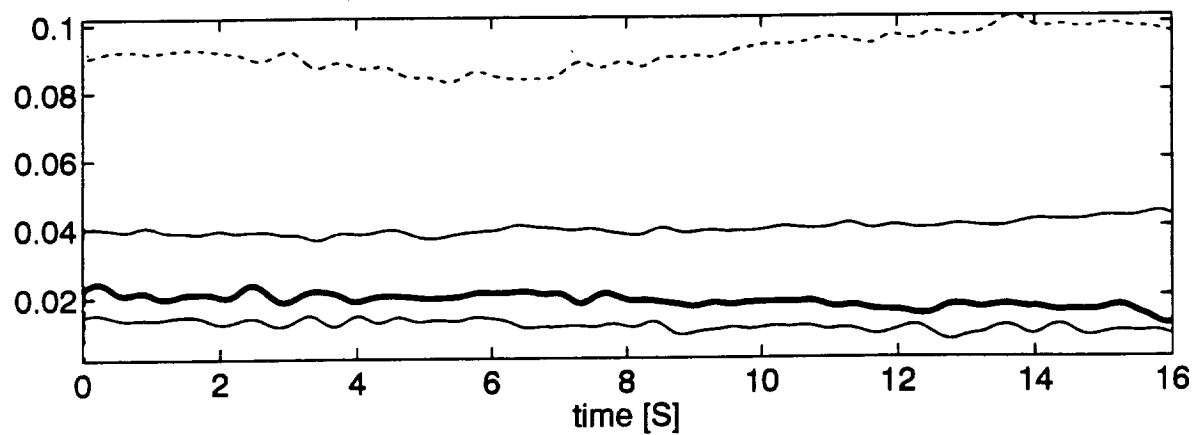


Figure 4 Conceptual diagram of the amplitude and phase extraction process.

amplitude fluctuation versus time, freq=80Hz



amplitude fluctuation versus time, freq=200Hz



amplitude fluctuation versus time, freq=500Hz

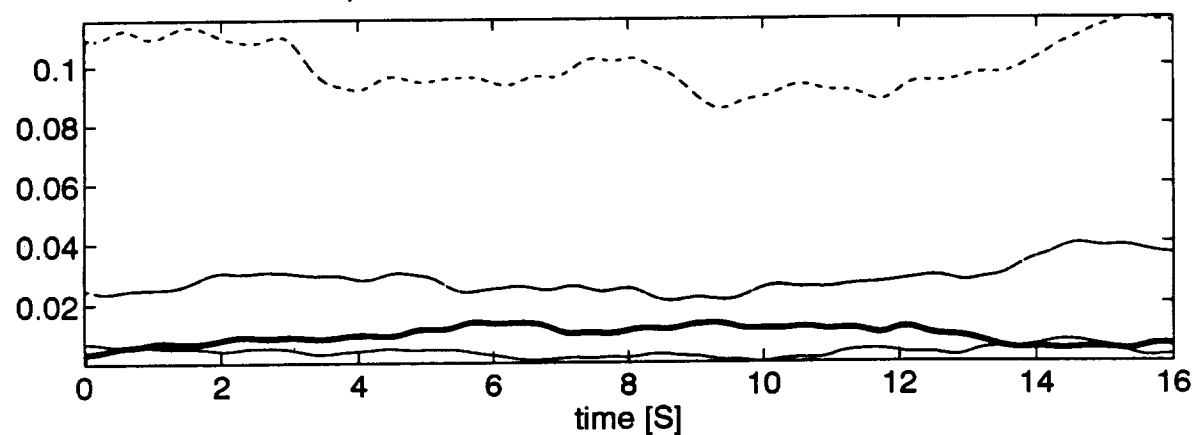
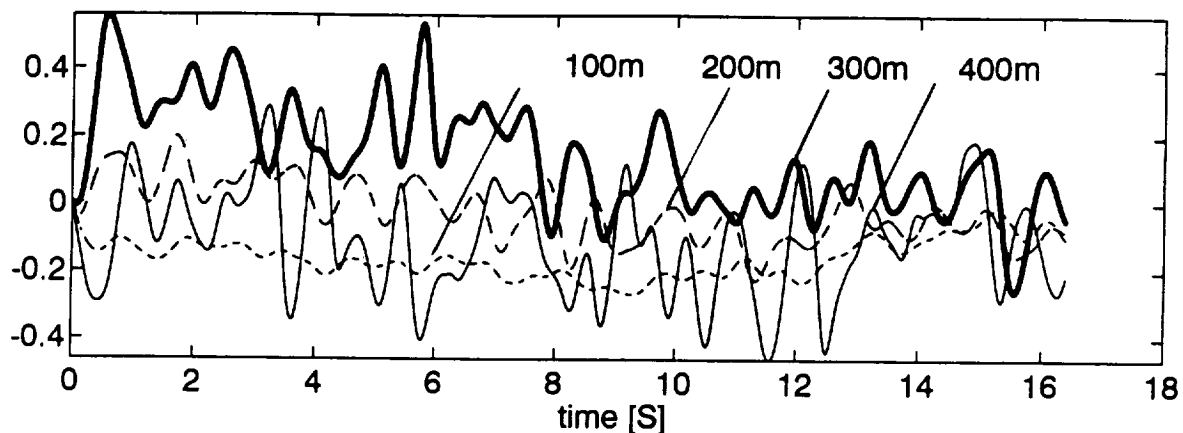
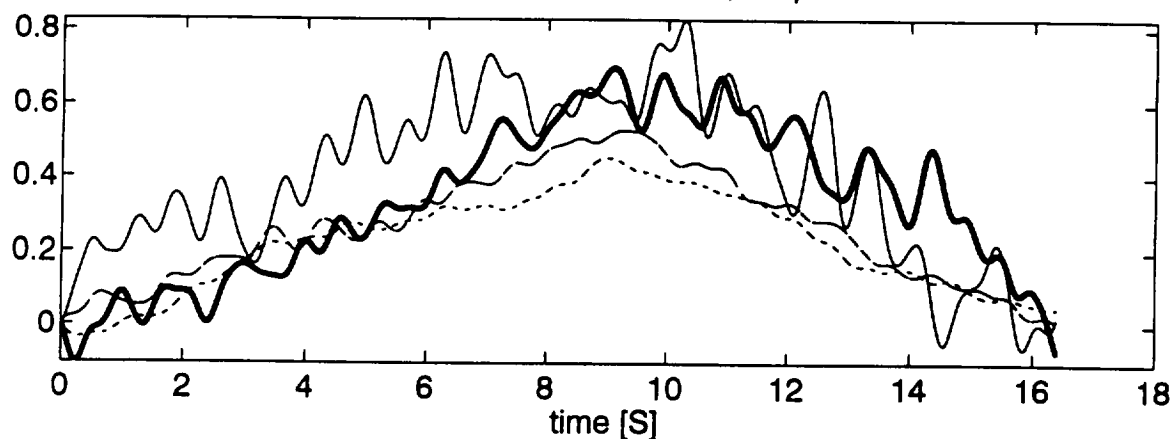


Figure 5 Amplitude fluctuations at distances 100 m - 400 m

phase fluctuation versus time, freq=80Hz



phase fluctuation versus time, freq=200Hz



phase fluctuation versus time, freq=500Hz

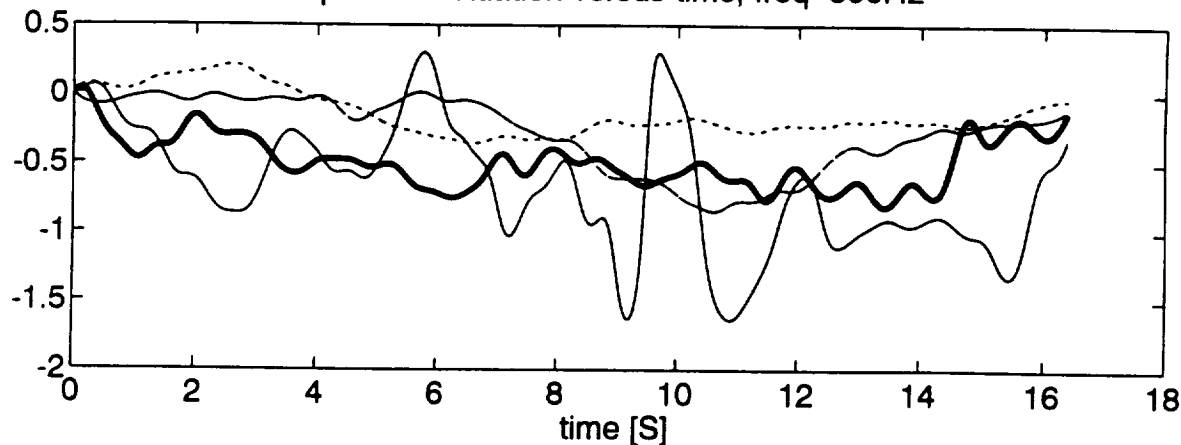


Figure 6 Phase fluctuations at distances 100 m - 400 m

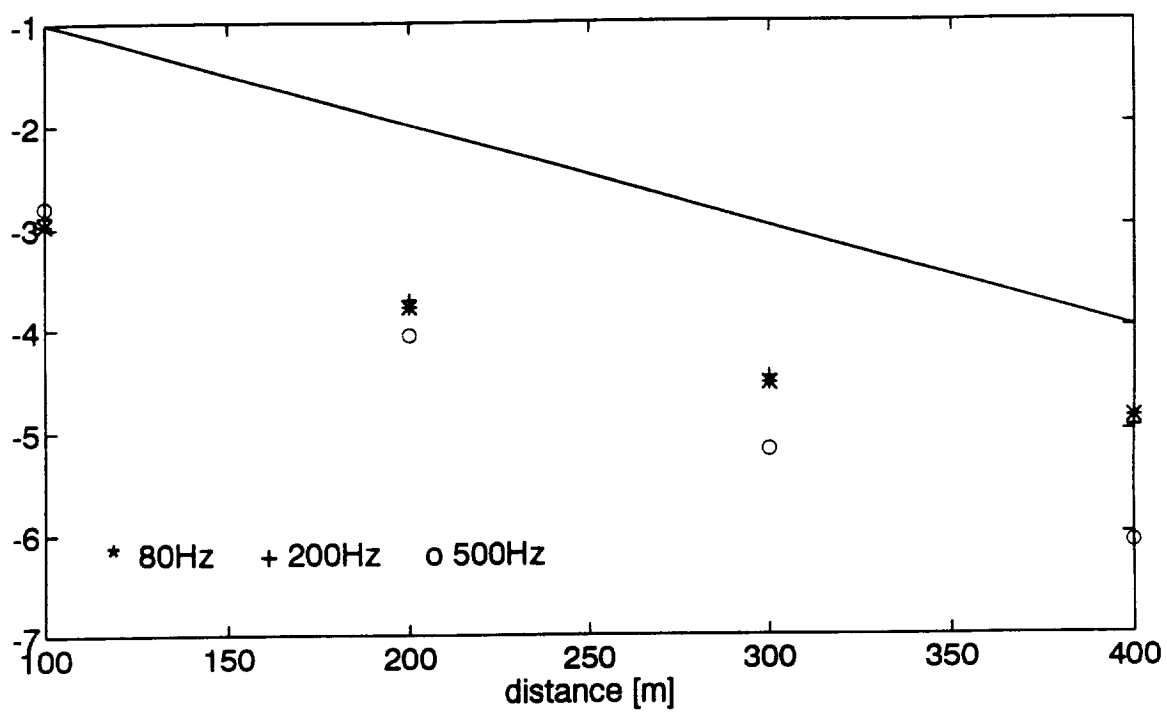


Figure 7 Log-average amplitude at different microphone positions.

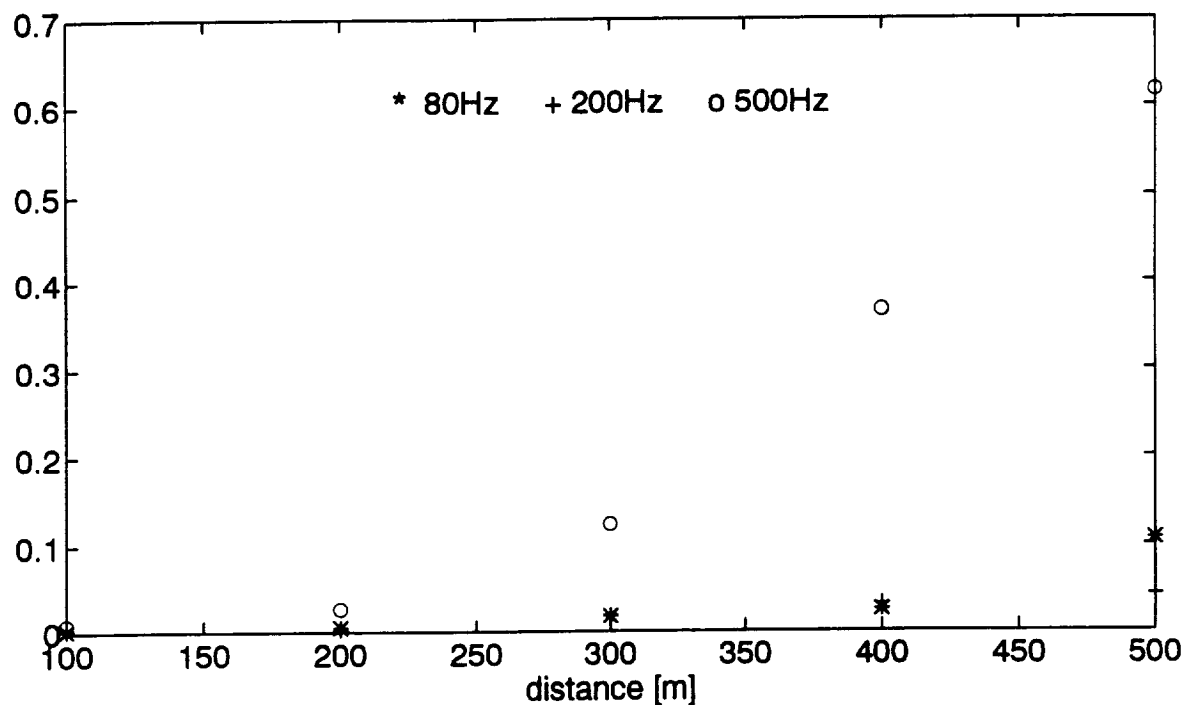


Figure 8 Mean square log-amplitude fluctuations, time_average=16s

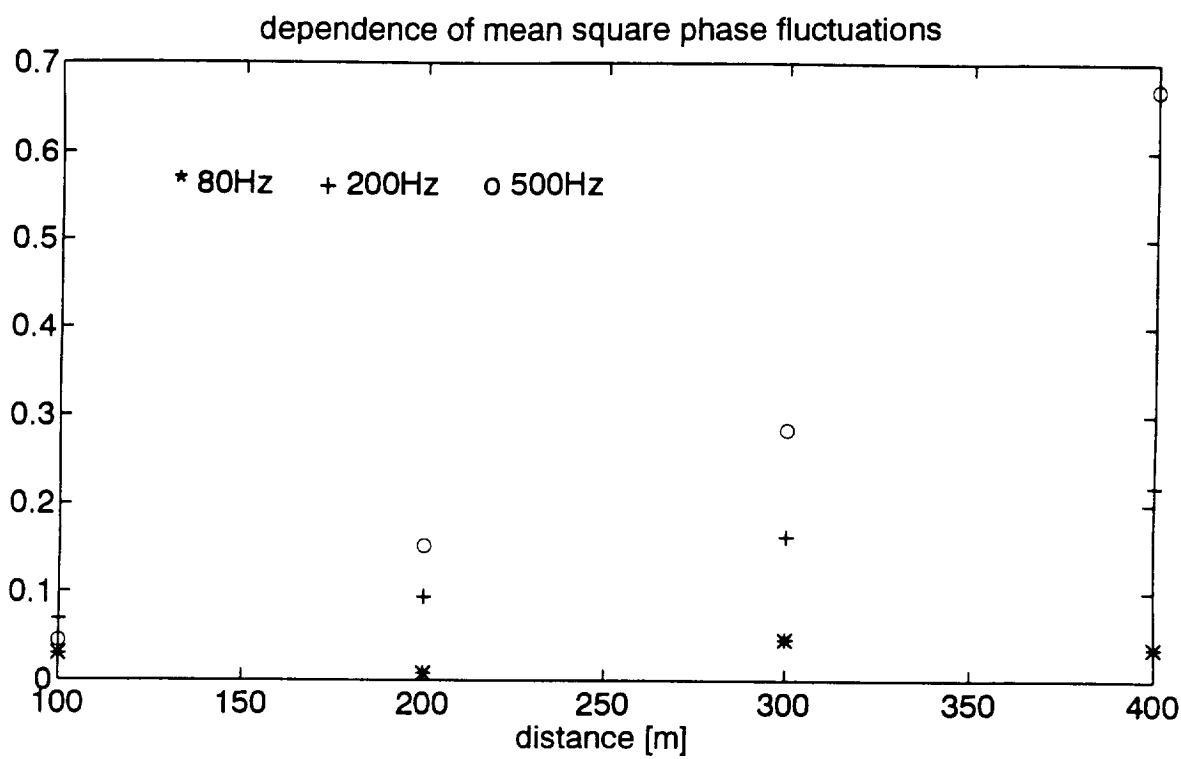


Figure 9 Mean square phase fluctuations versus distance.

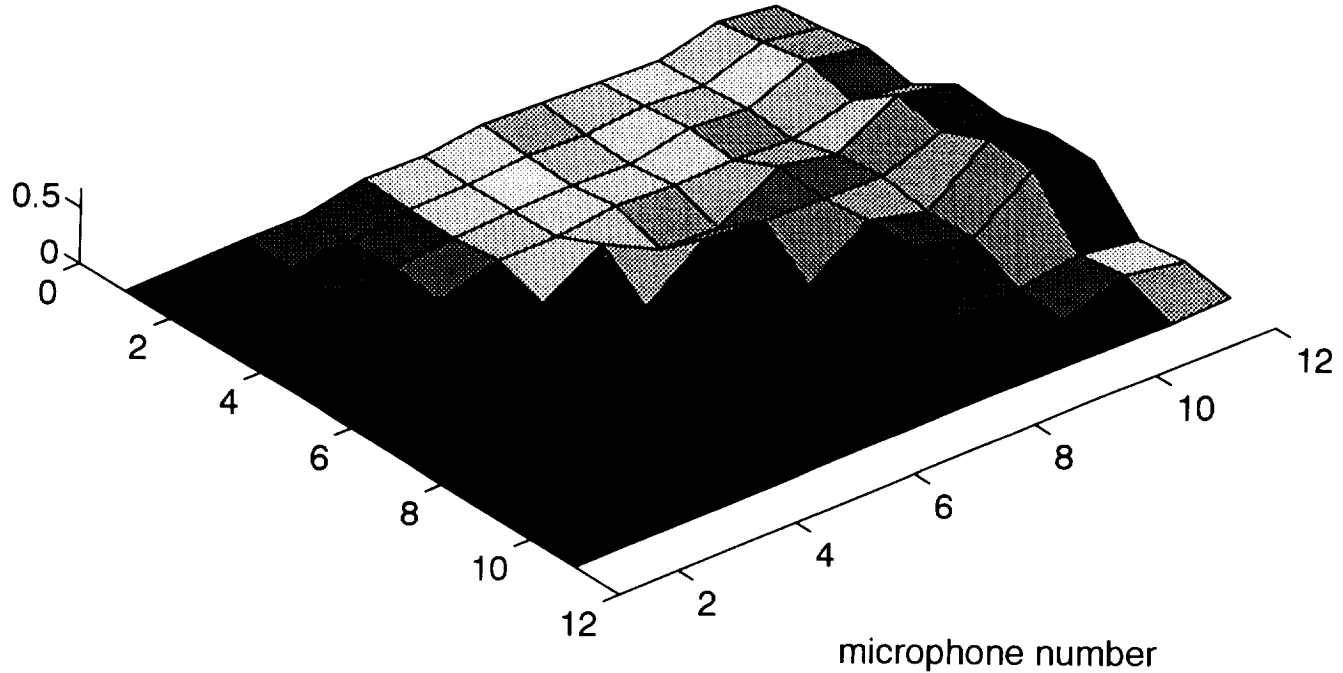


Figure 10 Mean square phase difference between microphones.

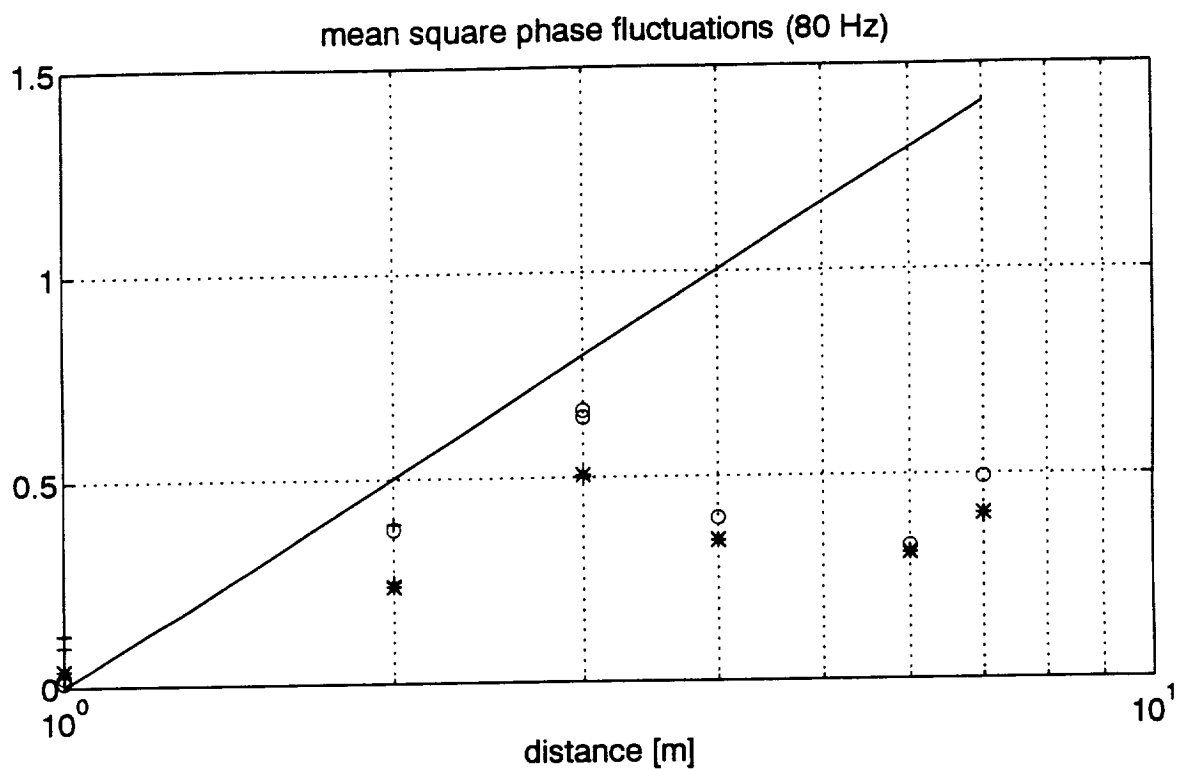


Figure 11 Mean square phase fluctuations in the transverse array.

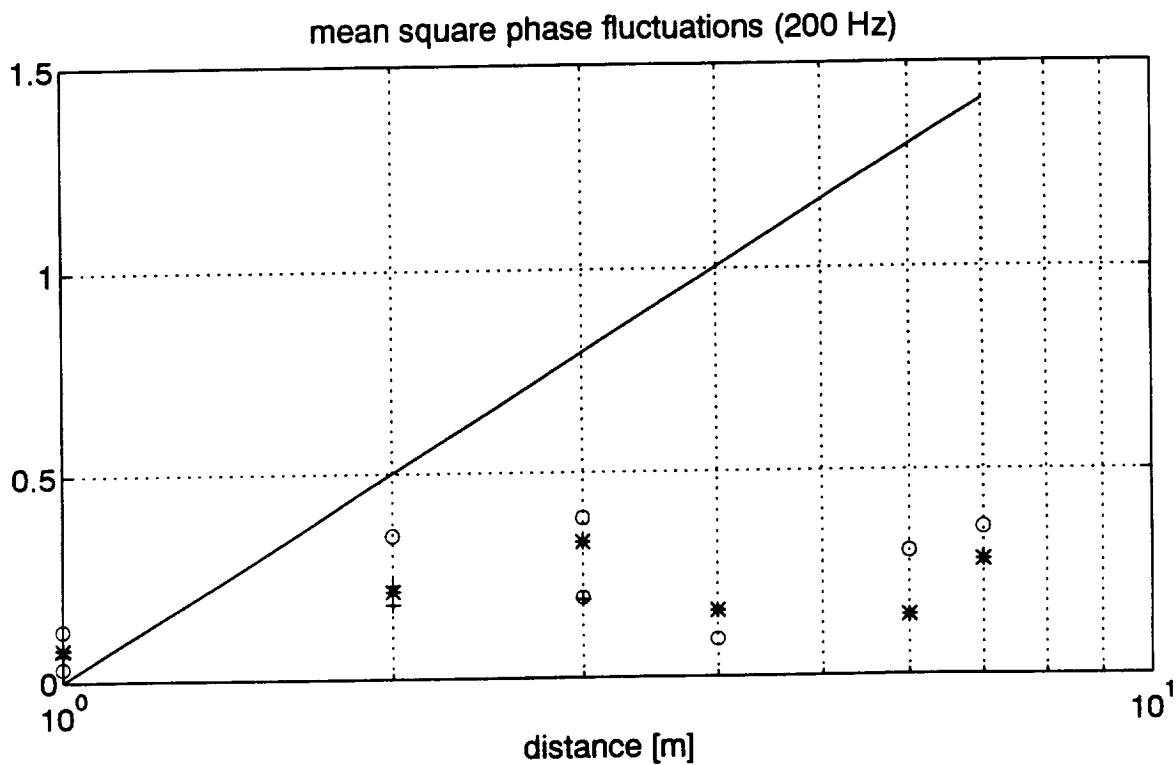


Figure 12 Mean square phase fluctuations in the transverse array.

N 9 4 - 2 4 2 1 7

DIMENSIONAL ANALYSIS OF ACOUSTICALLY PROPAGATED SIGNALS

Scott D. Hansen
Graduate Program in Acoustics
Pennsylvania State University
University Park, PA

340-71

Dennis W. Thomson
Department of Meteorology
Pennsylvania State University
University Park, PA

2016 82

F- 11

INTRODUCTION

Traditionally, long term measurements of atmospherically propagated sound signals have consisted of time series of multiminute averages. Only recently have continuous measurements with temporal resolution corresponding to turbulent time scales been available. With modern digital data acquisition systems we now have the capability to simultaneously record both acoustical and meteorological parameters with sufficient temporal resolution to allow us to examine in detail relationships between fluctuating sound and the meteorological variables, particularly wind and temperature, which locally determine the acoustic refractive index.

The atmospheric acoustic propagation medium can be treated as a nonlinear dynamical system, a kind of signal processor whose innards depend on thermodynamic and turbulent processes in the atmosphere. The atmosphere is an inherently nonlinear dynamical system. In fact one simple model of atmospheric convection, the Lorenz system⁽¹⁾, may well be the most widely studied of all dynamical systems. In this paper we report some results of our having applied methods used to characterize nonlinear dynamical systems to study the characteristics of acoustical signals propagated through the atmosphere. For example, we investigate whether or not it is possible to parameterize signal fluctuations in terms of fractal dimensions. For time series one such parameter is the limit capacity dimension. Nicolis and Nicolis were among the first to use the kind of methods we have to study the properties of low dimension global attractors⁽²⁾.

In this paper we show, for example, that the limit capacity dimensions for atmospherically propagated acoustic signals are greater than those of either the wind speed or the along (propagation) path wind component. Turbulence is the phenomenon which

most strongly controls fluctuations in the acoustic refractive index η . Variations in acoustic refractive index are a function of velocity, temperature and, to a lesser extent, humidity fluctuations. Written in terms of the turbulent structure function parameters and neglecting humidity, variations in η are

$$C_{AC}^2 = \alpha C_T^2 + \beta C_V^2 + \gamma C_T^2 C_V^2 \quad (1)$$

where α and β are constants. Gamma is not a constant but rather a function, in particular, of the stability (heat flux).

Although the use of nonlinear dynamical methods is now rapidly growing, they are not yet nearly so widely known as, e.g., linear Fourier methods⁽³⁾. Thus we summarize here the basic analysis method as well as the results of using it.

DIMENSIONAL ANALYSIS OF A TIME SERIES: SOME FUNDAMENTALS

When one is working out of doors it is virtually impossible to measure all of the potentially important environmental variables. Nevertheless it may be possible to extract most of the information necessary to define signal variability by analyzing appropriately combined acoustic and meteorological measurements.

Takens' theorem⁽⁴⁾ defines the largest embedding dimension which is needed to analyze a single time series and, thus, to obtain an accurate fractal dimension for the system. The embedding dimension is the state space in which an object can be visualized. For any system having a fractal dimension, e.g. the well known Lorenz attractor, Takens' theorem states that a maximum embedding dimension of $2d+1$ is needed, where d is the fractal dimension rounded to the next higher integer. Thus an embedding dimension of seven should define the Lorenz system, which has a fractal dimension of 2.06. A system might be described in fewer dimensions, but Takens' theorem sets an upper bound for the state space in which the attractor can be embedded.

In the analysis of a time series, if an embedding dimension is used which is less than prescribed by Takens' theorem, the fractal dimension may not be saturated (i.e., reached its peak value). However, as schematically shown in figure 1, if an embedding dimension of higher order is used, little, if any additional information will be gained⁽⁵⁾.

Practically it is important to work with the minimum required embedding dimension in order to minimize computational costs.

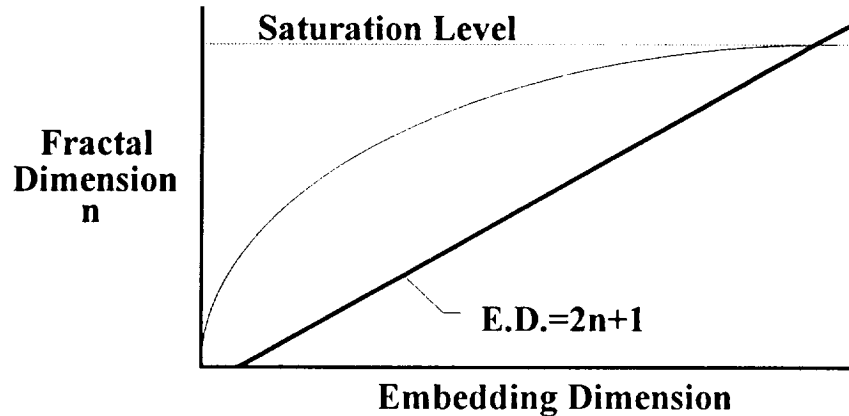


Figure 1. Fractal dimension as a function of embedding dimension

Lagging

In order to extract all information contained within a single time series it is necessary to reconstruct m single order equations. Let the single time series $X=F(t)$ be the set of points (x_1, x_2, x_3, \dots) which are separated by a distance Δx . First we approximate the first derivative of $F(t)$ to be

$$X' = \frac{F(t)}{dx} = \frac{F_{i+1} - F_i}{\Delta x} \quad (2)$$

Actually, there is redundant information in the first derivative, as F_i is the original time series. Therefore, an embedding dimension of two space is created when the original time series is shifted by one time step $(F_i, F_{i+1})^T$. For higher order systems this process is continued until one has created a state space which is large enough so that the attractor can be unfolded.

If the spacing between points in the approximation of the derivative is too small then points will appear to be totally correlated and cannot be considered as independent coordinates⁽⁶⁾. Similarly, if the spacing is too great adjacent points will appear to be unrelated (see figure 2).

In practice, instead of using successive points in the time series to calculate the derivatives, the time series is lagged by a certain number of points. Lagging consists of setting $X' = F'(t)$ equal to the $i+l$ th sample of $F(t)$, (i.e. i , $i+l$, $i+2l$, ...), where l is the size of the lag. Lagging the time series allows one to form a matrix as

$$\begin{pmatrix} F_i \\ F_{i+1} \\ F_{i+2l} \end{pmatrix} = \begin{pmatrix} x_1, & x_2, & x_3, & \dots \\ x_{1+l}, & x_{2+l}, & x_{3+l}, & \dots \\ x_{1+2l}, & x_{2+2l}, & x_{3+2l}, & \dots \end{pmatrix} = \begin{pmatrix} X \\ X' \\ X'' \end{pmatrix} \quad (3)$$

where each column of the matrix defines a single point in $(2d+1)$ phase space.

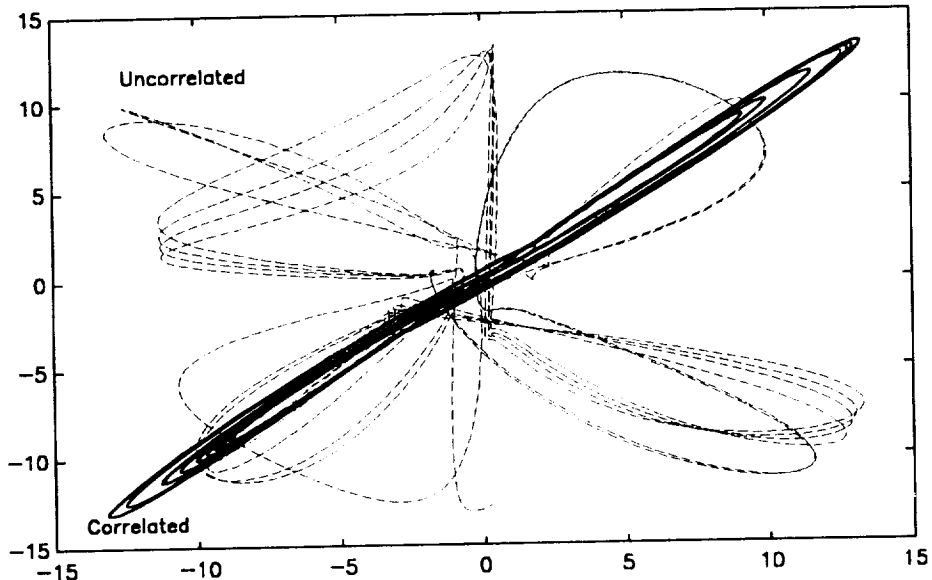


Figure 2. Lorenz attractor with correlated and uncorrelated lags

To estimate an appropriate value of the lag size, three methods are commonly used⁽⁷⁾, the autocorrelation time, mutual information, and visualization. For systems having an unknown fractal dimension the autocorrelation method appears to be the conservative approach. To determine the lag there are two possible ways of interpreting a graph of the autocorrelation time scale as shown in figure 3. One is to take the point halfway to the first zero crossing. A second approach is to determine the halfway point to where the autocorrelation curve becomes parallel to the x-axis. If no

zero crossing exists this is the only practical method. For the example shown the two methods yield lag sizes of 52 and 35, respectively.

Another method for estimating a proper lag is called mutual information. In this case one increases the lag size until no new information is gained and then defines that point as being the appropriate lag size.

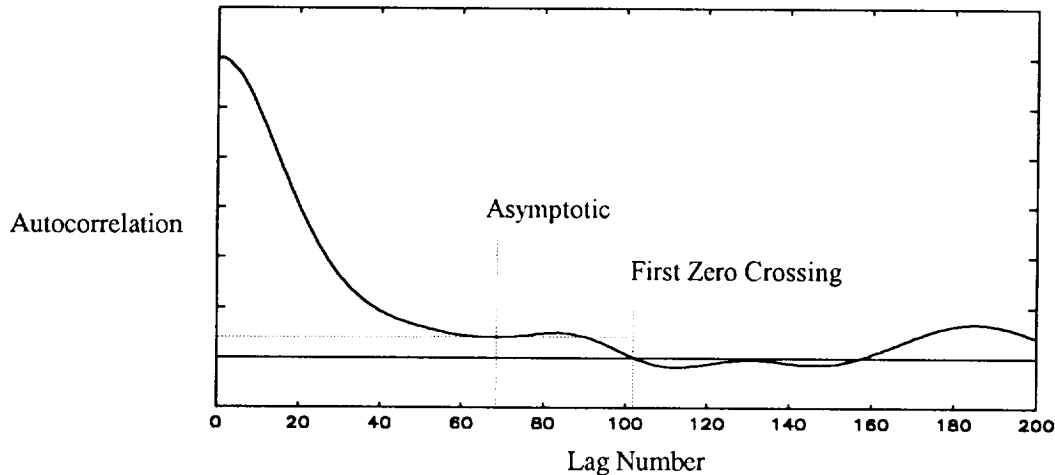


Figure 3. Autocorrelation of the Lorenz attractor

What is called visualization or visual reconstruction may also be used. Visualization is often used in situations where one has some prior knowledge of the system. This method consists of graphically reconstructing the attractor with various lags. If the topology of the attractor is known, e.g., as in the case of the Lorenz attractor, then the lag that appears closest to that for the real system is determined to be the appropriate one.

Limit Capacity Dimension

The limit capacity is one of four commonly used fractal dimensions: capacity, correlation, information, and Lyapunov. Determination of the limit capacity dimension is

made as follows⁽⁸⁾. If one lets $N(\varepsilon)$ represent the minimum number of m -dimensional cubes of length ε needed to enclose the time series, then as ε decreases one expects $N(\varepsilon)$ to increase.

$$N(\varepsilon) \propto \varepsilon^{-d_{cap}} \quad (4)$$

and therefore the capacity dimension is defined as:

$$d_{cap} = \lim_{\varepsilon \rightarrow 0} \frac{\log[N(\varepsilon)]}{\log[1/\varepsilon]} \quad (5)$$

The output of this limit capacity algorithm gives a lower bound to the dimension of the attractor.

Determining the Dimension from Graph

Figure 4 shows the result of applying the limit capacity algorithm to the Lorenz system. In this representation the bin numbers represent distances between points on the attractor. To estimate the limit capacity dimension of a data series a "stable plateau" region must be determined. Definition of the stable plateau may be subjective. Definition of optimal methods for determining the dimension and hence uncertainties in it are still being researched⁽⁹⁾.

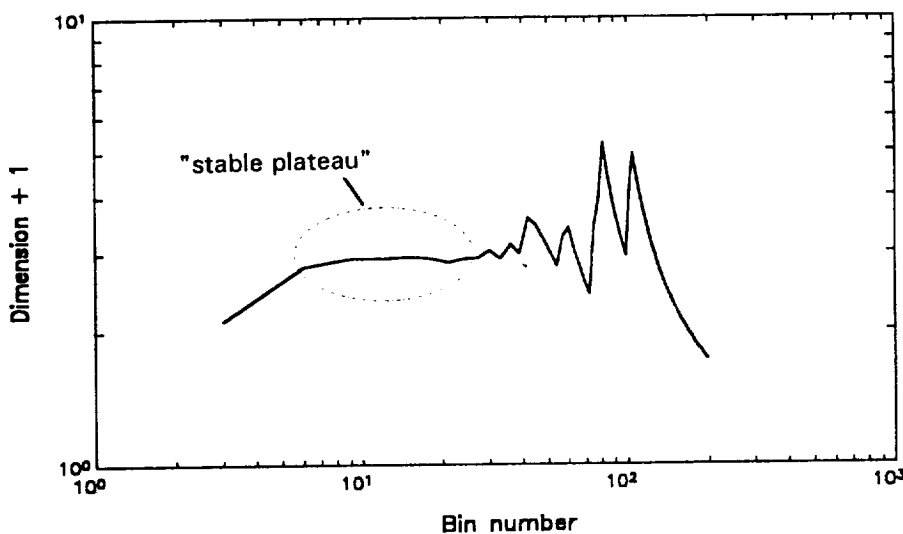


Figure 4. Limit capacity dimension of Lorenz attractor

ACOUSTICAL AND WIND SIGNALS STUDIED

We have applied the same methods as described above for the Lorenz system to hour long recordings of constant frequency sound signals, and to wind speed and the along path component of the wind. These measurements were made as part of the comprehensive Joint Acoustic Propagation Experiment (JAPE) study. Acoustic receivers were located 1 Km from the sound source and spaced logarithmically on a tower to a height of 32 meters. Three tones of 80, 200, and 500 Hz were transmitted. For this analysis the original 2048 samples per second were averaged to one quarter second. The corresponding wind time series had one-tenth second resolution. So far dimensional calculations for only the 80 and 500 Hz tones have been completed.

Lags were determined by calculating the autocorrelation time for each time series. Appropriate lags for the acoustic transmission loss (TL) signals varied between 12.5 and 187.5 seconds; lags for the wind signals ranged from 150 to 400 seconds. Wind speeds were less than 6 meters per second during the recording period. Correlation times of the TL signals measured at 0, 2, and 32 meters decreased both with height and frequency (figure 5).

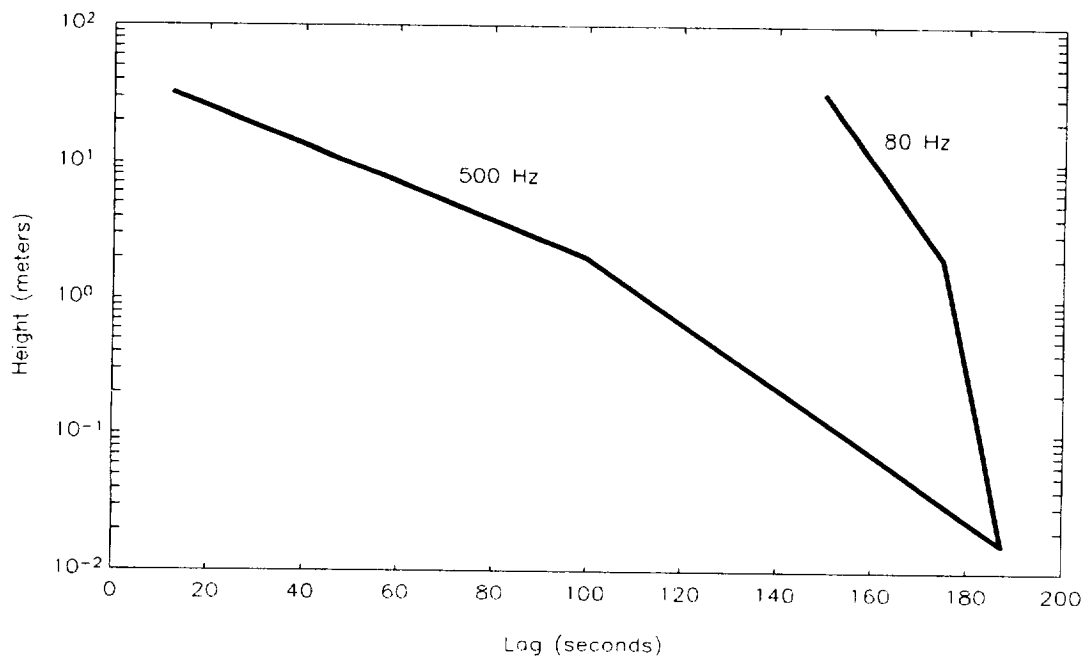


Figure 5. Correlation times vs. height for acoustic signals

Recall that for the Lorenz attractor an embedding dimension of seven was sufficient to unfold the attractor. However, for our acoustic and wind signals the dimension of the attractor was unknown. Thus it was necessary for us to calculate the limit capacity for a number of different embedding dimensions (figure 6). This was done repeatedly until it appeared that the dimensional information had saturated. Figure 6 shows the progression of the limit capacity dimension with increasing embedding dimensions until saturation was reached at roughly an embedding dimension of 12.

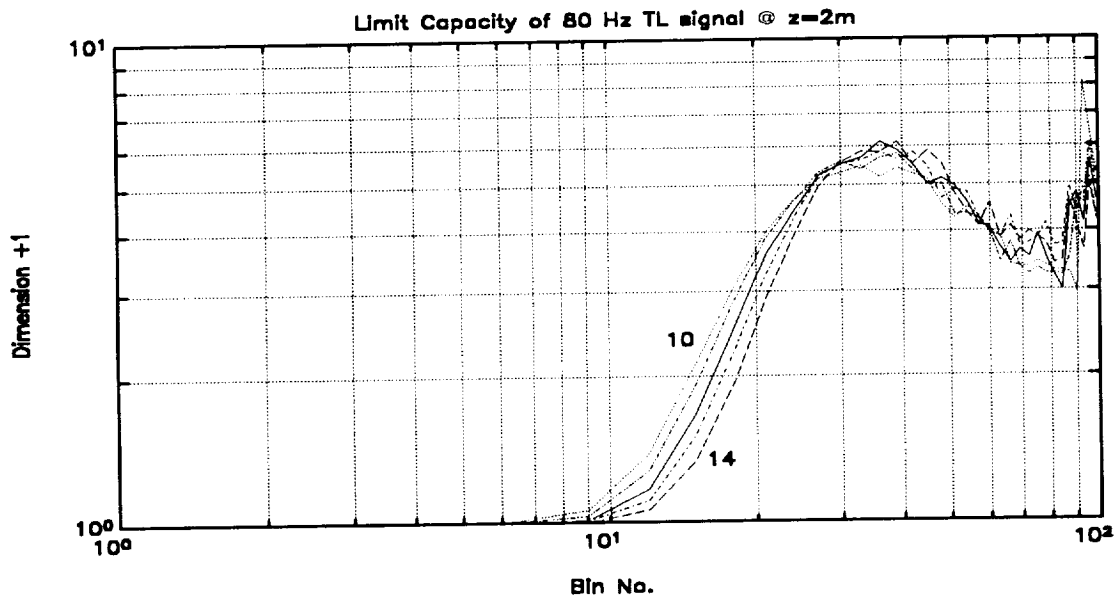


Figure 6: Dimension of 80 Hz tone at 2 meters for various embedding dimensions

Results

Tables I and II, respectively, summarize the calculated limit capacity dimensions for the acoustic signals, the wind speed and the along path component of the wind.

Table I. Limit Capacity Dimension for Acoustic signals

Embedding Dimension	0 m 80 Hz	0 m 500 Hz	2 m 80 Hz	2 m 500 Hz	32 m 80 Hz	32 m 500 Hz
9	4.19	4.69	4.18	4.39	4.42	4.57
10	4.50	4.60	4.31	4.56	4.61	4.82
11	4.34	4.85	4.55	4.64	4.63	4.76
12	4.19	4.87	4.73	4.71	4.81	4.89
13	4.13	4.91	4.68	4.66	4.96	4.95
14	4.44	4.87	4.77	4.53	4.89	4.95

Table II. Limit Capacity Dimension for Wind Speed and Along Path Component Signals

Embedding Dimension	2 m $(U^2+V^2)^{0.5}$	2m $W_{\text{along path}}$	32 m $(U^2+V^2)^{0.5}$	32m $W_{\text{along path}}$
9	3.01	3.47	2.58	2.33
10	3.12	3.43	2.33	2.07
11	3.05	3.4	2.21	*
12	3.07	3.35	*	*
13	2.96	3.03	*	*
14	2.97	2.98	*	*

* higher embedding dimensions were not able to be used due to the limited data set and high lag.

Graphical representation of the change in limit capacity dimension with height is shown in figure 7.

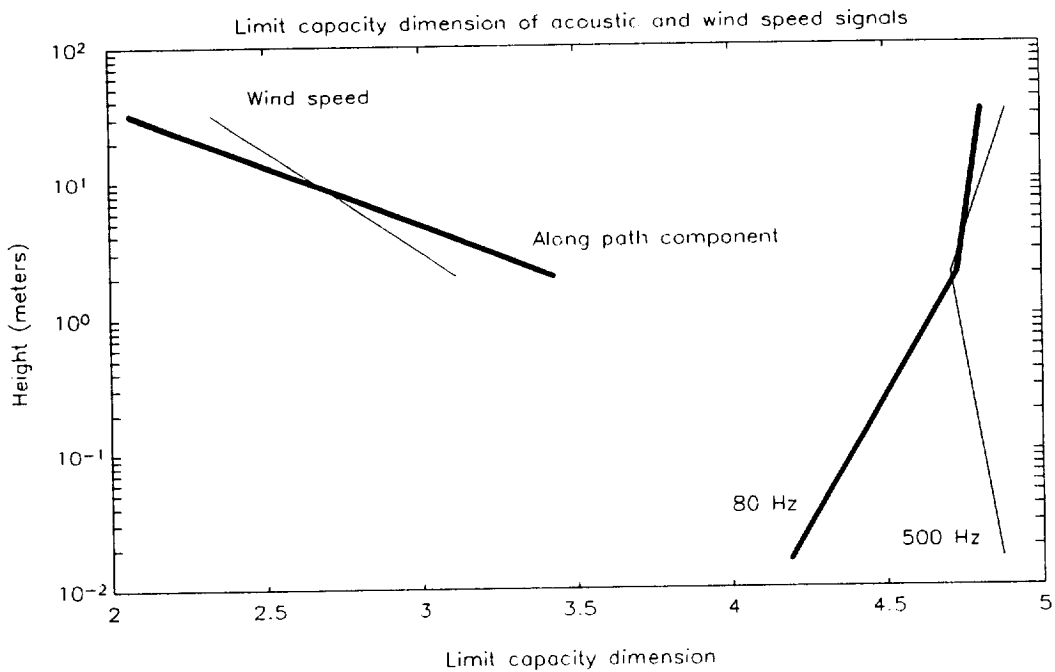


Figure 7. Limit Capacity of acoustic and wind signals

CONCLUSIONS

Low order limit capacity dimensions have been determined to exist for both the acoustic and wind time series. These results confirm the existence of local attractors. The acoustical multivariable dependent signals have higher order attractors than were found for the independent meteorological input variables.

The limit capacity dimension of the acoustic signals appears to increase with height and frequency. We believe that this is due to the role which large eddies (thermals) in the convective boundary layer (CBL) play in controlling intermittent space-time variations in the acoustic refractive index. The properties of propagated sound are sufficiently sensitive to those eddies so that tomographic methods may be used to indirectly measure their properties⁽¹⁰⁾.

We expect that with further dimensional analysis it will be possible to define low order dynamical models that will more precisely define the variability of acoustic signal fluctuations than can be done presently with linear methods. Further studies will require, however, several multihour time series recorded in both stable and unstable boundary layer conditions. The single hour time series recorded during JAPE is of insufficient length. Since large eddies appear to be the dominant signal controlling mechanism, it would also be helpful to have measurements over transmission paths ranging from about 2.5 to 10 km.

REFERENCES

- (1) Lorenz, Edward (1963) Deterministic nonperiodic flow. *J. Atmospheric Sciences* 20, 130 - 141.
- (2) Nicolis, C., and Nicolis G.(1980) Is there a climate attractor? , *Nature* (London) 311, 529-532.
- (3) Proceedings of the 1st Experimental Chaos Conference (1992), World Scientific.
- (4) Henderson, H., and Wells,R. (1988) Obtaining attractor dimensions from meteorological time series. *Advances in Geophysics* 30, 205 - 237.
- (5) Shirer, H. Nelson, The Pennsylvania State University Professor of Meteorology, personal communication.
- (6) Abarbanel, H.D.I., et. al. (Expected Oct 1993) The Analysis of Observed Chaotic Data in Physical Systems., *Physical Review*.
- (7) Thomson, D.W. and Henderson, H.W. (1992) Definitions of local atmospheric attractors using measurements made with surface-based remote sensing systems. *Proceedings of the 1st Experimental Chaos Conference*, Springer-Verlaag.
- (8) Rashed, S.N. (1990) *Chaotic dynamics of nonlinear systems*. Wiley-Interscience Press, New York.
- (9) Wells, R., et al. (1993) Improved Algorithms for Estimating the Correlation Dimension and the Associated Probable Errors. Report AM 114, Pennsylvania State University Department of Mathematics.
- (10) Wilson, D.K. (1992) Acoustic Tomographic Monitoring of the Atmospheric Boundary Layer. Ph.D. Dissertation in Acoustics, The Pennsylvania State University, University Park, Pennsylvania.

N 9 4 - 2 4 2 1 8

COMPARISON BETWEEN 1-MINUTE AND 15-MINUTE AVERAGES
OF TURBULENCE PARAMETERS

S 11-71

John M. Noble
U.S. Army Research Laboratory
Battlefield Environment Directorate
White Sands Missile Range, New Mexico 88002

26/6/83

P 10

ABSTRACT

Sonic anemometers are good instruments for measuring temperature and wind speed fast enough to calculate the temperature and wind structure parameters used to calculate the variance in the acoustic index of refraction. However, the turbulence parameters are typically 15-minute averaged point measurements. There are several problems associated with making point measurements and using them to represent a turbulence field. This paper will examine some of the sonic anemometer data analyzed from the Joint Acoustic Propagation Experiment (JAPE) conducted during July 1991 at DIRT Site located at White Sands Missile Range, New Mexico.

INTRODUCTION

A sonic anemometer is an instrument used to measure the u, v, and w components of the wind field and temperature with time. A sonic anemometer consists of a pair of acoustic transmitters and receivers, spaced from 10 to 25 cm apart, that send and receive acoustic pulses at the rate of several hundred times per second. The pulses are averaged to give a data rate of 10 Hz. Sonics provide the wind component and temperature data required for computing fluxes of heat, momentum, and moisture which define the state of the surface layer by the eddy correlation method.

Sonics operate on the principle that the travel time between transmitter and receiver is a function of the speed of sound plus the component of the wind speed in the direction of propagation. A sample is composed of two pulses: one pulse traveling in one direction and another pulse traveling in the opposite direction. If the two measured speed of sound

samples are subtracted, the difference will be twice the component of the wind speed along the axis of the transmitter-receiver since the temperature is independent of the direction of propagation. Two pairs of transmitter-receivers will provide the horizontal wind field and three pairs will provide the three-dimensional wind field. The sum of the two measurements will be proportional to the temperature since the wind speed component will be subtracted out. Figures 1 and 2 show an example of the output from a sonic anemometer.

There were five sonic anemometers used in this analysis located on a 100 ft walk-up tower at intervals of 2, 4, 8, 16, and 32 meters. They were located approximately 2 meters from the tower along an East-West axis. The graphs of the data use a notation of Sonic 1, 2, 3, 4, and 5 which corresponds to the heights given previously. As a check to see if the wind was blowing through the tower, a band of arrows is placed on the graph showing wind speed and direction. The band of arrows indicates the solid angle of the tower as "seen" by the sonic anemometers. All times shown, unless otherwise stated, are Greenwich Mean Time.

CALCULATING TURBULENCE PARAMETERS

From turbulence theory, the structure parameter C_x^2 in a locally isotropic field is defined by¹

$$C_x^2 = \frac{\langle [\chi(\vec{r}_1) - \chi(\vec{r}_2)]^2 \rangle}{|\vec{r}|^{2/3}} \quad (1)$$

where $|\vec{r}|$ is the spatial separation distance, $\chi(\vec{r})$ is the measured quantity at each point, and the angle brackets indicate performing an ensemble average. A sonic anemometer makes a measurement at a single point instead of at two points separated by a distance r . The above equation can be rewritten into a form usable for a single point sensor. Taylor's frozen turbulence hypothesis² states that the spatial separation of the turbulence can be calculated from the temporal separation (Δt) times the mean wind speed. This allows Eq. (1) to be written as

$$\overline{C_x^2} = \frac{[\chi(t_1) - \chi(t_2)]^2}{(u \Delta t)^{2/3}} \quad (2)$$

where $\chi(t)$ is the fluctuating quantity sampled at two instances with a temporal separation Δt , the overbar indicates a time average, and u is the mean wind speed. This equation allows

for the temperature and wind structure parameters to be calculated from the sonic anemometer data.

EXAMINATION OF RESULTS

The best place to begin is looking at a set of good turbulence data. Figure 3 shows a comparison between 1-minute and 15-minute averages of the wind structure parameter with time. The dashed line is the wind speed with time. The 1-minute averages show some variability about the 15-minute averages in the wind structure parameter. Forty minutes into the comparison, there is an increase in the wind structure parameter which translates into an increase in the mechanical turbulence. Figure 4 shows the wind speed and direction with time for the same time interval. The wind is not blowing through the tower, so the increase is not due to biasing from the tower and this trend is seen in each of the sensors along the height of the tower. In this case, the 15-minute averages track the trends quite well.

The next case appears to be very similar to the previous case. Figure 5 shows a comparison between 1-minute and 15-minute averages of the temperature structure parameter at 2 meters. The dashed line in this case is the temperature with time. As in Figure 3, the 15-minute averages track well with the 1-minute averages. In the previous case, the increase in the wind structure parameter appeared in each of the sensors; however, this does not hold true for this case. Figure 6 shows the comparison between 1-minute and 15 minute averages of the temperature structure parameter for the sensor located at 4 meters. In fact, the trend does not appear in any of the other sensors. This means that the 2 meter sensor was measuring a very localized phenomenon such as a person standing nearby or the heat from another instrument. Whatever the disturbance was, it persisted for an hour. This shows that one cannot just use the results from one sensor without examining the other sensors to determine whether or not the sensor being used is giving an adequate representation of the turbulence field.

Sometimes there is a more obvious source for the trend in the turbulence data. Figure 7 shows the comparison between the 1-minute and 15-minute averages of the temperature structure parameter at 2 meters. The trend is similar to the trend observed in Fig. 5. However, the source of this trend is the turbulent wakes of the tower. Figure 8 shows the wind speed and direction with time at the sensor. About 40 minutes into the measurement, the wind direction changes such that the tower is upwind from the sensor. When this occurs, the tower interferes with the normal turbulence field by modifying the

turbulence field. Therefore, the turbulence data cannot be used during the time the wind flow is coming through the tower.

The last case is a problem which occurs with any point measurement. Figure 9 shows the comparison between the 1-minute and 15-minute averages of the temperature structure parameter at 2 meters. This figure shows a large degree of variability between the 1-minute averages and the 15-minute averages. Looking at Fig. 10, the wind speed for most of the time is below 1 m/s. A wind speed this low causes problems in using the point measurements to represent the turbulence field. The turbulence field in this low of a wind speed becomes very localized. When the wind speed is this low, the turbulence measurement at one point will probably not correspond to a turbulence measurement at another point for the same height since the turbulence field is mainly influenced by the local obstacles.

CONCLUSIONS

Sonic anemometers are very good for measuring wind speed, wind direction, temperature, heat flux, momentum flux, temperature structure parameter, and wind structure parameter at a fairly fast rate of 10 Hz. However, care must be used in examining the analyzed data from the sensors. Wind blowing through the tower before reaching the sensor will modify the turbulence field giving poor data for calculating the turbulence parameters. This can go for personnel or animals walking by the sensor. A low wind speed of less than 1 m/s causes the turbulence field to be strongly affected by the local terrain giving poor homogeneity to the turbulence field. Therefore, Taylor's frozen turbulence hypothesis can breakdown.

ACKNOWLEDGEMENTS

I would like to thank my student short form, Barbara Malloy, for the amount of work which went into analyzing the hours of sonic anemometer data and producing the numerous graphs illustrating the effects mentioned in this paper. I would also like to acknowledge Prasan Chintawongvanich of the Physical Science Laboratory at New Mexico State University for writing the computer software used to analyze the data.

REFERENCES

1. G.A. Daigle, J.E. Piercy, and T.F.W. Embleton, "Effects of Atmospheric Turbulence on the Interface of Sound Waves Near a Hard Boundary," *J. Acoust. Soc. Am.* **64**, 622-630 (1978).
2. V.I. Tatarski, *The Effects of Turbulent Atmosphere on Wave Propagation*, translated and published by Israel Programs for Scientific Translations Ltd., Jerusalem, (1971).

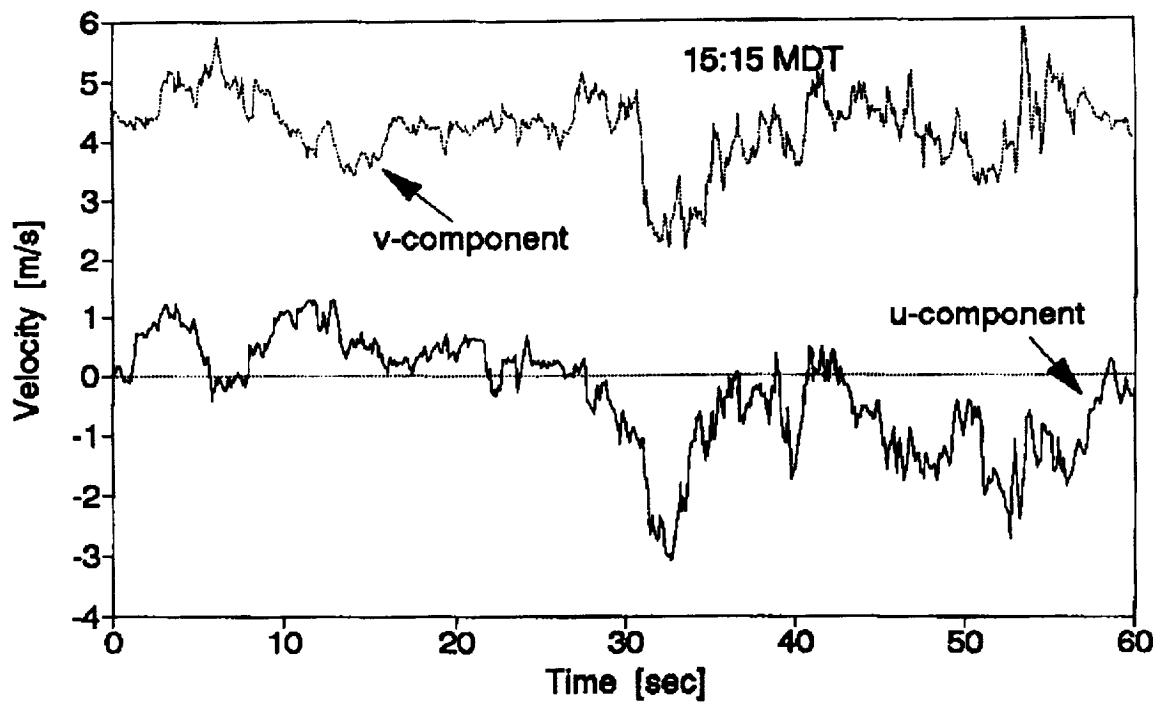


Figure 1. Sonic u and v wind components at 16 meters from August 28, 1991 at DIRT Site located at White Sands Missile Range, New Mexico.

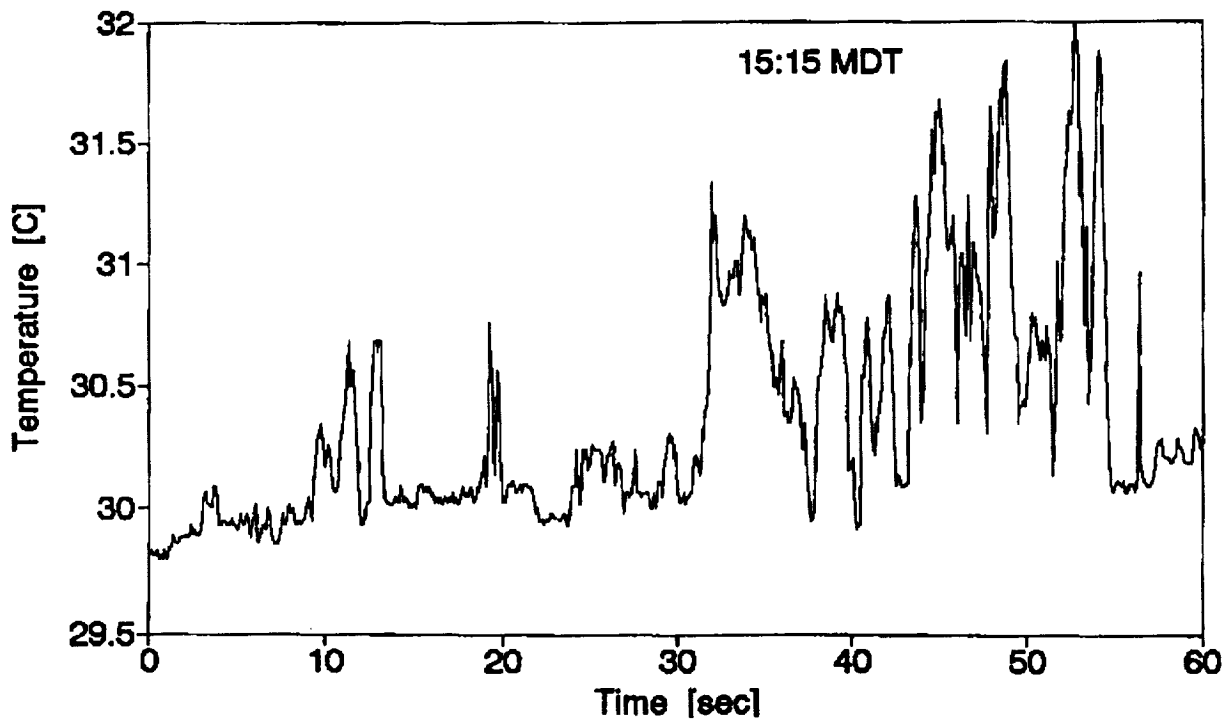


Figure 2. Sonic temperature at 16 meters from August 28, 1991 at DIRT Site located at White Sands Missile Range, New Mexico.

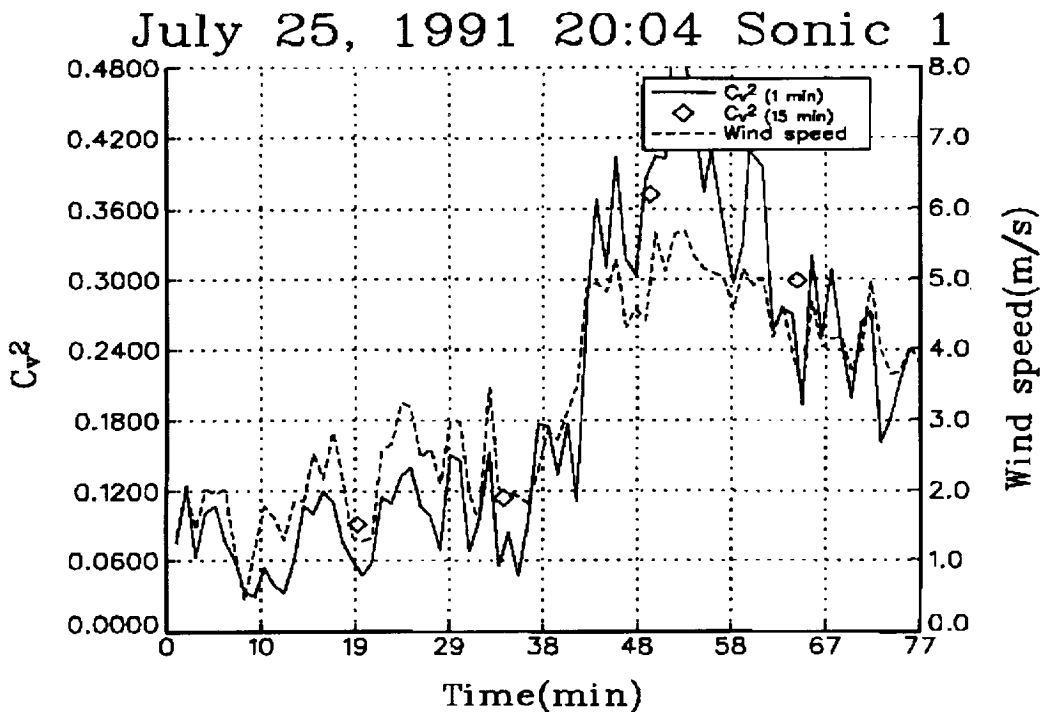


Figure 3. Plot of the 1-minute and 15-minute wind structure parameters along with 1-minute averaged wind speed with time at 2 meters.

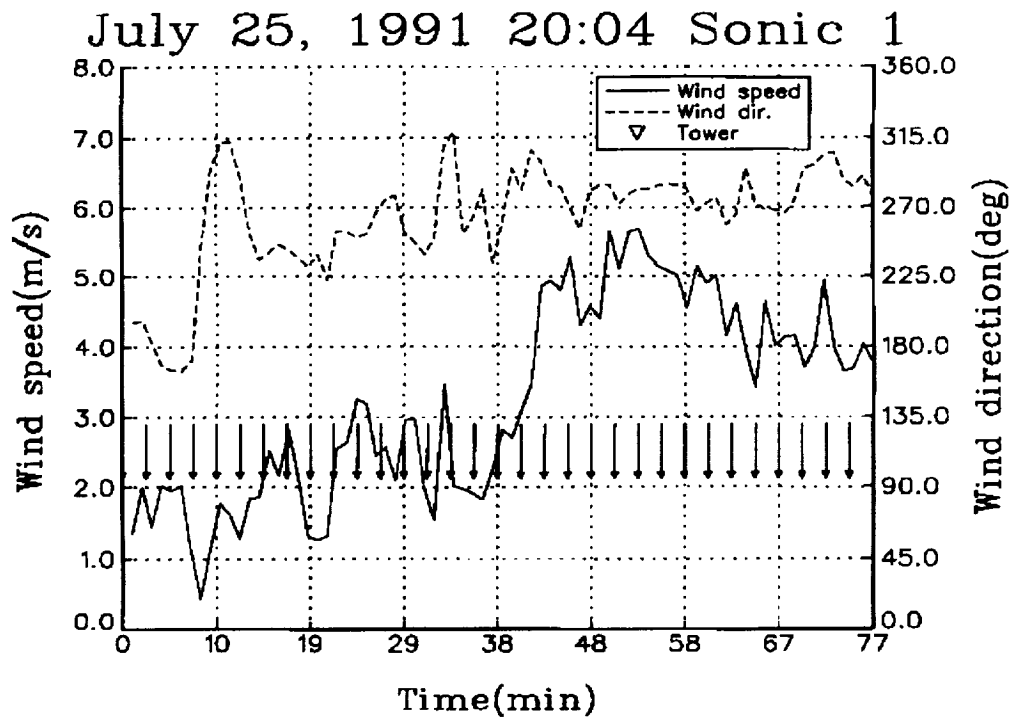


Figure 4. One-minute averaged wind speed and direction with time at 2 meters. Arrows indicate direction of tower from sonic anemometer.

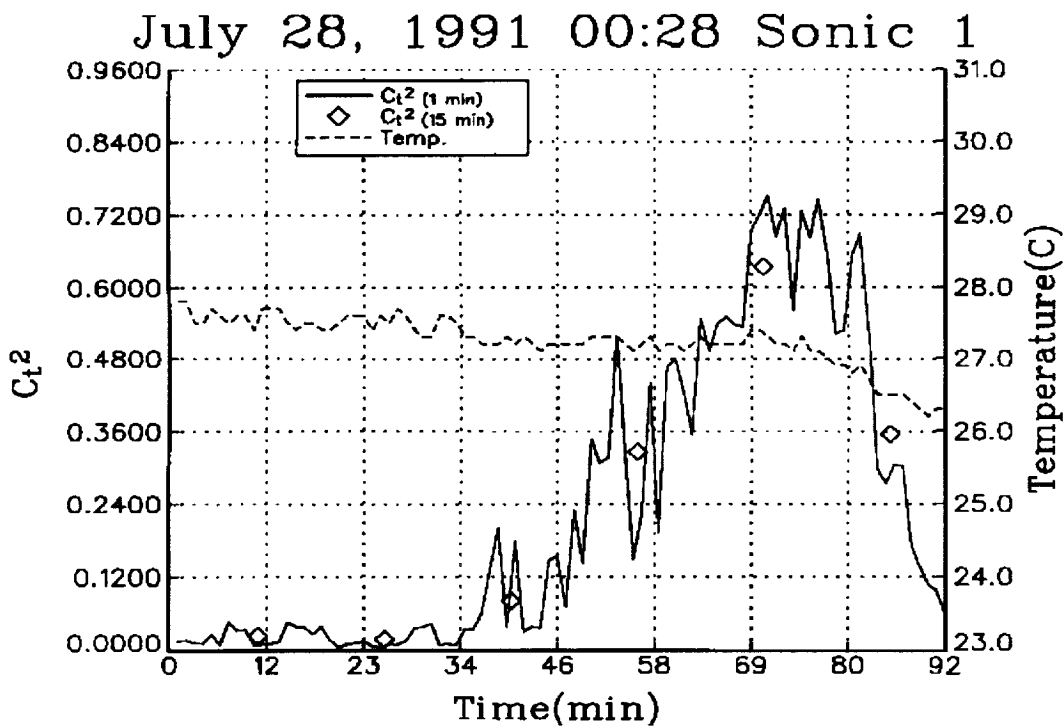


Figure 5. Plot of 1-minute and 15-minute averages of the temperature structure parameter and 1-minute averaged temperature with time at 2 meters.

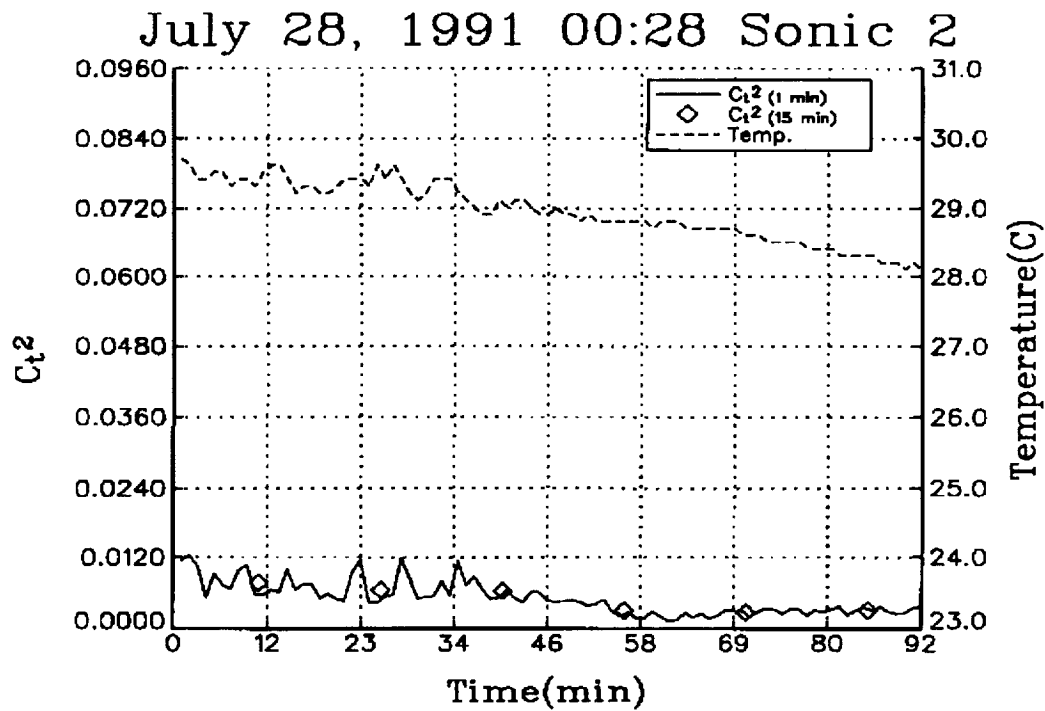


Figure 6. Plot of 1-minute and 15-minute averages of the temperature structure parameter and 1-minute averaged temperature with time at 4 meters.

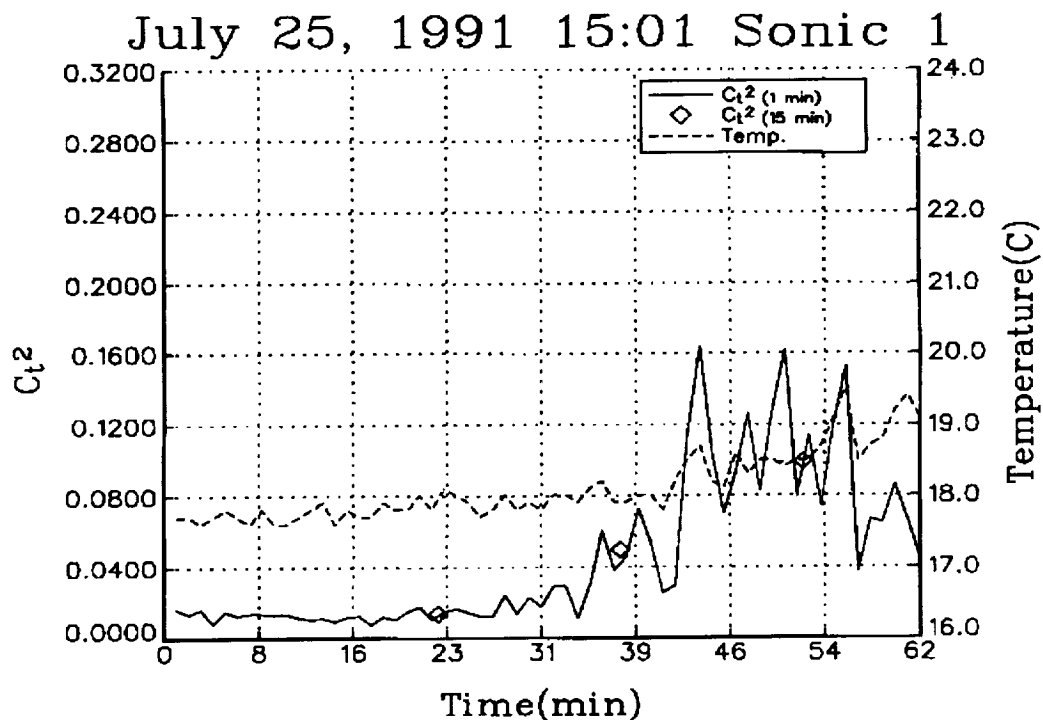


Figure 7. Plot of 1-minute and 15-minute averages of the temperature structure parameter and 1-minute averaged temperature with time at 2 meters.

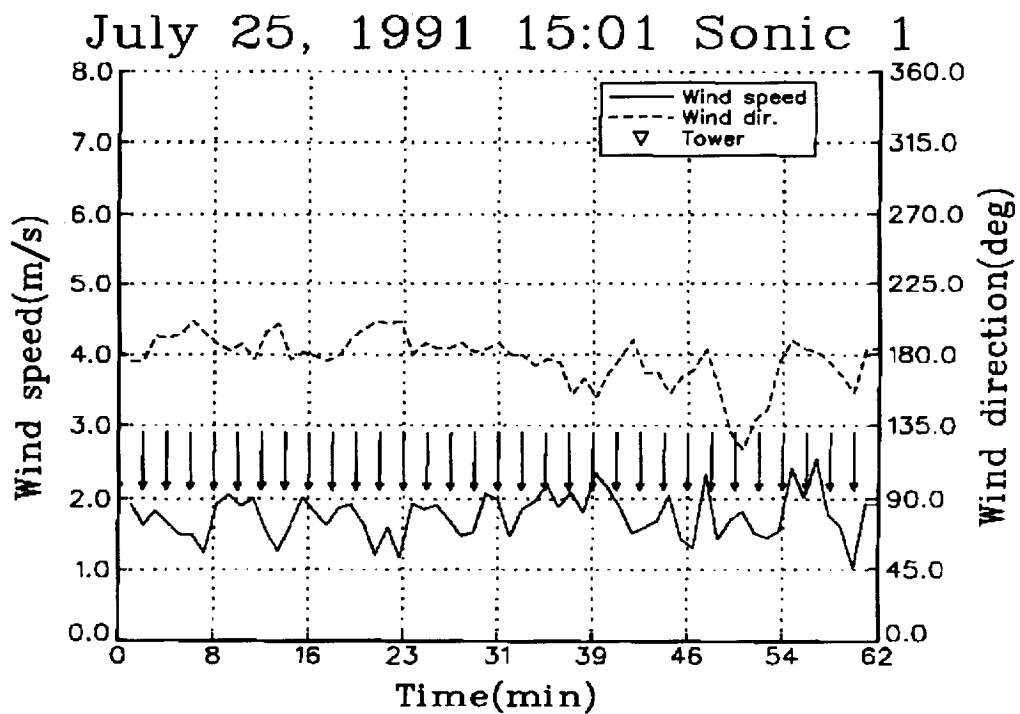


Figure 8. Plot of 1-minute averaged wind speed and direction with time at 2 meters. The arrows indicate the direction of the tower from the sonic anemometer.

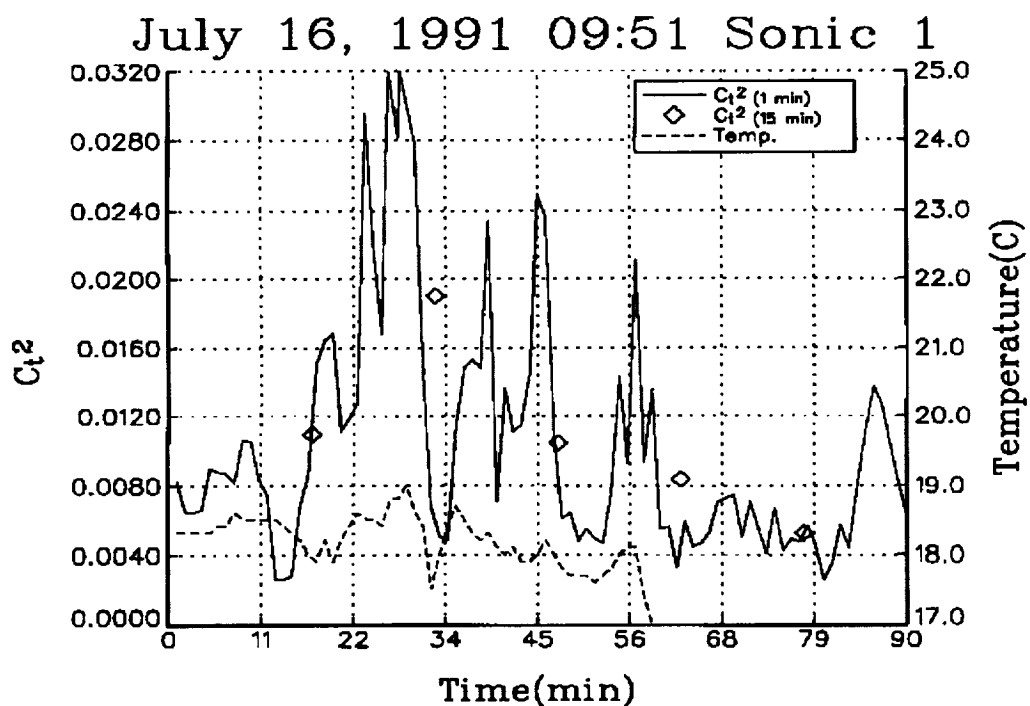


Figure 9. Plot of 1-minute and 15-minute averages of the temperature structure parameter and 1-minute averaged temperature with time at 2 meters.

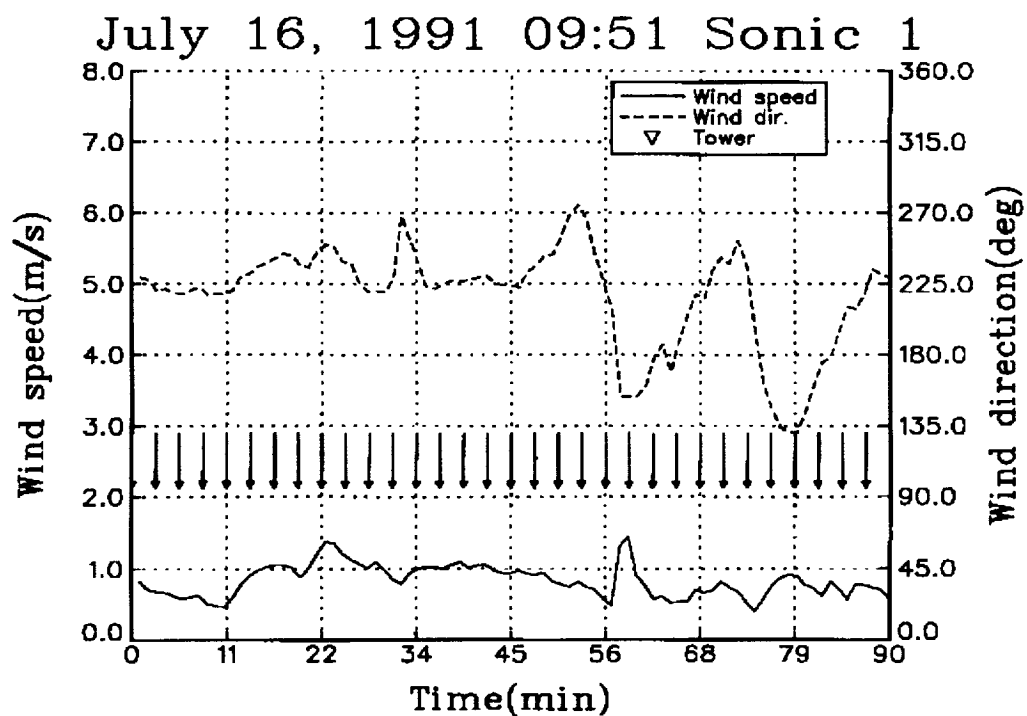


Figure 10. Plot of 1-minute averaged wind speed and direction with time at 2 meters. The arrows indicate the direction of the tower from the sonic anemometer.

N 94 - 24219

BEAMFORMING IN AN ACOUSTIC SHADOW

512-71
David Havelock

Michael Stinson

Gilles Daigle

N.R.C., Canada

10-24-7

201084

P-1

Abstract

The sound field deep within an acoustic shadow region is less well understood than that outside the shadow region. Signal levels are substantially lower within the shadow, but beamforming difficulties arise for other reasons such as loss of spatial coherence. Based on analysis of JAPE-91 data, and other data, three types of characteristic signals within acoustic shadow regions are identified. These signal types may correspond to different, intermittent signal propagation conditions. Detection and classification algorithms might take advantage of the signal characteristics. Frequency coherence is also discussed. The extent of coherence across frequencies is shown to be limited, causing difficulties for source classification based on harmonic amplitude relationships. Discussions emphasize short-term characteristics on the order of one second. A video presentation on frequency coherence shows the similarity, in the presence of atmospheric turbulence, between the received signal from a stable set of harmonics generated by a loudspeaker and that received from a helicopter hovering behind a hill.



N 94 - 24220

**ANALYSIS OF PASSIVE ACOUSTIC RANGING OF HELICOPTERS
FROM THE JOINT ACOUSTIC PROPAGATION EXPERIMENT**

Benny L. Carnes
John C. Morgan

U.S. Army Engineer Waterways Experiment Station
Vicksburg, Mississippi

PREFACE

The study reported herein was conducted by the U.S. Army Engineer Waterways Experiment Station (WES), Vicksburg, Mississippi, during fiscal year 1993. It was funded by WES under the Laboratory Discretionary Research Program.

This study was conducted under the general supervision of Mr. Bryant Mather, Director of the Structures Laboratory (SL), WES, and Mr. L. K. Davis, Chief of the Explosion Effects Division (EED), SL, and under the direct supervision of Dr. Benny L. Carnes, Acoustic/Seismic Research Team Leader and Project Coordinator, SL.

This report was prepared by Dr. Carnes and Mr. John C. Morgan, assigned to WES from the Illinois Institute of Technology Research Institute, Dayton, OH, office. Field data acquisition was conducted by Messrs. Larsen and Leo Koestler of the WES Instrumentation Services Division. Data analysis and preparation were performed by Messrs. Morgan and Travis Harrell, assigned to WES from the Atlantic Research Corporation. A significant contribution was made in the theoretical physics by Mr. John S. Furey, assigned to WES from the Atlantic Research Corporation.

At the time of publication of this report, Director of WES was Dr. Robert W. Whalin. The Commander was COL. Leonard G. Hassell, EN.

Contents

Preface

1 ----- Introduction

**Background
Objective**

2 ----- Analysis of Passive Acoustic Ranging (PAR)

Inherent Errors

Processing Methods

Cross Spectral Density

Successive Differences

Comparison of Methods

Refinement of PAR through Artificial Neural Networks

Back Propagation Training of an ANN

ANN Training, Testing, and Development

3 ----- Discussion and Conclusions

4 ----- Recommendations

Appendix A Simulated Sources

List of Figures

Title	
Figure 1.	Diagram of Source Approaching a Microphone
Figure 2.	Plot of Frequency vs Time of a Source
Figure 3.	Discrete Plot of Frequency Values
Figure 4.	Plot of Range Error as a Function of Time Step
Figure 5.	Histogram of Frequency through Approach and Departure
Figure 6.	Selected PSD Plots for 30 Second Extractions of Time Trace about CPA
Figure 7.	Selected PSD Plots for 15 Second Extractions of Time Traces about CPA
Figure 8.	Selected PSD Plots for 15 Second Extractions of Time Traces about CPA
Figure 9.	Selected PSD Plots for 15 Second Extractions of Time Traces about CPA
Figure 10.	PSD from Case C used as Sample Number One
Figure 11.	PSD from Case B used as Sample Number Two
Figure 12.	PSD from Case I used as Sample Number Three
Figure 13.	PSD from Case B used as Sample Number Four
Figure 14.	PSD from Case H used as Sample Number Five
Figure 15.	PSD from Case B used in Sample Number Six
Figure 16.	PSD from Case H used in Sample Number Seven
Figure 17.	PSD from Case B used in Sample Number Eight
Figure 18.	PSD From Case C used in Sample Number Nine
Figure 19.	PSD From Case C used in Sample Number Ten
Figure 20.	PSD From Case B used in Sample Number Eleven
Figure 21.	PSD From Case H used in Sample Number Twelve
Figure 22.	PSD From Case H used in Sample Number Thirteen
Figure 23.	PSD From Case G used in Sample Number Fourteen
Figure 24.	PSD From Case F used in Sample Number Fifteen
Figure 25.	PSD From Case G used in Sample Number Sixteen
Figure 26.	PSD From Case I used in Sample Number Seventeen
Figure 27.	PSD From Case H in Sample Number Eighteen
Figure A.1.	Sample of Input Screen from Moving Source Simulation Program

List of Tables

Title

Table 1. Simulated Helicopter Acoustic Data

Table 2. Results of CSD Analysis on Multiple Cases of Simulated Single Source Signals

Table 3. Experimental Helicopter Acoustic Data

Table 4. Results of CSD Analysis on Multiple Cases of Experimental Single Source Signals

Table 5. Results of SD Analysis on Multiple Cases of Simulated Single Source Signals

Table 6. Results of SD Analysis on Multiple Cases of Experimental Single Source Signals

Table 7. Index of Cases Used in First ANN Training

Table 8. Results of ANN Classification of First Training Case

Table 9. Index of Cases Used in Second ANN Training

Table 10. Results of ANN Classification of Second Training Case

INTRODUCTION

For more than twenty years, personnel of the U.S.A.E. Waterways Experiment Station (WES) have been performing research dealing with the application of sensors for detection of military targets. The WES research has included the use of seismic, acoustic, magnetic, and other sensors to detect, track, and classify military ground targets. Most of the WES research has been oriented toward the employment of such sensors in a passive mode. Techniques for passive detection are of particular interest in the Army because of the advantages over active detection. Passive detection methods are not susceptible to interception, detection, jamming, or location of the source by the threat. A decided advantage for using acoustic and seismic sensors for detection in tactical situations is the non-line-of-sight capability; i.e., detection of low flying helicopters at long distances without visual contact. This study was conducted to analyze the passive acoustic ranging (PAR) concept (previously developed at WES¹) using a more extensive data set from the Joint Acoustic Propagation Experiment (JAPE).

Background

The PAR concept exploits the repetitive nature of helicopter acoustic signatures to compute the range and velocity of a passing helicopter. The PAR method analyzes the change of the frequency of the signatures through time, known as the Doppler shift, and calculates these parameters using the Doppler shift equations on the signals as the helicopter passes through the closest point of approach (CPA). In the previously mentioned research, the basic equations governing the extraction of range and velocity for the PAR concept were presented. The PAR concept was used on one set of data for one helicopter at one site, and it produced promising results.

Objective

The objective of this research was to investigate constraints on the PAR concept to estimate the limitations of realistic operation under various environmental conditions, and to determine if the PAR concept will apply to multiple helicopters.

ANALYSIS OF PASSIVE ACOUSTIC RANGING (PAR)

In the previous WES investigation the equations governing the behavior of the Doppler shift as a function of velocity and range were presented. The scenario of a helicopter passing an acoustic sensor is shown in Figure 1. The time that the signal is received at the sensor, t_r , is equal to the time that it is emitted, t_e , plus the time of travel. If the emitting source travels with constant velocity, v , through CPA (see figure 1) then t_e , expressed as a function of t_r , is

$$t_e - t_{cpa} = \frac{t_r - t_{cpa} - \sqrt{\beta^2(t_r - t_{cpa})^2 + (1 - \beta^2)\rho^2}}{1 - \beta^2} \quad (1)$$

where β is the velocity of the source divided by the speed of propagation of the signal in the media and ρ is the CPA distance divided by the speed of propagation.

The general Doppler shift formula is

$$f_r = f_e \frac{dt_e}{dt_r} \quad (2)$$

which for the case under consideration, expressed in relevant kinematic parameters, is

$$\frac{dt_e}{dt_r} = \frac{(1 - \beta \sigma)}{(1 - \beta^2)}$$

where

$$\sigma = \frac{\beta(t_r - t_{cpa})}{\sqrt{\beta^2(t_r - t_{cpa})^2 + (1 - \beta^2)\rho^2}} \quad (3)$$

The Doppler shift is shown in figure 2 for various values of these parameters.

Inherent Errors

The basic method for the extraction of kinematic information from these time traces was to transform the time trace into the frequency domain. The sources had stable characteristic frequencies, which facilitated the extraction of the incoming and outgoing frequencies from these data. The velocity and fundamental frequency of the source were then computed, and frequency information as a function of time was obtained from transforms of selected windows of the time trace. As done in the previous study, these data were then used to determine the range by fitting

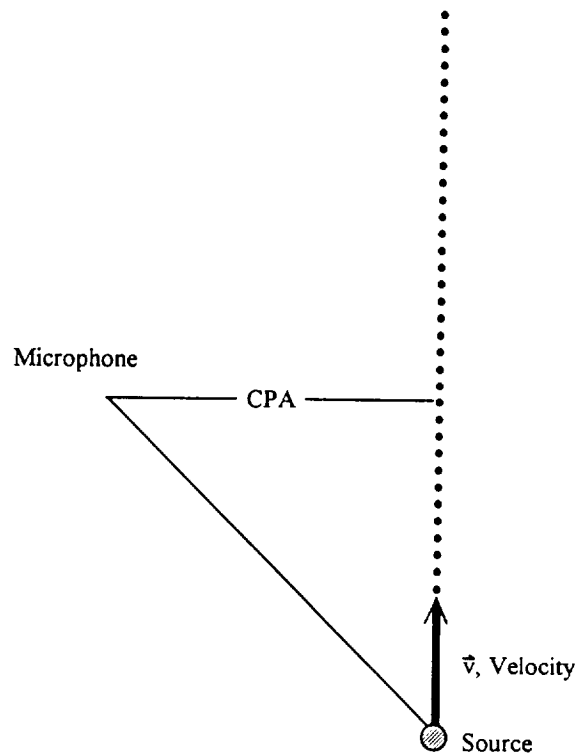


Figure 1. Diagram of source approaching a microphone.

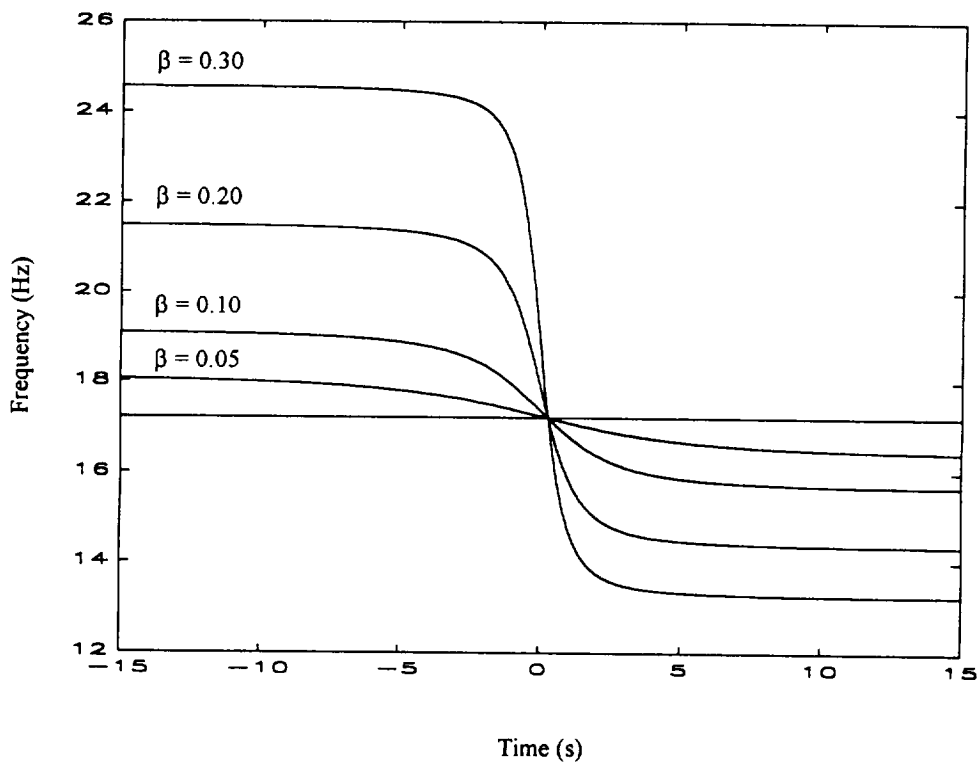


Figure 2. Plot of frequency vs time of a source with fundamental frequency of 17.2 Hz at a range of 100 m for beta=0.05,0.1,0.2, and 0.3.

the slope of the frequency versus time curve at CPA to the following:

$$\frac{df_e}{dt} = \frac{-\beta f_e}{\rho} \quad (4)$$

The key to this operation is the transformation from the time to the frequency domain because of the spreading of the data points through the Doppler shift. Since the slope of the curve is largest at CPA, the spacing of the individual points is sparsest in that region (as can be seen in figure 3). The accuracy of the slope calculation is dependent on the size of the time step of each window.

The usual approach used to produce a data set with frequency as a function of time from a time trace is to extract sections of the time trace and perform a fast Fourier transform (FFT) on each of these sections. The problem with the FFT method is that as the length, Δt , of the sections gets smaller, the resolution, Δf , of the frequency grows larger, since

$$\Delta f = 1 / \Delta t \quad (5)$$

In addition, there is an error that is inherent to the range calculation associated with the time step. Figure 4 contains graphs of range error as a function of time step for several values of velocity and range. It can be seen from these graphs that there are cases where this error is at a minimum when the time step is the smallest value. Large changes in the other kinematic parameters affect the error to a lesser extent. Several methods were tested in an attempt to overcome this basic problem.

Processing Methods

The two most successful processing methods were the cross spectral density (CSD) method and the method of successive differences (SD).

Cross Spectral Density

The CSD method which was initially proposed for this purpose in the previous study utilizes a phase analysis of the FFT of the signal to calculate the frequency of the signal. The FFT's of successive intervals are compared by conjugation and multiplication. For a pure frequency this method can give accurate results, but because of the nature of the FFT calculation,

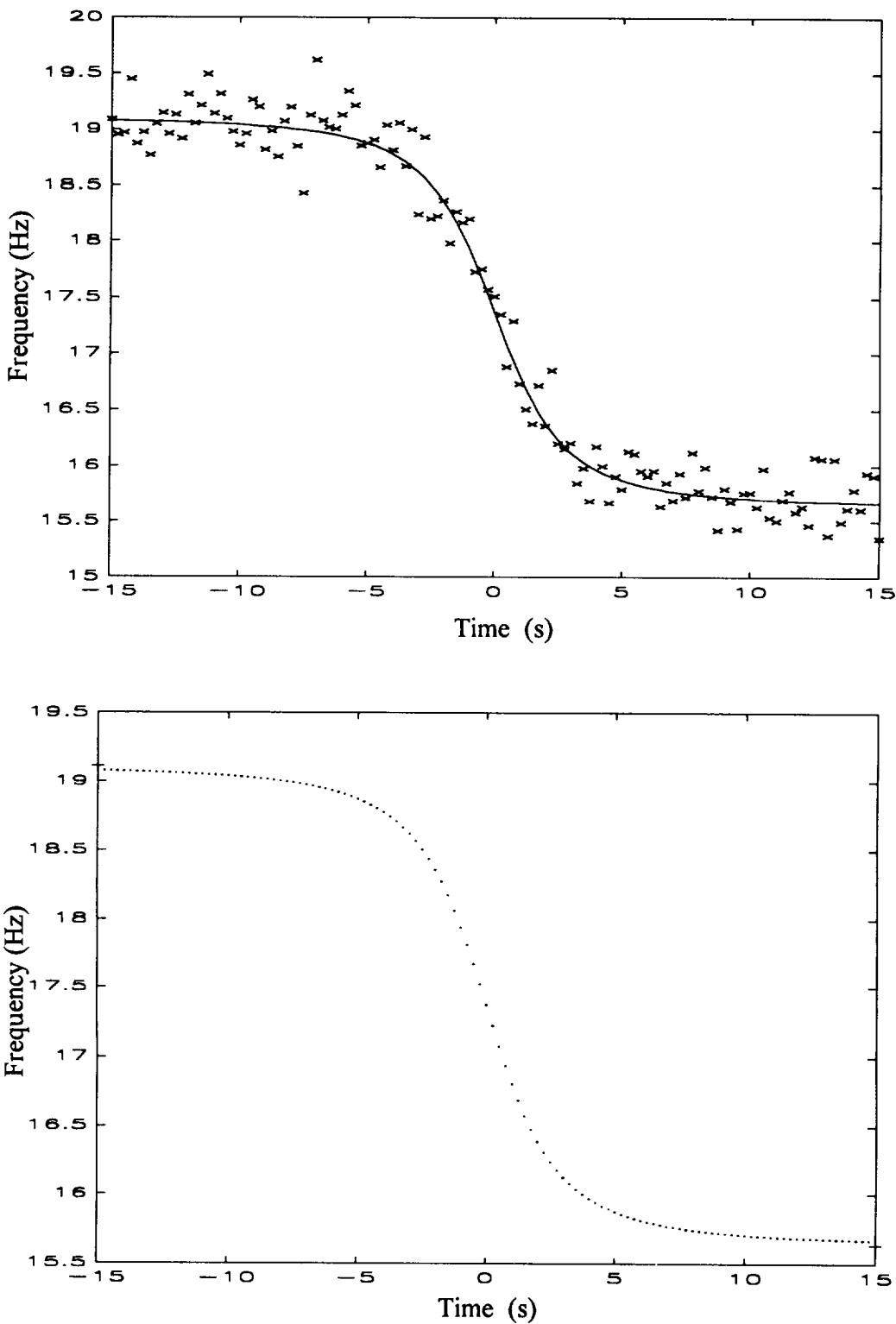


Figure 3. Discrete plot of frequency values for a time step of 0.25 sec with CPA at $t=0$ seconds.
 Note the spacing of the points near CPA. Top shows real data and fit, and the bottom shows an example of the ideal case.

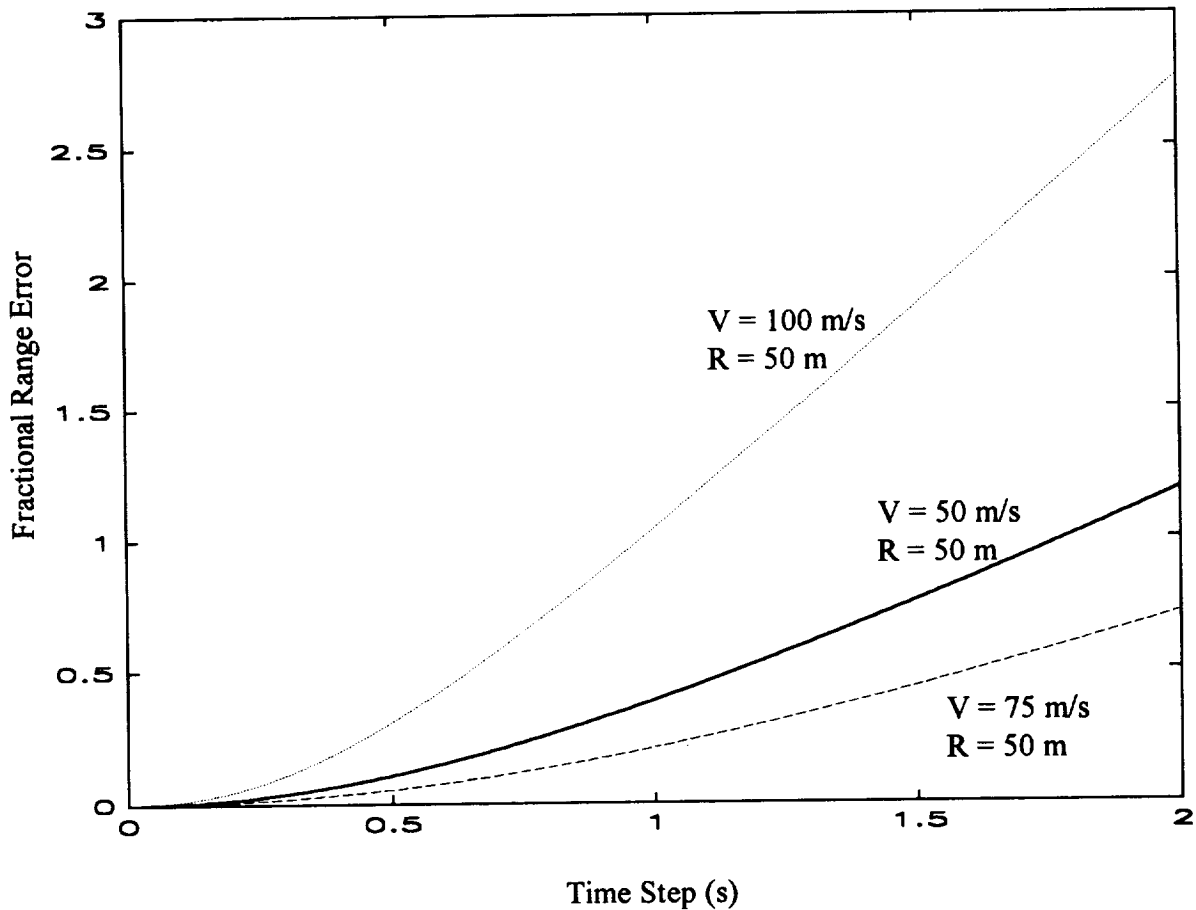


Figure 4. Fractional range error vs time step for various values of V and R .

peaks which are spaced nearby in frequency will overlap and interfere in the phase domain. It should be possible to obtain equations which will perform the CSD analysis for peaks containing multiple components, but it is necessary to know beforehand how many components are present. This may not be possible in a field application where any number of sources may pass the sensor.

The CSD method was tested on the simulated cases found in table 1. Error values (which can be found in table 2) were within expected limits of the values that were predicted in the graphs in figure 4. Further tests were performed using experimental data, and sources of this data are listed in table 3. The true values of position as a function of time were used to calculate velocity (actual values were obtained from radar telemetry). The predictions made by the CSD method and error values from these calculations can be found in table 4. Note that the error found in these tables is somewhat larger than predicted in figure 4. This is caused by the addition of background noise into the peaks that were used to calculate the accurate frequency.

The CSD allowed an accurate determination of the frequency from a small portion of the spectrum, but the deconvolution of multiple signals using this method had some limitations. The presence of multiple signals in a single peak is not accounted for in the derivation of this method. The condition of peaks that are overlapping or not fully resolved cause the phase information for a particular peak to be corrupted, thus severely complicating the deconvolution of the peak.

Successive Differences

Another way of extracting the frequency and velocity is to first perform an FFT on the entire sample of data (all the way through the approach and departure of the source). The results of the FFTs are shown in figures 5-9. The maxima on the ends of the u-shaped features in these figures are the frequency values of the source at the incoming and outgoing frequencies. It is possible to derive an analytic expression for the u-shaped features in the ideal case.

The problem of extracting frequency as a function of time was addressed using the method of successive differences. The frequency resolution limit from equation 5 was overcome by computing the FFT of two intervals with sufficient length to produce the desired resolution. The successive intervals for each FFT had starting points separated by the desired time step. The differences between these two spectra were computed, and the remaining positive portion of the difference contains the peak values of the frequencies that were added into the signal during that time interval.

Table 1. Simulated helicopter acoustic data.

<u>Name of Run</u>	<u>Fundamental Frequency (Hz)</u>	<u>Length of Run (Sec)</u>	<u>CPA (m)</u>	<u>Speed (m/s)</u>
Hela.dat	16	32	10	50
Helb.dat	16	32	50	50
Helc.dat	16	32	200	50
Held.dat	16	32	500	50
Hele.dat	16	32	10	100
Helf.dat	16	32	50	100
Helg.dat	16	32	200	100
Helh.dat	16	32	500	100
Heli.dat	16	32	10	250
Helj.dat	16	32	50	250
Helk.dat	16	32	200	250
Hell.dat	16	32	500	250

Table 2. Results of CSD analysis on multiple simulated single source signals.

Actual Fundamental Frequency	Calculated Fundamental Frequency			Actual CPA	Calculated CPA			Actual Speed	Calculated Speed		
	(Hz)	(Hz)	% Error		(m)	(m)	% Error		(m/s)	(m/s)	% Error
16	16.002	0.0125	10	19.87	98.7	50	49.99	0.02			
16	16.004	0.025	50	60.57	21.1	50	49.91	0.18			
16	16.017	0.10625	200	219.66	9.83	50	48.51	2.98			
16	16.047	0.29375	500	399.52	20.1	50	41.87	16.26			
16	15.998	0.0125	10	36.20	262	100	99.94	0.06			
16	16.000	0	50	77.16	54.3	100	99.92	0.08			
16	16.020	0.125	200	278.81	39.4	100	99.23	0.77			
16	16.094	0.5875	500	634.80	26.9	100	95.09	4.91			
16	16.003	0.01875	10	108.34	983.4	250	249.99	0.01			
16	16.013	0.08125	50	124.01	149.0	250	249.93	0.03			
16	16.001	0.00625	200	768.65	284.3	250	249.92	0.03			
16	16.003	0.01875	500	108.34	78.3	250	249.09	0.36			
100	100	0	10	0	100	50	49.99	0.02			
100	100.008	0.008	50	59.41	18.82	50	49.9	0.20			
100	100.101	0.101	200	219.79	9.895	50	48.4	3.20			
100	100.289	0.289	500	401.97	19.606	50	41.97	16.1			
100	100.002	0.002	10	34.32	243.2	100	99.99	0.01			
100	100.007	0.007	50	81.75	63.5	100	99.96	0.04			
100	100.125	0.125	200	275.08	37.54	100	99.23	0.77			
100	100.566	0.566	500	649.11	29.822	100	95.54	4.463			

Table 3. Experimental helicopter acoustic data.
From the JAPE, run indicates JAPE run number in WES database.

Case	Run
Case A	WSR147a
Case B	WSR148a
Case C	WSR149a
Case D	WSR150a
Case E	WSR151a
Case F	WSR152a
Case G	WSR156a
Case H	WSR157a

Table 4. Results of CSD analysis on experimental data.

Case	Radar Velocity	CSD Velocity	Percent Error Velocity	Radar Range	CSD Range	Percent Error Range
A	51.4	56.7	10.3	51.0	41.0	19.6
B	52.0	56.4	8.4	105.4	54.0	48.8
C	54.2	56.3	4.0	105.2	42.0	60.1
D	73.8	71.7	2.8	108.7	99.0	8.9
E	70.9	69.4	2.1	98.2	54.0	45.0
F	75.0	75.2	0.3	109.3	62.0	43.3
G	47.1	57.1	21.1	206.4	141.0	31.7
H	44.8	49.6	10.7	320.5	187.0	41.7

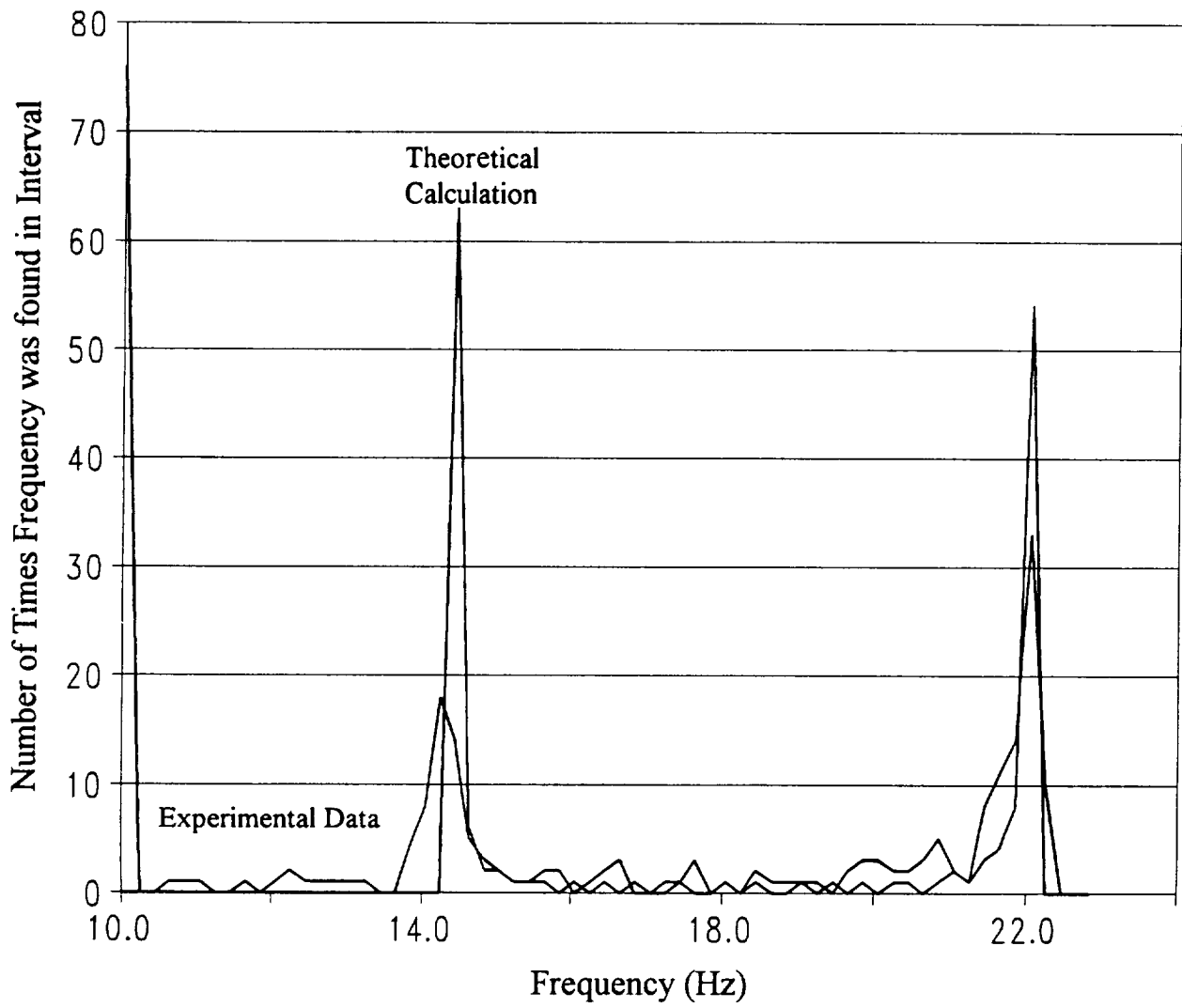


Figure 5. Histogram of frequency from approach through departure.

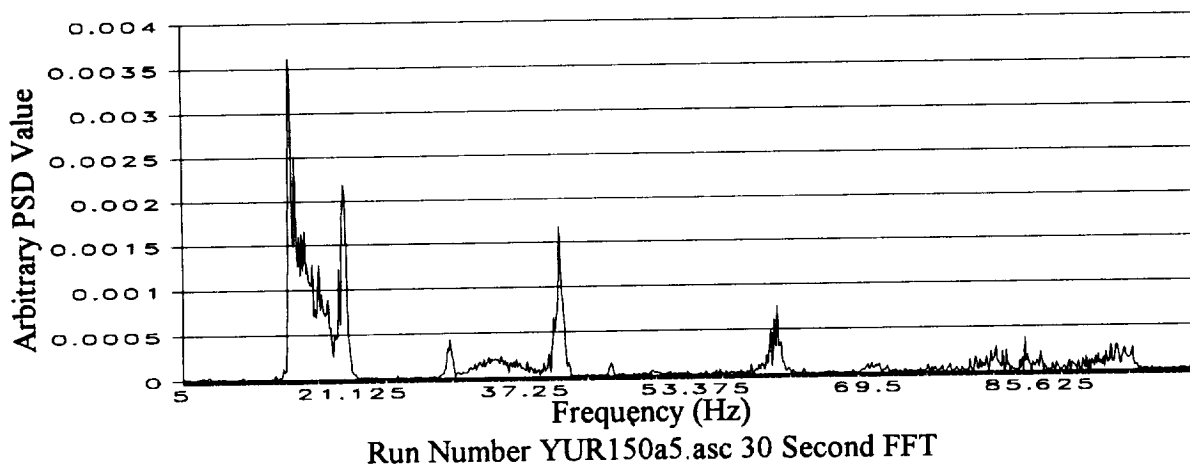
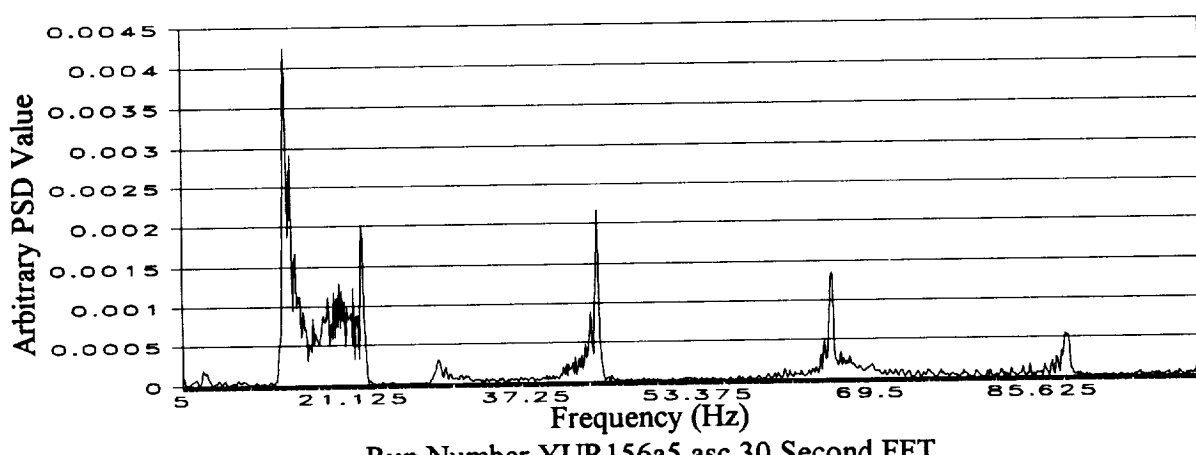
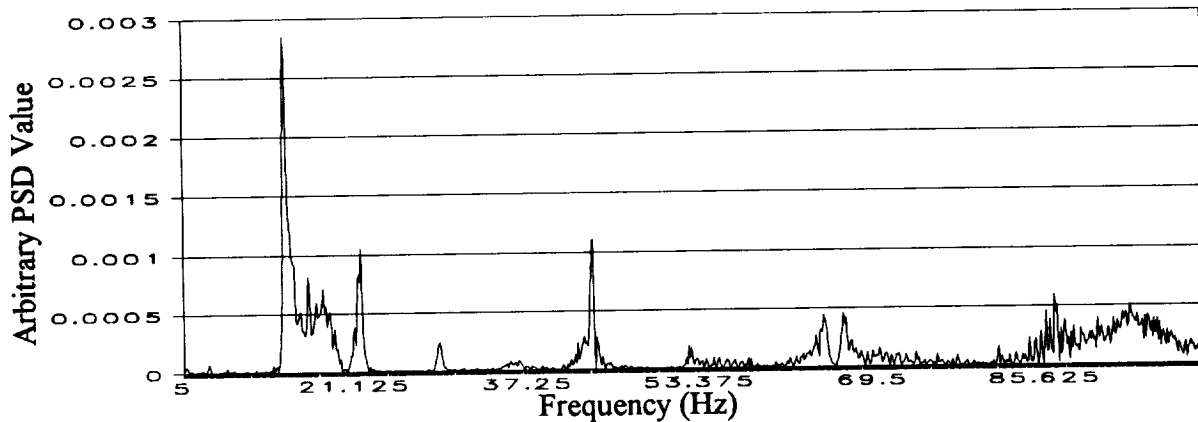


Figure 6. Selected PSD plots for 30 second extractions of time traces about CPA.

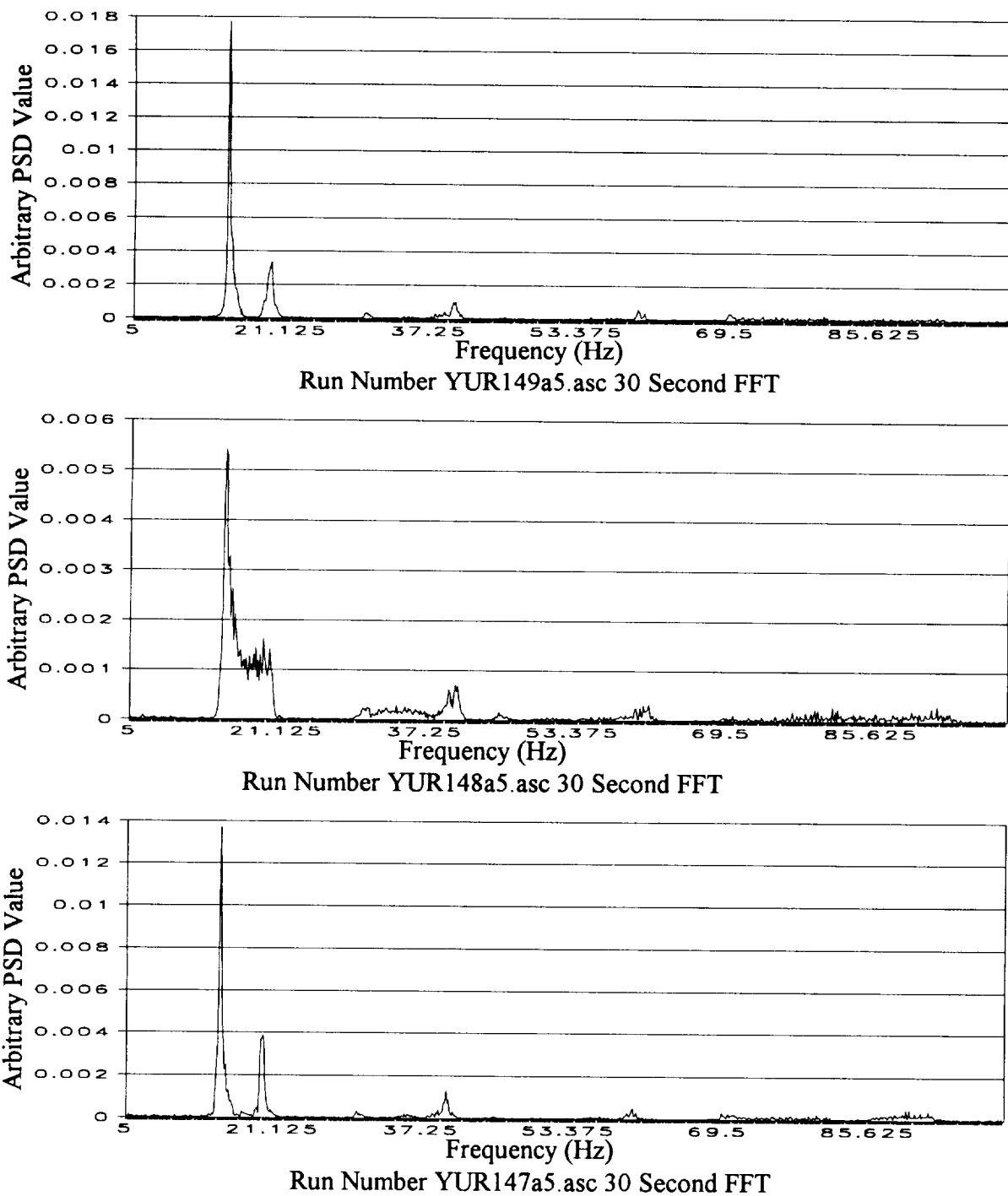


Figure 7. Selected PSD plots for 15 second extractions of time traces about CPA.

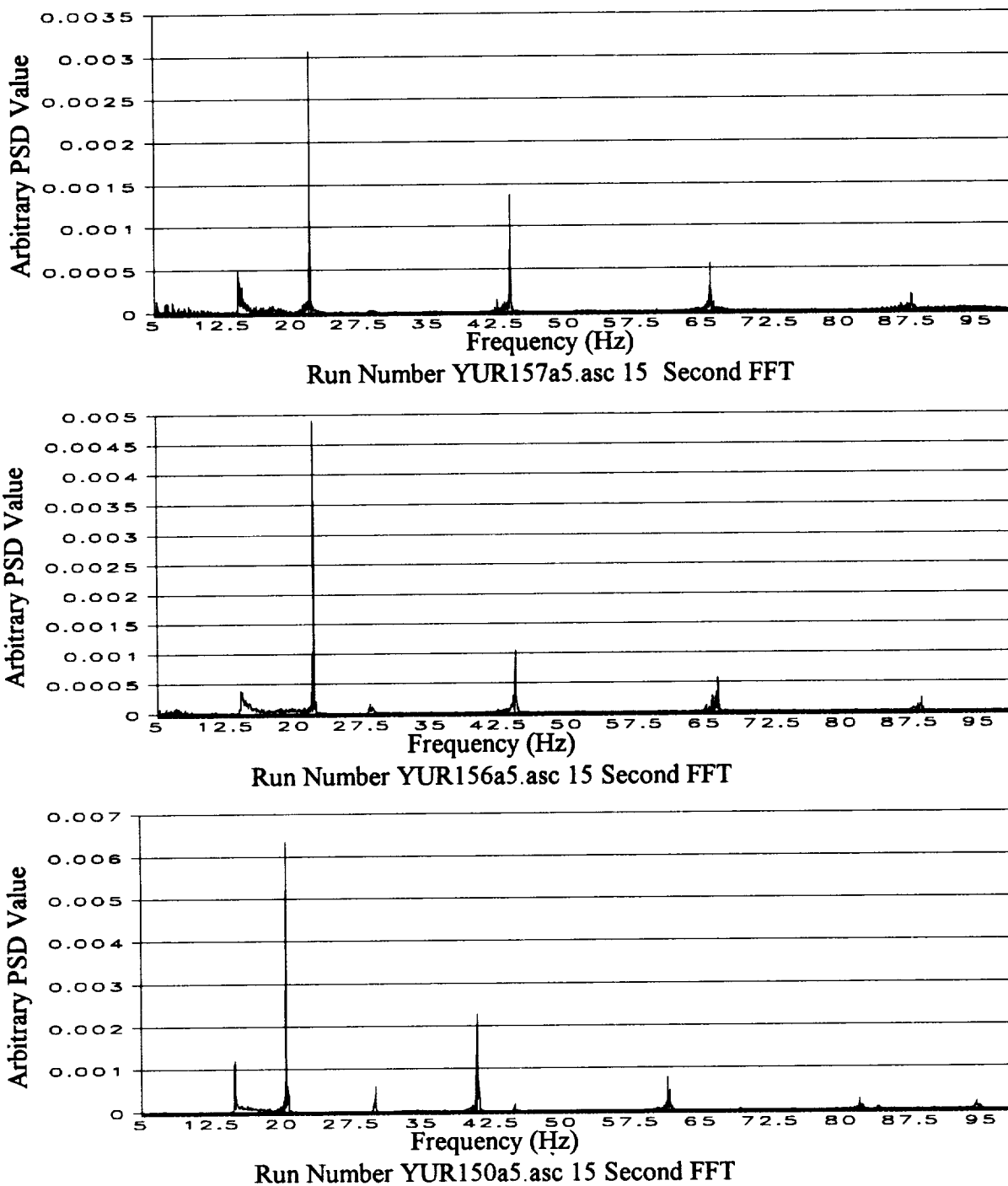


Figure 8. Selected PSD plots for 15 second extractions of time traces about CPA.

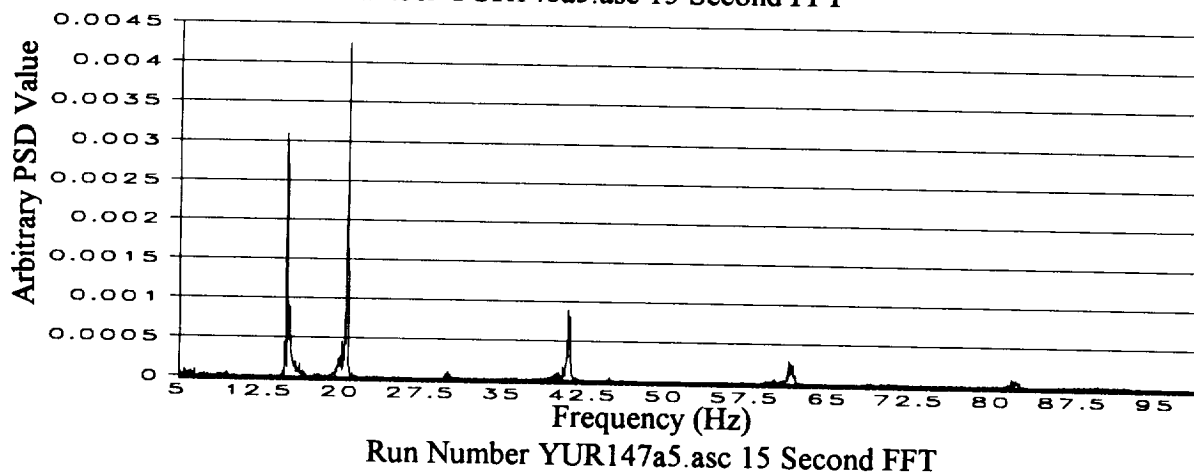
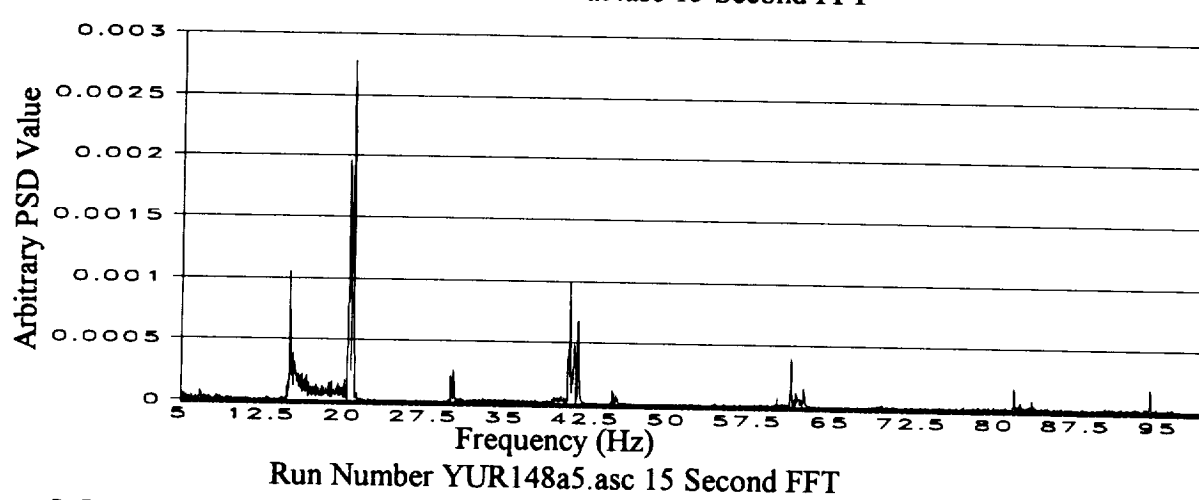
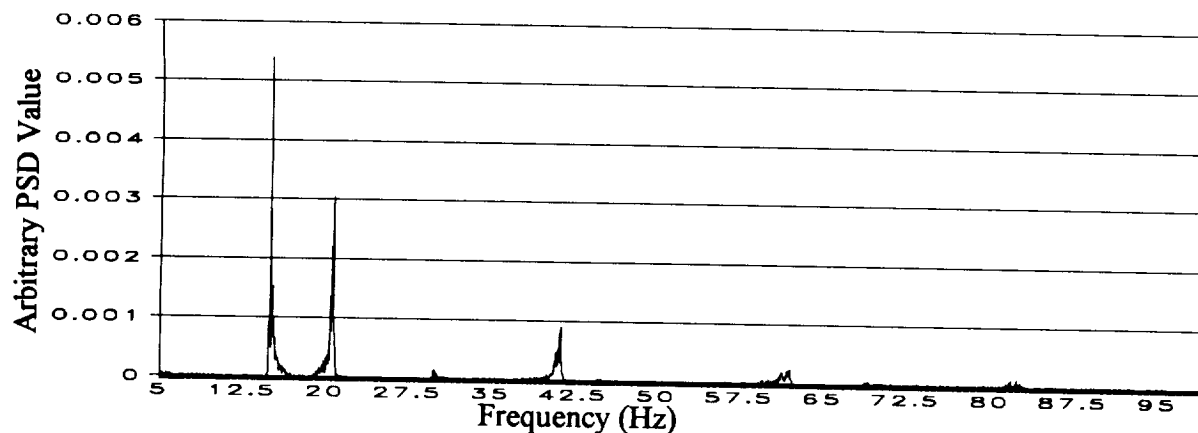


Figure 9. Selected PSD plots for 15 second extractions of time traces about CPA.

The method of successive differences exploits the fact that as the period in the sample to be transformed is increased, the resolution of the result will also increase. This method was adapted from a commonly accepted practice in nuclear spectroscopy. In determining the half-life of short-lived isotopes in nuclear physics, it is a common practice to acquire a spectrum and save it, then continue to acquire into that spectrum for some time. The difference between the two spectra will contain the amount of decays that occurred for each peak during that time, and a half-life calculation can easily be made. Similarly, the differences between two amplitude normalized high resolution FFTs will represent the changes that occurred during the period between the acquisition of the two time traces.

By first determining the incoming and outgoing frequencies, the stationary fundamental frequency of the source was calculated. From this information the time trace was then searched at a high resolution in order to determine the slope of the frequency versus time function as the fundamental peak passes through the stationary value. This process was automated along with peak search algorithms to identify peaks and extract frequency information from them. The values of range, velocity, and frequency were the output of this code. Errors in output from this method agree with what is expected from the theoretical limits.

Data processed with the CSD method was analyzed using this method. The results of the simulated and experimental runs, mentioned previously in tables 1 and 3, are presented in tables 5 and 6.

Comparison of Methods

While both methods produced results which agree with the theoretical analysis of the error in the ideal case, the SD method had an advantage over the CSD when there are multiple signals in a peak. In addition to the multiple peak problem, the CSD displayed a loss of accuracy when dealing with sections of time trace that had a duration of less than 0.25 second, but the SD has no such limit. It can be seen from figure 4, (which is a plot of error as a function of time step) that this 0.25 second limit gives an error as great as 15 percent for some cases. The disadvantage of the SD method is the intensive calculations which must be performed. The SD algorithm, written in the C programming language and executed on a 80486 class 33 MHz personal computer, took approximately twice the time to process a section that would be required for it to run in a real time mode, however this code was not optimized.

Table 5. Results of SD analysis on multiple simulated single source signals

Actual Fundamental Frequency	Calculated Fundamental Frequency			Actual CPA	Calculated CPA			Actual Speed	Calculated Speed		
	(Hz)	(Hz)	% Error		(m)	(m)	% Error		(m/s)	(m/s)	% Error
16.00	16.03	0.19	50.00	49.75	0.50	10.00	22.00	120.00			
16.00	16.03	0.16	50.00	47.88	4.25	50.00	40.00	20.00			
16.00	16.02	0.12	50.00	40.90	18.21	200.00	99.00	50.50			
16.00	16.19	1.19	50.00	25.68	48.65	500.00	64.00	87.20			
16.00	15.98	0.10	100.00	100.02	0.02	10.00	48.00	380.00			
16.00	16.02	0.12	100.00	98.79	1.21	50.00	68.00	36.00			
16.00	16.16	1.00	100.00	93.88	6.12	200.00	117.00	41.50			
16.00	16.26	1.60	100.00	79.83	20.17	500.00	194.00	61.20			
16.00	15.99	0.05	250.00	250.03	0.01	10.00	122.00	1120.00			
16.00	15.99	0.05	250.00	250.03	0.01	50.00	124.00	148.00			
16.00	16.17	1.08	250.00	248.68	0.53	200.00	240.00	20.00			
16.00	16.61	3.79	250.00	245.00	2.00	500.00	441.00	11.80			

Table 6. Results of SD analysis on experimental data.

Case	Radar Velocity	CSD Velocity	Percent Error Velocity	Radar Range	CSD Range	Percent Error Range
A	51.4	55.8	8.5	51.0	45.8	10.2
B	52.0	53.8	3.4	105.4	69.7	33.9
C	54.2	52.4	3.2	105.2	72.6	31.0
D	73.8	72.9	1.2	108.7	99.0	8.9
E	70.9	71.1	0.3	98.2	78.3	20.3
F	75.0	74.8	0.3	109.3	92.4	15.5
G	47.1	52.1	10.5	206.4	141.0	31.7
H	44.8	47.8	6.7	320.5	243.5	24.0

Both the CSD and SD methods were used with the equations from the previous study to calculate range, speed, and frequency information for a single source with some limited success. The problem of deconvoluting the signal was not solved at this time, but the key to developing a system for obtaining range information from multiple sources is to identify the number of sources present, and to track the signature peaks through their stationary frequencies.

Refinement of PAR through Artificial Neural Networks

The artificial neural network (ANN) is a computer algorithm that is modeled after the synapses and neurons in the brain. Recent research into the applications of this technique has found great success in classification and prediction using non-linear data. Investigations have been made using the ANN in a wide variety of fields and applications (including classification of military targets and medical diagnosis). The studies show that an ANN has the capability to learn a non-linear pattern. Because of this fact a study was planned to evaluate the feasibility of using an ANN to classify the source and possibly to determine the source type, quantity, velocity and range.

Back Propagation Training of an ANN

An ANN is an interconnected array of neurons. The first level of neurons, called the input layer, is connected to inner hidden layers of neurons by synapses. The last hidden layer of neurons is also connected to the output layer by synapses. The neurons in the hidden layers are made up of weight values which are established by training. The ANN is trained to recognize patterns in the data by learning many examples. The standard method of training is by back propagation. A transfer function for each neuron determines the value each neuron will output. Many possible modifications can be made to optimize the internal parameters of an ANN.

ANN Training, Testing, and Development

An ANN application was designed for the helicopter scenario and it was trained to recognize patterns in the data by learning many examples. The standard method of back propagation was used for training in this case. The standard sigmoid transfer function, as well as an input, output, and a single hidden layer of neurons, was chosen for the architecture of this network for

this application. Since there were only single runs of Huey and Blackhawk helicopters (no multiple runs) in the JAPE, a method to synthesize signals from more than one source was developed. A simulation code (further discussed in Appendix A) was also used to create signals from a third source. Data from each source were used in training the ANN.

The first ANN was trained on three data sets (listed in table 7), which included a single simulated source, a single helicopter (run WS147 from the JAPE) and a dual source synthesized from these two runs. A total of 350 one second time windows of the time traces were extracted from these three data sets at random, and 50 of these were retained for testing of the ANN. An FFT was performed on each of the 350 time windows, and the results were truncated to limit the frequency content to a range of 5 to 85 Hz. These frequency values were used as the input layer for the ANN. The ANN was then trained on the FFT of each of the 300 time windows until the average error was minimized. After the training was complete, the 50 one second windows retained for testing were fed into the ANN as inputs. The ANN was able to classify the source accurately 100 percent of the time, as can be seen in table 8.

After this initial success nine data sets were prepared on single and combinations of sources as shown in table 9. A total of 550 time windows were selected from these data sets, and 50 of these were again retained for testing. Another ANN was trained on the FFT of each of the 500 time windows to determine if the ANN could classify multiple helicopters. The ANN was able to classify the sources accurately 90 percent of the time in any of the combinations, and the results of the testing are presented in table 10. Selected FFT's from the test cases are presented in figures 10 - 27.

DISCUSSION AND CONCLUSIONS

It is feasible to develop the PAR concept into an algorithm that can be part of an operational sensor system. However, the PAR has several limitations discovered in this study that must be addressed before using such an algorithm. In the previous study the PAR concept was described as operable on a single sensor, but the selection of the time step for developing the Doppler shift curve is critical, depending on the speed of the source and the distance from the sensor. Selection of the wrong time step could cause the curve to have only one or two points during the Doppler shift, severely distorting the slope calculation. Because of this limitation, it would be advisable to use the PAR concept on multiple sensors. An array is not required (i.e., to perform beamforming), and the PAR algorithm can be used independently on each sensor (which can be

separated by relatively large distances). The PAR concept can also be used on multiple sources, but the Doppler shift curves for each of the sources present in the signal must be identified. Because of the mode of determining the range and velocity used by the PAR, the portion of the signals produced by each source must be used to produce separate Doppler shift curves for each source. The conventional methods of signal processing tested herein were not sufficient to produce the curves reliably for each source. Another limitation of the PAR concept is that the source has to pass through CPA and into the far-field before the calculation can be completed unless there is a priori knowledge of the stationary frequency of the source.

The use of an ANN to identify the sources and separate their signal contributions is feasible. However, only a limited test of the ANN for this purpose was performed in this study. It should be noted here that the 90 percent accuracy resulting from the ANN was probably not a major problem for application to the PAR concept. The ANN was not optimized, and was only trained with 500 examples. Training on additional samples would increase the accuracy of the ANN. The accuracy of the ANN classification was also affected by the distance from the sensor, because of degradation of the signal as it propagated through the atmosphere. The time windows were selected for distances up to 1.5 km from CPA, and the Doppler shift occurs within a few hundred meters of CPA. Therefore, the accuracy of the ANN classifier is higher in the area required for the analysis for the PAR concept. The use of an ANN could also be used to improve the response time of the PAR concept. Because of the capability of an ANN to identify the source, the calculation could be performed within a very short time of the source passing CPA.

RECOMMENDATIONS

The PAR concept has definite utility in the acoustic detection field, but because of the limitations discussed in this report, caution must be used in planning the deployment of a system with a PAR algorithm. A PAR algorithm might be more useful to supplement other acoustic detection algorithms (such as beamformers used in triangulation, etc.). The application of an ANN to the PAR concept using multiple sensors appears to have the necessary processing capability to overcome the limitations. The ability to classify and separate the sources in the measured signal allows the PAR algorithm to determine the stationary frequency and calculate the range and velocity of each source. These calculations can also be done as the source passes through CPA. A sequence of ANNs could also possibly be used to perform several portions of the signal processing required for the PAR concept. Further study of the PAR concept and the applicable ANN processing is recommended.

REFERENCE

¹ Olson, R.E., Cress, D.H. (1992). "Passive Acoustic Range Estimation of Helicopters," T.R. EL-92-13, U.S.A.E. Waterways Experiment Station, Vicksburg, Miss., 59 p.

Table 7. Index of cases used in first ANN training.

Case A	Simulated Source with 16 Hz Fundamental
Case B	WSR147a4 Blackhawk Helicopter from JAPE Data Set
Case C	Superposition of Cases A and B

Table 8. Results of ANN classification of first training case.

Case A		Case B		Case C		Results
Predicted	Actual	Predicted	Actual	Predicted	Actual	
0.00	0.00	0.00	0.00	0.99	1.00	Correct
1.00	1.00	0.00	0.00	0.00	0.00	Correct
1.00	1.00	0.00	0.00	0.00	0.00	Correct
1.00	1.00	0.00	0.00	0.03	0.00	Correct
0.00	0.00	1.00	1.00	0.00	0.00	Correct
0.00	0.00	1.00	1.00	0.00	0.00	Correct
0.00	0.00	1.00	1.00	0.00	0.00	Correct
0.00	0.00	1.00	1.00	0.00	0.00	Correct
1.00	1.00	0.00	0.00	0.00	0.00	Correct
0.00	0.00	1.00	1.00	0.00	0.00	Correct
0.99	1.00	0.01	0.00	0.00	0.00	Correct
0.00	0.00	1.00	1.00	0.00	0.00	Correct
0.00	0.00	0.00	0.00	1.00	1.00	Correct
0.00	0.00	1.00	1.00	0.00	0.00	Correct
1.00	1.00	0.00	0.00	0.00	0.00	Correct
1.00	1.00	0.00	0.00	0.00	0.00	Correct
0.00	0.00	1.00	1.00	0.00	0.00	Correct
0.00	0.00	0.02	0.00	1.00	1.00	Correct
0.00	0.00	0.00	0.00	1.00	1.00	Correct
0.00	0.00	1.00	1.00	0.00	0.00	Correct
0.01	0.00	0.00	0.00	1.00	1.00	Correct
1.00	1.00	0.00	0.00	0.00	0.00	Correct
0.00	0.00	1.00	1.00	0.00	0.00	Correct
0.00	0.00	0.08	0.00	0.99	1.00	Correct
0.00	0.00	0.00	0.00	1.00	1.00	Correct
0.98	1.00	0.06	0.00	0.01	0.00	Correct
1.00	1.00	0.00	0.00	0.00	0.00	Correct
0.81	1.00	0.01	0.00	0.00	0.00	Correct
0.00	0.00	0.00	0.00	1.00	1.00	Correct
1.00	1.00	0.00	0.00	0.00	0.00	Correct
0.00	0.00	0.00	0.00	1.00	1.00	Correct
0.00	0.00	0.00	0.00	1.00	1.00	Correct
1.00	1.00	0.00	0.00	0.00	0.00	Correct
0.00	0.00	0.00	0.00	1.00	1.00	Correct
1.00	1.00	0.00	0.00	0.00	0.00	Correct
0.00	0.00	0.00	0.00	1.00	1.00	Correct
1.00	1.00	0.04	0.00	0.00	0.00	Correct
0.00	0.00	0.00	0.00	1.00	1.00	Correct
1.00	1.00	0.00	0.00	0.00	0.00	Correct
0.97	1.00	0.18	0.00	0.00	0.00	Correct
0.00	0.00	1.00	1.00	0.00	0.00	Correct
1.00	1.00	0.00	0.00	0.00	0.00	Correct
1.00	1.00	0.00	0.00	0.00	0.00	Correct
0.00	0.00	0.00	0.00	1.00	1.00	Correct
1.00	1.00	0.00	0.00	0.00	0.00	Correct
0.98	1.00	0.16	0.00	0.00	0.00	Correct
0.00	0.00	0.00	0.00	1.00	1.00	Correct
0.00	0.00	1.00	1.00	0.00	0.00	Correct
0.00	0.00	0.00	0.00	1.00	1.00	Correct
0.00	0.00	0.00	0.00	1.00	1.00	Correct
0.00	0.00	0.02	0.00	1.00	1.00	Correct

Table 9. Index of cases used in second ANN training.

CASE	Description
Case A	Simulated Helicopter
Case B	Huey from Data Set WSMR010
Case C	Blackhawk from Data Set WS147
Case D	Two Summed Case A
Case E	Two Summed Case A and Case B
Case F	Two Summed Case A and Case C
Case G	Two Summed Case B
Case H	Two Summed Case B and Case C
Case I	Two Summed Case C

Table 10. Results of ANN classification of second training case.

	Case A	Case B	Case C	Case D	Case E	Case F	Case G	Case H	Case I	Results
actual	0.00	0.00	1.00	0.00	0.00	0.00	0.00	0.00	0.00	
predicted	0.00	0.00	1.00	0.00	0.00	0.00	0.00	0.00	0.00	Correct
actual	0.00	1.00	0.00	0.00	0.00	0.00	0.00	0.00	0.00	
predicted	0.00	1.00	0.00	0.00	0.00	0.00	0.00	0.00	0.00	Correct
actual	0.00	0.00	0.00	0.00	0.00	0.00	0.00	0.01	0.66	
predicted	0.00	0.00	0.00	0.00	0.00	0.00	0.00	0.00	1.00	Correct
actual	0.00	0.95	0.00	0.00	0.00	0.00	0.39	0.00	0.00	
predicted	0.00	1.00	0.00	0.00	0.00	0.00	0.00	0.00	0.00	Correct
actual	0.00	0.00	0.00	0.00	0.00	0.00	0.00	1.00	0.01	
predicted	0.00	0.00	0.00	0.00	0.00	0.00	0.00	1.00	0.00	Correct
actual	0.00	0.92	0.00	0.00	0.00	0.00	0.04	0.02	0.00	
predicted	0.00	1.00	0.00	0.00	0.00	0.00	0.00	0.00	0.00	Correct
actual	0.00	0.00	0.00	0.00	0.00	0.00	0.00	1.00	0.01	
predicted	0.00	0.00	0.00	0.00	0.00	0.00	0.00	1.00	0.00	Correct
actual	0.00	1.00	0.00	0.00	0.00	0.00	0.05	0.00	0.00	
predicted	0.00	1.00	0.00	0.00	0.00	0.00	0.00	0.00	0.00	Correct
actual	0.00	0.00	1.00	0.00	0.00	0.00	0.00	0.00	0.00	
predicted	0.00	0.00	1.00	0.00	0.00	0.00	0.00	0.00	0.00	Correct
actual	0.00	0.00	0.46	0.00	0.00	0.00	0.00	0.04	0.00	
predicted	0.00	0.00	1.00	0.00	0.00	0.00	0.00	0.00	0.00	Correct
actual	0.00	0.99	0.00	0.00	0.00	0.00	0.03	0.00	0.00	
predicted	0.00	1.00	0.00	0.00	0.00	0.00	0.00	0.00	0.00	Correct
actual	0.00	0.00	0.00	0.00	0.00	0.00	0.00	1.00	0.01	
predicted	0.00	0.00	0.00	0.00	0.00	0.00	0.00	1.00	0.00	Correct
actual	0.00	0.00	0.00	0.00	0.00	0.00	0.00	0.99	0.01	
predicted	0.00	0.00	0.00	0.00	0.00	0.00	0.00	1.00	0.00	Correct
actual	0.00	0.28	0.00	0.00	0.00	0.00	0.00	0.93	0.00	
predicted	0.00	1.00	0.00	0.00	0.00	0.00	0.00	0.00	0.00	Incorrect
actual	0.00	0.00	0.11	0.00	0.00	1.00	0.00	0.00	0.00	
predicted	0.00	0.00	0.00	0.00	0.00	1.00	0.00	0.00	0.00	Correct
actual	0.00	0.00	0.00	0.00	0.00	0.00	1.00	0.00	0.00	
predicted	0.00	0.00	0.00	0.00	0.00	0.00	1.00	0.00	0.00	Correct
actual	0.00	0.00	0.00	0.00	0.00	0.08	0.00	0.00	0.97	
predicted	0.00	0.00	0.00	0.00	0.00	0.00	0.00	0.00	1.00	Correct

Table 10. Results of ANN classification of second training case (continued)

	Case A	Case B	Case C	Case D	Case E	Case F	Case G	Case H	Case I	Results
actual	0.00	0.00	0.00	0.00	0.00	0.00	0.00	1.00	0.01	
predicted	0.00	0.00	0.00	0.00	0.00	0.00	0.00	1.00	0.00	Correct
actual	0.00	0.00	0.31	0.00	0.66	0.00	0.00	0.00	0.00	
predicted	0.00	0.00	1.00	0.00	0.00	0.00	0.00	0.00	0.00	Incorrect
actual	0.00	1.00	0.00	0.00	0.00	0.00	0.00	0.00	0.00	
predicted	0.00	1.00	0.00	0.00	0.00	0.00	0.00	0.00	0.00	Correct
actual	0.00	0.00	0.00	0.00	0.60	1.00	0.00	0.00	0.00	
predicted	0.00	0.00	0.00	0.00	1.00	0.00	0.00	0.00	0.00	Correct
actual	0.00	0.00	0.00	0.00	0.00	0.00	0.99	0.02	0.00	
predicted	0.00	0.00	0.00	0.00	0.00	0.00	1.00	0.00	0.00	Correct
actual	0.00	0.00	0.00	0.00	0.00	0.00	1.00	0.00	0.00	
predicted	0.00	0.00	0.00	0.00	0.00	0.00	1.00	0.00	0.00	Correct
actual	0.00	0.00	0.79	0.00	0.00	0.00	0.00	0.00	0.00	
predicted	0.00	0.00	1.00	0.00	0.00	0.00	0.00	0.00	0.00	Correct
actual	0.00	1.00	0.00	0.00	0.00	0.00	0.00	0.00	0.00	
predicted	0.00	1.00	0.00	0.00	0.00	0.00	0.00	0.00	0.00	Correct
actual	0.00	0.00	0.00	0.00	0.00	0.00	0.00	1.00	0.01	
predicted	0.00	0.00	0.00	0.00	0.00	0.00	0.00	1.00	0.00	Correct
actual	0.00	0.01	1.00	0.00	0.00	0.00	0.00	0.00	0.00	
predicted	0.00	0.00	1.00	0.00	0.00	0.00	0.00	0.00	0.00	Correct
actual	0.00	0.00	1.00	0.00	0.00	0.00	0.00	0.00	0.00	
predicted	0.00	0.00	1.00	0.00	0.00	0.00	0.00	0.00	0.00	Correct
actual	0.00	0.00	0.00	0.00	0.00	0.00	0.00	0.00	0.00	
predicted	0.00	0.00	0.00	0.00	0.00	0.00	0.00	0.00	0.00	Correct
actual	0.00	0.00	0.00	0.00	0.00	0.00	0.00	1.00	0.01	
predicted	0.00	0.00	0.00	0.00	0.00	0.00	0.00	0.00	0.00	Correct
actual	0.00	0.00	0.00	0.00	0.00	0.00	0.00	1.00	0.00	
predicted	0.00	0.00	0.00	0.00	0.00	0.00	1.00	0.00	0.00	Correct
actual	0.00	0.00	0.00	0.00	0.00	0.00	0.00	0.00	0.00	
predicted	0.00	0.00	0.00	0.00	0.00	0.00	0.00	0.00	1.00	Correct
actual	0.00	0.03	0.00	0.00	0.00	0.00	0.96	0.01	0.00	
predicted	0.00	1.00	0.00	0.00	0.00	0.00	0.00	0.00	0.00	Incorrect
actual	0.00	1.00	0.00	0.00	0.00	0.00	0.00	0.00	0.00	
predicted	0.00	1.00	0.00	0.00	0.00	0.00	0.00	0.00	0.00	Correct
actual	0.00	0.00	0.00	0.00	0.00	0.00	0.00	0.05	0.67	
predicted	0.00	0.00	0.00	0.00	0.00	0.00	0.00	0.00	1.00	Correct
actual	0.00	1.00	0.00	0.00	0.07	0.00	0.00	0.00	0.00	
predicted	0.00	1.00	0.00	0.00	0.00	0.00	0.00	0.00	0.00	Correct

Table 10. Results of ANN classification of second training case. (concluded)

	Case A	Case B	Case C	Case D	Case E	Case F	Case G	Case H	Case I	Results
actual	0.00	0.00	0.00	0.00	1.00	0.00	0.00	0.00	0.00	
predicted	0.00	0.00	0.00	0.00	1.00	0.00	0.00	0.00	0.00	Correct
actual	0.00	1.00	0.00	0.00	0.00	0.00	0.00	0.00	0.00	
predicted	0.00	1.00	0.00	0.00	0.00	0.00	0.00	0.00	0.00	Correct
actual	0.00	1.00	0.00	0.00	0.00	0.00	0.00	0.00	0.00	
predicted	0.00	1.00	0.00	0.00	0.00	0.00	0.00	0.00	0.00	Correct
actual	0.00	1.00	0.00	0.00	0.00	0.00	0.00	0.00	0.00	
predicted	0.00	1.00	0.00	0.00	0.00	0.00	0.00	0.00	0.00	Correct
actual	0.00	0.00	0.00	0.00	0.00	0.00	0.00	1.00	0.01	
predicted	0.00	0.00	0.00	0.00	0.00	0.00	0.00	1.00	0.00	Correct
actual	0.00	1.00	0.00	0.00	0.00	0.00	0.00	0.00	0.00	
predicted	0.00	1.00	0.00	0.00	0.00	0.00	0.00	0.00	0.00	Correct
actual	0.00	0.00	0.00	0.00	0.00	0.00	0.00	0.88	0.07	
predicted	0.00	0.00	0.00	0.00	0.00	0.00	0.00	1.00	0.00	Correct
actual	0.00	0.00	1.00	0.00	0.00	0.00	0.00	0.00	0.00	
predicted	0.00	0.00	1.00	0.00	0.00	0.00	0.00	0.00	0.00	Correct
actual	0.00	0.99	0.48	0.00	0.00	0.00	0.00	0.00	0.00	
predicted	0.00	0.00	1.00	0.00	0.00	0.00	0.00	0.00	0.00	Incorrect
actual	0.00	0.00	0.00	0.00	0.00	0.00	0.00	0.09	0.64	
predicted	0.00	0.00	0.00	0.00	0.00	0.00	0.00	0.00	1.00	Correct
actual	0.00	0.00	0.98	0.00	0.00	0.00	0.00	0.00	0.00	
predicted	0.00	0.00	1.00	0.00	0.00	0.00	0.00	0.00	0.00	Correct
actual	0.00	1.00	0.00	0.00	0.00	0.00	0.00	0.00	0.00	
predicted	0.00	1.00	0.00	0.00	0.00	0.00	0.00	0.00	0.00	Correct
actual	0.00	0.00	0.00	0.00	0.00	0.00	0.00	0.99	0.01	
predicted	0.00	0.00	0.00	0.00	0.00	0.00	0.00	1.00	0.00	Correct
actual	0.00	0.00	0.00	0.00	0.00	0.00	0.00	0.99	0.01	
predicted	0.00	0.00	0.00	0.00	0.00	0.00	0.00	1.00	0.00	Correct
actual	0.00	0.00	0.67	0.00	0.00	0.00	0.00	0.01	0.00	
predicted	0.00	0.00	0.00	0.00	0.00	0.00	0.00	1.00	0.00	Incorrect
actual	0.00	0.00	0.00	0.00	0.00	0.00	1.00	0.00	0.00	
predicted	0.00	0.00	0.00	0.00	0.00	0.00	1.00	0.00	0.00	Correct

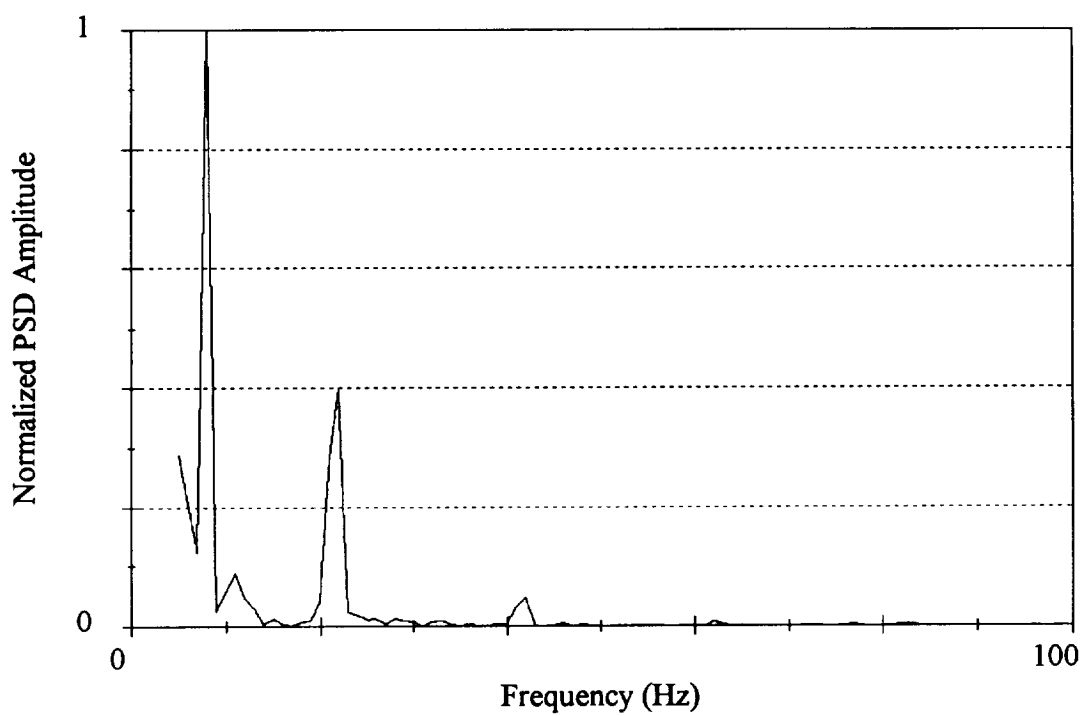


Figure 10. PSD from case C used as sample number one.

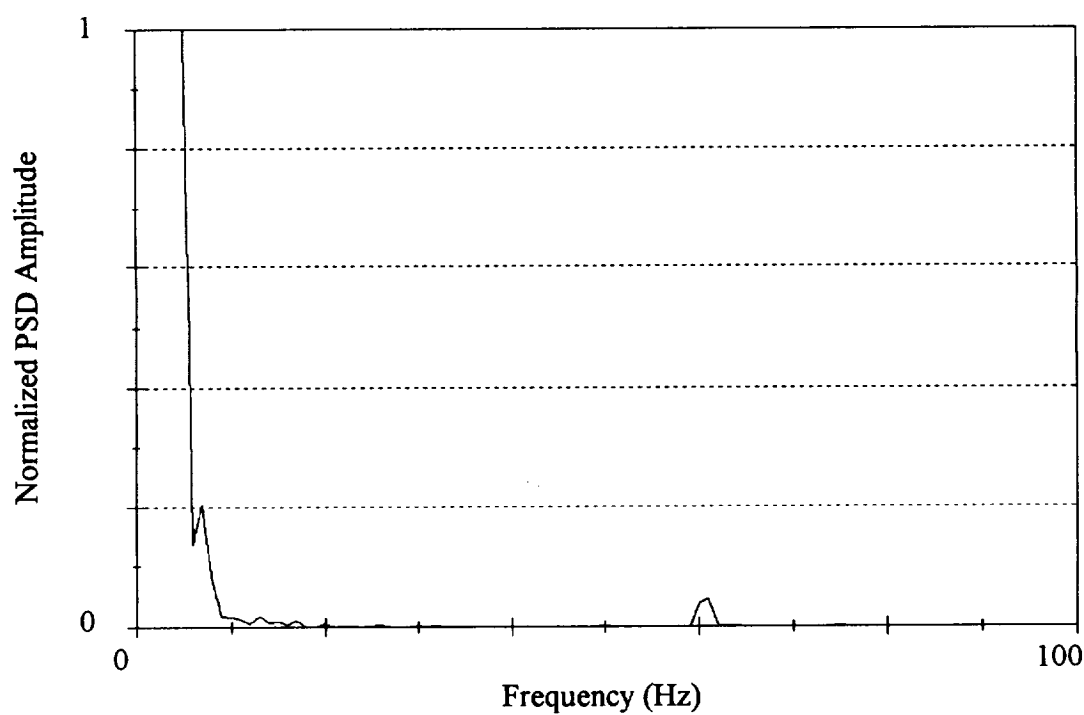


Figure 11. PSD from case B used as sample number two.

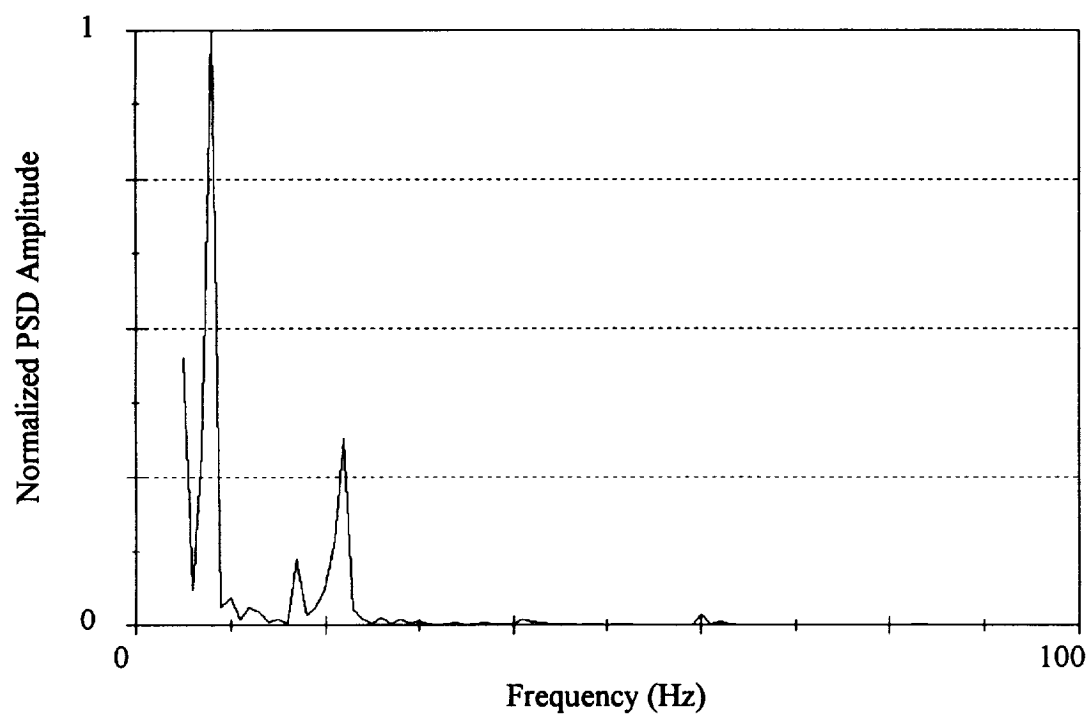


Figure 12. PSD from case I used as sample number three.

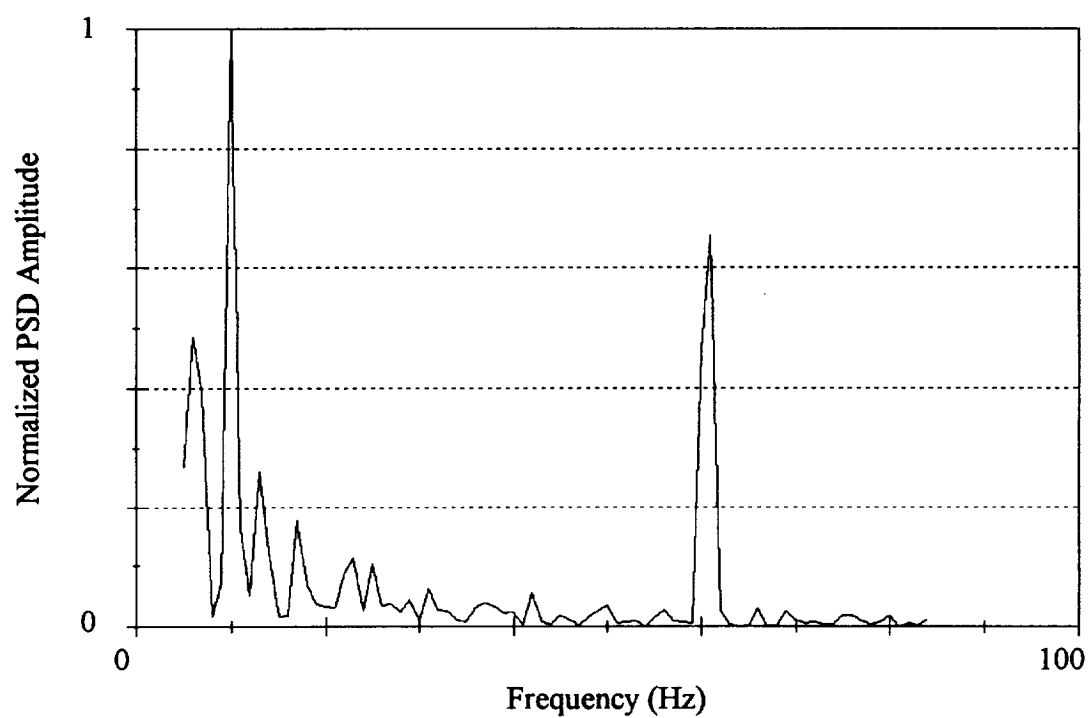


Figure 13. PSD from case B used as sample number four.

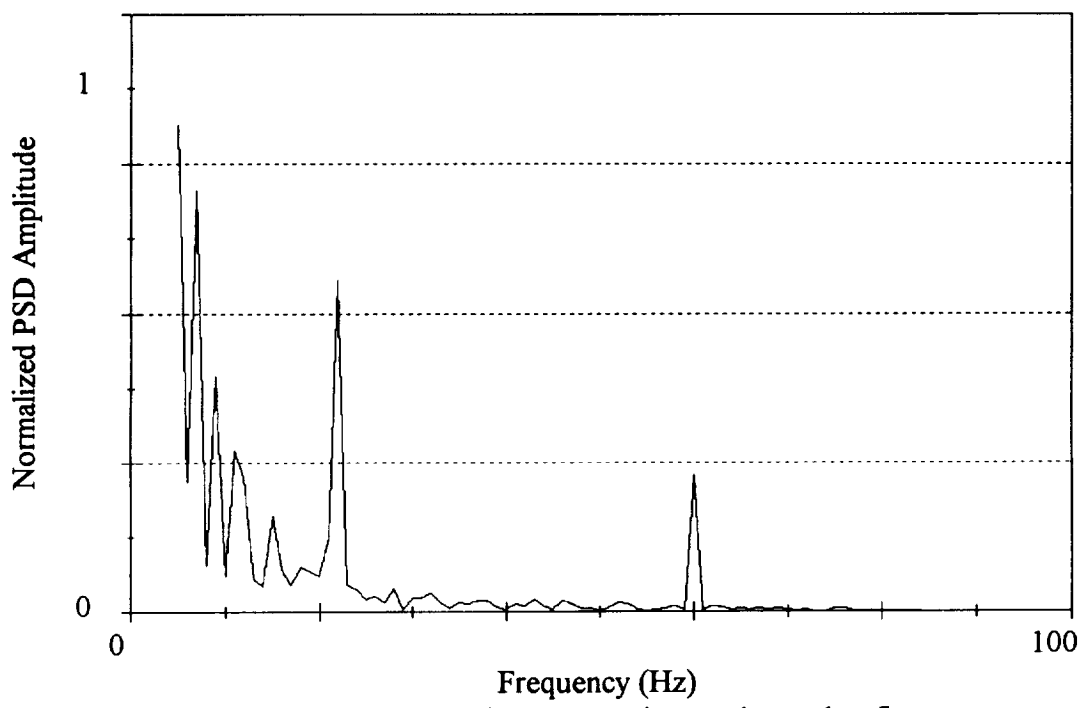


Figure 14. PSD from case H in sample number five.

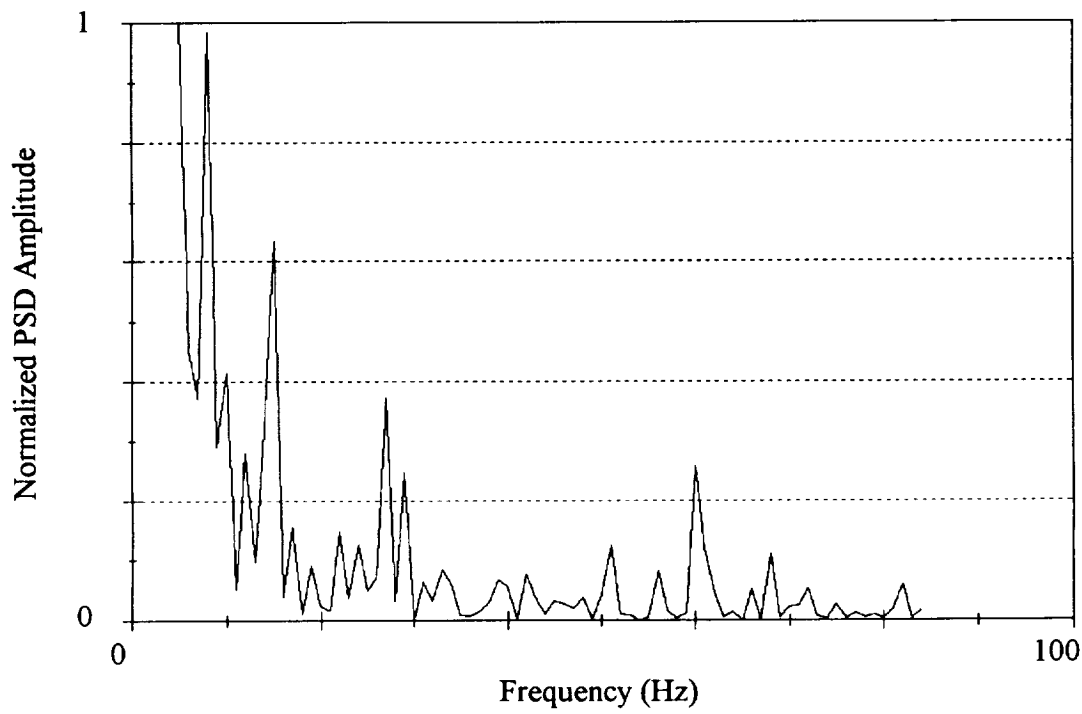


Figure 15. PSD from case B in sample number six.

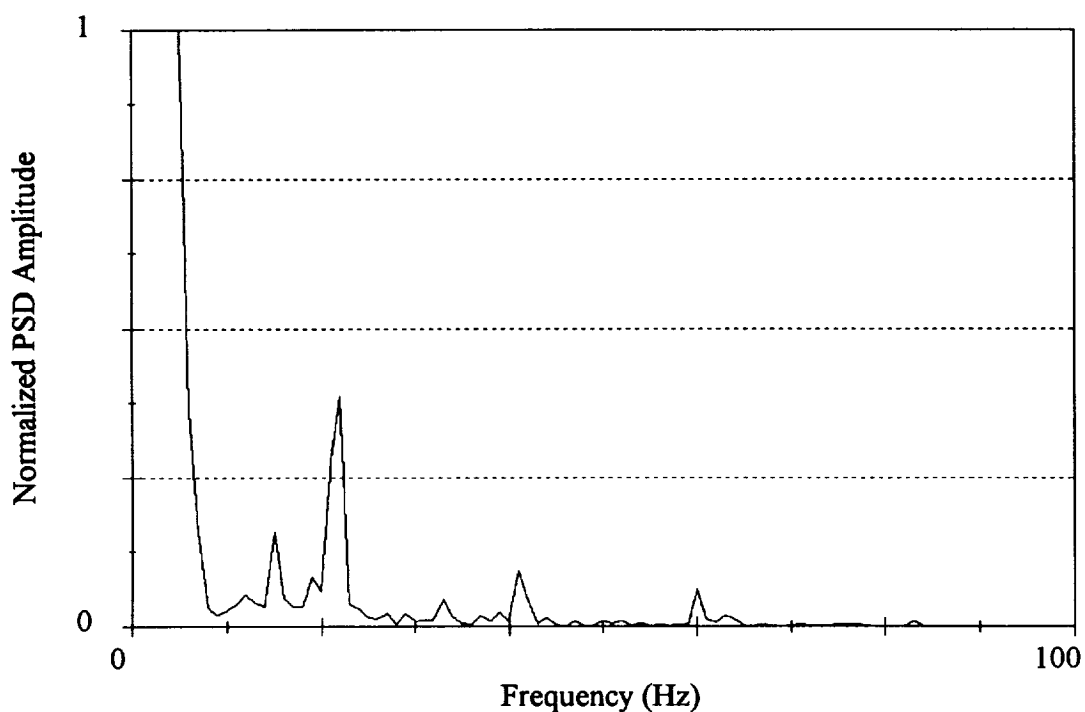


Figure 16. PSD from case H in sample number seven.

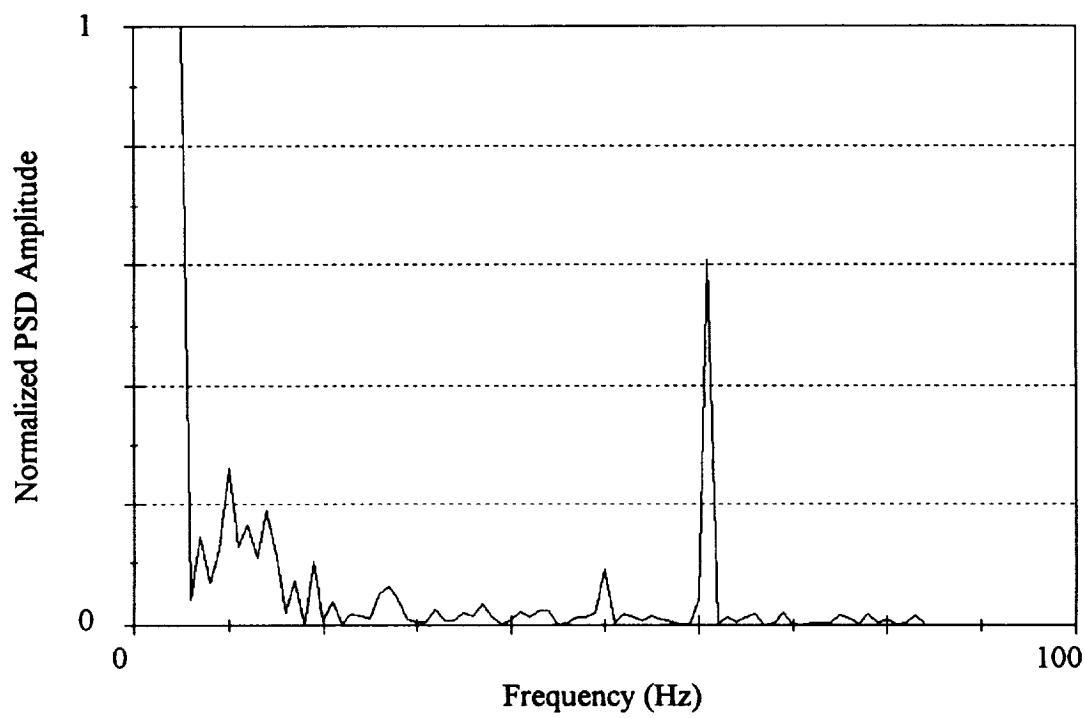


Figure 17. PSD from case B in sample number eight.

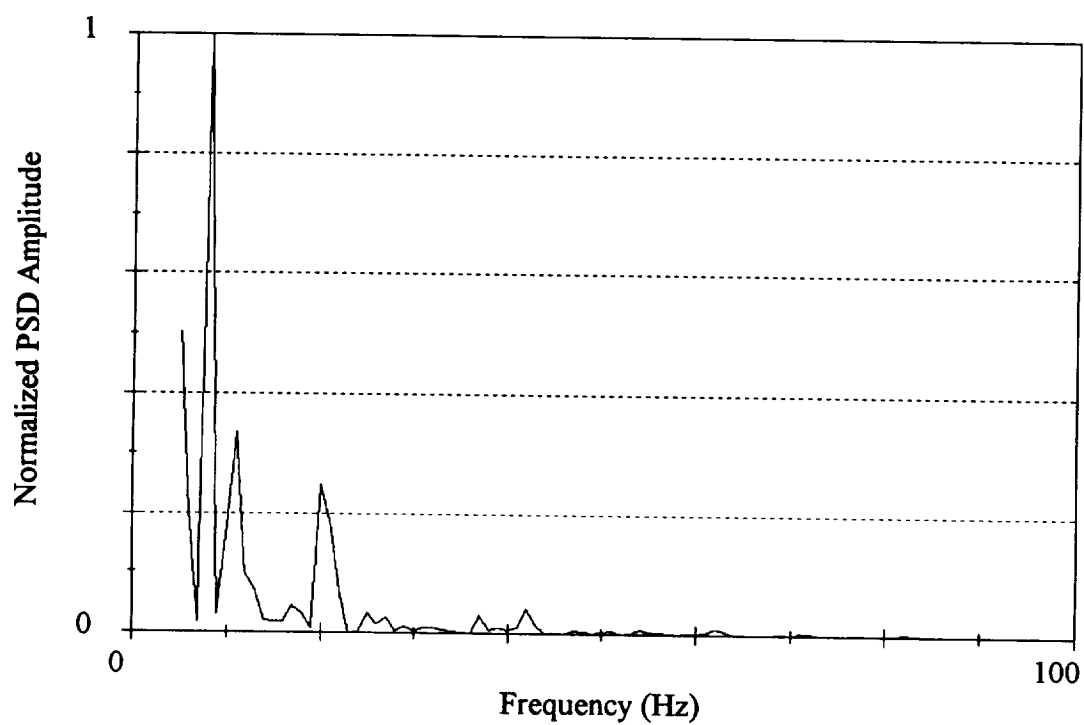


Figure 18. PSD from case C in sample number nine.

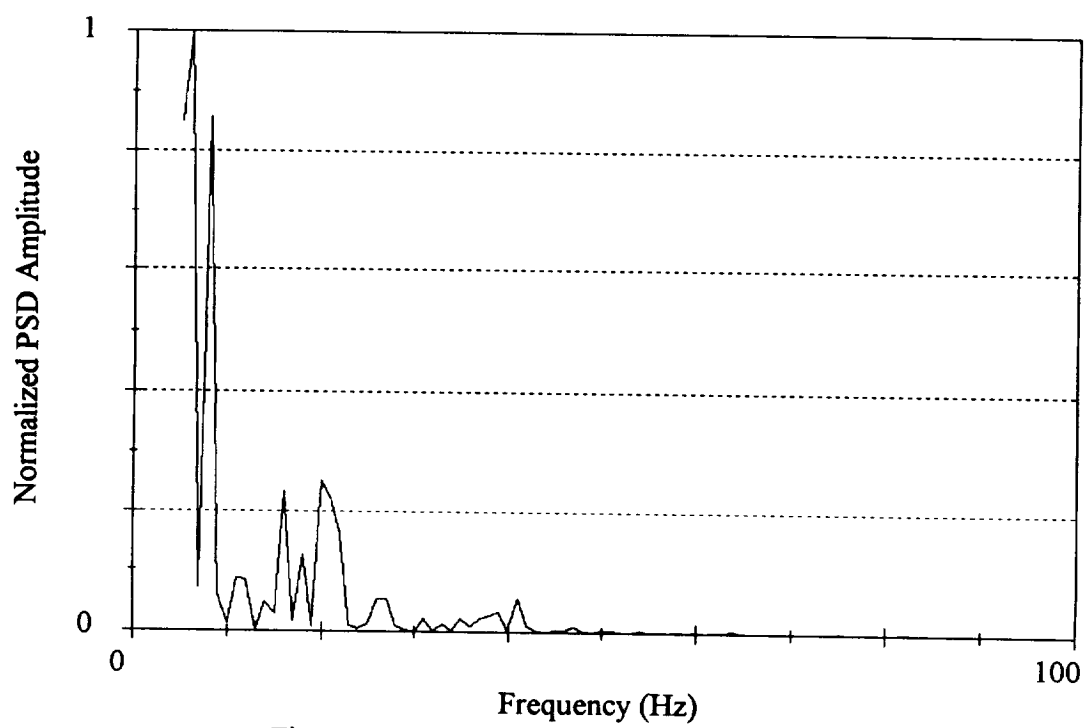


Figure 19. PSD from case C in sample number ten.

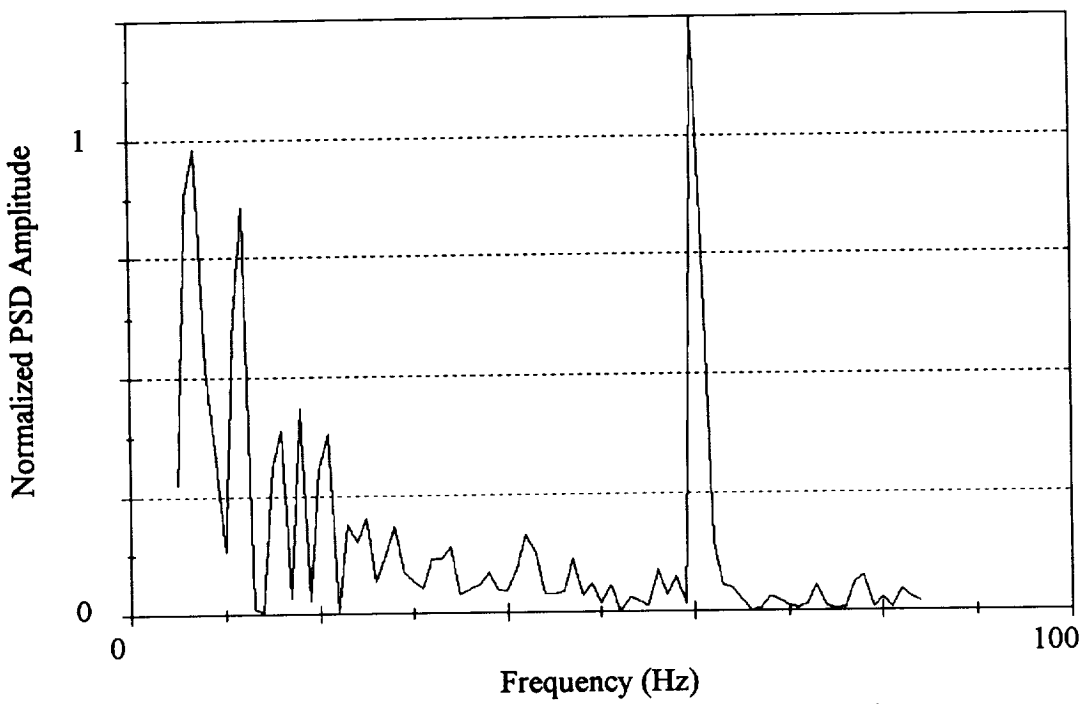


Figure 20. PSD from case B in sample number eleven.

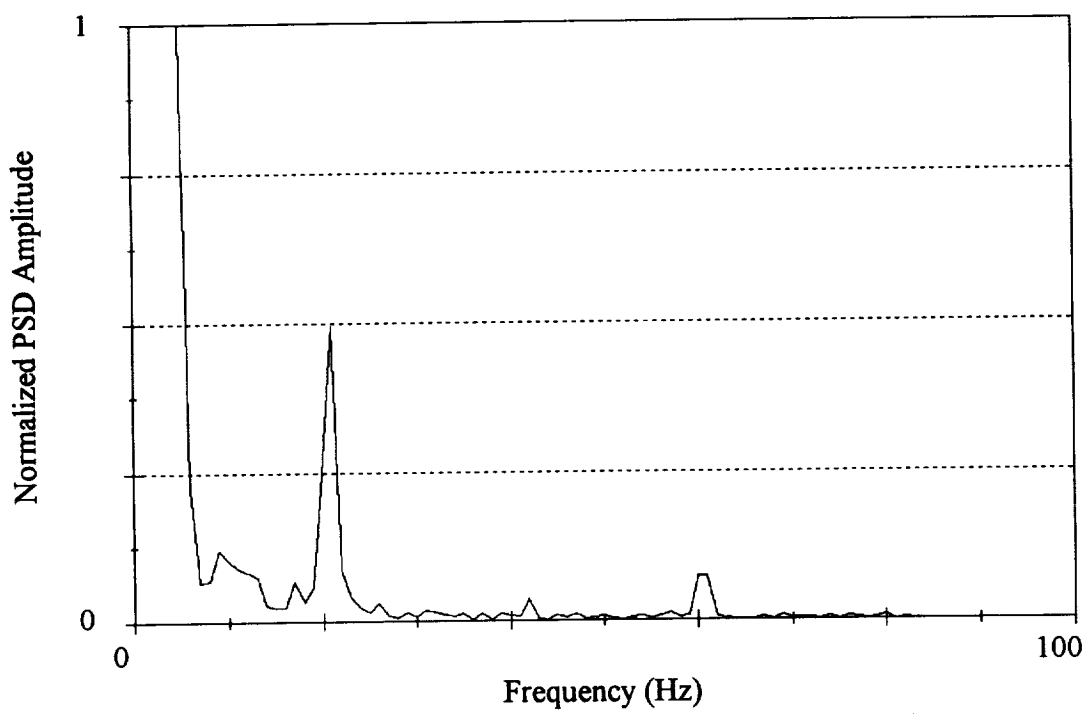


Figure 21. PSD from case H in sample number twelve.

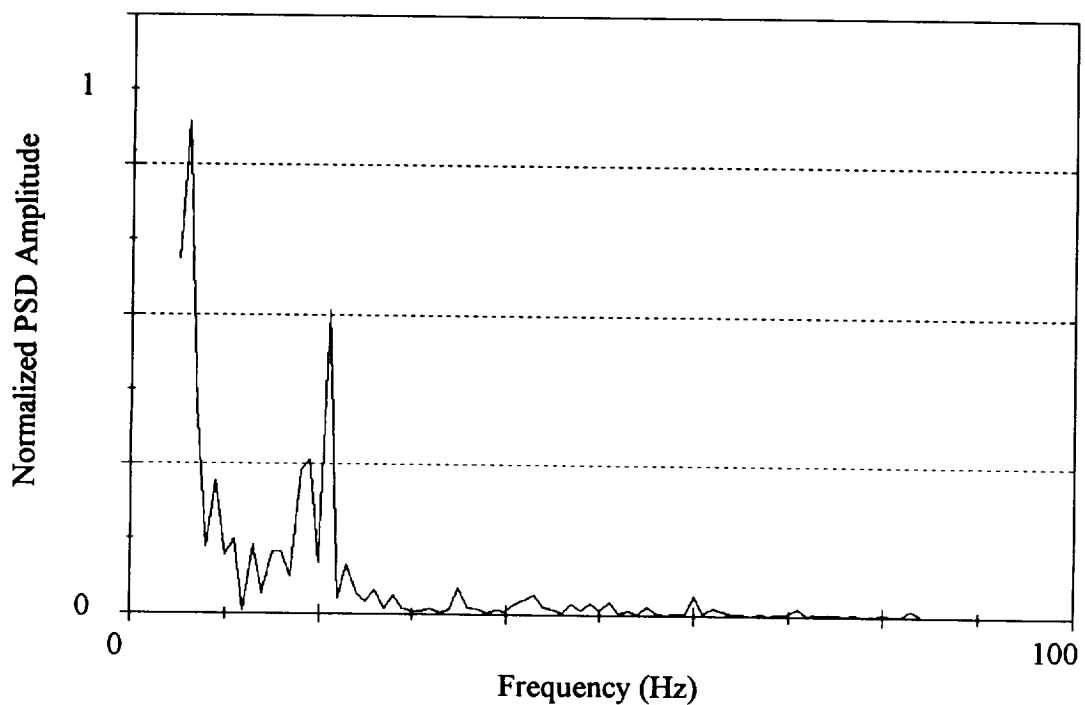


Figure 22. PSD from case H in sample number thirteen.

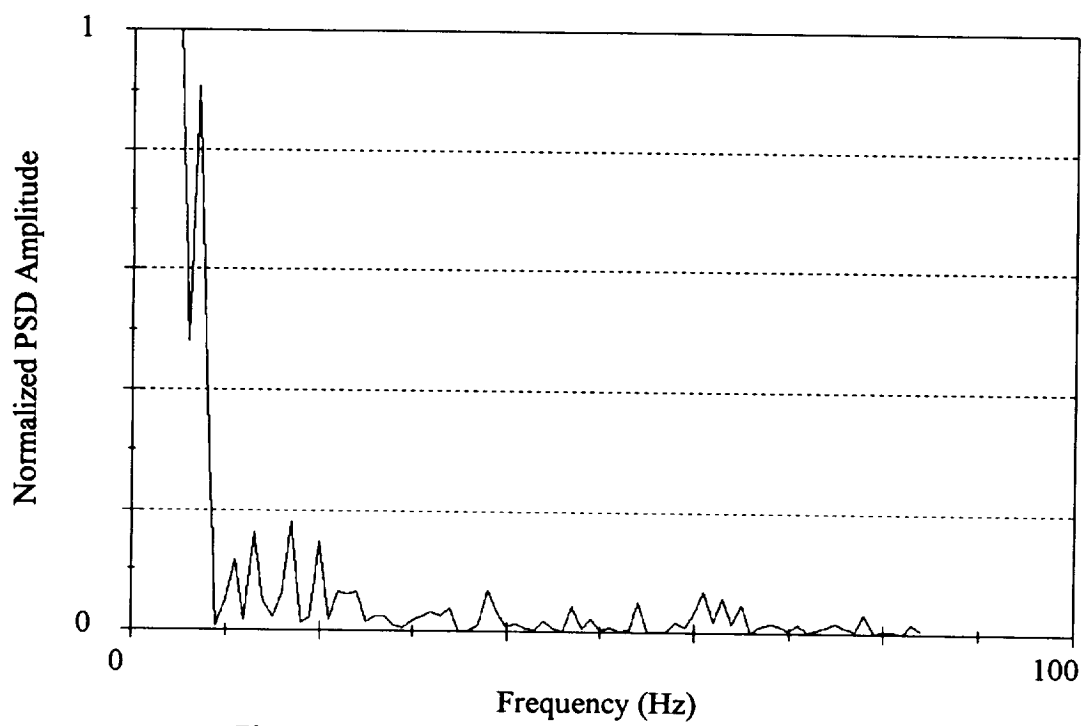


Figure 23. PSD from case G in sample number fourteen.

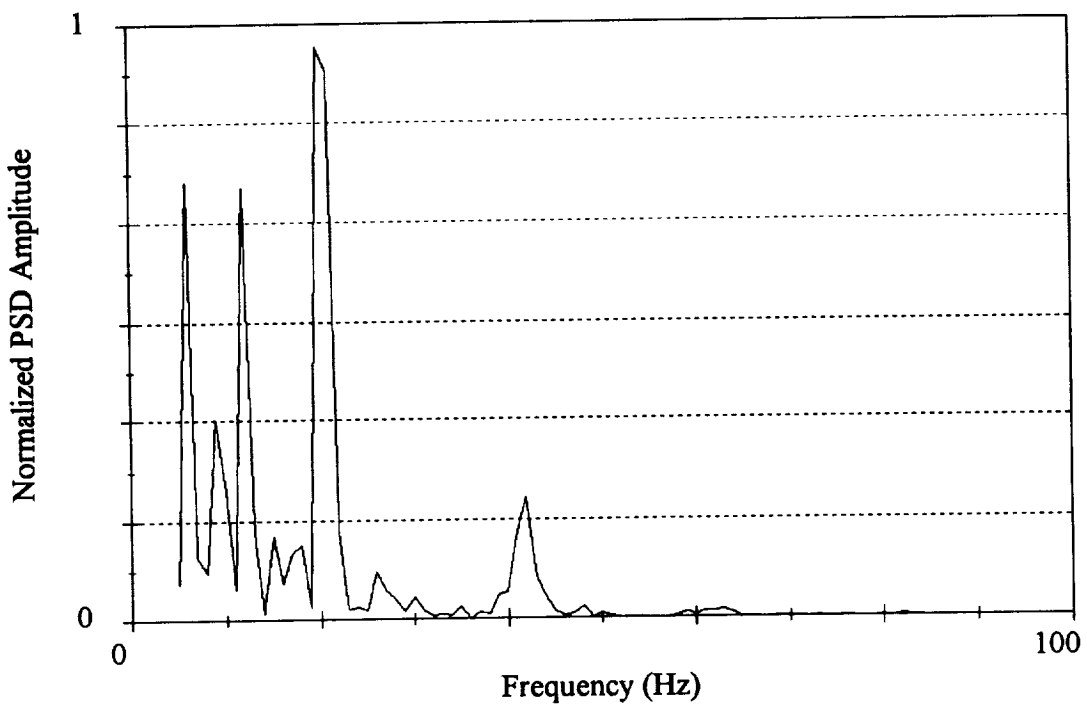


Figure 24. PSD from case F in sample number fifteen.

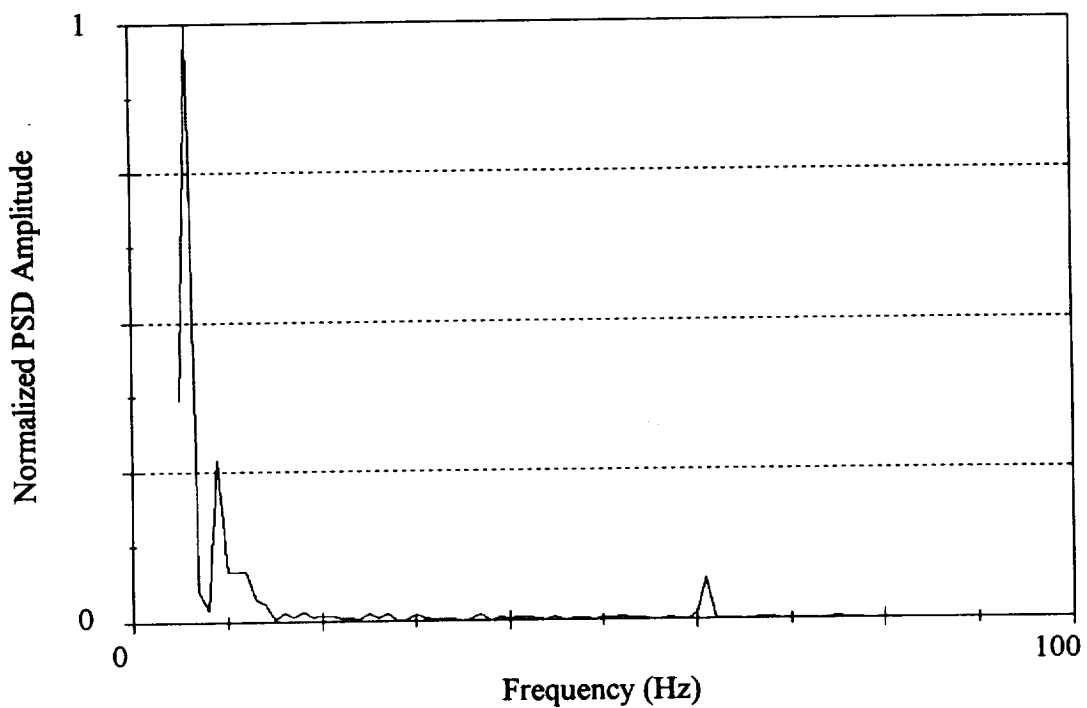


Figure 25. PSD from case G in sample number sixteen.

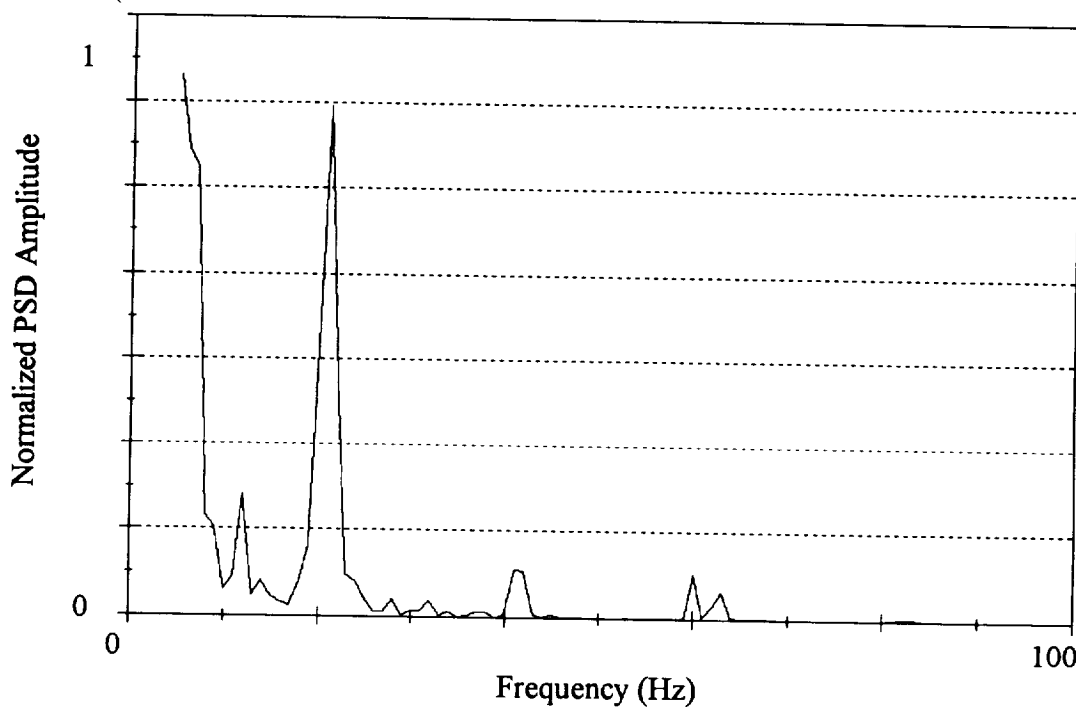


Figure 26. PSD from case I in sample number seventeen.

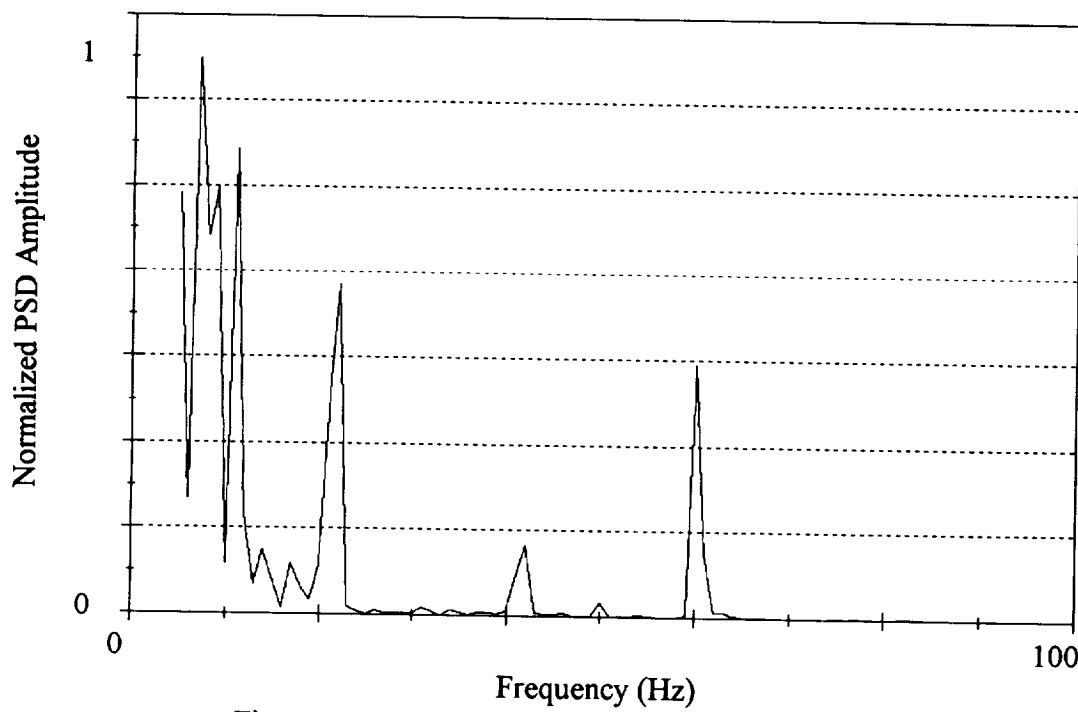


Figure 27. PSD from case H in sample number eighteen.

APPENDIX A SIMULATED SOURCES

In order to eliminate noise and effects that were associated with signals measured at field sites, and to provide any given case desired for testing, a computer code that would simulate a moving source was programmed. The code, which was written in Visual Basic, allowed the user to control the initial position, velocity, frequency, and phase of up to three sources, in addition to the positions of up to three microphones. The output of these three microphones was recorded into three files in an ASCII format. A sample input screen from this program can be seen in figure A.1.

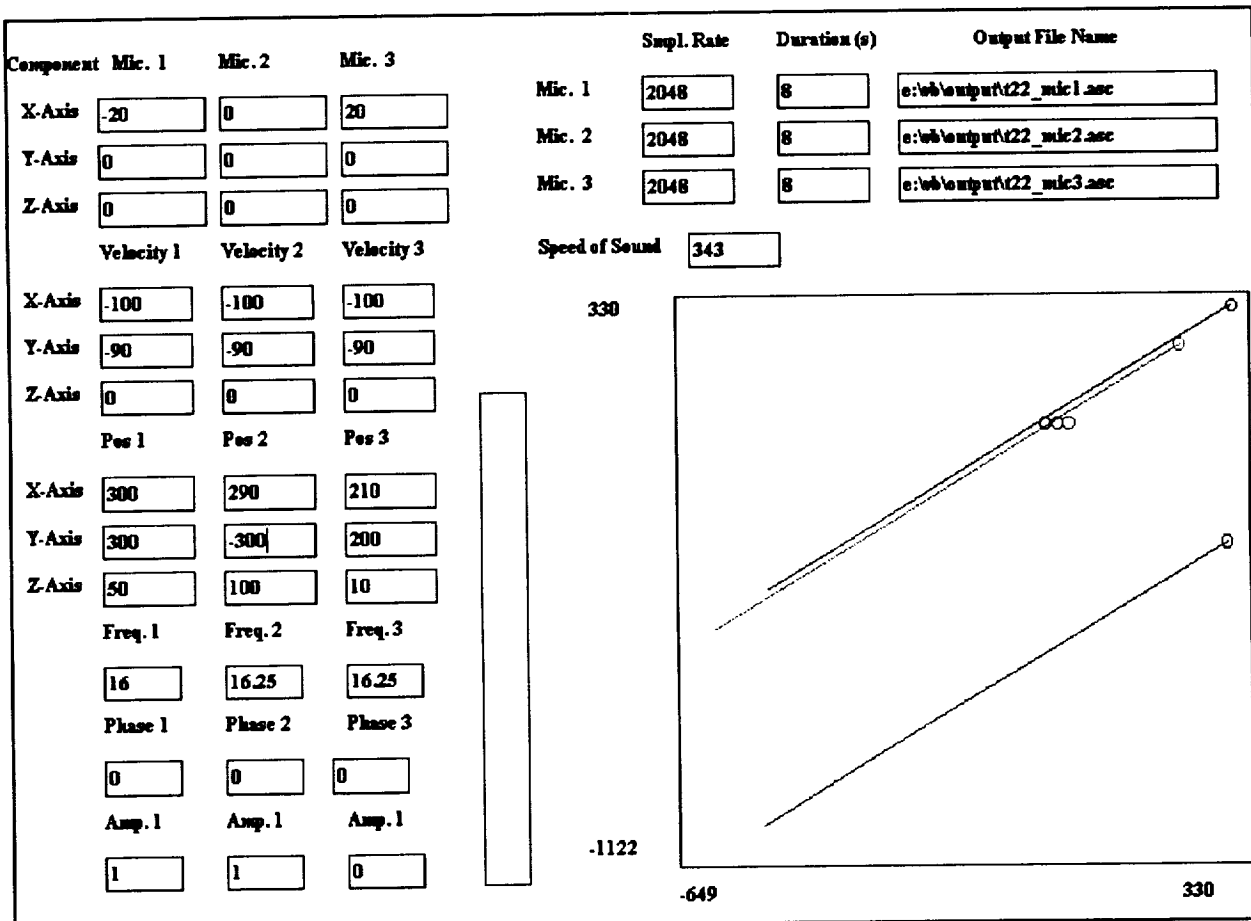


Figure A.1. Sample of input screen from moving source simulation program.

N94-24221

ACOUSTIC TARGET DETECTION AND CLASSIFICATION
USING NEURAL NETWORKS¹

James A. Robertson
Mark Conlon
IIT Research Institute
4140 Linden Ave., Suite 201
Dayton, OH 45432

SUMMARY

This research demonstrates a neural network approach to the classification of acoustic emissions of ground vehicles and helicopters. Data collected during the Joint Acoustic Propagation Experiment conducted in July of 1991 at White Sands Missile Range, New Mexico was used to train a classifier to distinguish between the spectrums of a UH-1, M60, M1 and M114. An output node was also included that would recognize background (i.e. no target) data. Analysis revealed specific hidden nodes responding to the features input into the classifier. Initial results using the neural network were encouraging with high correct identification rates accompanied by high levels of confidence.

INTRODUCTION

The strong and definable acoustic emissions from ground vehicles, helicopters and aircraft make systems employing acoustic sensing attractive. Sources such as engines, tracks, rotor systems and propulsion systems generate emissions which acoustic sensors can use to determine target line of bearing, range and identification. These sensors can provide passive detection at relatively large distances without the line-of-sight restrictions radar systems impose.

The fidelity of an acoustic target classifier becomes crucial in applications such as identification friend or foe (IFF), border monitoring and smart mines. It is vital that the identification is correct with a high level of confidence. Traditional approaches to designing a classifier consist of extracting a number of candidate features from a training set from which a final feature set is selected for the logic design. The performance of the classifier depends upon how closely the test or recall database resembles the training database. If the classifier does poorly, the database could be extended to include more data; however, this could lead to a situation where individual classes might not be separable. In general, traditional classifiers will

¹ Work performed on contract at IIT Research Institute,
DLA900-86-C-0022

do well over test databases which use training databases which encompass the range of target conditions anticipated.

Unfortunately, databases are rarely this comprehensive. The signature variations due to the environment, terrain, vehicle maintenance, and other dynamic conditions are difficult to predict and impossible to fully characterize.

An exceptional classifier should be flexible, robust and be able to cope with varying levels of noise and still correctly identify most target samples. It should be able to deal with a complex system which may not be fully understood. Most importantly, it must be able to generalize from a limited amount of training data and maintain good performance on data which may contain only some similarities to the training set.

The difficulty of the problem suggests that a neural network (NN) may provide a viable solution.

NEURAL NETWORK OVERVIEW

A NN is a system which mimics the computational ability of biological systems. They consist of large numbers of interconnected neurons (nodes). These neurons take data from sensors or other neurons, perform simple operations on the data and pass it on to another neuron.

One of the most popular networks for applications is backpropagation(BP). BP is a multi-layer feed forward NN. The meso-structure of a typical three layer feed forward NN is shown in Figure 1. These layers are referred to as the input, hidden and output layers. The interconnection between the i th input node and the h th hidden node is referred to as W_{ih} , whereas the interconnection between the h th hidden node and the j th output node is referred to as W_{hj} . A set of features is applied to the input node, then the NN processes this data calculating the activation levels of the hidden and output nodes. The output of a neural network used for classification may be referred to as the class activation level. The number of input features determines the number of input nodes. The number of output nodes is determined by the number of target classes. The number of hidden nodes, and if necessary, hidden layers, is generally application specific.

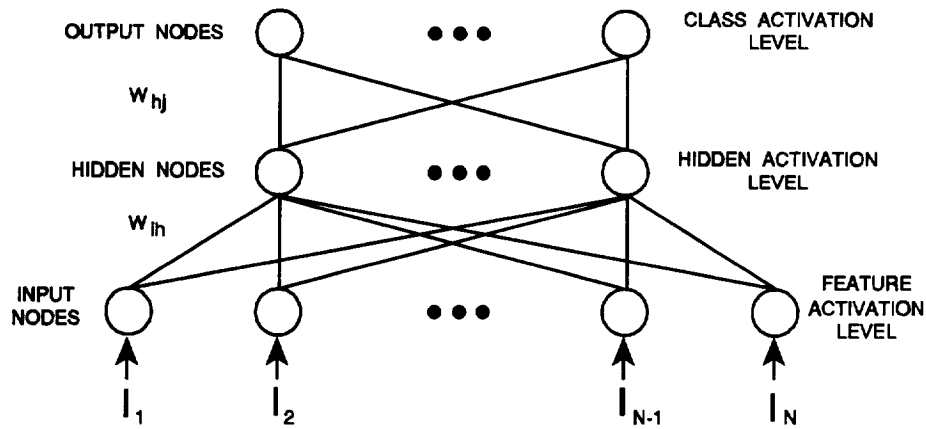


Figure 1. Meso-structure of a multi-layer feed forward NN

Figure 2 illustrates the processing that occurs at the neuron level in a NN. After summing the input values multiplied by the interconnections plus the jth nodes threshold associated with it, a transfer function is used to scale the neuron's responses to incoming signals. Many types of transfer functions exist including threshold-logic, hard-limit, continuous-function and radial basis. Two of the more common continuous transfer functions, the sigmoid and modified sigmoid, are shown. A sample calculation of the jth activation level is also shown.

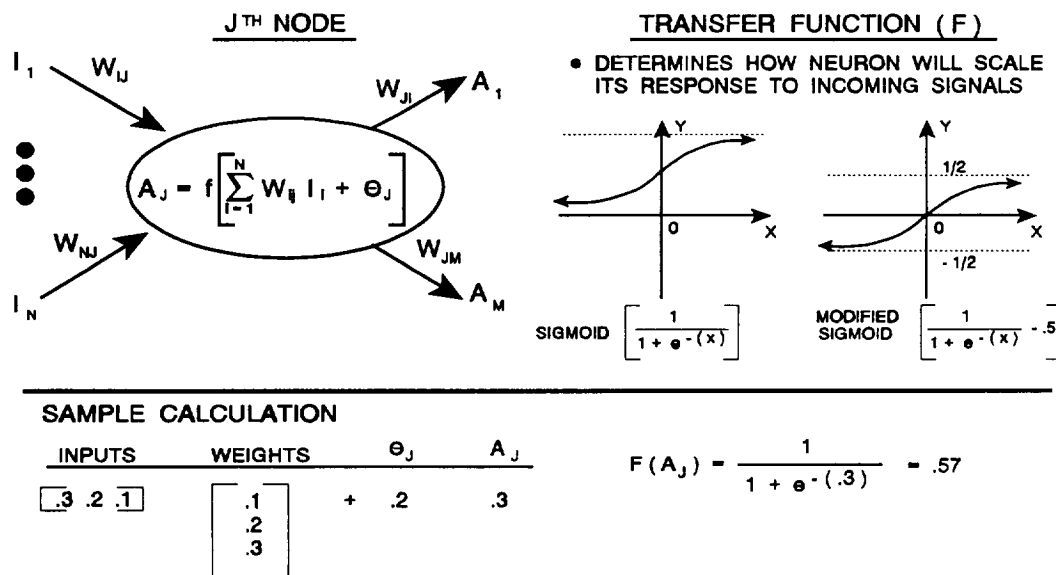


Figure 2. Micro-structure of a NN

BP uses a generalized delta rule for learning. This rule allows the error to affect all layers of the interconnection weights. The method of learning is supervised where actual training data is used. Initially, the weights and threshold are randomized to small values, usually between 0 and 1 or -0.5 and +0.5. Adjustments to the weights and thresholds in all layers are made according to the difference between the desired output activation level and the actual activation level as shown in equation 1.

$$\text{ERROR} = C_j (1 - C_j) (C_j^k - C_j) \quad (1)$$

where:

C_j = actual output of jth node

C_j^k = desired output of jth node

The advantages of NNs have been reported by many researchers (ref. 1). The most attractive reason for using a NN, particularly for target classification, is its ability to generalize. A NN has the ability to generalize and find similar features to that of the training database. For a classifier to be successful in an unknown and poorly characterized environment, it must have the ability to generalize. Another advantage is a NNs' ability to store and distinguish many patterns. This is alluring as both the number of classes and the variability within the class increase.

Researchers have also noted some limitations and disadvantages using a NN. BP in particular suffers from lengthy training sessions. There are ways to reduce the training time by adding momentum (ref. 2), scaling inputs, thresholds and weights, and adapting the learning rates after each iteration (ref. 3). However, even after optimizing for speed, training sessions may still be lengthy. A NN is specific for a certain application. After it has been trained to identify n classes, adding a new class, n + 1, requires retraining the NN. Another disadvantage is the difficulty associated with selecting the number of hidden nodes in a NN. General formulas to determine the number of hidden nodes (e.g. Lippman ref. 4, Hecht-Nielson ref. 5) may help for an initial guess; however, the particular application appears to be the driving force. Selecting too many hidden nodes may cause the NN to memorize the input patterns as opposed to generalize. Selecting too few hidden nodes may yield an unstable NN incapable of forming complex decision regions.

EXPERIMENT

Acoustic data was collected at White Sands Missile Range, Dirt Site in July, 1991 during the Joint Acoustic Propagation Experiment (JAPE) by personnel from MIT Lincoln Laboratory. All data was lowpass filtered at 670 Hz and sampled at 2kHz at MIT Lincoln Laboratory. Single channel data was selected from six different trials notated by trial numbers as shown in Table 1.

Table 1. JAPE data set

JAPE TRIAL NUMBER	TARGET	DESCRIPTION
015507	UH1	100 knots, 150 m Alt.
080507	M1	20 mph
092508	M60	20 mph
115509	M114	15-20 mph
095amb	none	background
084508	M60	idle, 750 rpm

The selected data was segmented into 1 second samples, and Hanning windowed. The power spectrum was then estimated for each sample. The amplitude values from 1 Hz to 150 Hz were used as input into the NN. The NN meso-structure consisted of 150 input nodes, 80 hidden nodes and 5 output nodes. The output nodes represent each target class: UH1, M1, M60, M114 and background (no target). In order to increase convergence all inputs, weights, thresholds and outputs were normalized between -0.5 and +0.5. The error term was adjusted to properly apply the modified sigmoid transfer function as shown in equation 2.

$$d_j = (c_j + 1/2) (1/2 - c_j) (c_j^k - c_j) \quad (2)$$

where:

c_j = actual output of jth neuron

c_j^k = desired output of jth neuron

A momentum term was used to decrease oscillations and decrease training time. All training continued until the rms error over the entire training set was less than 1%. Approximately 20-30% of the data set was not used in training sessions but saved for effectiveness testing.

RESULTS

A closer look at the hidden activation levels may provide insight into the operation of the NN. The hidden activation level is the actual output of a hidden node. Ideally the knowledge stored in the hidden layer is abstracted from the information contained in the input pattern. A

wide variety of features can be represented in the hidden layer. This layer often shows which hidden nodes become activated in response to a particular input pattern.

Figure 3 shows sample input, hidden activation level and class activation level when the target was a UH-1. The NN was able to map the differing inputs into a relatively invariant set of hidden activation levels and class activation levels. Comparing the hidden activation levels for the UH-1 target to the hidden activation levels from other target class samples revealed that certain nodes were responding to the input patterns. The 22nd and 32nd hidden nodes appeared to be most useful for distinguishing the UH-1 from the M60. The 20th hidden node appeared to be most useful for distinguishing between the UH-1 and the APC, whereas the 40th node was the most useful for distinguishing between the UH-1 and the M1.

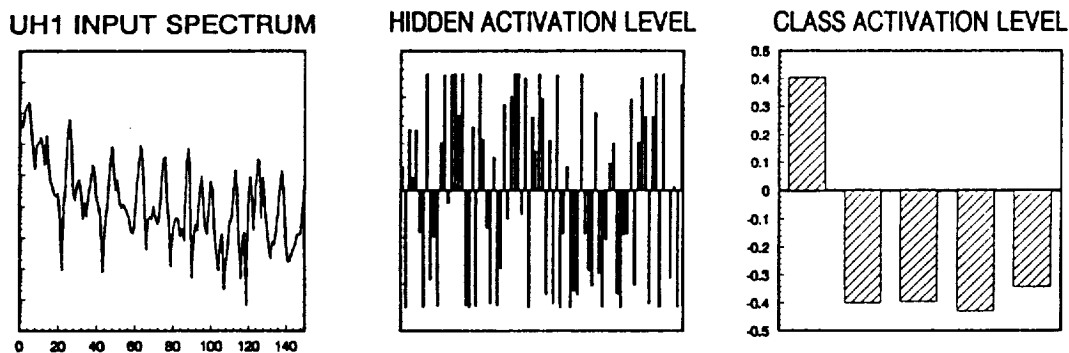


Figure 3 UH1 NN input, hidden and class activation levels

Figures 4 through 7 show samples of the M1, M60, APC and background NN results. A similar hidden node analysis was done to yield the distinguishing nodes as listed in Table 2.

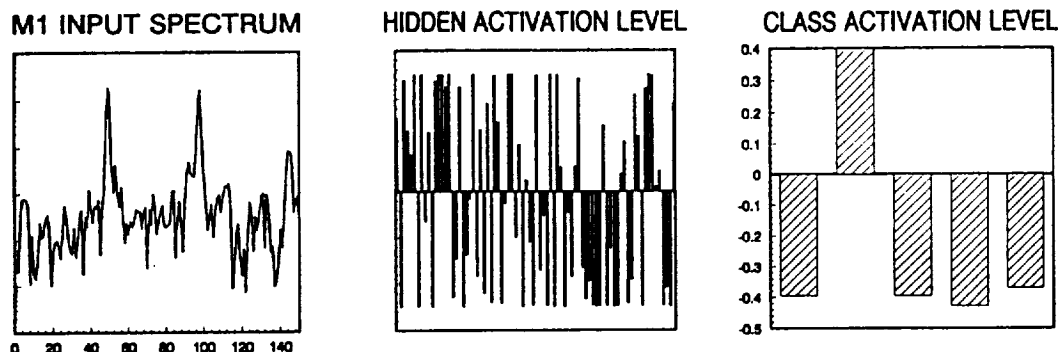


Figure 4 M1 NN input, hidden and class activation levels

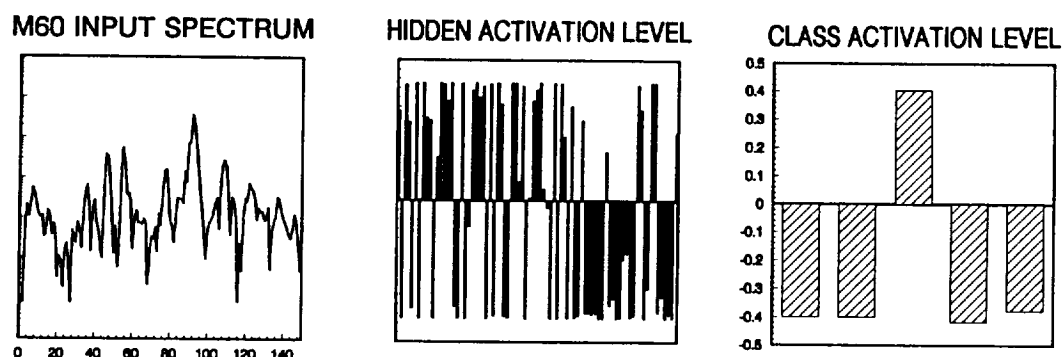


Figure 5 M60 NN input, hidden and class activation levels

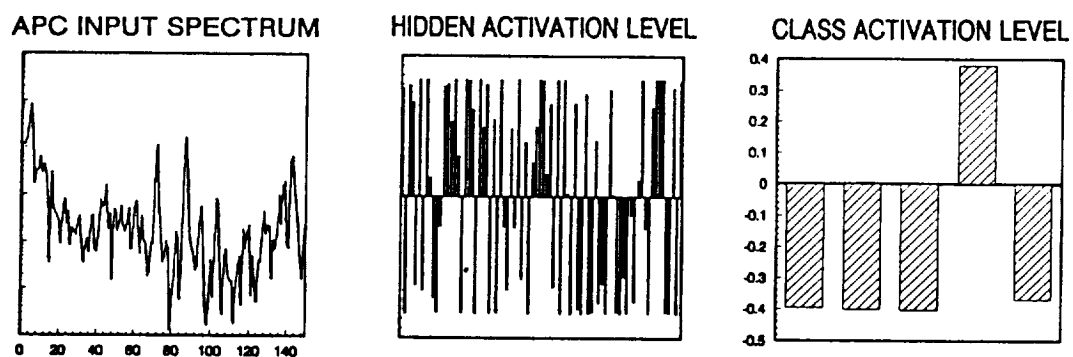


Figure 6 M114 NN input, hidden and class activation levels

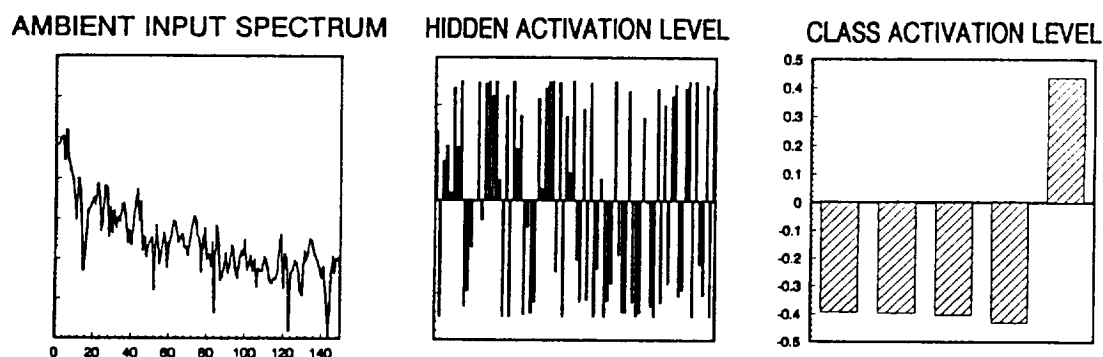


Figure 7 Ambient NN input, hidden and class activation levels

Table 2. Hidden nodes for class separation

Target	UH-1	M1	M60	APC	Ambient
UH-1	-	19,40,74	18,19,22,32, 52,74,75	18,19,20, 52,74	-
M1	19,40,74	-	40	20,40	17,29,40,64, 74,78
M60	18,19,22,32, 52,74,75	40	-	20,22,75,78	18,22,29,32, 52,56,64,68, 74,75,78
APC	18,19,20, 52,74	20,40	20,22,75,78	-	18,20,29,52, 74
Ambient	-	17,29,40,64, 74,78	18,22,29,32, 52,56,64,68., 74,75,78	18,20,29,52, 74	-

Analysis of the hidden nodes also revealed that some nodes did not assist in the classification of any of the targets. Hidden nodes, numbers 2, 16, 34, 46, 73 and 79, yielded the same hidden activation level for all inputs. This suggests that the NN could have learned the same amount of information with less hidden nodes.

The test set was used to determine overall correct classification. Results showed greater than 98% classification for all classes. A system user may want to know how confident an identification is at a particular time. Confidence levels were calculated for each class by using the difference of the highest activation level and the second highest class activation level divided by the maximum activation level difference. Values should range between 0.0 and 1.0. Ideally confidence levels should be high for correct identifications and low for incorrect identifications. The confidence levels of the NN shown in Figure 8 adhere to these guidelines. Notice that for each of the classes, if the NN identification was correct the confidence level was 0.9 or above. However, when the NN identification was incorrect the confidence level was 0.6 or below.

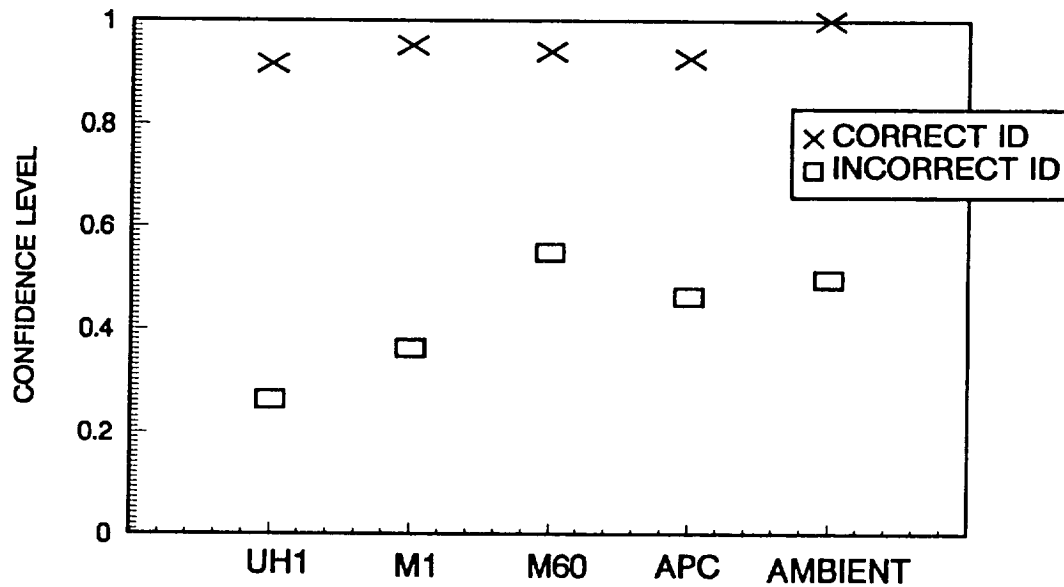


Figure 8 Confidence levels for a trained NN: correct ID vs incorrect ID

CONCLUSIONS

A NN has been used to successfully identify the acoustic emissions of ground vehicles and helicopters. Initial analysis indicates that a high level of confidence can be associated with the identification using a NN classifier. The hidden node analysis demonstrated that the hidden layer is distinguishing between classes using the target specific input features. The analysis also indicated that a smaller number of hidden nodes would suffice for this particular example. The use of ambient or background data as an output class could prove quite useful in determining when no target is present.

A NN trained using a fairly large database could improve the classification performance of existing acoustic sensors. The generalization capability characteristic of a NN will enhance the performance of acoustic sensors.

REFERENCES

1. Maren, A., Harston, C., Pap, R., Handbook of Neural Computing Applications, Academic Press, Inc., San Diego, 1990.
2. Rumelhart, D., McClelland, J., Parallel Distributed Processing, MIT Press, Cambridge, Massachusetts, 1988.
3. Fahlman, S.E., " An empirical study of learning speed in backpropagation networks", Carnegie Mellon Technical Report, CMU-CS-88-162, June 1988.

4. Lippman, R.P., " An introduction to computing with neural nets", IEEE ASSP magazine, April 1987.
5. Hecht-Nielsen, R., "Kolmogorov's mapping neural network existence theorem", Proc. First Int'l Joint Conf. Neural Networks, San Diego, CA, June 1987.
6. Marple, S., Digital Spectral Analysis, Prentice-Hall, Inc., Englewood Cliffs, New Jersey, 19

**PRELIMINARY ANALYSIS OF THE JAPE GROUND VEHICLE TEST
DATA WITH AN ARTIFICIAL NEURAL NETWORK CLASSIFIER**

Nathan F. Larsen

Ben L. Carnes

Waterways Experiment Station
Vicksburg, MS

S15-71

JULY 7

P-8

INTRODUCTION

Remotely sensing and classifying military vehicles in a battlefield environment have been the source of much research over the past 20 years. The ability to know where threat vehicles are located is an obvious advantage to military personnel. In the past active methods of ground vehicle detection such as radar have been used, but with the advancement of technology to locate these active sensors, passive sensors are preferred. Passive sensors detect acoustic emissions, seismic movement, electromagnetic radiation, etc., produced by the target and use this information to describe it. Deriving the mathematical models to classify vehicles in this manner has been, and is, quite complex and not always reliable. However, with the resurgence of artificial neural network (ANN) research in the past few years, developing models for this work may be a thing of the past. The purpose of this paper is to present preliminary results from an ANN analysis to the tank signatures recorded at the Joint Acoustic Propagation Experiment (JAPE) at the US Army White Sands Missile Range, NM, in July 1991.

BACKGROUND**Neural Networks**

An ANN can be trained to find generalized patterns in data. The ANN is trained by analyzing a series of training examples for which the appropriate response is known. Once the ANN has been sufficiently trained, it can process unknown data and indicate which category or pattern the data most closely fits. The advantages of an ANN over an analytic model are twofold. First, an ANN is a general algorithm. It can be used in countless applications and its basic structure never changes, while a model must be modified for each investigation. The second advantage is speed. Given a sufficient training set and moderate computing power, an ANN can be developed to classify data in a fraction of the time it would take to produce a model to perform the same function.

Acoustic Data Acquisition

The acoustic data were acquired during the JAPE by placing microphones at several distances from the test track. The data used in this paper were measured by a microphone located 10 m from the center of the track. The track was approximately 3.5 km long and was relatively flat and straight. The microphones were placed 1 km from the south end of the track near the south tower. The tank started at either end of the track and passed at a constant velocity, generally about 20 kph. A total of ten runs were acquired for each tank, five in the early morning (0000 to 0600 hours) and five in the late morning (0900- 1100).

Tank Descriptions

The tanks used at JAPE were an M1 and M60, both US vehicles. Both of these tanks were used to train the ANN. The M60 was the United States' main battle tank during the 1960's. It's powered by a 750 hp diesel engine and weighs 52.6 tonnes. The M1 is the current US main battle tank. It uses a 1500 hp gas turbine engine and weighs 57.1 tonnes. The turbine engine in the M1 gives it a unique acoustic signature that is different from most tanks.

PROCEDURE

Neural Network Configuration

An ANN consists of a network of neurons. Each neuron is a crude mathematical equivalent of a biological neuron. It receives multiple inputs, sums them, passes this sum through a transfer function (usually a sigmoid formula), and outputs the result. These neurons are generally placed in layers. The outputs from the neurons in the previous layer neurons are fed into the input of the neurons in the current layer. Each input to a neuron is weighted, and it is these weights that are altered when the ANN undergoes the iterative training process. The greater the weight the greater the influence that input has on the output. By changing these weights, the ANN selects which features in the training set are important for classification.

The ANN program used was freeware obtained over the Internet network and was written in the C programming language. It was tested extensively with simple pattern recognition problems and proved to be robust. The software was compiled to run under DOS using the Intel 32-bit C compiler, as well as on the Cray Y-MP under UNIX.

Three basic ANN configurations were tested. The first two had one hidden layer with 20 and 50 neurons, respectively. The last had two hidden layers with 50 neurons in the first layer and 20 in the second. The output layer consisted of two neurons. The first yielded a

one for an M1 and a zero for an M60, while the second produced a zero for an M1 and a one for an M60. All neurons implemented the sigmoid transfer function and were fully connected. All networks were trained by the backpropagation technique.

Training Set

Selection

The primary training set consisted of two complete early morning runs, one of an M60 and one of an M1. Both travelled 1 km south of the closest point of approach (CPA) to the microphones to 2.5 km north of CPA. The first set was selected to determine if this minimum number of runs would be sufficient to train an ANN to recognize tank signatures from other runs. In addition, a second set of four runs was briefly used to determine if one pass in each direction was sufficient for each vehicle. It consisted of the two passes used in the first set plus two passes of the vehicles travelling from north to south.

Processing

The recorded acoustic data were digitized by an 80486 Personal Computer (PC) based 16-bit Analog to Digital (A/D) board at 2048 samples per second. Fast Fourier transforms (FFT's) were performed on each second of this data with only 1 through 100 Hz retained for the training set. Only FFT magnitude information was used. Each FFT was normalized to the largest frequency component within it. Table 1 shows the training sets used.

Training Procedure

The one second FFTs were ordered randomly in the training set without regard to run or time into the run. The ANN program took this random training set and trained itself by sequentially passing through the set. So while the training set was random, the randomness was the same for every iteration. One iteration was defined to be one complete pass through the training set. Several combinations of ANN configurations and training parameters were used (Table 2).

Testing Set

Selection

Two test sets were used. The first consisted of two runs, one each of the M60 and M1. One north to south pass was chosen at random from the early morning passes for each vehicle. The second set also contained two runs, but both were south to north passes. As

with the first set, one run was chosen from the early morning passes. This second set was used because it matched the vehicle direction of the first training set. See Table 3 for more information.

Processing

The processing of the testing sets was identical to the training sets, with the exception that both testing sets contained 700 examples.

Testing Procedure

Since randomness in the testing set is not important, the examples were placed in temporal order by run number. The ANN processed this data using the neural weights it calculated during its training phase. Table 2 shows which test sets were tested with each ANN configuration.

RESULTS

The percentages of correct classifications for ANN with 0.9 momentum, 0.7 training rate, and training set 1 are shown in Figure 1. Most of the percentages hovered around 60 percent, with the 50 neuron case classifying the best on test set 1 with an average of 63 percent correct. The two layer ANN (50 and 20 neurons) performed the best on the second test set at 63 percent as well. The same tests using a momentum of 0.7 produced the results illustrated in Figure 2. This decrease in momentum rate improved the performance of the 20 and 50 neuron cases to over 60 percent for the second test set, but slightly decreased the two layer performance.

The responses from the individual vehicle passes in the test sets for the 0.9 momentum and 0.7 training rate configuration are shown in Figure 3. The M1 pass performed better than the M60 pass for test set 1, with the opposite being true for the second set. For the 0.7 momentum case in Figure 4 the ANN predicted the M1 better than the M60 for all cases except for the 20 neuron case using the second test set.

ANN configuration three (Table 2) was trained using the second training set (Table 1). It correctly identified the vehicle 63 percent of the time, an improvement of 5 percent over using the first training set.

CONCLUSIONS

From the training and testing sets used, the average correct prediction rate was between 60 and 70 percent. This prediction accuracy is remarkable considering the small amount of analysis performed. Altering the number of iterations and number of neurons seemed to have little effect on this percentage. However, this percentage can probably be improved significantly by improving the training set. The frequency range used (1 to 100 Hz) was probably too narrow in bandwidth and too low in frequency. Also, the number of passes used in the training set was probably too few.

RECOMMENDATIONS

To improve the prediction accuracy of the ANN several improvements are suggested below.

1. **Improve the training set** - This includes increasing and shifting the frequency range of the FFT and increasing its frequency bin widths. Also, training the ANN only on acoustic data when the tank is relatively close to the microphone may improve the response, because of the capability of an ANN to generalize information.
2. **More training examples** - The one ANN trained on four vehicle passes showed some improvement over the two vehicle pass case. More examples could be obtained by using data gathered from several neighboring microphones and geophones.
3. **Optimize the ANN configuration** - Adjusting the momentum, training rates, hidden layers, and neurons per layer would significantly improve the accuracy. Additional adjustments include changing the neural transfer function and connection configuration.

Table 1. Vehicle runs used in the training set.

Training Set Number	JAPE Run Number	Vehicle	Number of Examples	Total Examples
1	078	M1	375	750
	090	M60	375	
2	078	M1	350	1400
	079	M1	350	
	090	M60	350	
	091	M60	350	

Note: Even numbered runs are south to north

Odd numbered runs are north to south

Table 2. ANN training combinations.

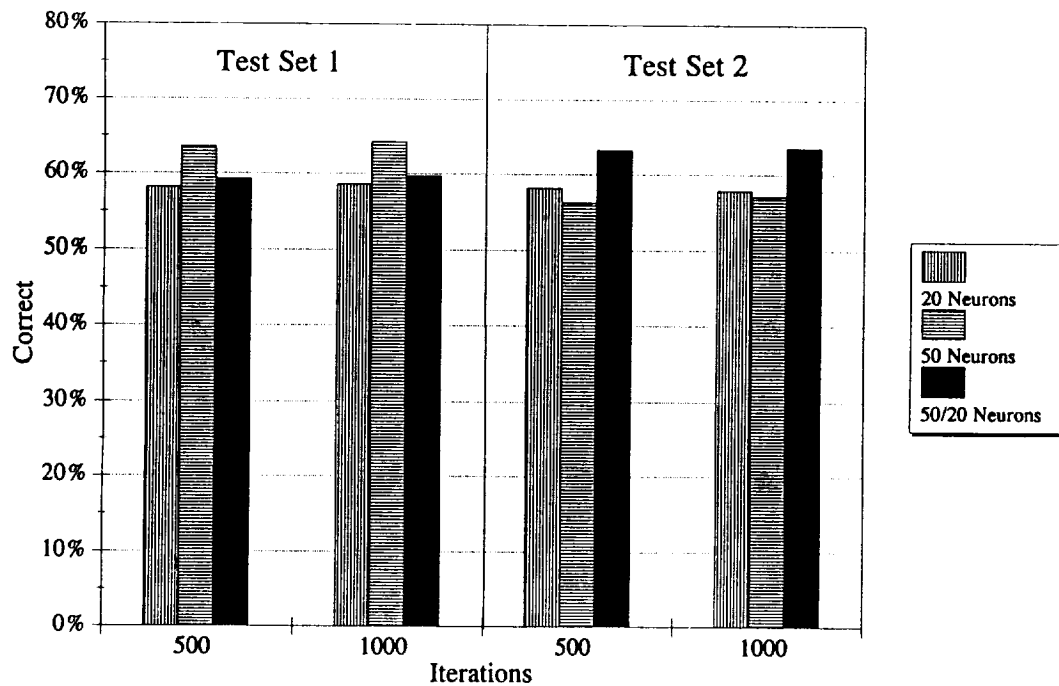
Combination	Momentum	Learning Rate	Number of Layers	Neurons in Layer 1	Neurons in Layer 2	Iterations	Evaluated Using Test Set 1	Evaluated Using Test Set 2
1	0.9	0.7	1	20	N/A	500	YES	YES
2	0.9	0.7	1	50	N/A	500	YES	YES
3	0.9	0.7	2	50	20	500	YES	YES
4	0.9	0.7	1	20	N/A	1000	YES	YES
5	0.9	0.7	1	50	N/A	1000	YES	YES
6	0.9	0.7	2	50	20	1000	YES	YES
7	0.7	0.7	1	20	N/A	250	NO	YES
8	0.7	0.7	1	50	N/A	250	NO	YES
9	0.7	0.7	2	50	20	250	NO	YES
10	0.7	0.7	1	20	N/A	500	YES	YES
11	0.7	0.7	1	50	N/A	500	YES	YES
12	0.7	0.7	2	50	20	500	YES	YES

Table 3. Vehicle runs used in the test set.

Test Set Number	JAPE Run Number	Vehicle	Number of Examples	Total Examples
1	077	M1	350	700
	091	M60	350	
2	076	M1	350	700
	086	M60	350	

Note: Odd numbered runs are north to south

Even numbered runs are south to north



**Figure 1. ANN Configuration Comparison
0.9 Momentum, 0.7 Training Rate, Training Set 1**

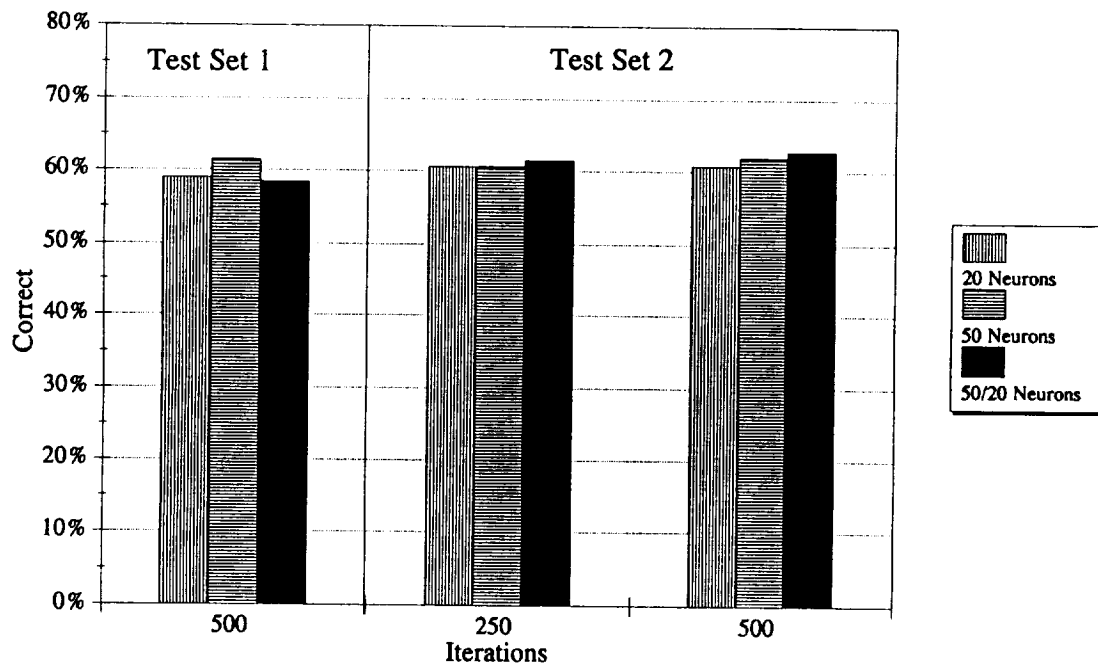


**Figure 2. ANN Configuration Comparison
0.7 Momentum, 0.7 Training Rate, Training Set 1**

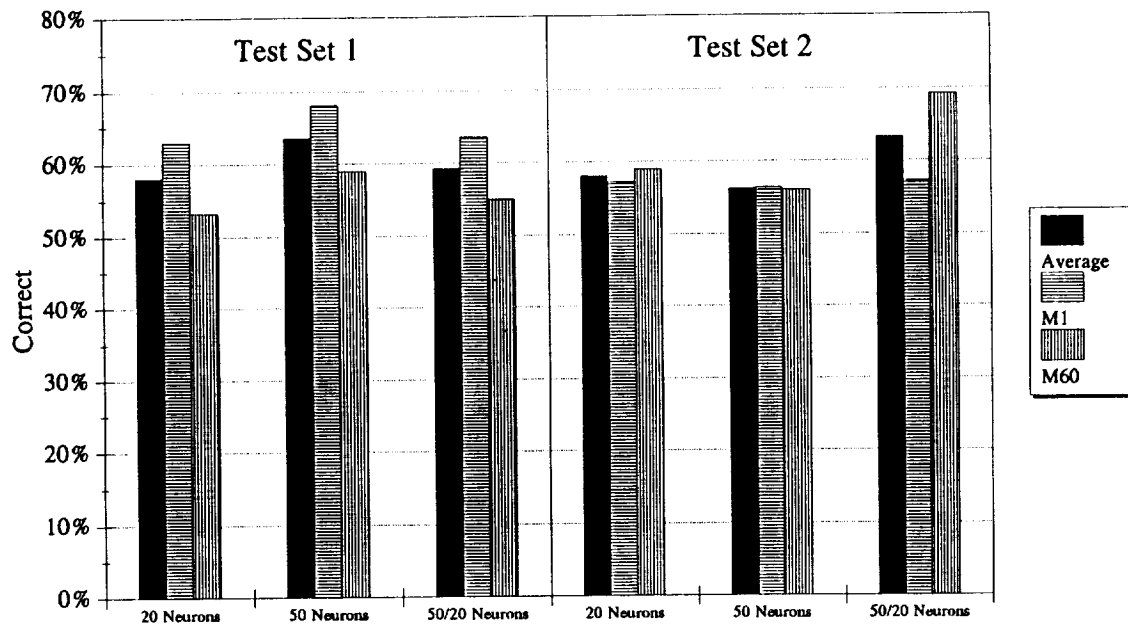


**Figure 3. Individual Run Responses
0.9 Momentum, 0.7 Training Rate, 500 Iterations**

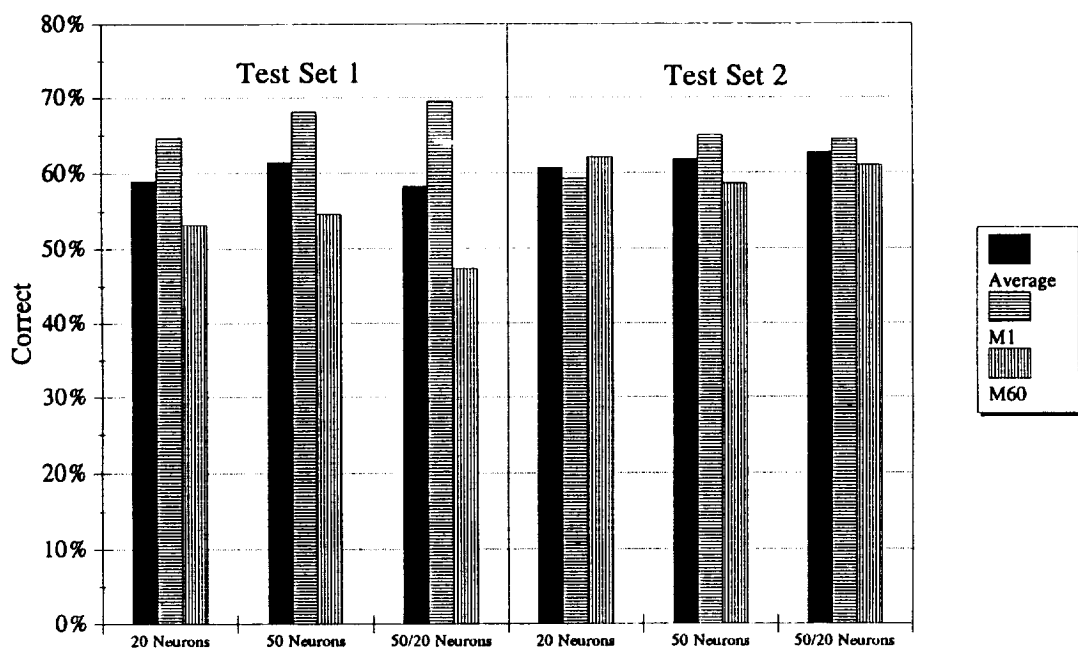


**Figure 4. Individual Run Responses
0.7 Momentum, 0.7 Training Rate, 500 Iterations**

REPORT DOCUMENTATION PAGE			Form Approved OMB No. 0704-0188
<p>Public reporting burden for this collection of information is estimated to average 1 hour per response, including the time for reviewing instructions, searching existing data sources, gathering and maintaining the data needed, and completing and reviewing the collection of information. Send comments regarding this burden estimate or any other aspect of this collection of information, including suggestions for reducing this burden, to Washington Headquarters Services, Directorate for Information Operations and Reports, 1215 Jefferson Davis Highway, Suite 1204, Arlington, VA 22202-4302, and to the Office of Management and Budget, Paperwork Reduction Project (0704-0188), Washington, DC 20503.</p>			
1. AGENCY USE ONLY(Leave blank)	2. REPORT DATE	3. REPORT TYPE AND DATES COVERED	
	December 1993	Conference Publication	
4. TITLE AND SUBTITLE		5. FUNDING NUMBERS	
Joint Acoustic Propagation Experiment (JAPE-91) Workshop		WU 505-63-70-02	
6. AUTHOR(S) William L. Willshire, Jr. and David Chestnutt, Compilers			
7. PERFORMING ORGANIZATION NAME(S) AND ADDRESS(ES) NASA Langley Research Center Hampton, VA 23681-0001		8. PERFORMING ORGANIZATION REPORT NUMBER L-17331	
9. SPONSORING/MONITORING AGENCY NAME(S) AND ADDRESS(ES) National Aeronautics and Space Administration Washington, DC 20546-0001 NASA Langley Research Center, Hampton, Virginia 23681-0001 University of Mississippi, Oxford, Mississippi 38677		10. SPONSORING/MONITORING AGENCY REPORT NUMBER NASA CP-3231	
11. SUPPLEMENTARY NOTES			
12a. DISTRIBUTION/AVAILABILITY STATEMENT Unclassified-Unlimited Subject Category 71		12b. DISTRIBUTION CODE	
<p>13. ABSTRACT (<i>Maximum 200 words</i>) The Joint Acoustic Propagation Experiment (JAPE), performed under the auspices of the NATO AC/243, Panel 3, Research Study Group 11 (RSG-11) on Automatic Pattern Recognition in Battlefield Surveillance with Mechanical Waves, was conducted at the White Sands Missile Range, New Mexico, USA, during the period July 11-28, 1991. JAPE consisted of various short and long range propagation experiments using various acoustic sources including speakers, propane cannons, helicopters, a 155mm howitzer, and static high explosives. Of primary importance to the performance of these tests was the extensive characterization of the atmosphere during these tests. This atmospheric characterization included turbulence measurements.</p> <p>A workshop to disseminate the results of JAPE-91 was held in Hampton, Virginia on April 28, 1993 at the conclusion of the 27th meeting of the RSG-11. The workshop was jointly sponsored by the University of Mississippi and the National Aeronautics and Space Administration (NASA). This report is a compilation of the presentations made at the workshop along with a list of attendees and the agenda.</p>			
14. SUBJECT TERMS Long range; Sound propagation; Ground effects; Meteorological effects; Terrain masking neural networks		15. NUMBER OF PAGES 197 16. PRICE CODE A09	
17. SECURITY CLASSIFICATION OF REPORT Unclassified	18. SECURITY CLASSIFICATION OF THIS PAGE Unclassified	19. SECURITY CLASSIFICATION OF ABSTRACT	20. LIMITATION OF ABSTRACT

